Characterization and Flow of Food and Mineral Powders

A thesis presented in partial fulfillment of the requirements for the degree of

Doctor of Philosophy
in
Engineering

at Massey University, Manawatū,
New Zealand.

Horng Yuan Saw

2016

Abstract

Powders are important commodities across different industries, such as the food and pharmaceutical industries. In these industries, powders are usually made, mixed, milled, packaged, and stored; these operations require the powders to move and flow under desired conditions and different stress levels. Failure to flow will cause hindrances to production; therefore knowledge of powder flow or flowability is important. There is a constant demand for accurate, reliable, and robust measurement and characterization methods for powder flowability.

Powders behave differently under varying conditions; the behaviour of a powder is influenced by particle size distribution, and powder handling and processing conditions. There is to date no one "standard" method to characterize powder flowability; it is common to use a variety of methods and devices to measure flow properties and provide insight into the behaviour and flow characteristics of powders under different conditions.

The flow properties of model food and mineral powders were measured and assessed by shear testing, compression via tapping, fluidization, and powder tumbling. Shear testing was done with an annular shear cell following Jenike (1964) and Berry, Bradley and McGregor (2014). Compression via tapping was performed according to a procedure in the dairy industry (Niro, 1978) and the European Pharmacopoeia (Schüssele & Bauer-Brandl, 2003). Fluidization was used to measure powder bed expansion and bed collapse following the powder classification framework provided by Geldart and co-workers (Geldart, 1973; Geldart, Harnby, & Wong, 1984; Geldart & Wong, 1984, 1985). Powder tumbling was performed in a novel *Gravitational Displacement Rheometer*, GDR, which measured the motion and avalanche activity of powders that moved under their own weight when rotated in a cylinder at different drum speed levels.

The flow data from each characterization method were evaluated individually with regards to particle size distribution and then assessed collectively. The findings presented and discussed include the i) demonstration of the dominant influence of surface-volume mean particle diameter on powder flow properties, ii) characterization of flowability based on Jenike's arbitrary flow divisions, iii) development of new correlations for the estimation of powder cohesion and bulk density at low preconsolidation stresses, iv) demonstration of hopper outlet diameter as a measure of flowability, v) demonstration of the limited utility of Hausner ratio as a flowability index, vi) substantiation of von Neumann ratio as a sensitive and useful indicator for identifying the onset of bubbling in fluidized beds using bed pressure fluctuation data, and vii) demonstration of the utility of standard deviation of the GDR load cell signal as an indicator of powder avalanche activity. These findings provide improved understanding and knowledge of powder flowability; they can be used to assist and facilitate the development of new techniques and solutions relevant to the handling and processing of powders especially in the food and pharmaceutical industries.

Acknowledgement

I thank and praise my Lord and Saviour Jesus Christ for making everything possible.

My heartfelt acknowledgment and gratitude go to the people listed below; they have made various contributions to the completion of this Ph.D. thesis:

Ruth Saw, my beloved wife, soul mate, and best friend, my beloved mother Madam Yoke Yee Hor, and sisters Pek Wan Saw and Pek En Saw.

Professor Clive E. Davies, Principal Supervisor, and Professor Anthony H. J. Paterson and Professor Jim R. Jones, Co-supervisors, School of Engineering and Advanced Technology, Massey University.

Ann-Marie Jackson, John Edwards, Clive Bardell, Nick Look, Anthony Wade, and Kerry Griffiths, technical services staff of School of Engineering and Advanced Technology, Massey University.

Michele Wagner, Linda Lowe, Glenda Rosoman, Gayle Leader, Trish O'Grady, and Dilantha Punchihewa, administrative staff of School of Engineering and Advanced Technology, Massey University.

Professor Paul J. Moughan, Professor Harjinder Singh, John Henley-King, Dr. Guillaume Brisson, Dr. Emile S. Webster, and Janiene Gilliland of Riddet Institute.

Professor Fernando J. Muzzio of Rutgers University, Associate Professor Tony Howes of the University of Queensland, Dr. Kalyana Pingali and Casey Kick of Western Michigan University, and Dr. Abraham S. Chawanji of Fonterra Research Centre.

Pastors Dale and Rachel Meacheam, Pastor Nick Ling, friends from Vision Church Palmerston North, and Pastor Lionel Smith.

Pastor Ezra Chin and friends from Emmanuel Church Kota Kinabalu, Malaysia.

Table of Content

List of Figures

List of Tables

Nomenclature

A_p	Surface area of material [m^2]
a_s, b_s	Fitting parameters of Equations 3.8 and 3.9 [units according to usage]
a_t, b_t	Fitting parameters of Equations 4.1 [units according to usage]
B	Minimum width of outlet required for mass flow from a hopper [m]
C	Cohesion [Pa]
C^*	Estimated cohesion [Pa]
C_0	Cohesion at zero preconsolidation stress [Pa]
c_1, c_2	Fitting parameters of Equation 4.9 [units according to usage]
d_{pi}	Incremental mean particle diameter [m] which is the mean of the sum of upper and lower nominal apertures in sieve analysis
d_{10}	Particle diameter at 10% in a cumulative size distribution [m]
d_{32}	Surface-volume mean particle diameter [m]
$d_{32,M}$	Surface-volume mean particle diameter measured with Mastersizer 2000 [m]
$d_{32,S}$	Surface-volume mean particle diameter measured with sieve analysis [m]
d^*_{32}	Surface-volume mean particle diameter calculated with Mastersizer data using bins equivalent to a full sieve analysis according to BS 410; powder in the range of 0–38 μm has been grouped together and assigned a mean particle diameter of 19 μm in the calculation [m]
d_{50}	Particle diameter at 50% in a cumulative size distribution [m]
d_{90}	Particle diameter at 90% in a cumulative size distribution [m]
FF	Powder flow function [-]
F_{10}	Fraction of fines smaller than 10 μm calculated with Mastersizer data [-]
F_{20}	Fraction of fines smaller than 20 μm calculated with Mastersizer data [-]
F_{30}	Fraction of fines smaller than 30 μm calculated with Mastersizer data [-]
F_{38}	Fraction of fines smaller than 38 μm calculated with Mastersizer data [-]
F_{45}	Fraction of fines smaller than 45 μm calculated with Mastersizer data [-]
ff	Jenike hopper flow factor [-]
g	Gravitational acceleration [m s^{-2}]
H	Powder bed height [m]
H_{mf}	Bed height at incipient fluidization [m]
H_R	Hausner ratio [-]
$H_{R,1250}$	Hausner ratio at 1250 taps [-]
$H^*_{R,1250}$	Hausner ratio estimated with Equation 4.9 and c_1 and c_2 values in Table 4.2 [-]
i	Label for data point [-]
k_1, k_2	Fitting parameters of Equation 3.7 [units according to usage]

k_{C1}, k_{C2}	Fitting parameters of Equation 4.10 [units according to usage]
k_{F1}, k_{F2}	Fitting parameters of Equation 4.15 [units according to usage]
k_{G1}, k_{G2}	Fitting parameters of Equations 3.14 and 3.15 [units according to usage]
k_{J1}, k_{J2}	Fitting parameters of Equations 3.12 and 3.13 [units according to usage]
k_{N1}, k_{N2}	Fitting parameters of Equations 3.10 and 3.11 [units according to usage]
$k_{s,M1}$, $k_{s,M2}$	Fitting parameters of Equation 3.6 [units according to usage]
$k_{t,M1}$, $k_{t,M2}$	Fitting parameters of Equation 4.2 [units according to usage]
m_0	Powder mass in the loose poured state [g]
m_{tap}	Powder mass after N^{th} taps [g]
N	Number of taps [-]
n (of Chapter 3)	Shear index of Warren-Spring equation [-]
n (of Chapter 5)	Number of data points [-]
n_1, n_2	Fitting parameters of Equation 4.5 [units according to usage]
P	Applied pressure [Pa]
T (of Chapter 3)	Powder tensile strength [Pa]
T^{-1} (of Chapter 5)	Inverse of von Neumann ratio, Equation 5.2 [-]
t_c	Time required for hindered settling, Equation 5.3 [s]
U	Superficial gas velocity [m s^{-1}]
U_{bv}	Minimum vigorous bubbling velocity [m s^{-1}]
U_{mb}	Minimum bubbling velocity [m s^{-1}]
$U_{mb,v}$	Experimental minimum bubbling velocity detected by visual inspection of bed surface [m s^{-1}]
$U_{mb,\sigma}$	Minimum bubbling velocity estimated using the plot of σ:U and determining U for σ=0 by extrapolation [m s^{-1}]
U_{mf}	Minimum fluidizing velocity [m s^{-1}]
V_B	Bulk volume of material [m^3]
$V_{Initial}$	Initial volume of powder bed in the GDR after the powder was shaken horizontally and vertically for an unreported fixed number of times and allowed to settle under its own weight [m^3]
V_{New}	Volume of powder in GDR measured at the first 11 revolutions [m^3]
V_p	Volume of material [m^3]
x (of Chapter 5)	Sample variable; bed pressure drop [Pa]
x_i (of Chapter 2)	Volume fraction of particles in i^{th} mean particle diameter range in sieve analysis [-]

Greek letters

ΔP_b	Bed pressure drop [Pa]

ΔP_d	Distributor pressure drop [Pa]
Φ_w	Kinematic angle of wall friction [^{o}]
δ_e	Effective angle of internal friction [^{o}]
ε_{mb}	Bed voidage at bubbling onset [-]
ε_{mf}	Bed voidage at incipient fluidization [-]
μ (of Chapter 3)	Coefficient of friction [-]
μ (of Chapter 5)	Gas viscosity, Equation 5.3 [N s m^{-2}]
θ_a	Minimum angle for which avalanches are observed [^{o}]
θ_p	Semi-included angle of the conical section of a hopper [^{o}]
θ_s	Minimum angle which triggers powders to slip [^{o}]
ρ_0	Initial or loose poured bulk density [kg m^{-3}]
$\rho_{0,mNZS3111}$	Loose poured bulk density measured by the modified NZS3111 method [kg m^{-3}]
ρ_B	Bulk density [kg m^{-3}]
ρ_g	Gas density [kg m^{-3}]
ρ_p	Particle density [kg m^{-3}]
ρ_{tap}	Tapped density [kg m^{-3}]
$\rho^*_{0,1}$	Loose poured bulk density estimated with Equation 4.1 and a_t and b_t values in Appendix 4.1 [kg m^{-3}]
$\rho^*_{0,2}$	Loose poured bulk density estimated with Equation 4.1, a_t values in Appendix 4.1 and b_t=0.0427, the average value determined with the data of milled and spray-dried lactose powders, sand, and refractory dust [kg m^{-3}]
$\rho^*_{0,3}$	Loose poured bulk density estimated with Equation 4.2 and $k_{t,M1}$ and $k_{t,M2}$ values in Appendix 4.1 [kg m^{-3}]
σ (of Chapter 3)	Consolidation stress [Pa]
σ (of Chapter 5)	Standard deviation, Equation 5.1 [Pa]
σ_c	Major consolidation stress [Pa]
σ_{crit}	Critical stress developed in an arch surface [Pa]
σ^*_c/σ^*_y	Estimated ratio of major consolidation stress to unconfined yield stress [-]
σ_D	Major stress developed in a dome or pipe [Pa]
σ_{pre}	Preconsolidation stress [Pa]
$\sigma_{pre,min}$	Minimum preconsolidation stress [Pa]
σ_{ws}	Standard deviation of GDR drum weight shift [kg]
$\sigma_{ws,5RPM}$	Standard deviation of GDR drum weight shift at 5 RPM [kg]
$\sigma_{ws,10RPM}$	Standard deviation of GDR drum weight shift at 10 RPM [kg]
$\sigma_{ws,15RPM}$	Standard deviation of GDR drum weight shift at 15 RPM [kg]
$\sigma_{ws,20RPM}$	Standard deviation of GDR drum weight shift at 20 RPM [kg]
σ_y	Unconfined yield stress [Pa]

τ	Shear stress [Pa]
τ_{pre}	Constant shear stress at preshear [Pa]
τ_{ss}	Steady-state shear stress [Pa]
ω	Angular velocity [rad s^{-1}]

Chapter 1 – Introduction

1.1 Background

Consumers come across powders every day. For example, they consume a variety of food powders such as flour, salt, spices, sugar, coffee, and milk powders, and they also use different detergents for different cleaning purposes on a daily basis. Because of consumers' demand, powders have become important commodities in many different industries especially the food industry, which is of significant relevance to countries like New Zealand.

Powders are complex multiphase systems; they comprise solid particles that can come in different particle sizes and shapes, air that is in the spaces or voids between particles, and liquid or moisture that can be in the air in the interparticle voids, in the particles, and attached to the surface of the particles. Rietema (1984) made the following observations concerning powders; the observations sum up the complexity of powders and also give an indication of the challenges that are present in the handling and processing of powders across different industries.

- Powders can withstand a certain degree of deformation, but they are not a solid
- Powders can be made to flow, but they are not a liquid
- Powders can be compressed, but they are not a gas

In the food and pharmaceutical industries, powders such as lactose powders are made, handled, and processed in operations that involve mixing, milling, packaging, and storage. For these operations to run effectively and efficiently, the powders must be made to move or flow, lest there will be hindrances in production. Knowledge of powder flow or flowability is therefore important to the making, handling, and processing of powders. This calls for measurement and characterization methods for powder flowability that are accurate, reliable, and robust.

There is no one way or "standard" to measure and characterize powder flowability because powders can behave like a solid, a liquid, or a gas depending on intrinsic properties such as particle size distribution, and the handling and processing conditions in which the powders are subjected to. For this reason, comprehensive measurement and characterization of flowability that involve different methods and devices are necessary. A variety of methods such as shear testing (Jenike, 1964) and powder tumbling (Kaye, Gratton-Liimatainen, & Faddis, 1995) have been developed and proposed. But it should be noted that each flow characterization method is generally developed and used for a specific process or application, and therefore captures only flow information that is within a specific set of conditions, *e.g.* static or dynamic conditions and over a limited range of applied stresses. Each method usually has limited utility beyond its scope of measurement and application.

In this work, the flow properties of model food and mineral powders were measured and assessed with four characterization methods, namely shear testing, compression via tapping, powder aeration or fluidization, and powder tumbling. Shear testing was performed with an annular shear cell according to the protocol developed by Berry, Bradley and McGregor (2014), which was based on Jenike (1964). Powder compression via tapping was done following a procedure commonly used in the dairy industry (Niro, 1978) and the European Pharmacopoeia (Schüssele & Bauer-Brandl, 2003). Fluidization was used to evaluate the expansion and collapse of aerated powder beds following the powder classification framework provided by Geldart and co-workers (Geldart, 1973; Geldart, Harnby, & Wong, 1984; Geldart & Wong, 1984, 1985). Powder tumbling was carried out in a novel *Gravitational Displacement Rheometer* (GDR), which measured the avalanche activity of powders that moved under their own weight when rotated in a cylindrical drum; the concept of the GDR was developed by Davies and co-workers (Davies, Tallon, Fenton, Brown, & Peterson, 2002; Davies, Williams, Tallon, Fenton, & Brown, 2004) and the GDR was used by Muzzio and co-workers, see for example A. M. Faqih, Chaudhuri, Alexander, et al. (2006), Faqih, Chaudhuri, Muzzio, et al. (2006), and Vasilenko, Glasser and Muzzio (2011).

The flow data from each characterization method were first evaluated individually with regards to particle size distribution. Subsequently, the flow data from all four methods were assessed collectively. The aim of this work was to provide improved understanding and knowledge of powder flowability, which can then be used to further assist and facilitate the development of new techniques and solutions relevant to the handling and processing of powders especially in the food and pharmaceutical industries.

1.2 Thesis Structure

There are seven chapters in this thesis as listed below. Chapter 2 to Chapter 6 each contains the following main sections: i) Introduction, ii) Literature Review, iii) Research Aims, iv) Materials, Methods and Analysis, v) Results, vi) Discussion, and vii) Conclusions. In Chapter 7, a reiteration of the significant findings of this work is given. Appendix 1.1 gives a list of publication from this work as of 22 February 2016.

- Chapter 1 – Introduction
- Chapter 2 – Preparation of model powders and characterization of physical properties
- Chapter 3 – Powder shear testing
- Chapter 4 – Powder compression via tapping
- Chapter 5 – Gas-fluidization
- Chapter 6 – Powder tumbling
- Chapter 7 – Summary

Chapter 2 – Preparation of Model Powders and Characterization of Physical Properties

2.1 Introduction

Selected food and mineral powders were prepared and used as model powders in this work; they included commercial milled and spray-dried lactose powders, sand, refractory dust from the alumina industry, and glass beads. Lactose powders were of primary interest; they are important commodities in the food and pharmaceutical industries commonly used as ingredients in the formulation of food and as excipients and diluents in pharmaceuticals. Sand, powders from the alumina industry, and glass beads are common model powders in fluidization, see for example Geldart (1972) and Baeyens and Geldart (1974) for sand, and Abrahamsen and Geldart (1980a, 1980b) for alumina powders and glass beads.

The model powders of this work comprised firstly powders that were used as received and secondly powders with altered particle size distributions made by sieving the powders that were used as received. Using systematic protocols, the particle size distribution and particle shape were measured and recorded. Mean particle diameter and size distribution, which play key roles in influencing powder flowability, were defined and measured by laser diffraction method and sieve analysis. Particle shape was observed with an optical microscope. The relationships between mean particle diameter, span of particle size distribution, and fraction of fines were then examined and discussed; fines were defined as particles smaller than 45 μm following Abrahamsen and Geldart (1980a).

2.2 Literature Review

2.2.1 Particle size distribution and mean particle diameter

Powder systems usually comprise particles of different diameters unless they are specifically made and prepared with mono-sized particles. A variety of techniques for measurement of particle size distribution and particle diameter are available for individual particles and powder systems; these techniques can measure different ranges of particle diameter and they include sieve analysis (>50 μm), optical analysis (1–100 μm), sedimentation and elutriation (>1 μm), permeability analysis (>1 μm), and laser diffraction (0.1–600 μm) (Coulson, Richardson, Backhurst, & Harker, 2002). In this work, the laser diffraction method and sieve analysis were used. The laser diffraction method has been used on lactose powders, see for example Ilić, Kása Jr., Dreu, Pintye-Hódi and Srčič (2009), and poly-component powder systems, see for example Choi et al. (2009).

Figure 2.1 shows a plot of volume percentage against incremental mean particle diameter, and Figure 2.2 shows a plot of cumulative volume fraction against incremental mean particle diameter; real data are used and the plots are typical representations of particle size

distribution measured by laser diffraction. From Figure 2.2, particle diameters d_{10}, d_{50}, and d_{90} can be obtained graphically; d_{10}, d_{50}, and d_{90} represent mean particle diameter at 10%, 50%, and 90% in a cumulative size distribution respectively and they are used to calculate the span of the size distribution, see Equation 2.1.

$$\text{Span} = \frac{d_{90} - d_{10}}{d_{50}} \tag{2.1}$$

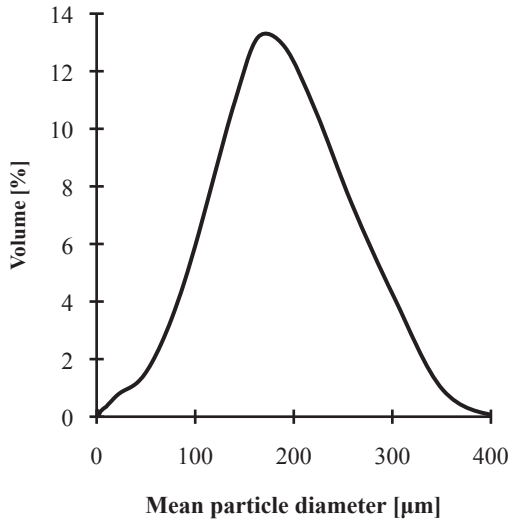

Figure 2.1 An example of particle size distribution with real data; plot of volume percentage versus incremental mean particle diameter

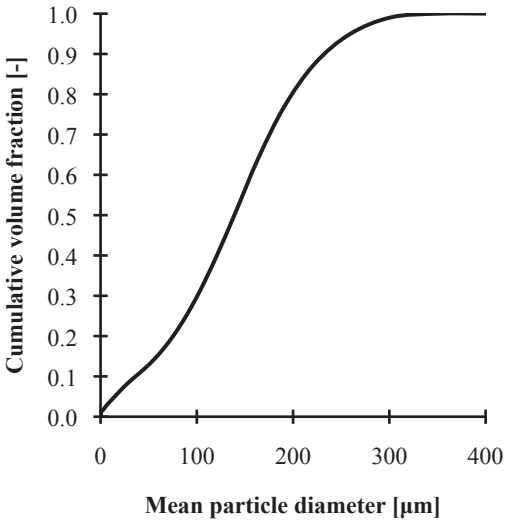

Figure 2.2 An example of particle size distribution with real data; plot of cumulative volume fraction versus incremental mean particle diameter

In powder fluidization where interaction and balance between gravity and the drag force exerted by fluidizing gas on aerated particles are important, the relevant mean particle diameter is the surface-volume mean particle diameter, d_{32}, see for example Geldart (1973, 1990), Kunii and Levenspiel (1991), and Khoe, Ip and Grace (1991). Geldart (1973) classified the gas-fluidization of powders under ambient conditions into four distinct groups using a plot of the difference between particle density and fluid density against d_{32}; Geldart noted later that "*it is now almost universally accepted that for packed and fluidized beds the relevant particle size is the surface-volume diameter*" (Geldart, 1990). Particle diameter d_{32} is also known as Sauter diameter; it has been used as a size descriptor in the compression via tapping of powders, see for example Abdullah and Geldart (1999).

In this work, d_{32} was the mean particle diameter of primary interest. For a non-spherical or irregularly shaped particle, d_{32} is defined as the diameter of an equivalent sphere that has the same ratio of external particle surface area to particle volume. For a powder system containing a

mixture of particles of different sizes and shapes, the corresponding d_{32} is given by Equation 2.2; x_i is the volume or mass fraction of particles in the i^{th} mean particle diameter range [-] and d_{pi} is the mean of the sum of upper and lower nominal apertures, also known as the incremental mean particle [μm], see for example Geldart (1990), Kunii and Levenspiel (1991), Coulson et al. (2002), and McCabe, Smith and Harriott (2005).

$$d_{32} = \frac{1}{\sum_{i=1}\left(x_i / d_{pi}\right)} \tag{2.2}$$

2.2.2 Fines fraction

According to Abrahamsen and Geldart (1980a), Khoe et al. (1991), and Bruni, Lettieri, Newton and Barletta (2007), and in the context of fluidization, fines in powder systems were defined as particles smaller than 45 μm. The value or boundary of 45 μm is arbitrary and the demarcation of fines can change depending on research context. For example, Dry, Judd and Shingles (1983) assigned powders smaller than 22 μm as fines in addition to those smaller than 45 μm in their fluidization work involving fine powders. In the work by Lorences, Patience, Diez and Coca (2003) on the effects of fines on collapsing fluidized beds, fines were defined as particles smaller than 10 μm and those in between 10–20 μm, 20–25 μm, 25–32 μm, and 32–44 μm.

The fines fraction in a powder can be determined by sieve analysis on a percentage weight basis. Recommended procedures for sieve analysis can be found in Coulson et al. (2002) and McCabe et al. (2005). There are different types of standard sieves or screens; common standard sieves include the British Standard (BS 410), the Institute of Mining and Metallurgy (IMM) of the United Kingdom, and the Tyler and American Society for Testing Materials (ASTM) of the United States (Coulson, et al., 2002). In sieve analysis, a series of sieves is arranged serially in a stack with each lower sieve being of a smaller aperture size; the selection of sieves depends on the closeness of the aperture size and the ratio of aperture sizes of consecutive sieves is usually between $2^{1/4}$ and 2. The stack of sieves is usually vibrated with a mechanical shaker at 50 Hz for up to 20 min. The particle size obtained on each sieve is d_{pi}; recall Equation 2.2.

Sieve analysis is limited by the availability of the smallest sieve, which is usually the sieve with the aperture size of 38 μm or 45 μm. The ability of particles passing through each successive sieve also influences sieve analysis; as fines are cohesive and that interparticle forces are dominant, the particles can agglomerate, form lumps, and adhere to the sieves. These limitations are overcome with the use of more sophisticated methods such as laser diffraction, which can make measurement on a wet basis, and hence better disperse fine particles to give more accurate measures of fines fraction on a mass or volume basis. The resolution of the laser

diffraction method is also higher and particles as small as 0.1 μm can be measured. A major drawback of the laser diffraction method is the cost of the apparatus.

2.2.3 Particle shape

The model powders used in this work were milled and spray-dried lactose powders, sand, refractory dust from the alumina industry, and glass beads. These powders consisted of particles that came in different shapes, and particle shape was observed and determined from photomicrographs.

Lactose powders come in various shapes depending on their manufacturing processes. For example in the work by Shaffer, Paterson, Davies and Hebbink (2011), crystalline lactose particles that were grown in supersaturated lactose agar gels and controlled conditions in the laboratory were tomahawk-shaped. But lactose samples obtained from a manufacturing line for comparison were found to contain individual particles with damaged or distorted tomahawk shapes; the differences in particle shape were attributed to the crystallization and recovery stages involved in a typical manufacturing process. Fu et al. (2012) investigated the particle shape of three samples of commercial lactose powders and showed that two samples comprised individual particles that were angular and irregularly shaped; the other sample contained particles that were rounded or spherical.

Sand commonly used as model powders in fluidization were reported as round, rounded, angular, and sharp, see for example Geldart (1972) and Baeyens and Geldart (1974). Alumina powders in fluidization were rounded or angular, see for example Abrahamsen and Geldart (1980a, 1980b) and Geldart and Wong (1985). Glass beads or ballotini were spherical, see for example Abrahamsen and Geldart (1980a, 1980b).

2.2.4 Influence of particle size distribution, mean particle diameter, and fines fraction on powder behaviour

In this work, the first step to characterizing powder flowability was the characterization of physical properties of powders; the key physical properties identified were d_{32}, span of particle size distribution, and fines fraction. Due to the complexity of powder systems, more than one physical property was required to explain powder flowability and also to correlate the experimental results from different flow characterization methods; this has actually been advocated by earlier researchers such as Khoe et al. (1991). Accurate measurement and characterization of particle size distribution, d_{32}, and fines fraction were therefore necessary.

The influence of particle size distribution, d_{32}, and fines fraction on the flowability of powders is significant; this has been demonstrated with selected powders under different conditions in shear testing, powder compression via tapping, fluidization, and powder tumbling. For instance, Kurz and Münz (1975) showed the influence of particle size distribution and mean

particle diameter measured by sedimentation on the flow properties of limestone powders measured with a Jenike shear cell. Abdullah and Geldart (1999) demonstrated the influence of d_{32} and fines fraction on the aerated and tapped densities of fluid cracking catalyst and aluminium trihydroxide powders. Geldart and co-workers showed how d_{32} and fines fraction affected the bed expansion and collapse of fluidized beds; the powders of investigation included glass beads, alumina powders, catalysts, and fly ash (Abrahamsen & Geldart, 1980a, 1980b; Geldart, 1973; Geldart & Wong, 1984, 1985). Webster and Davies (2006, 2010) demonstrated that powders from different Geldart Powder Groups (Geldart, 1973) gave different avalanche activity when tumbled in a rotating drum at different drum speeds.

2.2.5 Summary of literature review

Central to the characterization of powder flowability is the measurement and characterization of physical properties of powders. In the context of this work, which involved powder shear testing, compression via tapping, fluidization, and tumbling, the key powder physical properties measured included d_{32}, span of particle size distribution, fines fraction, and particle shape. These physical properties are not new powder descriptors; they are necessities in powder characterization due to the complexity of powder systems. The influence of d_{32}, span of particle size distribution, and fines fraction on the flow properties of powders obtained with different characterization techniques have been demonstrated with various types of powders in the work by other researchers.

2.3 Aims

1. To measure the d_{10}, d_{50}, and d_{90} of model milled and spray-dried lactose powders, sand, refractory dust, and glass beads by laser diffraction method and sieve analysis.
2. To determine the particle size distribution, span, d_{32}, and fraction of fines smaller than 10 μm, 20 μm, 30 μm, 38 μm, and 45 μm of the model powders.
3. To determine the particle shape of the model powders by optical microscopy.
4. To investigate the relationships between d_{32}, span of particle size distribution, and fines fraction of the model powders.

2.4 Materials, Methods and Analysis

2.4.1 Materials and preparation of model powders

A total of thirteen milled lactose powders, two spray-dried lactose powders, four sand samples, three refractory dust samples, and two glass beads samples were prepared and used in different powder flow experiments. Each powder type was given a code: LP for lactose monohydrate, LM

for milled lactose, LT for spray-dried lactose, S for sand, RD for refractory dust, and B for glass beads.

For milled lactose powders, three samples were commercial powders of DMV-Fonterra Excipients, New Zealand that were used as received; they were lactose monohydrate Pharmatose® 70M (LP1), Pharmatose® 350M (LP4), and milled Hydrous Refined Lactose 100-mesh (LM1). The other ten samples were made by sieving either LP1 or LM1 with selected BS 410 sieves mounted on an electromagnetic sieve shaker (Model EMS-8, Electrolab, India). Two sieving procedures were used. In *Procedure 1*, 500 g of powder were sieved at 20 Watt for 20 min; lactose powders LM2, LM3, LM6, LM7, LM8, LP2, and LP3 were made following this procedure. In *Procedure 2*, 50 g of LM1 were sieved at 20 Watt for 5 min, and lactose powders LM4, LM5, and LM9 were made. The sieve apertures used in Procedure 1 and Procedure 2 are listed in Appendix 2.1.

Spray-dried lactose samples LT1 and LT2 were made from a commercial spray-dried lactose monohydrate powder (SuperTab®, DMV-Fonterra Excipients, New Zealand) using Procedure 1. Samples of sand, refractory dust, and glass beads were obtained from Professor Clive E. Davies, School of Engineering and Advanced Technology, Massey University. Sand S1 and SB, and glass beads B8 were used as received. Sand S2 and S3 were made from S1 using Procedure 1, and RD1, RD2 and RD3 were made from the refractory dust using the same procedure; see Appendix 2.1 for sieve apertures.

2.4.2 Measurement of particle size distribution, diameters d_{10}, d_{50}, d_{90}, and span of size distribution

The particle size distribution of milled and spray-dried lactose powders, sand, and refractory dust was measured by laser diffraction method on a wet and volume-weighted bases with a Mastersizer 2000 (Malvern Instruments Ltd., UK). The equipment was controlled online with a computer and used the 300 RF lens and small volume sample unit. The solvent for lactose powders was isopropanol and water was used for the rest of the model powders. The following are the refractive indices for each powder and solvent: 1.533 for lactose, 1.48 for sand, 1.76 for refractory dust, 1.378 for isopropanol, and 1.33 for water. The default *Polydisperse* model was selected to characterize the size distribution and determine d_{10}, d_{50}, and d_{90}; the span of size distribution was calculated with Equation 2.1. The reproducibility of the Mastersizer was checked randomly with selected powders.

The particle size distribution of selected powders was also determined by sieve analysis. Fifty or 100 g of sample were sieved with selected BS 410 sieves mounted on an electromagnetic sieve shaker (Model EMS-8, Electrolab, India) at 20 Watt for 20 min following the recommendations by Coulson et al. (2002) and McCabe et al. (2005). The plot of cumulative mass fraction versus incremental mean particle diameter was constructed and d_{10}, d_{50}, and d_{90}

were determined graphically. Equation 2.1 was used to determine the span of size distribution. The reproducibility of the sieve analysis was checked with selected powders.

2.4.3 Determination of surface-volume mean particle diameters $d_{32.M}$, d^*_{32}, and $d_{32,S}$

With the available particle size distribution data sets, three values of surface-volume mean particle diameter, namely $d_{32,M}$, d^*_{32}, and $d_{32,S}$ were calculated with Equation 2.2 for comparison purposes. Diameter $d_{32,M}$ is the surface-volume mean particle diameter determined directly with the Mastersizer 2000. Diameter d^*_{32} is the surface-volume mean particle diameter calculated with the Mastersizer data using bins equivalent to a full sieve analysis according to BS 410; the powder in the range of 0–38 μm is grouped together and assigned a mean particle diameter of 19 μm in the calculation. Diameter $d_{32,S}$ is the surface-volume mean particle diameter calculated with the sieve analysis data.

2.4.4 Determination of fines fraction F_{10}, F_{20}, F_{30}, F_{38}, and F_{45}

Fines fraction was calculated with the Mastersizer data; F_{10}, F_{20}, F_{30}, F_{38}, and F_{45} are the fraction of fines smaller than 10 μm, 20 μm, 30 μm, 38 μm, and 45 μm respectively.

2.4.5 Examination of particle shape

Selected powder samples were examined with a compound microscope (Model BX60, OLYMPUS®, Japan) under *Differential Interference Contrast* optic settings using the x20 objective lens. The powders were dispersed in 518N immersion oil (ZEISS, Germany), and images of particles were captured with an AxioCam HRc camera (ZEISS, Germany) that was connected to the microscope and controlled online with a computer; the photomicrographs were saved as JPEG files.

2.5 Results

2.5.1 Particle size distribution, span of size distribution, diameters $d_{32.M}$, d^*_{32}, and $d_{32,S}$, and fines fraction of model powders

Figure 2.3 and Figure 2.4 show the particle size distribution of milled lactose powder LP4 measured with the Mastersizer 2000; the shapes of the plots are typical for a powder comprising particles of different sizes.

The plots of volume percentage versus incremental mean particle diameter for the rest of the powders are given in Appendix 2.2; repeat measurements with powders LP4, LM8, LM3, LM5, S1, S2, S3, RD1, RD2, and RD3 show high reproducibility.

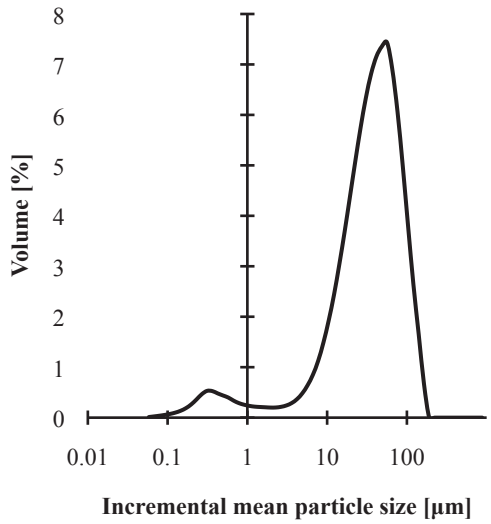

Figure 2.3 Particle size distribution of milled lactose LP4; plot of volume percentage versus incremental mean particle diameter

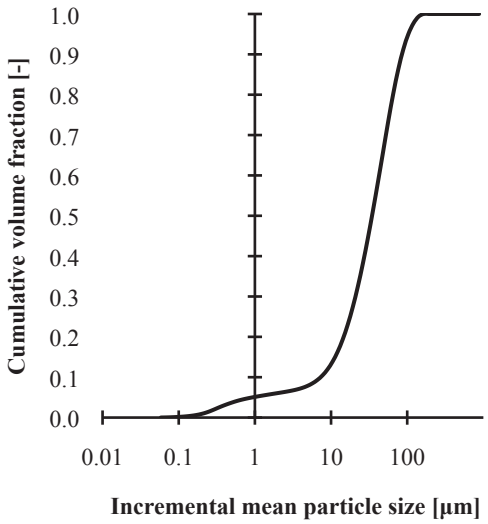

Figure 2.4 Particle size distribution of milled lactose LP4; plot of cumulative volume fraction versus incremental mean particle diameter

The values of d_{10}, d_{50}, d_{90}, $(d_{90}–d_{10})/d_{50}$, $d_{32.M}$, d^*_{32}, and $d_{32,S}$ for milled and spray-dried lactose powders, sand, and refractory dust are listed in Table 2.1. Comparing $d_{32.M}$, d^*_{32}, and $d_{32,S}$ for milled lactose powders, the values of $d_{32.M}$ are lowest and the values of $d_{32,S}$ are generally highest. The $d_{32,S}$ for LP4, LM7, LM8, and LM9 is not measurable. For spray-dried lactose LT1 and LT2, $d_{32.M}$ is lowest and d^*_{32}, and $d_{32,S}$ are close. The $d_{32.M}$, d^*_{32}, and $d_{32,S}$ for sand S1, S2, and S3 are similar. For refractory dust RD1, RD2, and RD3, the values of $d_{32.M}$, d^*_{32}, and $d_{32,S}$ are different.

The span of particle size distribution ranges from 0.74 to 2.26 for milled lactose powders, 0.73 to 1.50 for spray-dried lactose powders, 0.79 to 1.43 for sand, and 0.91 to 1.62 for refractory dust. As d^*_{32} decreases, the span of the size distribution generally increases.

Listed in Table 2.2 are the F_{10}, F_{20}, F_{30}, F_{38}, and F_{45} for milled and spray-dried lactose powders, sand, and refractory dust. It is observed that fines fraction generally increases with decreasing d^*_{32}.

Table 2.1 Diameters d_{10}, d_{50}, d_{90}, $d_{32.M}$, d^*_{32}, $d_{32,S}$, and span $(d_{90}–d_{10})/d_{50}$ for milled and spray-dried lactose powders, sand, and refractory dust

Powder	**Mastersizer 2000 data**			$(d_{90}–d_{10})/d_{50}$	$d_{32,M}$	d^*_{32}	$d_{32,S}$
	d_{10} **[µm]**	d_{50} **[µm]**	d_{90} **[µm]**	**[-]**	**[µm]**	**[µm]**	**[µm]**
Unsieved milled lactose							
LP4	7.3	34.5	85.3	2.26	4.4	28.9	– [a]
LM1	14.4	108.5	256.2	2.23	9.7	58.0	106.1
LP1	88.6	257.0	538.4	1.75	37.1	150.8	153.7
Sieved milled lactose							
LM7	7.1	37.4	81.6	1.99	5.6	29.9	– [a]
LM8	9.0	56.1	110.2	1.80	9.4	39.3	– [a]
LM9	10.2	64.4	125.3	1.79	10.3	43.3	– [a]
LM4	16.1	139.5	239.7	1.60	17.8	65.1	121.4
LM2	26.9	112.9	190.8	1.45	20.0	73.4	95.3
LP2	36.4	139.0	232.3	1.41	19.8	83.6	106.0
LM3	81.8	143.2	219.2	0.96	27.8	110.7	110.9
LM5	40.5	251.8	403.7	1.44	31.9	113.4	160.7
LM6	141.7	242.0	386.5	1.01	42.1	163.7	185.2
LP3	178.2	263.4	373.0	0.74	60.6	223.0	203.0
Spray-dried lactose							
LT1	15.7	47.3	86.8	1.50	5.9	35.8	43.9
LT2	75.8	113.8	158.6	0.73	15.5	102.2	93.8
Sand							
S3	19.5	36.7	60.3	1.11	31.7	28.7	29.3
S1	23.3	52.2	97.8	1.43	41.6	40.1	39.6
S2	51.2	76.7	111.8	0.79	72.3	76.9	70.3
Refractory dust							
RD3	8.8	25.9	50.8	1.62	16.6	23.3	37.1
RD1	18.2	56.8	107.5	1.57	32.5	41.5	56.7
RD2	43.8	71.9	109.1	0.91	58.5	66.6	62.1

[a] Not measurable by sieve analysis

Table 2.2 Fines fraction F_{10}, F_{20}, F_{30}, F_{38}, and F_{45} for milled and spray-dried lactose powders, sand, and refractory dust

Powder	d^*_{32} **[µm]**	F_{10} **[-] (<10 µm)**	F_{20} **[-] (<20 µm)**	F_{30} **[-] (<30 µm)**	F_{38} **[-] (<38 µm)**	F_{45} **[-] (<45 µm)**
Unsieved milled lactose						
LP4	28.9	0.119	0.274	0.382	0.514	0.585
LM1	58.0	0.069	0.125	0.157	0.197	0.221
LP1	150.8	0.018	0.030	0.037	0.045	0.050
Sieved milled lactose						
LM7	29.9	0.126	0.260	0.351	0.476	0.551
LM8	39.3	0.100	0.182	0.229	0.302	0.355
LM9	43.3	0.090	0.160	0.200	0.261	0.304
LM4	65.1	0.062	0.116	0.147	0.180	0.195
LM2	73.4	0.050	0.087	0.099	0.111	0.121
LP2	83.6	0.035	0.062	0.078	0.098	0.110
LM3	110.7	0.030	0.043	0.046	0.047	0.047
LM5	113.4	0.034	0.059	0.074	0.092	0.102
LM6	163.7	0.024	0.035	0.040	0.044	0.045
LP3	223.0	0.012	0.015	0.017	0.018	0.018
Spray-dried lactose						
LT1	35.8	0.066	0.129	0.204	0.330	0.415
LT2	102.2	0.023	0.023	0.023	0.024	0.025
Sand						
S3	28.7	0.003	0.097	0.240	0.471	0.615
S1	40.1	0.005	0.059	0.134	0.263	0.348
S2	76.9	0.000	0.000	0.001	0.011	0.030
Refractory dust						
RD3	23.3	0.103	0.337	0.508	0.709	0.803
RD1	41.5	0.039	0.108	0.165	0.258	0.324
RD2	66.6	0.011	0.016	0.020	0.045	0.080

2.5.2 Particle shape of model powders

Figure 2.5 (a) to 2.5 (d) show photomicrographs of lactose powder LP1, from which LP2 and LP3 are made. LP1 contains particles that are of tomahawk shape, see Figure 2.5 (a), distorted or damaged tomahawk shapes, see Figures 2.5 (b) and 2.5 (c), and traces smaller particles that are of irregular and angular shapes, see Figure 2.5 (d).

Figures 2.6 (a) and 2.6 (b) show the photomicrographs of lactose powder LP4, which is of the smallest d^*_{32} in this work; LP4 contains particles that are of irregular and angular shapes. Figure 2.6 (b) highlights the presence of fine particles of irregular shapes.

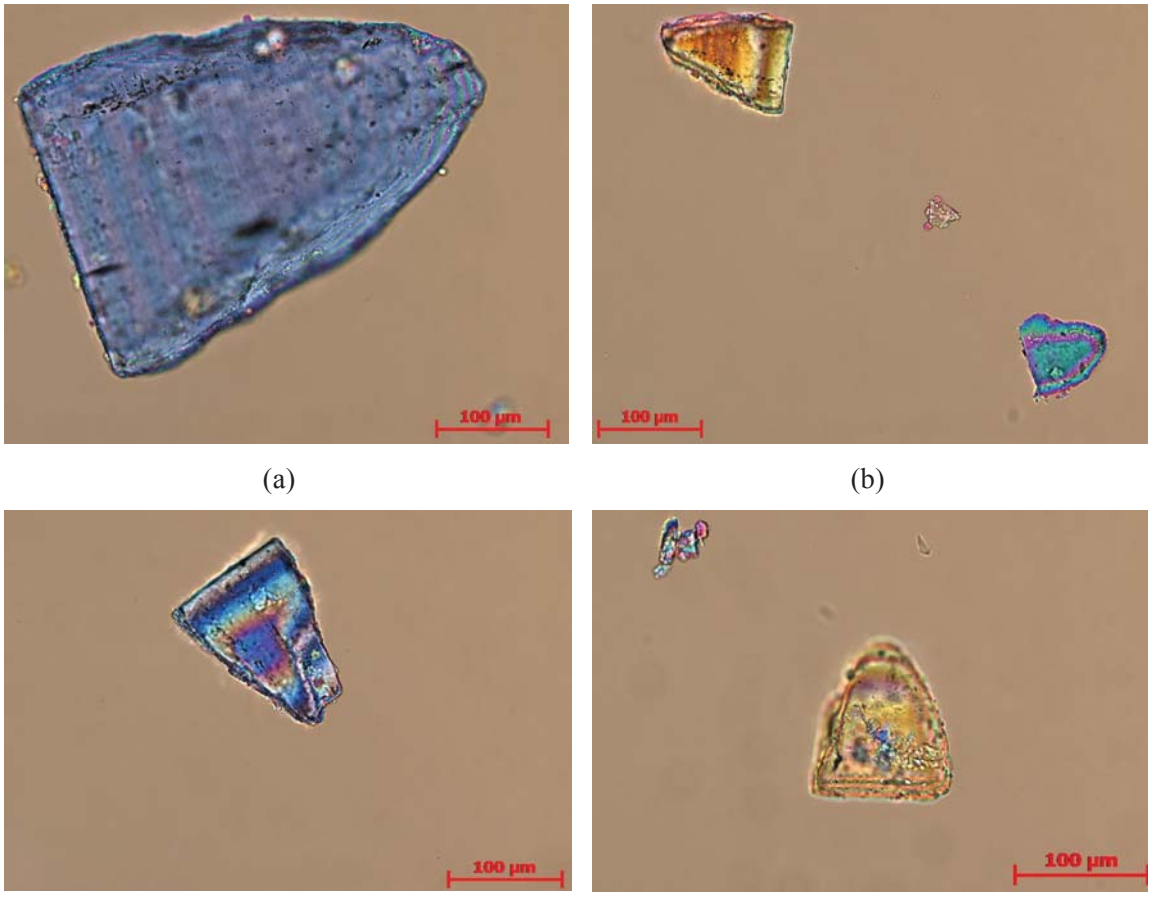

(a) (b)

(c) (d)

Figure 2.5 Particle shape of milled lactose powder LP1

(a) (b)

Figure 2.6 Particle shape of milled lactose powder LP4

In Figures 2.7 (a) and 2.7 (b), the photomicrographs of lactose powder LM1 are shown; LM1 is the parent material from which the rest of the LM powders are made. Both figures show that the particle shapes are irregular and angular.

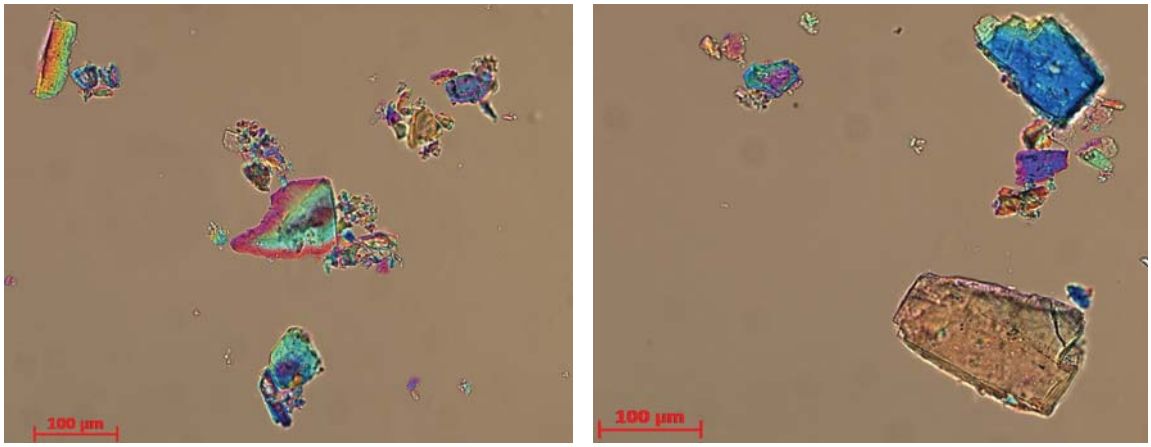

(a) (b)

Figure 2.7 Particle shape of milled lactose powder LM1

The particle shape of spray-dried lactose powder LT1 is shown in Figures 2.8 (a), 2.8 (b), and 2.8 (c). With reference to Figures 2.8 (a) and 2.8 (b), the particles seem rounded or spherical; Figure 2.8 (b) also shows smaller particles that seem angular or irregularly shaped. In Figure 2.8 (c), the agglomeration of particles is observed, forming irregularly shaped particles.

Figures 2.9 (a) and 2.9 (b) show the particle shape of sand S1; the particles are mainly rounded or spherical; particles of uneven shapes are also observed.

Figures 2.10 (a), 2.10 (b), 2.10 (c), and 2.10 (d) show the particle shape of refractory dust RD1 at different magnification. RD1 comprises particles that appear approximately spherical, see Figures 2.10 (a) and 2.10 (b), and particles that are irregularly shaped and angular, see Figures 2.10 (c) and 2.10 (d).

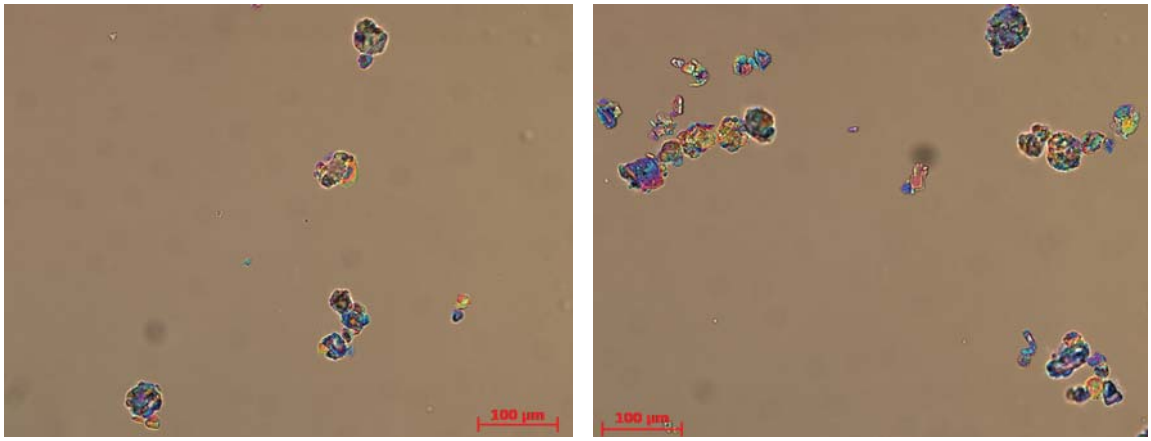

(a) (b)

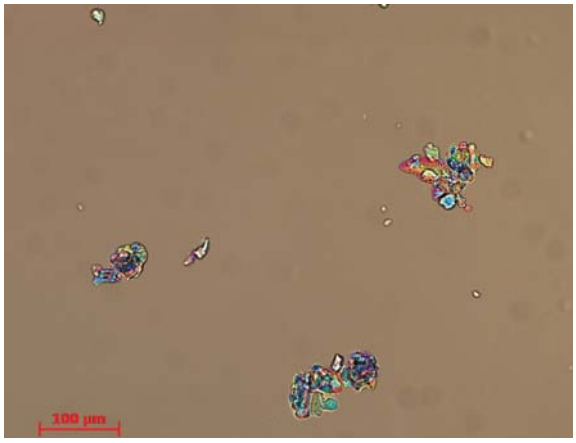

(c)

Figure 2.8 Particle shape of spray-dried lactose powder LT1

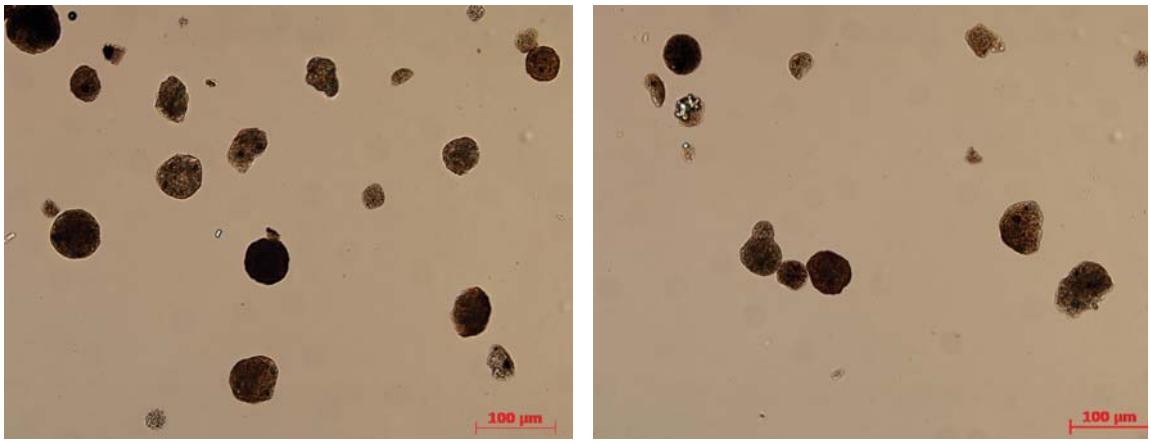

(a) (b)

Figure 2.9 Particle shape of sand S1

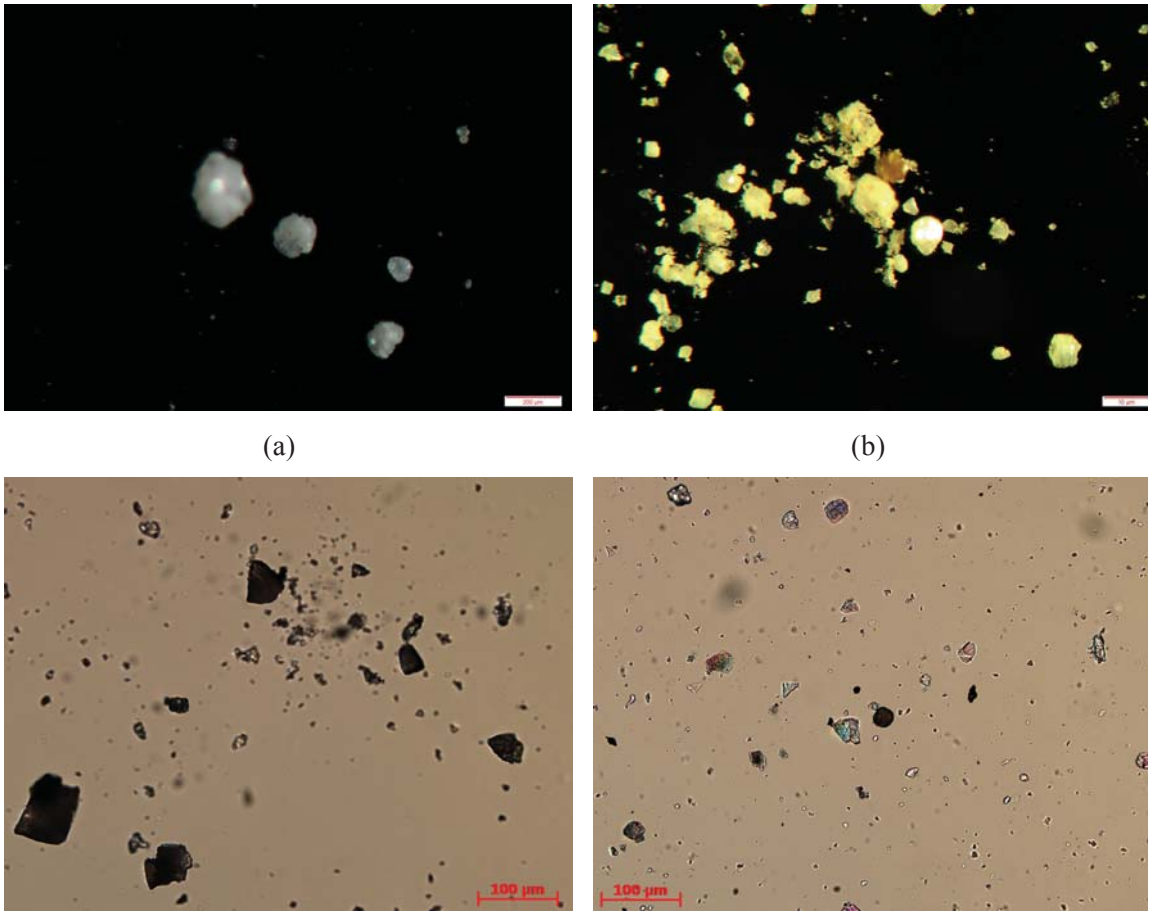

(a) (b)

(c) (d)

Figure 2.10 Particle shape of refractory dust RD1

2.5.3 Relationships between d^*_{32}, span of particle size distribution, and fines fraction

Figure 2.11 shows d^*_{32} plotted against $(d_{90}–d_{10})/d_{50}$; the plot is scattered and no general trend seems to occur for the model milled and spray-dried lactose powders, sand, and refractory dust.

Figure 2.12 shows $1/d^*_{32}$ plotted against F_{45}; $1/d^*_{32}$ increases with increasing F_{45} and the relationship seems to show apparent linear trends for each powder type. Figure 2.13 shows $1/d^*_{32}$ plotted against fines fraction for 13 milled lactose powders; the plot demonstrates linear trends and distinct dependence of $1/d^*_{32}$ on fines fraction <10 µm, <20 µm, <30 µm, <38 µm, and <45 µm, and are representative of the data of spray-dried lactose, sand, and refractory dust.

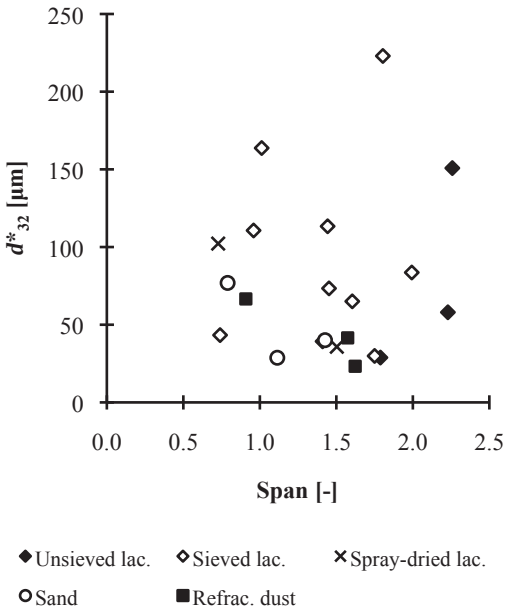

Figure 2.11 Plot of d^*_{32} versus span of particle size distribution

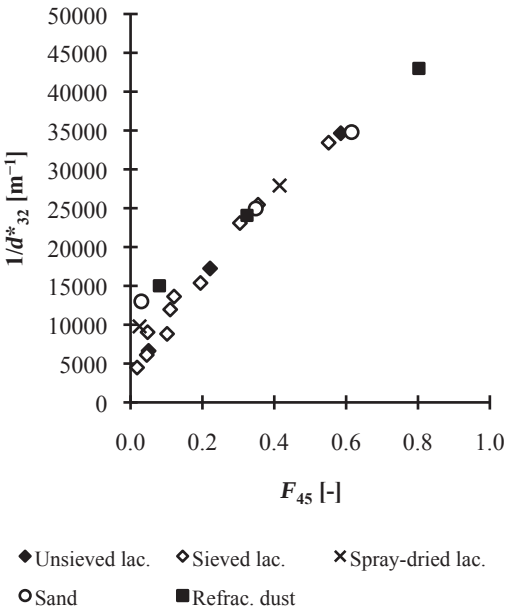

Figure 2.12 Plot of d^*_{32} versus F_{45}

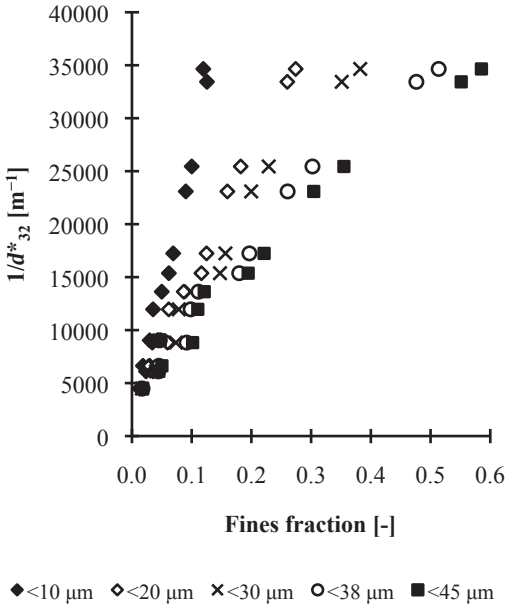

Figure 2.13 Plot of $1/d^*_{32}$ versus fines fraction for milled lactose powders

2.6 Discussion

The model powders prepared and used in this work consisted of particles of different sizes regardless of powder type; this is shown in the measured particle size distribution. Observations from the photomicrographs are also consistent with the size distribution data. The model powders comprise particles of irregular shape, but particle shape has not been described quantitatively.

The measurement of d_{32} is sensitive to the method used; recall and compare the values of $d_{32,M}$, $d_{32,S}$, and d^*_{32} in Table 2.1. Caution should be taken and the measurement protocol used should be clearly specified for reproducibility. Figure 2.14 shows the relationship between d^*_{32} and $d_{32,M}$; the slopes of the data are influenced by powder type and fines fraction. The values of $d_{32,M}$ are significantly low because the Mastersizer 2000 is capable of accurately measuring particles as small as 0.06 μm on a wet basis for any size distribution. With the inclusion of size distribution data generated under such high resolution in the calculation of $d_{32,M}$, low $d_{32,M}$ values are obtained. At a coarser resolution, where powders in the range of 0–38 μm are lumped together and assigned a mean particle diameter of 19 μm so that bins equivalent to a full BS 410 sieve analysis are used in the calculation of d^*_{32}, higher values are obtained. By linear regression and forcing the fitting line through the origin, Equation 2.3 with R^2=0.976 is obtained for milled lactose powders, Equation 2.4 with R^2=0.996 for spray-dried lactose powders, Equation 2.5 with R^2=0.978 for sand, and Equation 2.6 with R^2=0.968 for refractory dust.

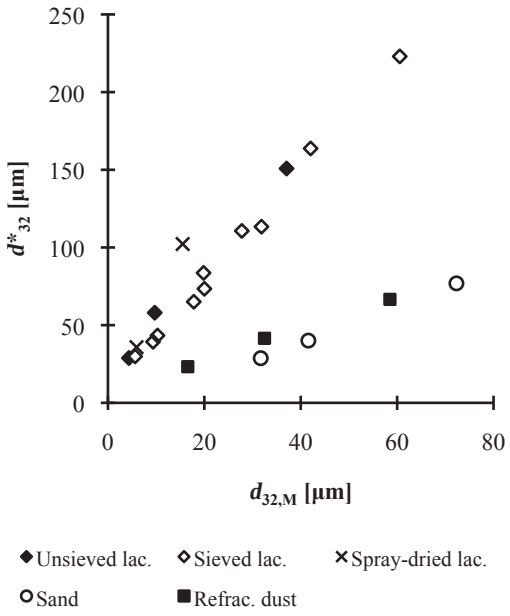

Figure 2.14 Plot of d^*_{32} versus $d_{32,M}$

$$d^*_{32} = 3.845 d_{32,M} \tag{2.3}$$

$$d^*_{32} = 6.520 d_{32,M} \tag{2.4}$$

$$d^*_{32} = 1.022 d_{32,M} \tag{2.5}$$

$$d^*_{32} = 1.185 d_{32,M} \tag{2.6}$$

With reference to Figure 2.11, the relationship between d^*_{32} and span is uncertain. An implication is that the empirical approach used is insufficient. It also suggests that the combined

use of d_{10}, d_{50}, and d_{90} to calculate span is incapable of capturing the size distribution data accurately when compared to d^*_{32}.

The data of d_{32}, span, and fines fraction presented in this chapter, primarily the d^*_{32} data, will be used in the discussion and interpretations of powder flowability measured by shear testing, compression via tapping, fluidization, and powder tumbling in subsequent chapters.

2.7 Conclusions

The particle size distribution and particle shape of model milled and spray-dried lactose powders, sand, and refractory dust were measured to respectively generate data sets and photomicrographs that will be used in the coming chapters of this thesis for the discussion and interpretations of powder flowability measured by shear testing, compression via tapping, fluidization, and powder tumbling. The key size distribution descriptor is d^*_{32}, which is the surface-volume mean particle diameter calculated with Mastersizer data using bins equivalent to a full sieve analysis according to BS 410. Diameter d^*_{32} is a useful single index that represents size distribution accurately and captures the influence of fines fraction directly. It should also be noted that measurement of d_{32} is sensitive to the methods used.

Chapter 3 – Powder Shear Testing

3.1 Introduction

Fine powders do not flow well due to their cohesive nature. Cohesion arises from interparticle forces that can exist in different forms, such as van der Waals forces, electrostatic forces, magnetic forces, mechanical interlocking between particles, capillary interactions, liquid bridging between particles, and combinations of these (McGlinchey, 2005). Cohesion is directly related to powder physical properties such as particle size distribution, see for example Kurz and Münz (1975), and poses significant influences on the mechanical and flow properties at the bulk level.

Interparticle forces and their influence on powder flowability can be measured and characterized. Many workers in the field consider powder shear testing as a classical powder flow characterization method. The science behind shear testing is attributed to Jenike (1964); in his classical work on the storage and flow of bulk solids, the theory and scientific approach of shear testing were given, and shear testing was developed primarily for the design of storage hoppers and silos. Variants of shear cells have subsequently been developed, such as the Jenike shear cell (Jenike, 1964) and the annular shear cell (Carr & Walker, 1968), and they have been used across many different industries on many different powders. A list of shear cells of different design is given by Schwedes (2003). Recently, shear testing has been recorded as an international powder characterization standard (Carson & Wilms, 2006).

The work in this chapter involves the shear testing of selected fine powders in an annular shear cell at consolidation stresses below 5 kPa; shear testing is used to provide qualitative and quantitative measures of powder flowability. Included in this chapter are the measurement and analysis of yield locus, cohesion, powder flow function, consolidated bulk density, and the determination of B, which is the minimum width of outlet required for mass flow from a hopper, and proposed by Jenike (1975) as a measure of powder flowability.

3.2 Literature review

The literature on shear testing is vast; there is a substantial number of books and articles on this subject besides the work by Jenike (1964), see for example Nedderman (1992) and Schulze (2008). It is the aim of this literature review to provide concise information that is directly relevant to the context of the work here; the emphasis of the review is on yield locus, cohesion, powder flow function, bulk density under consolidation, and hopper outlet B.

For extensive reading on shear testing, the following key documents are recommended: Jenike (1964), Nedderman (1992), and Schulze (2008). The papers by Molerus (1975, 1978) are helpful in regards to the theory of yield of cohesive powders and the effect of interparticle forces on powder flow behaviour.

3.2.1 Yield locus, major consolidation and unconfined yield stresses, and effective angle of internal friction

In shear tests, a powder sample goes through a series of normal consolidations under different loads and horizontal shearing at constant velocity by moving the top platen of the shear cell. The aim is to measure the yield limits of the consolidated powder bed, commonly known as the yield locus (Schulze, 2008); a yield locus is the relationship between shear stress, τ, and consolidation stress, σ. There are two steps in the measurement of a point on a yield locus, namely *preshear* and *shear to failure*. In preshear, the powder is first subjected to a defined preconsolidation stress, σ_{pre}, and then sheared until the shear stress reaches a constant value, τ_{pre}, which will remain unchanged with further shearing; the bulk density of the powder is also unchanged at this point. This is a steady state condition in which powder failure or flow occurs; the flow at preshear is referred to *steady state flow*.

After preshear, the powder bed is in a *critically consolidated state*. To obtain a yield point, the bed is sheared at a lower consolidation stress; incipient flow or failure commences when the shear stress reaches a sufficient value. At this point, the particles that are sheared will dilate and move past each other, resulting in a decrease in bulk density, shear resistance, and shear stress. The shear stress that characterizes the incipient failure, and hence the yield limit point is the maximum shear stress (Schulze, 2008). When the measurement of preshear and shear to failure is repeated at different stress levels, a family of yield loci will be generated.

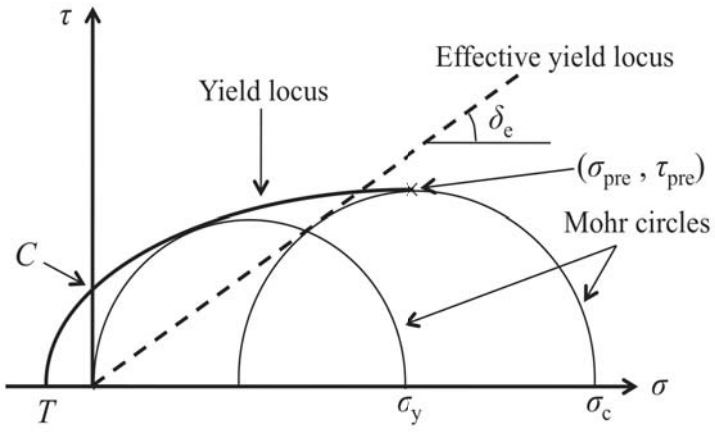

Figure 3.1 Plot of shear stress versus consolidation stress with a yield locus, two Mohr circles, and the effective yield locus

Figure 3.1 shows a plot of τ versus σ; on the plot are a yield locus, two Mohr circles, and a line known as the effective yield locus. A yield locus is the relationship between τ and σ, which usually exhibits concave curvature, see for example Jenike (1964), Carson and Wilms (2006), and Berry and Bradley (2007); the curvature is often evident at very low consolidation stresses.

The intercept of the yield locus at the ordinate gives a value of cohesion, C, and at the abscissa a value of tensile strength, T.

The yield locus can be conveniently represented by an empirical mathematical expression. Ashton et al. (1965) proposed a general equation in the form of Equation 3.1 for yield loci at constant bulk densities; this expression is known as the *Warren-Spring* equation. In their work, measurements of yield locus were performed with a Jenike shear cell and the values of T were independently measured with a diametrical split cell; the "best fit" method was used to fit the measured data. Parameter n is known as the *shear index* and it ranges from 1 to 2. When n equals to unity, Equation 3.1 becomes Equation 3.2; μ is the coefficient of friction that equals to C/T. Equation 3.2 is known as the *Coulomb Yield Criterion* (Nedderman, 1992) and it applies to yield loci that exhibit linear trends. Consistent with Equation 3.1, the Coulomb Yield Criterion is also empirical.

$$\left(\frac{\tau}{C}\right)^n = \frac{\sigma}{T} + 1 \tag{3.1}$$

$$\tau = \mu\sigma + C \tag{3.2}$$

Major consolidation or principal stress, σ_c, and unconfined yield stress, σ_y, are two important consolidation stresses derived from the yield locus. Both σ_c and σ_y are crucial to the formation of arches at hopper outlets that obstruct powder gravity flow; this is illustrated in Figure 3.2. An arch generally forms when the internal strength or major stress, σ_D, developed by the powder in a hopper under σ_c is greater than the stresses acting within the surface of the arch. For flow to happen, the stress in the exposed surface of the arch, which is σ_y, needs to be overcome; hence the powder flows when σ_D is greater than σ_y (Jenike, 1964).

Following measurements with Jenike shear cells and Jenike's analysis procedure (Jenike, 1964; Schulze, 2008), σ_c and σ_y are obtained using two Mohr circles, as shown in Figure 3.1. A Mohr circle is drawn tangentially to the yield locus and intersects at point (σ_{pre}, τ_{pre}), where steady state flow is assumed to occur, to obtain σ_c; this circle represents the stresses developed in the powder at the end of consolidation. The value of σ_y is obtained with another Mohr circle that passes through the origin, tangential to the yield locus.

The effective yield locus is a straight line that passes through the origin; it is tangential to the Mohr circle drawn through the endpoint of the yield locus, (σ_{pre}, τ_{pre}), see Figure 3.1. The slope of the straight line is $\tan(\delta_e)$ and δ_e is the *effective angle of internal friction*, which is regarded as a measure of internal friction at steady state; δ_e is required for the design of hopper according to Jenike's procedure (Jenike, 1964; Schulze, 2008).

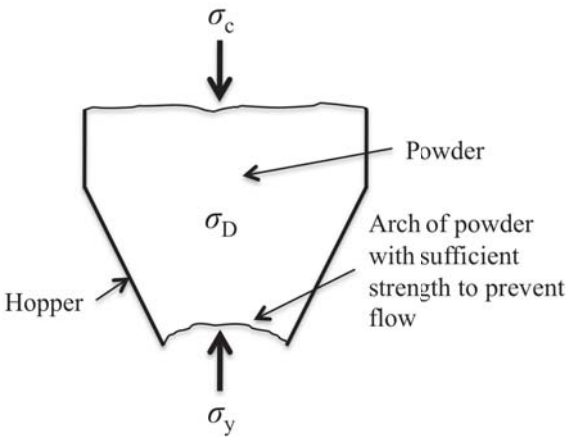

Figure 3.2 Arching in the gravity flow of a powder from a hopper, adapted from Rhodes (1998)

With annular shear cells, powders can be consolidated and subjected to continuous shear displacement or shearing and re-shearing under a given σ; the powders transition from "pure shear" to "simple shear" and to a pseudo-steady state under such operations, see Berry and Bradley (2007) and Berry et al. (2014). Berry et al. (2014) demonstrated with model limestone powders that shear stress first increased to a peak value, which is τ_{pre}, and then decreased to and fluctuated at a steady state value, τ_{ss}, irrespective of the initial σ. However, some powders such as tomato ketchup flavour displayed significant changes in shear behaviour with increasing shear displacement (Berry & Bradley, 2007); the yield locus of tomato ketchup flavour measured at steady state was lower than the yield locus at minimum shear displacement. Based on Berry and Bradley (2007) and Berry et al. (2014), the two possible ways of measuring yield loci with annular shear cells are i) measuring τ and σ within a small total shear displacement with the assumption that relative differences between τ_{pre} and τ_{ss} are small, and ii) subjecting the powder to a large initial shear displacement to pass the peak value of τ_{pre} and measuring τ and σ in the pseudo-steady state region.

To derive values of σ_y, linear lines are used to fit the yield data and the cut-off point for σ_{pre} is $\sigma_{pre}/3$, which is consistent with the stress limitation of Jenike shear cells; this method assumes linear yield data and gives maximum hopper outlet design (Berry & Bradley, 2007). For a yield locus that exhibits convex curvature, a quadratic function can be used to fit the data and a minimum σ_y is obtained (Berry & Bradley, 2007). Berry et al. (2014) justified that linear regression actually gives better reproducibility than curve fitting because a curve fit picks up natural scatters in the yield data; however they also cautioned that a linear fit contains consistent error and only allows for linear interpretation of yield data. To derive σ_c, Berry and Bradley (2007) and Berry et al. (2014) recommended the use of a Mohr circle that intersects tangentially with a linear yield locus and passes through point (σ_{pre}, τ_{ss}) instead of (σ_{pre}, τ_{pre}). The value of (σ_{pre}, τ_{ss}) is lower than (σ_{pre}, τ_{pre}); hence a minimized value of σ_c is derived. Berry and Bradley (2007)

noted that since it is the steady state flow stresses that consolidate a powder, the use of (σ_{pre}, τ_{ss}) is "more correct" for outlet design calculations.

The effects of powder bed depth and shear rate on yield locus and powder flow function measured with annular shear cells, and repeatability are also investigated by Berry and Bradley (2007). It was concluded that bed depth and shear rate have insignificant effect on yield locus and powder flow function, and the measured yield loci are reproducible.

3.2.2 Powder flow function and numerical characterization of powder flowability

The ratio of σ_c to σ_D is termed the Jenike *hopper flow factor*, *ff*; see Equation 3.3. A high value of *ff* represents poor flowability because a high value of σ_c means greater consolidation and a low value of σ_D indicates the possibility of arching is high (Jenike, 1964). Recalling the definitions of σ_c, σ_D, and σ_y in Section 3.2.1 and Figure 3.2, σ_D has to be greater than σ_y for powder failure or flow to happen; therefore a flow–no flow criterion in the form of Equation 3.4 is obtained; σ_y is a function of σ_c and the plot of experimental σ_y against σ_c gives a graphical representation known as *powder flow function*, FF.

Hopper flow factor, $$ff = \frac{\sigma_c}{\sigma_D} \tag{3.3}$$

For powder flow, $$\frac{\sigma_c}{ff} > \sigma_y \tag{3.4}$$

The limiting FF values or conditions for flow can be determined with Equation 3.5, which is a straight line with a slope of 1/*ff*. Based on this, Jenike (1964) suggested four divisions or classifications of powder flow, namely *very cohesive* or *non-flowing*, *cohesive*, *easy flowing*, and *free flowing*, see Table 3.1; these divisions are arbitrary and they are known as Jenike's criteria for powder flowability. The limiting FF values and criteria for flowability can be superimposed on the σ_c:σ_y plot to give the boundaries for transition in powder flow and hence qualitative flow information; an example is given in Figure 3.3.

Limiting condition for flow, $$\frac{\sigma_c}{ff} = \sigma_y \tag{3.5}$$

Table 3.1 Jenike's limiting flow function values and arbitrary powder flow divisions (Jenike, 1964)

Jenike's Limiting FF Values	Arbitrary Powder Flow Divisions
FF < 2	Very cohesive and non-flowing
2 < FF < 4	Cohesive
4 < FF < 10	Easy-flowing
10 < FF	Free-flowing

There are two typical flow functions in Figure 3.3; Line A is for a free flowing powder and Line B is for a cohesive powder. For the free flowing powder, the flow function is generally constant and its flow behaviour is unaffected by σ_c. For the cohesive powder, the flow function increases with σ_c and is nonlinear, as demonstrated with Line B; this trend is common for most powders that show a certain degree of cohesiveness, see for example Kurz and Münz (1975). With reference to Line B, the cohesive powder tends to flow better under high consolidation stresses and its flow becomes poor at low stress levels.

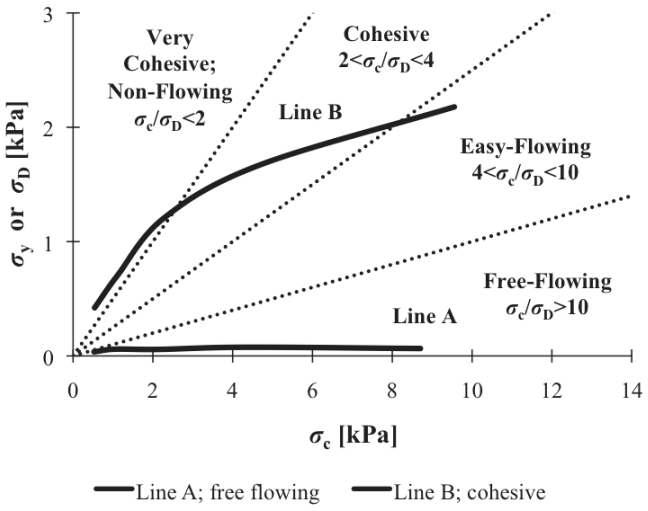

Figure 3.3 Examples of powder flow functions with real data and Jenike's criteria for powder flowability

The utility of classifying powder flowability according to Jenike's criteria has been commonly used, see for example Stanley-Wood et al. (1993), Teunou et al. (1999), and Vasilenko, Glasser and Muzzio (2011). However, there are two shortcomings in Jenike's classification.

First, it should be noted that Jenike had conveniently forgone some precision in his analysis in order to achieve brevity in powder flow definition, see Jenike (1964); therefore caution should be exercised in the use of the classification. It is also worth noting that the original

intent of his work was for the design of storage hoppers and silos, and not the characterization of powder flowability.

Second, it is not possible to completely describe powder flowability with only one numerical value on the σ_c:σ_y plot because powder flow function changes with increasing consolidation stress; the general exception is powders that are *free flowing*. Therefore, the σ_c/σ_y at a particular consolidation stress cannot be used to infer flowability at other stress levels. For accurate flow characterization, several numbers and flow function curves are required (Jenike, 1964; Schulze, 2008).

3.2.3 Cohesion

Cohesion, *C*, is the shear stress of a consolidated powder when no normal stress is applied to the shear plane; it is related to the interparticle forces that must be overcome before powder failure or flow commences (Schulze, 2008). With reference to Figure 3.1, *C* is obtained by extrapolating the yield locus to the τ-axis of the σ:τ plot. Besides powder flow function, *C* is an important powder and flow property; the following lists three key investigations on the *C* of fine powders that have prompted the interest in *C* in this work.

Orband and Geldart (1997) investigated the relationships between the *C* of lactose powders and soda ash and d_{32}. *C* was measured at consolidation stresses below 15 kPa and in the unconsolidated state with a torsional device that operated on a principle similar to that of an annular shear cell; the apparatus measured *C* directly and eliminated the yield locus extrapolation step. The plot of *C* against d_{32} for each powder revealed a critical particle diameter; the critical diameter was 52–60 μm for lactose powders and 50 μm for soda ash. Below the critical diameter, *C* increased progressively with decreasing particle diameter and was a function of consolidation stress. Above the critical diameter, constant values of *C* that fluctuated between 0.1 kPa and 0.2 kPa were observed; the powders were "free flowing" and the influence of consolidation stress was insignificant. Orband and Geldart further noted the dependence of *C* on the reciprocal of particle diameter and σ_{pre}, but made no proposal on any correlation that could simultaneously relate *C* to both factors.

Vasilenko et al. (2011) measured the *C* of selected pharmaceutical blends at 3–15 kPa with a rotational shear cell and correlated the data with the Flow Index determined with the Gravitational Displacement Rheometer, GDR; the Flow Index is an indicator of powder avalanche activity measured during the rotation of the drum of the GDR. A linear relationship between *C* and the Flow Index was observed, and the slope of the straight line changed with the composition of the pharmaceutical blends. In a later report, Vasilenko, Koynov, Glasser and Muzzio (2013) observed similar and consistent findings; their measurements were done with selected catalyst powders and over a lower consolidation stress range, 0.5–3 kPa.

The approach used by Vasilenko and colleagues is empirical, and they have demonstrated correlations between C, which is a powder flow property measured under consolidated and confined conditions, and the GDR Flow Index, which is a measure of powder flowability under unconfined conditions, see Faqih, Chaudhuri, Alexander, et al. (2006) and Faqih, Chaudhuri, Muzzio, et al. (2006). However, there has not been evaluation and discussion on the correlation between the GDR Flow Index and cohesion under zero consolidation stress, C_0, which is the stress of unconsolidated powders that has to be overcome for flow to initiate under unconfined conditions; there is therefore scope for further investigation.

In this chapter, the C and C_0 of selected powders are determined and their relationships with particle diameter and σ_{pre} are investigated. Correlations between C_0 and the GDR Flow Index are assessed and discussed in Chapter 6, which is on powder tumbling.

3.2.4 Bulk density under consolidation

In shear testing, powders are consolidated in a confined environment at different normal stresses prior to shearing. When a normal stress is applied, particle rearrangement takes place; the particles slide past one another and fill up the interparticle voids in the powder bed. The packing density of the powder increases and the bulk volume decreases.

During consolidation, bulk density, ρ_B, changes as a function of consolidation stress; ρ_B increases monotonically with increasing stress and then approaches an asymptotic value, see for example Malave, Barbosa-Canovas and Peleg (1985). The asymptotic value is the solid particle density; it is a physical limit that is not reached in practice.

Various empirical correlations have been proposed to model ρ_B as a function of consolidation stress; the correlations contain fitting parameters that are obtained from regression lines. Some correlations are given by Kawakita and Lüdde (1971), Malave et al. (1985), and Gu, Arnold and McLean (1992); they are estimation tools that can conveniently model the ρ_B of different types of powder within a specified range of consolidation stresses in spite of their lack of theoretical or physical background. Many workers in the field overlook this lack for the sake of the utility of the correlations. In this work, five correlations are used to model ρ_B as a function of σ_{pre}; they have been selected from Kawakita and Lüdde (1971), Malave et al. (1985), and Gu et al. (1992).

The first correlation is Equation 3.6, which is commonly used on food powders, see for example Malave et al. (1985). Equation 3.6 follows Equation 3.7, which was shown by linear regression to successfully model the ρ_B of food powders subjected to applied pressure P [Pa] in the range of ~4–6 kPa (Peleg & Mannheim, 1973; Peleg, Mannheim, & Passy, 1973); ρ_0 is initial or loose poured bulk density [kg m^{-3}], and $k_{s,M1}$, $k_{s,M2}$, k_1, and k_2 are fitting parameters. Parameter k_1 is the extrapolated ρ_B at unit pressure and k_2 is the slope of the straight line which represents the change of ρ_B due to pressure P, termed *compressibility*. With reference to Equation 3.6, the

difference between ρ_B and ρ_0 is normalized with ρ_0, $[(\rho_B-\rho_0)/\rho_0]$; a straight line is obtained when $[(\rho_B-\rho_0)/\rho_0]$ is plotted against $\log(\sigma_{pre})$. Parameter $k_{s,M1}$ is the value of $[(\rho_B-\rho_0)/\rho_0]$ at unit stress and $k_{s,M2}$ is the powder compressibility (Malave, et al., 1985). This equation cannot be applied at $\sigma_{pre}=0$.

$$\frac{\rho_B-\rho_0}{\rho_0}=k_{s,M1}+k_{s,M2}\log\sigma_{pre} \tag{3.6}$$

$$\rho_B=k_1+k_2\log P \tag{3.7}$$

The second correlation, Equation 3.8, is commonly known as the Kawakita equation; it has been used to model the ρ_B of pharmaceutical and metallic powders, see for example Kawakita and Lüdde (1971). Equation 3.8 is termed "Sone's model" in the work involving food powders by Malave et al. (1985); they have demonstrated that Equation 3.8 can model the ρ_B of selected food powders obtained by vibration, tapping, and mechanical compression, and with good reproducibility. The rearrangement of Equation 3.8 gives Equation 3.9, and $1/a_s$ and $1/a_sb_s$ are estimated by linear regression. At $\sigma_{pre}=0$, Equation 3.8 returns a value of ρ_0. When σ_{pre} approaches infinity, a_s represents the asymptotic value of $[(\rho_B-\rho_0)/\rho_B]$.

$$\frac{\rho_B-\rho_0}{\rho_B}=\frac{a_sb_s\sigma_{pre}}{1+b_s\sigma_{pre}} \tag{3.8}$$

$$\frac{\rho_B\sigma_{pre}}{\rho_B-\rho_0}=\frac{1}{a_s}\sigma_{pre}+\frac{1}{a_sb_s} \tag{3.9}$$

The choice of the next three correlations used here is made based on Gu et al. (1992). In their investigation, a total of 16 correlations were used to model the ρ_B of powders such as sand, sugar, alumina, coal, and glass beads at consolidation stresses ranging from 0.37 kPa to 50 kPa. The correlations were assessed statistically with an algorithm for least-squares estimation of nonlinear parameters and three correlations that best fitted the ρ_B data were identified. Equation 3.10 is known as the Nutting model, which is rearranged as Equation 3.11 for the estimation of fitting parameters k_{N1} and k_{N2} by linear regression. Equation 3.12 is the Johanson model and its rearrangement into Equation 3.13 enables the determination of k_{J1} and k_{J2} by linear regression. Equation 3.14 was proposed by Gu et al. (1992) and k_{G1} and k_{G2} are estimated by linear regression with Equation 3.15. Equation 3.8, the Kawakita equation, was one of the 16 correlations evaluated by Gu et al. (1992) but with the selected powders and stress range used,

the variance of ρ_B estimated with Equation 3.8 was large; hence Equation 3.8 was not recommended by the authors.

$$\rho_B = \rho_0 \exp\left(k_{N1} \sigma_{pre}^{\ k_{N2}} \right) \tag{3.10}$$

$$\ln\left[\ln\left(\frac{\rho_B}{\rho_0} \right) \right] = k_{N2} \ln \sigma_{pre} + \ln k_{N1} \tag{3.11}$$

$$\rho_B = \rho_0 \left(1 + k_{J1} \sigma_{pre} \right)^{k_{J2}} \tag{3.12}$$

$$\log\left(\frac{\rho_B}{\rho_0} \right) = k_{J2} \log \sigma_{pre} + k_{J2} \log k_{J1} \tag{3.13}$$

$$\rho_B = \rho_0 + k_{G1} \sigma_{pre}^{\ k_{G2}} \tag{3.14}$$

$$\log\left(\rho_B - \rho_0 \right) = k_{G2} \log \sigma_{pre} + \log k_{G1} \tag{3.15}$$

There is limited information on the relationships between the fitting parameters of the ρ_B correlations and powder physical properties such as particle diameter in the literature. The following are three useful but inconclusive initial findings from three preceding investigations.

Peleg (1978) presented a plot of compressibility, k_2 of Equation 3.7, against C measured by shear testing for selected food powders; he demonstrated that a straight line fitted the data well and further suggested that k_2 could be used as a parameter to indicate the flowability of powders.

Kawakita and Lüdde (1971) plotted the a_s and b_s data of white alundum powders against particle diameter in the range of 2 μm to 20 μm and demonstrated the dependencies of a_s and b_s on particle diameter; a_s decreased with increasing particle diameter and the b_s data showed a change of slope and a minimum at ~3 μm.

Yamashiro et al. (1983) showed a plot of C for powders such as glass beads, calcium carbonate, iron powders, and talcum versus $1/b_s$; C was measured by shear testing at an unspecified consolidation stress. It was demonstrated that b_s generally increased with increasing particle diameter but scatter and discontinuities were observed on the plot because of the differences in the physical properties of the powders used, which had not been further explored.

3.2.5 Minimum width of hopper outlet for mass flow

Jenike (1975) proposed the determination of B, which is the minimum width of hopper outlet required to assure powder mass flow under gravity from hoppers, as a measure of powder flowability.

Powder mass flow is a uniform and steady state flow through the hopper outlet under gravity, in which the bed surface of the powder remains level until it reaches the sloping section of the hopper. Mass flow is influenced by *hopper half angle*, θ_p, which is the angle between the sloping hopper wall and the vertical. Hopper half angle is primarily dependent on the angle of internal friction and the *angle of wall friction*; the angle of wall friction represents the friction between the powder and the wall of the hopper (Jenike, 1964).

Following Jenike (1975), B is given by Equation 3.16, where g is gravity acceleration [m s^{-2}] and σ_{crit} is the critical stress developed in an arch surface [Pa]. $H(\theta_p)$ is a factor determined by the hopper half angle, and Equation 3.17 gives an approximate expression for conical hoppers. To calculate B, a list of steps following the Jenike's hopper design procedure (Jenike, 1964) is required; they are summarized below.

$$B = \frac{H(\theta_p)\sigma_{crit}}{\rho_B g} \tag{3.16}$$

$$H(\theta_p) = 2.0 + \frac{\theta_p}{60} \tag{3.17}$$

The first few steps involve the measurement of a family of yield loci of a powder with a shear cell under different loads, followed by Mohr circles analysis to obtain the values of σ_y and σ_c, and hence powder flow functions, and the values of δ_e; these have been reviewed in Sections 3.2.1 and 3.2.2.

Next is the measurement of *kinematic angle of wall friction*, Φ_w; it is determined from the *wall yield locus* measured by shear testing in which a powder is sheared against a sample of the hopper wall material, usually at decreasing applied normal consolidation stresses (Jenike, 1964; Schulze, 2008). The consolidation stress acting between the powder and wall material is the wall normal stress, σ_w. The powder is first sheared at a selected σ_w until the wall shear stress, τ_w, becomes constant; shearing at steady state conditions is reached. Subsequently, σ_w is reduced and the powder is sheared until another constant value of τ_w is obtained. This procedure is repeated to obtain several pair values of (σ_w, τ_w) which are used to construct the wall yield locus; the locus is typically a straight line that passes through the origin on the σ_w:τ_w plot. The wall yield locus is a yield limit that describes the τ_w necessary to shift the powder continuously across the wall surface under certain σ_w at steady state conditions, and Equation 3.18 gives the value of Φ_w.

$$\Phi_w = \tan^{-1}\left(\frac{\tau_w}{\sigma_w}\right) \tag{3.18}$$

To obtain *ff* and θ_p, the *flow factor charts* developed by Jenike (1964) are required. A flow factor chart is the plot of Φ_w versus θ_p at a specified value of δ_e. On the chart is a series of lines that represent different values of *ff* that range from 1.1 to 4.0, and a line that gives the limiting value of θ_p to ensure mass flow as a function of Φ_w. The line divides into core and mass flow; mass flow is achieved below this line and above it core flow takes place. The *ff* values in the Jenike's flow factor charts were measured for a conical hopper and a wedge-shaped hopper with a slot outlet for δ_e values of 30^o, 40^o, 50^o, 60^o, and 70^o. An example on how to use the chart to estimate the values of θ_p and *ff* is available in Rhodes (1998). In this thesis, all calculations have been done using the flow factor charts in Rhodes (1998).

Fitzpatrick, Barringer and Iqbal (2004) reported the flow properties of 13 food powders which included salt, sugar, starch, flour, and cellulose powder. FF and δ_e were measured with an annular shear cell at consolidation stresses below 8 kPa, and Φ_w was measured with a Jenike shear cell at consolidation stresses below 6 kPa; the cylindrical base of the cell was replaced with a flat plate made of 304 stainless steel. It was found that δ_e ranged from 40^o to 65^o, Φ_w ranged from ~12^o to ~27^o, and θ_p ranged from 15^o to 35^o. The authors noted that as a rule of thumb, θ_p of 20^o is often used for achieving mass flow, but further demonstrated that θ_p could vary by up to 15^o for some food powders.

The final steps in calculating *B* involve the determination of σ_{crit}, the critical stress developed in an arch surface, which requires information on FF and *ff*, and the value of bulk density, $\rho_{B,crit}$, that is associated with σ_{crit}. An illustration on how σ_{crit} is obtained is given in Figure 3.4; the intercept of the flow function with the $\sigma_D=(1/ff)\sigma_c$ line gives the value of σ_{crit}. Note that no flow occurs when σ_y is greater than σ_c/ff, and flow happens when σ_y is lower than σ_c/ff. The value of $\rho_{B,crit}$ can be obtained if its relationship with (σ_c, σ_{crit}) is known.

In spite of the proposal by Jenike (1975) on the use of *B* as a measure of flowability, there is no traceable work in the literature that emphasizes on the utility of *B* as a powder flow indicator, and on how *B* relates to the output of other flow characterization methods.

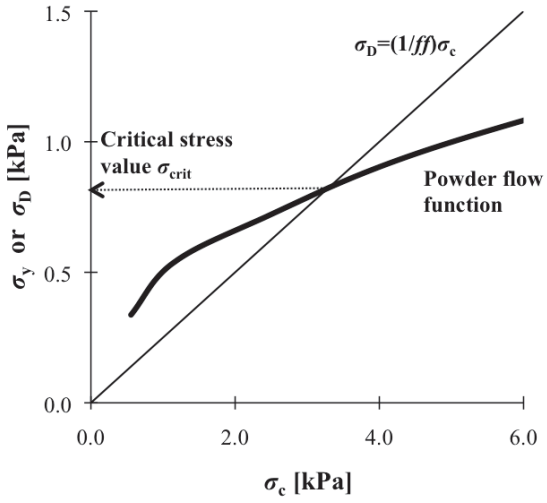

Figure 3.4 Determination of critical stress developed in an arch surface with powder flow function and hopper flow factor

3.2.6 Summary of literature review

The literature review of this chapter covers powder shear testing and the protocol developed by Jenike (1964); it includes yield locus, cohesion, powder flow function, ρ_B under consolidation, and B, the minimum width of hopper outlet required for mass flow. Parameters C, C_0, and B have been singled out for further investigation.

The shear testing by Jenike provides a scientific basis for the qualitative and quantitative characterization of powder flowability; caution should be practised because shear tests that are restricted to a particular stress level is not capable of providing information on powder flow behaviour at other stress regions. Therefore, measurement over a range of consolidation stresses should be carried out to generate several sets of yield locus and powder flow function for comprehensive and accurate flow information.

Cohesion is the shear stress of a consolidated powder in the absence of consolidation stress; it relates to the interparticle forces that must be overcome before failure or flow commences. It has been demonstrated by Orband and Geldart (1997) that C relates directly to d_{32} and a critical d_{32} or diameter range exists; C increases almost linearly with decreasing d_{32} below this critical value. However, the combined influence of d_{32} and σ_{pre} on C has not yet been fully explored and quantified.

It has also been shown that C, which is a measure of interparticle forces in consolidated powders, can relate directly to powder avalanche activity in the GDR (Vasilenko, et al., 2011; Vasilenko, et al., 2013); powder avalanche reflects powder flowability under unconfined conditions. The reason for such observation is still largely unknown, and there has not been further assessment of the relationship between powder avalanching and C_0, the cohesion of

unconsolidated powder that is more likely to directly influence powder avalanching; this will be addressed later in Chapter 6.

Powders are consolidated in shear testing; ρ_B changes as a function of σ_{pre} and empirical correlations with two fitting parameters each can be used to model ρ_B and σ_{pre}, recall Kawakita and Lüdde (1971), Malave et al. (1985), and Gu et al. (1992). Little is known about the relationships between the fitting parameters and powder properties such as d_{32}, though early evidence suggests connections between the fitting parameters, C, and particle diameter, see for example Kawakita and Lüdde (1971), Peleg (1978), and Yamashiro et al. (1983).

Hopper outlet B can be used as a measure of powder flowability (Jenike, 1975); however the relationships between B and particle size distribution and the output of other flow characterization methods remain unknown.

3.3 Aims

1. To measure the yield locus, σ_c, σ_y, δ_e, ρ_B, and Φ_w of samples of milled and spray-dried lactose powders, fine sand, and refractory dust with an annular shear cell at σ_{pre} below 5 kPa.
2. To characterize the flowability of the selected powders according to the Jenike's arbitrary powder flow divisions.
3. To determine the C and C_0 of the selected powders, and correlate them with d^*_{32} and σ_{pre}.
4. To model the ρ_B of the selected powders with Equations 3.6, 3.8, 3.10, 3.12, and 3.14, and correlate the fitting parameters of the equations with d^*_{32}.
5. To determine the B for the selected powders, investigate its relationship with d^*_{32}, and discuss its utility as a measure of powder flowability.

3.4 Materials, Methods and Analysis

3.4.1 Materials

The powders used in this work are the milled and spray-dried lactose powders, sand, and refractory dust listed in Table 2.1. Diameter d^*_{32} is the surface-volume mean diameter calculated with the Mastersizer data using bins equivalent to a full sieve analysis according to BS 410; powder in the range 0–38 μm is grouped together and assigned a mean diameter of 19 μm.

3.4.2 Measurement of yield locus, powder flow function, effective angle of internal friction and bulk density

Shear tests were performed under ambient conditions (20–24^{o}C, 36–54% relative humidity) with an annular shear cell (Brookfield Engineering Laboratories Inc., USA) that was connected to a

computer; the volume of the trough was 230 cm^3 and the volume of the vane lid was 33 cm^3. All operations were computer-controlled with customized software; the test options selected were *Geometric Spacing of Consolidation Levels* and *Measurements at the Tangent Load*.

A standard procedure was used for each powder sample; it involved preconsolidation and shearing to a critical state, followed by shearing at a lower normal stress to obtain a yield point. The σ_{pre} used were 0.31 kPa, 0.61 kPa, 1.20 kPa, 2.41 kPa, and 4.85 kPa. A family of five yield loci was created and each yield locus was constructed with four normal stresses that were lower than the respective σ_{pre}.

Linear backward extrapolation of the yield locus to the *y*-axis of the σ:τ plot gave an estimate of C, and the value of C_0 was obtained from the plot of C against σ_{pre}. Mohr circles were drawn to determine the values of σ_y and σ_c; the σ_c:σ_y pairs for each powder constitute its powder flow function. Angle δ_e was obtained by drawing a straight line through the origin and tangential to the bigger Mohr circle, and $\delta_e = \tan^{-1}(\tau/\sigma)$.

The annular shear cell also measured the *in situ* ρ_B of each powder at σ_{pre} of 0.31 kPa, 0.61 kPa, 1.20 kPa, 2.41 kPa, and 4.85 kPa.

3.4.3 Measurement of kinematic angle of wall friction

Wall friction tests were performed under ambient conditions (20–24^oC, 35–55% relative humidity) with the same annular shear cell (Brookfield Engineering Laboratories Inc., USA). The hopper wall material was the PFT-507 lid, which had a smooth bottom surface made of 304 stainless steel with 2B finish. All operations were computer-controlled and the default test option was *Even Spacing of Displacement Levels*. The powder was first consolidated up to ~4.8 kPa and sheared to steady state conditions. The powder was then consolidated and sheared at 10 decreasing σ_w that ranged from ~4.8 kPa to ~0.48 kPa; the steady state τ_w at each normal stress was measured. Ten pair values of (τ_w, σ_w) were used to construct the wall yield locus.

3.4.4 Analysis

3.4.4.1 Powder flow function and Jenike's arbitrary powder flow divisions

Unconfined yield stress, σ_y, was plotted against major consolidation stress, σ_c. The Jenike's limiting flow function values and arbitrary powder flow divisions, namely *very cohesive* or *non-flowing*, *cohesive*, *easy flowing*, and *free flowing*, were superimposed on the σ_c:σ_y plot; powder flow behaviour was read directly from the plot as a function of σ_{pre}.

3.4.4.2 Cohesion

A primary aim of this work was to correlate C with d^*_{32}, and σ_{pre}; this was done following the Coulomb Yield Criterion, $\tau=\mu\sigma+C$ (Equation 3.3). According to the Coulomb criterion, the shear

stress required to fracture a consolidated powder bed is the sum of the frictional contact stresses involved in the sliding between particles, term $\mu\sigma$, and C. The processes that take place when a powder bed undergoes shear deformation are complex; they have been described and reviewed by Schulze (2008). According to Schulze (2008), shear failure occurs in a zone and not a simple plane, and the thickness of the shear zone is apparently dependent on mean particle size, ~5–20 particle diameters for particle larger than ~100 μm and ~200 particle diameters for very fine powder. When a bed of consolidated particles is sheared, the particles in the shear zone react against the applied normal stress to free themselves sufficiently to force themselves past one another. This relative movement results in bed dilation, which affects the maximum shear stress at incipient flow.

Following Molerus (1993) who derived a theoretical expression for C in an unconsolidated powder, C in a polydisperse bulk powder under consolidation is expected to relate to the number of interparticle contact points, and hence co-ordination number. The number of particle-particle contacts is not directly measurable, but is expected to depend on the particle surface area per unit volume. For a shear zone of constant cross-sectional area, the number of particle contacts will depend on the zone thickness, which can be deduced if the following are known: i) ρ_B as a function of σ_{pre}, and ii) bed dilation.

For (i), it is assumed that the ρ_B measured in static tests is predictive of the ρ_B when the bed is sheared at the same σ_{pre}. For (ii), direct measurement of bed dilation is not available; however as C relates to the forces that must be overcome before flow commences, the dilation will produce a normal reaction stress that is assumed to be equal to the σ_{pre}. Thus, C is postulated to be a function of particle surface area per unit volume of the powder bed and the dilation force per unit area across the shear zone, per Equation 3.19.

$$C \propto f\left(\text{Surface area per unit volume, Dilation force per unit area}\right) \tag{3.19}$$

By definition, the d_{32} of a particle of density ρ_p enables the direct calculation of the surface area, A_p, of a volume of material, V_p, also of density ρ_p, when it is divided into spheres of d_{32}; $A_p/V_p = 6/d_{32}$. However in this work, the parameter of interest is the particle surface area divided by the volume of bulk powder, V_B. For a powder of bulk density ρ_B comprising particles of density ρ_p, it follows from simple algebra that $A_p/V_B = 6\rho_B/\rho_p d_{32}$. The ρ_p of milled and spray-dried lactose powders is ~1,540 kg m^{-3} (G. Niro, 2012). The following are the ρ_p of the other powders in kg m^{-3} measured with a specific gravity bottle and distilled water: ~2,470 for S3, ~2,120 for S1, ~2,130 for S2, ~3,200 for RD3, ~3,010 for RD1, and ~2,750 for RD2.

The dilation force per unit area term was written non-dimensionally and relative to the minimum preconsolidation stress, $\sigma_{pre,min}$, applied to the bed, and became $\sigma_{pre}/\sigma_{pre,min}$. Equation 3.19 was written algebraically per Equation 3.20, with the assumption of a power law

relationship; the integer 6 in the term $6\rho_B/\rho_p d_{32}$ was lumped with the prefactor m; m, a, and b are experimental fitting parameters and their values were determined by regression analysis.

$$C = m\left(\frac{\rho_B}{\rho_p d^*_{32}}\right)^a \left(\frac{\sigma_{pre}}{\sigma_{pre,min}}\right)^b \tag{3.20}$$

3.4.4.3 Bulk density under consolidation

The profiles of ρ_B at σ_{pre} of 0.31 kPa, 0.61 kPa, 1.20 kPa, 2.41 kPa, and 4.85 kPa were modelled with Equations 3.6, 3.8, 3.10, 3.12, and 3.14. By linear regression, Equations 3.6, 3.9, 3.11, 3.13, and 3.15 were used to estimate the values of fitting parameters $k_{s,M1}$, $k_{s,M2}$, a_s, b_s, k_{N1}, k_{N2}, k_{J1}, k_{J2}, k_{G1}, and k_{G2}. Each fitting parameter was then plotted against $1/d^*_{32}$ and the trend displayed was examined.

3.4.4.4 Hopper outlet *B*

Hopper outlet B was calculated with Equations 3.16 and 3.17 following Jenike's procedure outlined in Section 3.2.5; B was then plotted against d^*_{32} and the trend was examined and discussed with regards to powder flowability.

3.5 Results

3.5.1 Yield locus

Figure 3.5 shows the yield data for milled lactose powders LP4, LM1, LM2, LP1, and LP3, sand S1, and refractory dust RD1; they are selected to cover the full size range of the test powders, *viz* d^*_{32}=~23–223 μm, and all the data are for σ_{pre}=1.2 kPa. By inspection of the plot, the data exhibit apparent linear trends, and the trends seen here are also typical of the data obtained at σ_{pre} of 0.31 kPa, 0.61 kPa, 2.41 kPa, and 4.85 kPa. The yield data of all the powders used in this work are given in Table A3.1 in Appendix 3.1. Repeat measurements with powders LM1, LM9, LP1, and LP4 show that the data are reproducible.

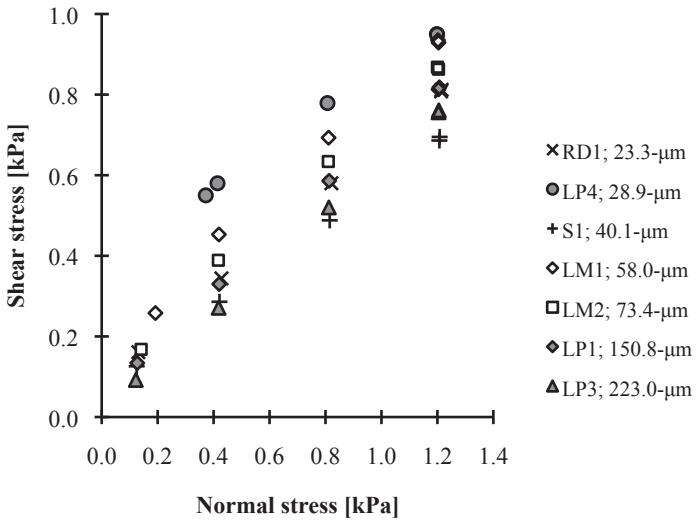

Figure 3.5 Plot of shear stress versus normal stress at a preconsolidation stress of 1.2 kPa for milled lactose LP4, LM1, LM2, LP1, and LP3, sand S1, and refractory dust RD1 with d^*_{32} ranging from ~23–223 µm

3.5.2 Powder flow function

Figure 3.6 shows the powder flow functions of 13 milled lactose powders, and Figure 3.7 shows the powder flow functions of spray-dried lactose LT1 and LT2, sand S1, S2 and S3, refractory dust RD1, RD2 and RD3; superimposed on the figures are Jenike's arbitrary powder flow divisions, *viz very cohesive* ($\sigma_c/\sigma_D<2$), *cohesive* ($2<\sigma_c/\sigma_D<4$), *easy flowing* ($4<\sigma_c/\sigma_D<10$), and *free flowing* ($\sigma_c/\sigma_D>10$), where σ_D is the major stress developed in a dome or pipe, see Jenike (1964). In general, the flow functions are nonlinear with an indication of improved powder flow at higher σ_c. For cohesive powders, such as LP4 in Figure 3.6, the flow function reflects higher yield stresses and exhibits changing slopes with increasing σ_c. For free flowing powders, such as LP3 in Figure 3.6 and most of the powders in Figure 3.7, the flow functions are relatively constant regardless of σ_c.

With reference to Figure 3.6 and σ_c=~2 kPa which corresponds to σ_{pre}=1.2 kPa, powders such as LP4, LM7, LM8, and LM9 show signs of transitioning into the next arbitrary flow division; there are four flow divisions at σ_{pre}=1.2 kPa. The divisions are reduced to three at σ_c=~4 kPa (σ_{pre}=2.41 kPa) and to two at σ_c beyond 8 kPa (σ_{pre}=4.85 kPa).

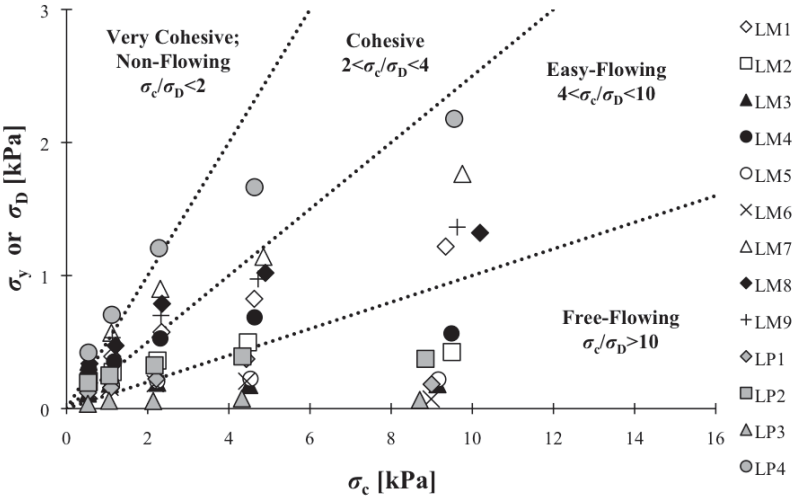

Figure 3.6 Powder flow functions of 13 milled lactose powders and Jenike's arbitrary powder flow divisions

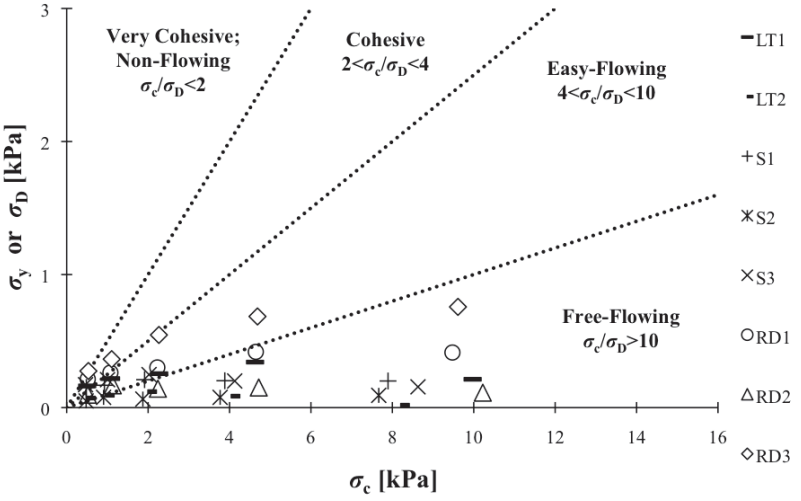

Figure 3.7 Powder flow functions of spray-dried lactose LT1 and LT2, sand S1, S2 and S3, refractory dust RD1, RD2 and RD3, and Jenike's arbitrary powder flow divisions

3.5.3 Cohesion

Figure 3.8 shows C plotted against σ_{pre} for milled lactose LP4, LM7, LM8, LM1, and LM9; at σ_c=~2 kPa (σ_{pre}=1.2 kPa), LP4 is *very cohesive*, and LM7, LM8, and LM9 are *cohesive*, and LM1 sits very closely to the boundary that separates the Jenike's arbitrary *cohesive* flow division from the *easy flowing* division, recall Figure 3.6. By inspection, C increases monotonically up to σ_{pre}=1.2 kPa, and beyond that C seems to increase at different rates.

Figure 3.9 shows C plotted against σ_{pre} for milled lactose LM4, LP2, and LM2; the powders are *easy flowing* at σ_{pre}=1.2 kPa. Consistent with Figure 3.8, C increases monotonically

when σ_{pre} is between 0.31 kPa and 1.2 kPa, but the C for LM4 and LM2 increase to 2.41 kPa. Beyond 2.41 kPa, C decreases for all three powders.

Figure 3.10 shows C plotted against σ_{pre} for milled lactose LM3, LM5, LP1, LM6, and LP3, which are *free flowing* powders at σ_{pre}=1.2 kPa. In general, the C values are small, below 0.1 kPa. By inspection, the C data for LM3, LM5, LP1, and LM6 increase linearly up to 1.2 kPa; the trend exhibited by LP1 is similar to that of *easy flowing* lactose powders in Figure 3.9. Beyond 1.2 kPa, C either levels off, see LM3 and LM5, or decreases after reaching a peak value, see LP1 and LM6. The C of LP3 exhibits a different trend; the C values are relatively constant with increasing σ_{pre}.

Figure 3.11 shows the C data of spray-dried lactose LT1 and LT2, sand S1, S2 and S3, and refractory dust RD1, RD2 and RD3 plotted against σ_{pre}; the trends exhibited are consistent with the trends in Figures 3.8, 3.9, and 3.10. Powder RD3 shows a trend similar to that of a *cohesive* powder, RD1 follows the *easy flowing* trend, and the other powders are *free flowing*.

Figure 3.12 shows C_0 plotted against d^*_{32}; see Appendix 3.2 for the estimation of C_0 values. By inspection of Figure 3.12, C_0 generally decreases with increasing d^*_{32}. The data for milled lactose are scattered. The data for spray-dried lactose powders, sand, and refractory dust seem to respectively follow an apparent linear trend. Figure 3.13 shows the C_0 plotted against $\rho_B/(\rho_p d^*_{32})$; C_0 in general increases when $\rho_B/(\rho_p d^*_{32})$ increases. The data for milled lactose and refractory dust are scattered and the data for spray-dried lactose powders and sand show apparent linear trends.

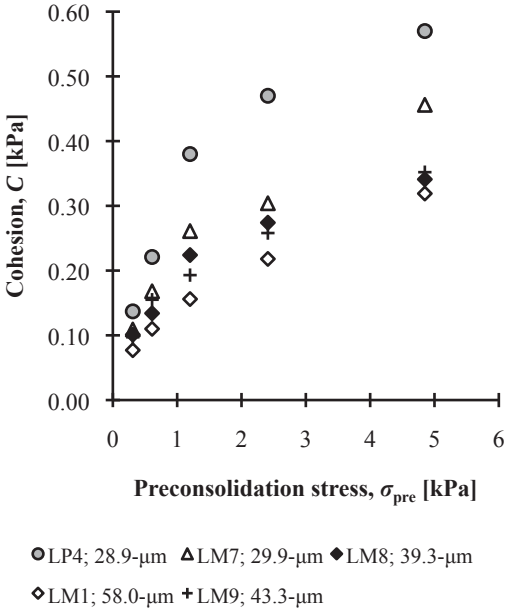

Figure 3.8 Plot of C versus σ_{pre}; milled lactose LP4 is *very cohesive* and LM7, LM8, LM1, and LM9 are *cohesive* at σ_{pre}=1.2 kPa

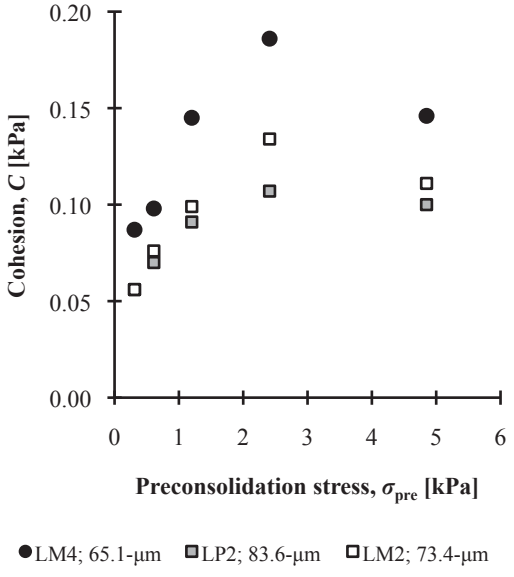

Figure 3.9 Plot of C versus σ_{pre}; milled lactose LM4, LP2, and LM2 are *easy flowing* at σ_{pre}=1.2 kPa

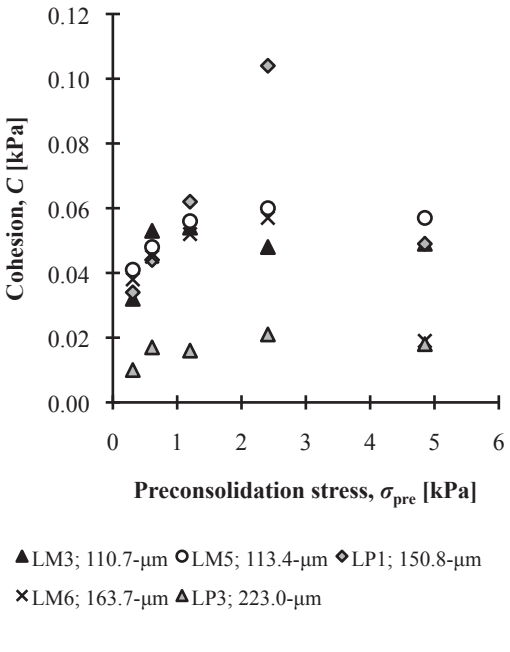

Figure 3.10 Plot of C versus σ_{pre}; milled lactose LM3, LM5, LP1, LM6, and LP3 are *free flowing* at σ_{pre}=1.2 kPa

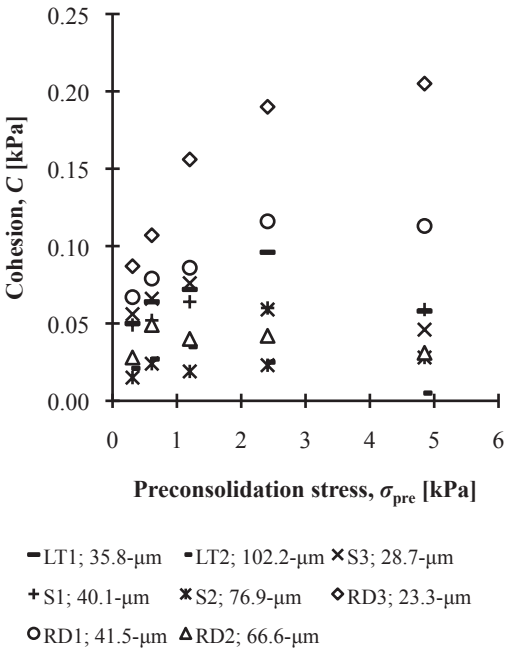

Figure 3.11 Plot of C versus σ_{pre} for spray-dried lactose LT1 and LT2, sand S1, S2 and S3, and refractory dust RD1, RD2 and RD3

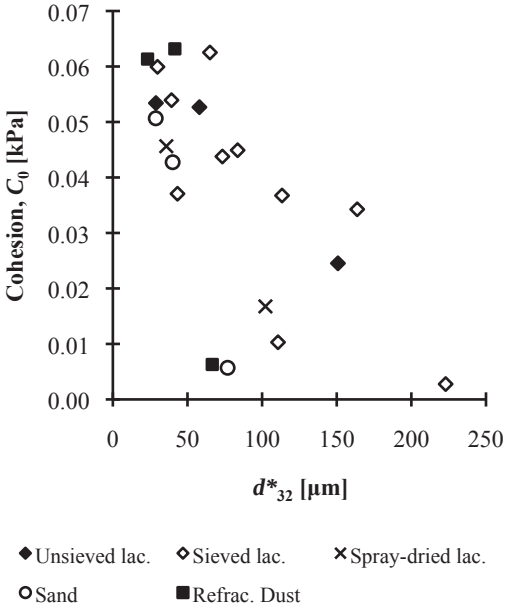

Figure 3.12 Plot of cohesion at zero preconsolidation stress, C_0 versus d^*_{32}

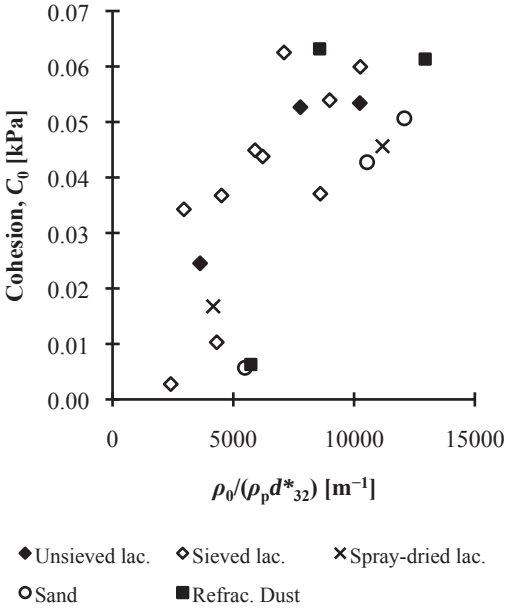

Figure 3.13 Plot of cohesion at zero preconsolidation stress, C_0 versus $\rho_0/(\rho_p d^*_{32})$

Figure 3.14 shows the C of milled lactose powders plotted against $\rho_B/(\rho_p d^*_{32})$; the figure is plotted to demonstrate the influence of surface area per unit volume on C, recall Equations 3.19 and 3.20. By inspection of the figure, the data for each σ_{pre} appear to follow a linear trend,

and linear regression of the data gives the following R^2 values: 0.94 at 0.31 kPa, 0.95 at 0.61 kPa, 0.93 at 1.20 kPa, 0.92 at 2.41 kPa, and 0.95 at 4.85 kPa. The value of parameter a of Equation 3.20 is ~1.

Figure 3.15 shows C plotted against $\rho_B/(\rho_p d^*_{32})$ for spray-dried lactose powders; C increases with increasing σ_{pre} up to σ_{pre}=2.41 kPa and then decreases, and the changes in C are smaller than the C for milled lactose powders. In Figure 3.16, the C data for sand are plotted against $\rho_B/(\rho_p d^*_{32})$; consistent with the data of spray-dried lactose powders in Figure 3.15, the changes in C are small and the data become scattered when $\rho_B/(\rho_p d^*_{32})$ increases. Figure 3.17 shows C plotted against $\rho_B/(\rho_p d^*_{32})$ for refractory dust; the trends displayed are consistent with those of milled lactose powders in Figure 3.14, but the C data of refractory dust at 2.41 kPa and 4.85 kPa seem similar.

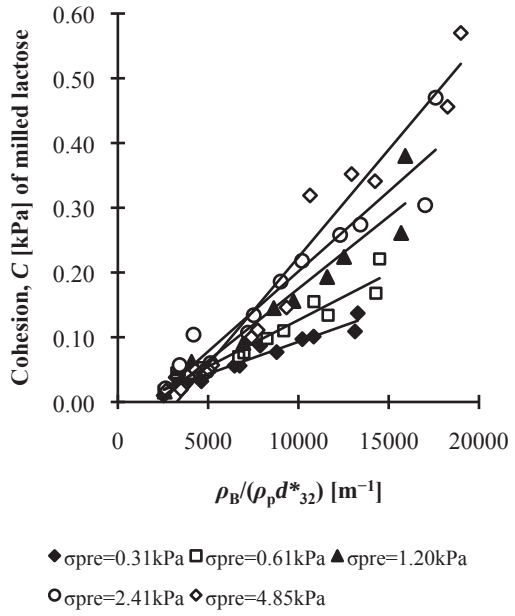

Figure 3.14 Plot of C versus $\rho_B/(\rho_p d^*_{32})$ for milled lactose powders

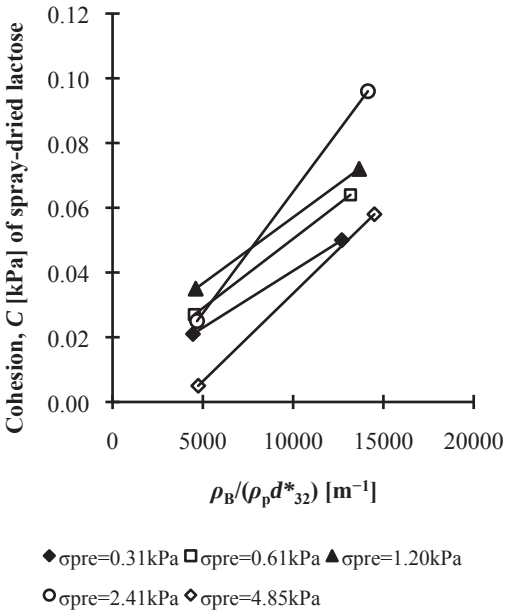

Figure 3.15 Plot of C versus $\rho_B/(\rho_p d^*_{32})$ for spray-dried lactose powders

The C data for milled lactose powders are plotted against $[\rho_B/(\rho_p d^*_{32})][(\sigma_{pre}/\sigma_{pre,min})^{0.3}]$, see Figure 3.18; an exploratory analysis suggests an optimal value of ~0.3 for b of Equation 3.20. The corresponding value for m of Equation 3.20 is 10.878×10^{-6} kPa m with R^2=0.89; hence Equation 3.21 is obtained for milled lactose powders, where C^* is the estimated cohesion [kPa].

$$C^* = 10.878 \times 10^{-6} \left(\frac{\rho_B}{\rho_p d^*_{32}} \right) \left(\frac{\sigma_{pre}}{\sigma_{pre,min}} \right)^{0.3}, \qquad 0.31 \text{ kPa} \le \sigma_{pre} \le 4.85 \text{ kPa} \tag{3.21}$$

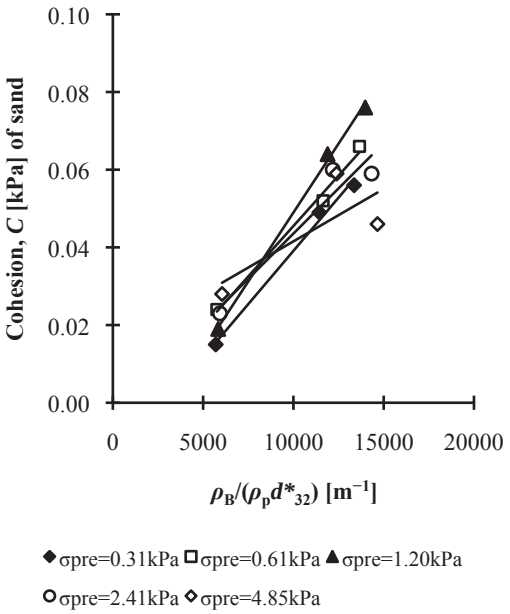

Figure 3.16 Plot of C versus $\rho_B/(\rho_p d^*_{32})$ for sand

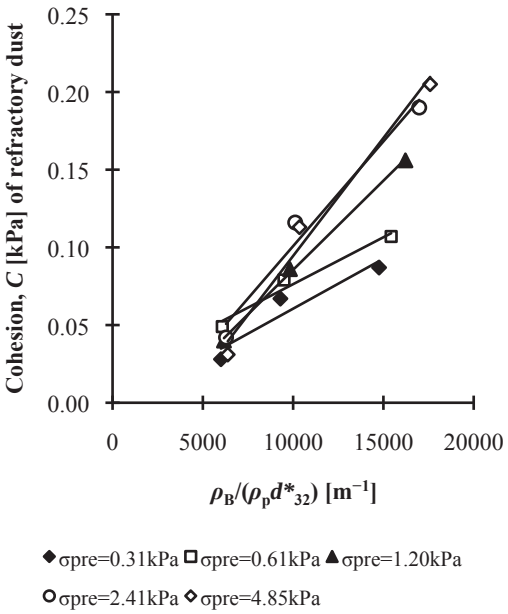

Figure 3.17 Plot of C versus $\rho_B/(\rho_p d^*_{32})$ for refractory dust

Using a=1 and b=0.3, the m values for spray-dried lactose powders, sand, and refractory dust are obtained. For spray-dried lactose powders, the value of m is 3.740×10^{-6} kPa m with R^2=0.95, see Figure 3.19 and Equation 3.22; only the data measured at σ_{pre}=0.31–2.41 kPa are used for regression because the C data show deviation at σ_{pre}= 4.85 kPa, recall Figure 3.15. For sand, m equals to 3.690×10^{-6} kPa m with R^2=0.92, see Figure 3.20 and Equation 3.23; this value is obtained with the C data at σ_{pre}=0.31–1.20 kPa. The value of m for refractory dust is 5.971×10^{-6} kPa m with R^2=0.92, see Figure 3.21 and Equation 3.24; this value is for σ_{pre}=0.31–2.41 kPa.

$$C^* = 3.740 \times 10^{-6} \left(\frac{\rho_B}{\rho_p d^*_{32}} \right) \left(\frac{\sigma_{pre}}{\sigma_{pre,min}} \right)^{0.3}, \qquad 0.31 \text{ kPa} \le \sigma_{pre} \le 2.41 \text{ kPa} \tag{3.22}$$

$$C^* = 3.690 \times 10^{-6} \left(\frac{\rho_B}{\rho_p d^*_{32}} \right) \left(\frac{\sigma_{pre}}{\sigma_{pre,min}} \right)^{0.3}, \qquad 0.31 \text{ kPa} \le \sigma_{pre} \le 1.20 \text{ kPa} \tag{3.23}$$

$$C^* = 5.971 \times 10^{-6} \left(\frac{\rho_B}{\rho_p d^*_{32}} \right) \left(\frac{\sigma_{pre}}{\sigma_{pre,min}} \right)^{0.3}, \qquad 0.31 \text{ kPa} \le \sigma_{pre} \le 2.41 \text{ kPa} \tag{3.24}$$

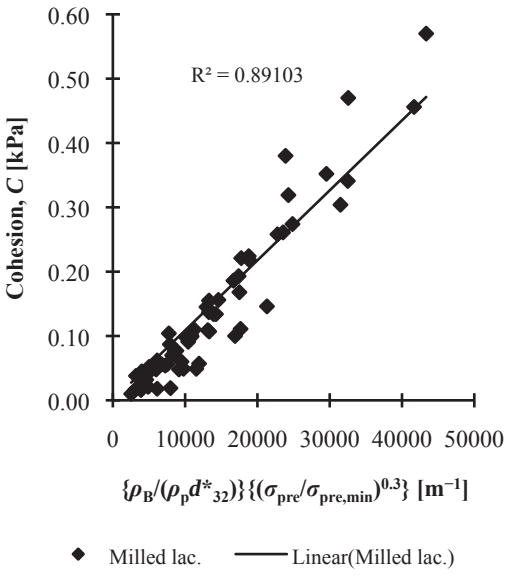

Figure 3.18 Plot of C versus $\rho_B/(\rho_p d^*_{32})(\sigma_{pre}/\sigma_{pre,min})^{0.3}$ for milled lactose powders; σ_{pre} is from 0.31–4.85 kPa

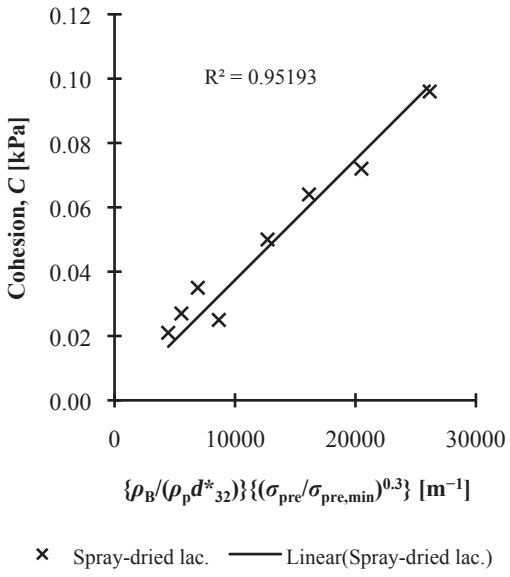

Figure 3.19 Plot of C versus $\rho_B/(\rho_p d^*_{32})(\sigma_{pre}/\sigma_{pre,min})^{0.3}$ for spray-dried lactose powders; σ_{pre} is from 0.31–2.41 kPa

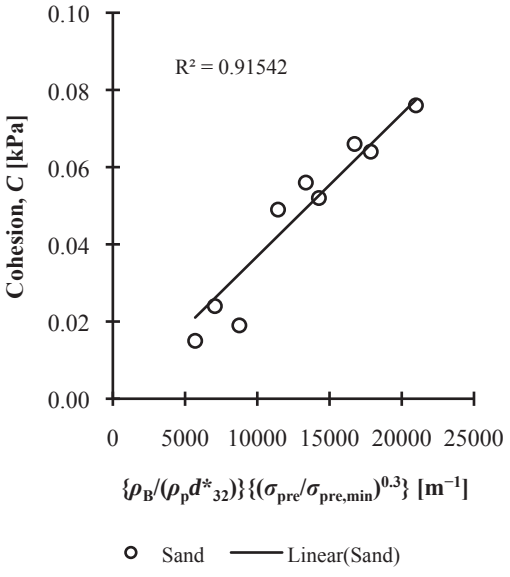

Figure 3.20 Plot of C versus $\rho_B/(\rho_p d^*_{32})(\sigma_{pre}/\sigma_{pre,min})^{0.3}$ for sand; σ_{pre} is from 0.31–1.20 kPa

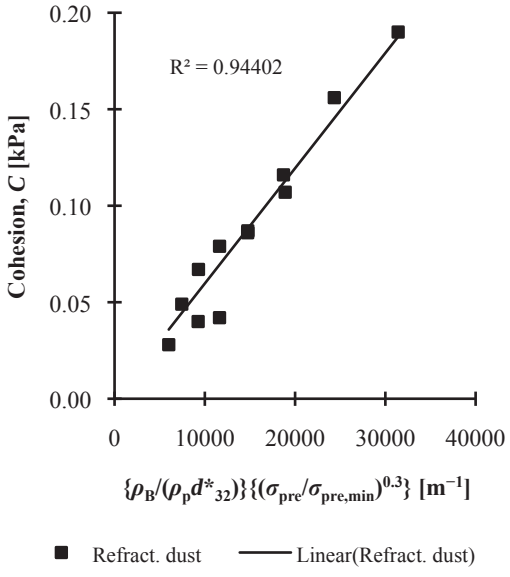

Figure 3.21 Plot of C versus $\rho_B/(\rho_p d^*_{32})(\sigma_{pre}/\sigma_{pre,min})^{0.3}$ for refractory dust; σ_{pre} is from 0.31–2.41 kPa

3.5.4 Bulk density under consolidation

Figure 3.22 shows the ρ_B profiles of powders RD1, LP4, S1, LM9, LM1, and LP1; ρ_B increases monotonically with increasing σ_{pre} and this trend is true for all the powders used. Also plotted in Figure 3.22 are repeat measurements for LP4, LM9, LM1, and LP1; the data are reproducible.

Between σ_{pre} of 0.31–4.85 kPa, ρ_B ranges from 591–995 kg m^{-3} for milled lactose powders, 701–800 kg m^{-3} for spray-dried lactose, 933–1040 kg m^{-3} for sand, and 1099–1309 kg m^{-3} for refractory dust.

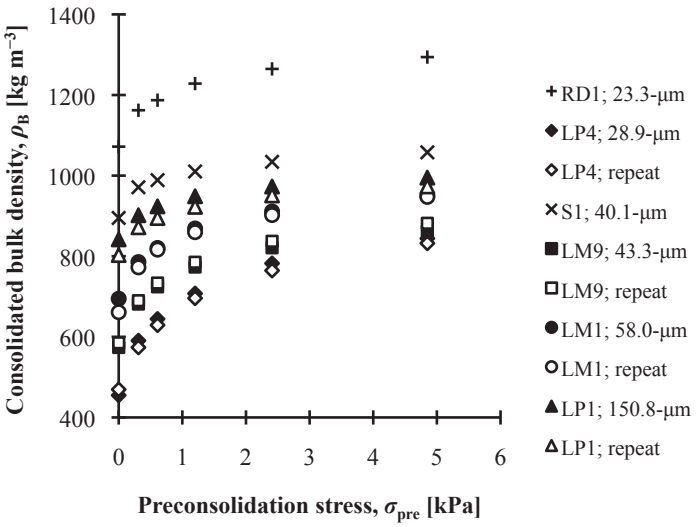

Figure 3.22 Plot of consolidated bulk density versus preconsolidation stress for powders RD1, LP4, S1, LM9, LM1, and LP1

Each ρ_B value is an average calculated with a total of eight ρ_B values that are measured by the annular shear cell at each σ_{pre}. Inspection of the ρ_B data for all powders and σ_{pre} shows that the differences between the eight measured values are small; the standard deviation ranges from 0.1 kg m^{-3} to 5.5 kg m^{-3} for milled lactose powders, 0.7 kg m^{-3} to 3.1 kg m^{-3} for spray-dried lactose powders, 0.5 kg m^{-3} to 4.9 kg m^{-3} for sand, and 0.6 kg m^{-3} to 4.8 kg m^{-3} for refractory dust. This is insignificant when compared to the measured ρ_B; therefore the average ρ_B values are used in subsequent analysis.

Figure 3.23 shows $[(\rho_B-\rho_0)/\rho_0]$ plotted against $\log(\sigma_{pre})$ for Equation 3.6, Figure 3.24 shows $[\rho_B\sigma_{pre}/(\rho_B-\rho_0)]$ plotted against σ_{pre} for Equation 3.9, Figure 3.25 shows $\ln[\ln(\rho_B/\rho_0)]$ plotted against $\ln(\sigma_{pre})$ for Equation 3.11, Figure 3.26 shows $\log(\rho_B/\rho_0)$ plotted against $\log(\sigma_{pre})$ for Equation 3.13, and Figure 3.27 shows $\log(\rho_B-\rho_0)$ plotted against $\log(\sigma_{pre})$ for Equation 3.15; only the data for LP4, S1, RD1, LM1, and LP3 are included for demonstration purposes. With reference to Figures 3.23 to 3.27, the data are well fitted with straight lines; the trends are representative of the rest of the powders used in this work. The values of $k_{s,M1}$ and $k_{s,M2}$ of Equation 3.6 are listed in Appendix 3.3, a_s and b_s of Equation 3.8 in Appendix 3.4, k_{N1} and k_{N2} of Equation 3.10 in Appendix 3.5, k_{J1} and k_{J2} of Equation 3.12 in Appendix 3.6, and k_{G1} and k_{G2} of Equation 3.14 in Appendix 3.7.

Figure 3.28 shows the relationships between $k_{s,M1}$ of Equation 3.6 and $1/d^*_{32}$ for milled lactose powders, spray-dried lactose powders, sand, and refractory dust; the graph suggests the

data follow straight lines with different slopes. Similar trends are observed with the $k_{s,M2}$ data, as shown in Figure 3.29. The plots of a_s, k_{N1}, k_{J2}, and k_{G1} against $1/d^*_{32}$ individually shows apparent linear relationships with different slopes, see Figures 3.30, 3.31, 3.32, and 3.33; this is consistent with Figure 3.28 and Figure 3.29.

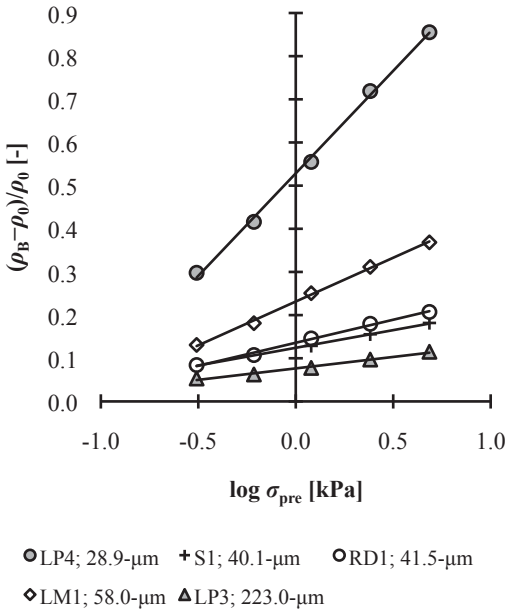

Figure 3.23 Plot of $(\rho_B-\rho_0)/\rho_0$ versus log σ_{pre} for Equation 3.6

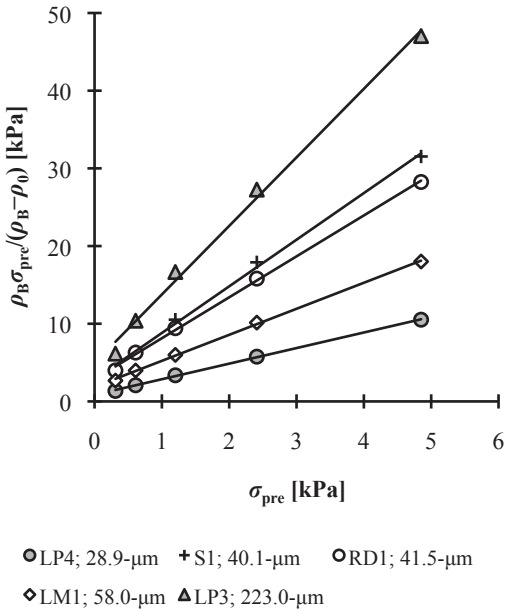

Figure 3.24 Plot of $\rho_B\sigma_{pre}/(\rho_B-\rho_0)$ versus σ_{pre} for Equation 3.9

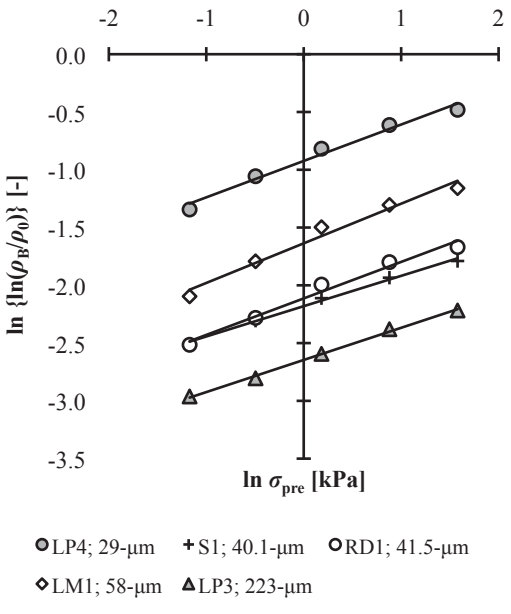

Figure 3.25 Plot of ln [ln(ρ_B/ρ_0)] versus ln σ_{pre} for Equation 3.11

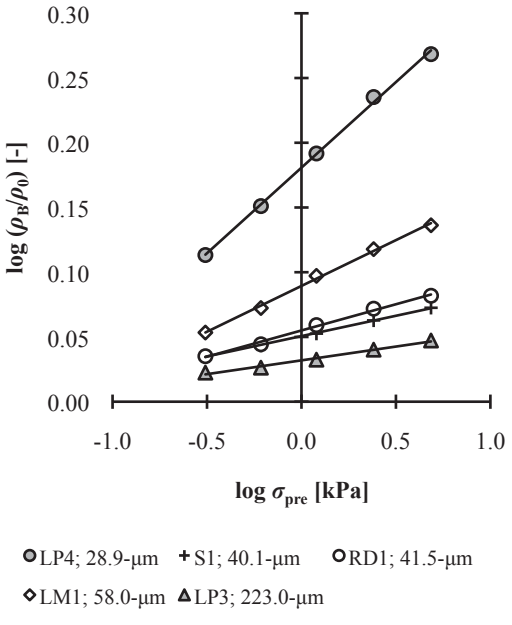

Figure 3.26 Plot of log (ρ_B/ρ_0) versus log σ_{pre} for Equation 3.13

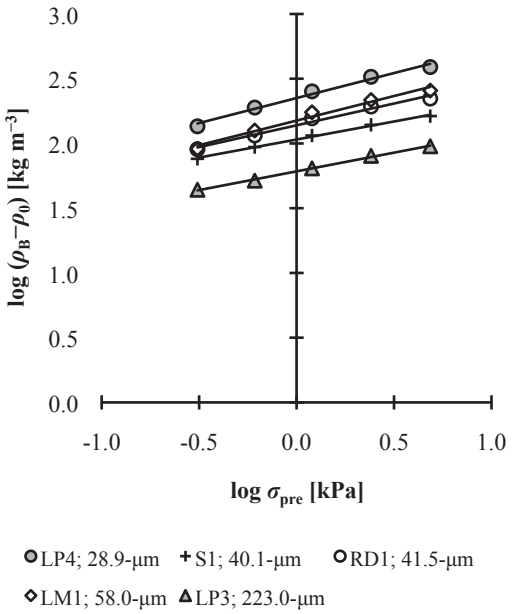

Figure 3.27 Plot of log (ρ_B–ρ_0) versus log σ_{pre} for Equation 3.15

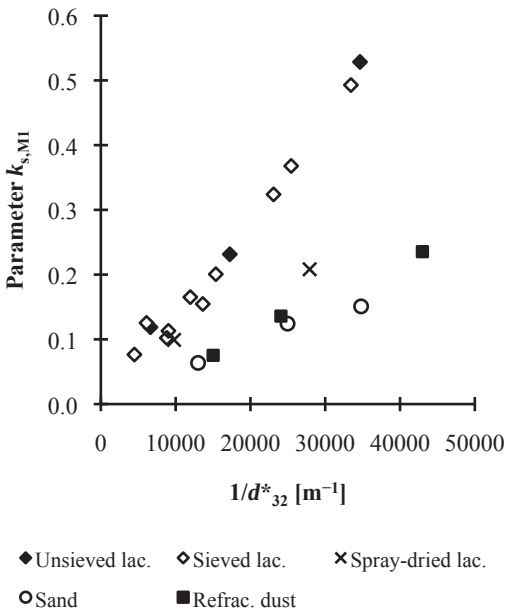

Figure 3.28 Plot of $k_{s,M1}$ of Equation 3.6 versus $1/d^*_{32}$

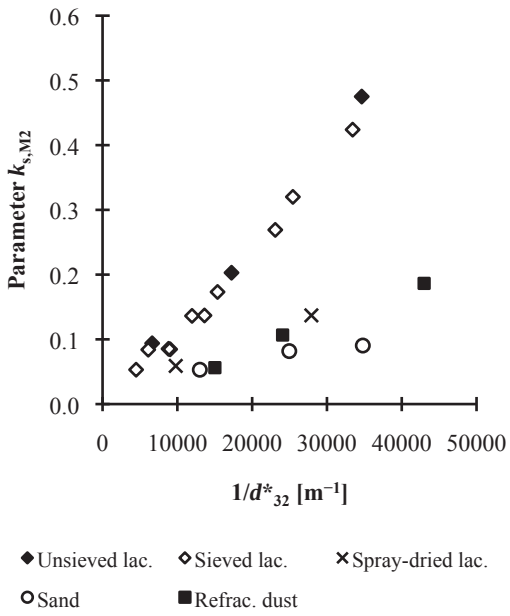

Figure 3.29 Plot of $k_{s,M2}$ of Equation 3.6 versus $1/d^*_{32}$

When b_s, k_{N2}, k_{J1}, and k_{G2} are respectively plotted against $1/d^*_{32}$, the data for the different powders exhibit different trends, see Figures 3.34, 3.35, 3.36, and 3.37. For milled lactose data, a change of slope seems to consistently occur between 15,000 m^{-1} and 20,000 m^{-1}. With the limited data sets, the spray-dried lactose powders and refractory dust data seem relatively constant. The sand data suggest linear trends.

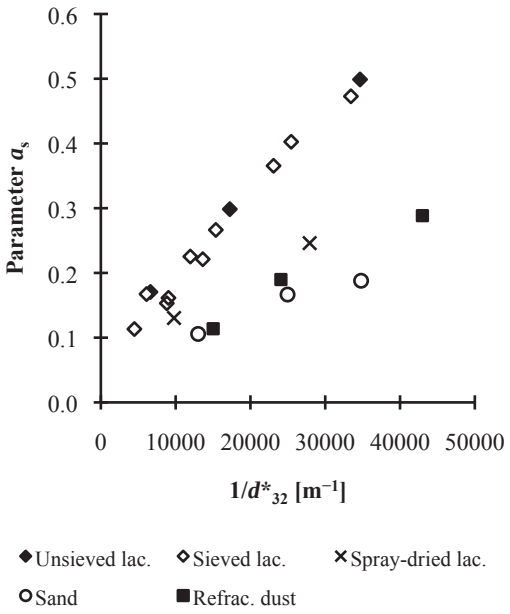

Figure 3.30 Plot of a_s of Equation 3.8 versus $1/d^*_{32}$

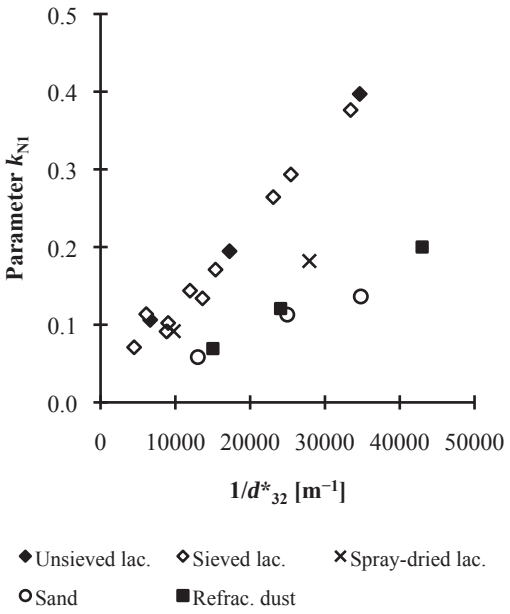

Figure 3.31 Plot of k_{N1} of Equation 3.10 versus $1/d^*_{32}$

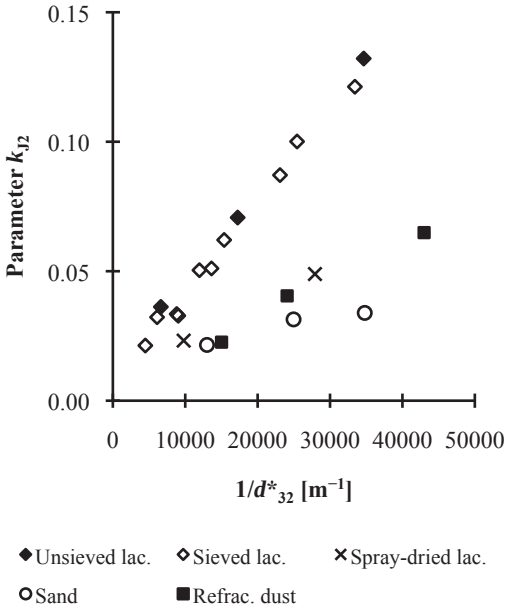

Figure 3.32 Plot of k_{J2} of Equation 3.12 versus $1/d^*_{32}$

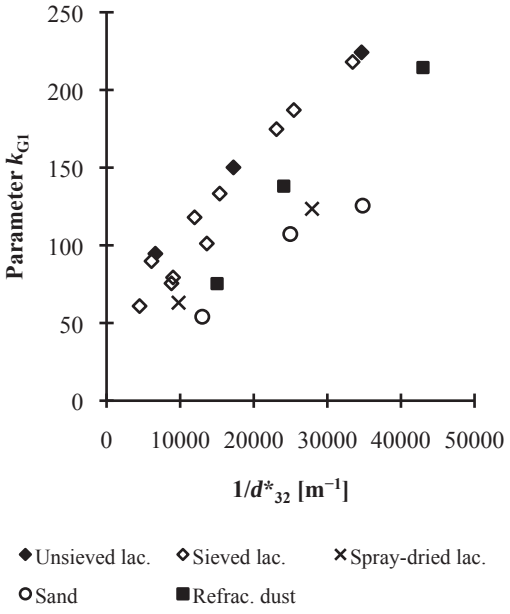

Figure 3.33 Plot of k_{G1} of Equation 3.14 versus $1/d^*_{32}$

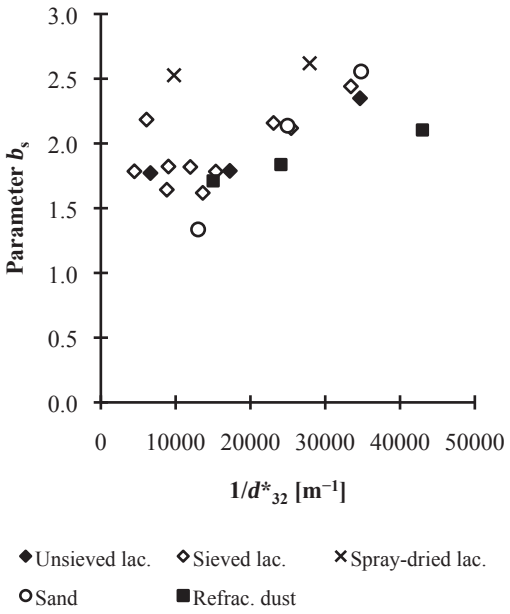

Figure 3.34 Plot of b_s of Equation 3.8 versus $1/d^*_{32}$

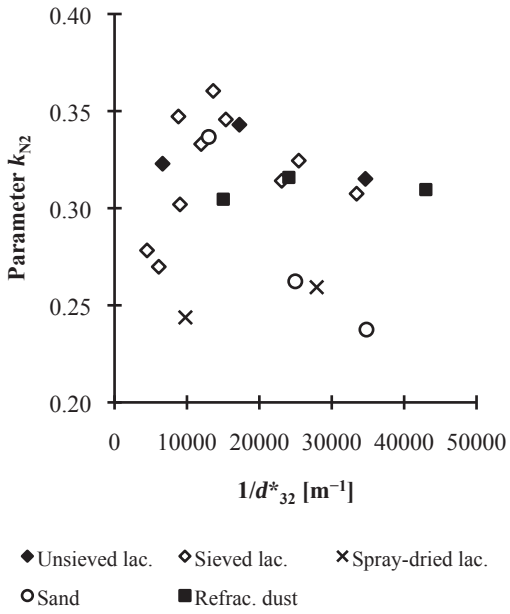

Figure 3.35 Plot of k_{N2} of Equation 3.10 versus $1/d^*_{32}$

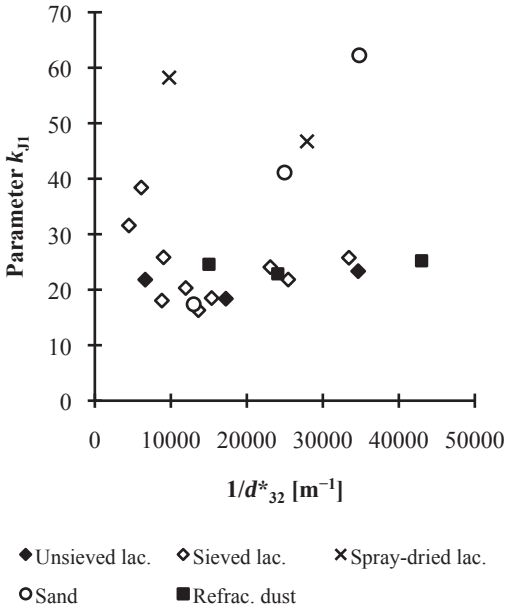

Figure 3.36 Plot of k_{J1} of Equation 3.12 versus $1/d^*_{32}$

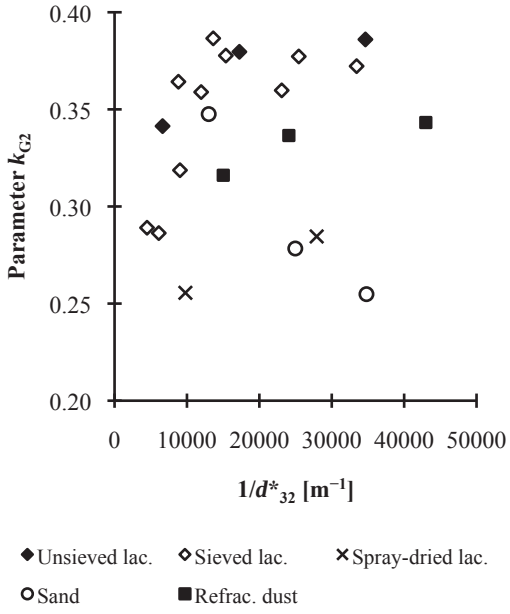

Figure 3.37 Plot of k_{G2} of Equation 3.14 versus $1/d^*_{32}$

The ρ_B of milled lactose powders is modelled as a function of σ_{pre} and $1/d^*_{32}$. With reference to Figure 3.38, which demonstrates that the $k_{s,M1}$ and $k_{s,M2}$ of Equation 3.6 for milled lactose powders follow straight lines, Equation 3.25 and Equation 3.26 are obtained by regression and forcing the fitting lines through the origin; the coefficient of determination, R^2, is greater than 0.97. Figure 3.39 shows the relationship between ρ_0 and $1/d^*_{32}$ for milled lactose powders; in

spite of relatively greater scatter at $1/d^*_{32} < 10{,}000$ m^{-1}, regression shows that ρ_0 relates linearly to $1/d^*_{32}$, giving Equation 3.27. The substitution of Equations 3.25, 3.26, and 3.27 into Equation 3.6 gives Equation 3.28, which correlates estimated bulk density, ρ^*_B, of milled lactose powders consolidated in an annular shear cell with $1/d^*_{32}$ and σ_{pre} in the range of 0.31–4.85 kPa. Figure 3.40 shows $(\rho^*_B - \rho_B)/\rho_B$ plotted against ρ_B, where ρ_B is the measured bulk density; the ρ^*_B values are within −8% and +10% of ρ_B.

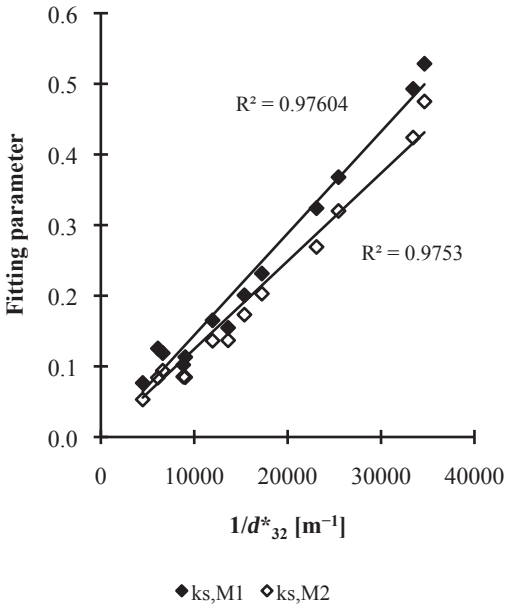

Figure 3.38 Plot of $k_{s,M1}$ and $k_{s,M2}$ of Equation 3.6 versus $1/d^*_{32}$ for milled lactose powders

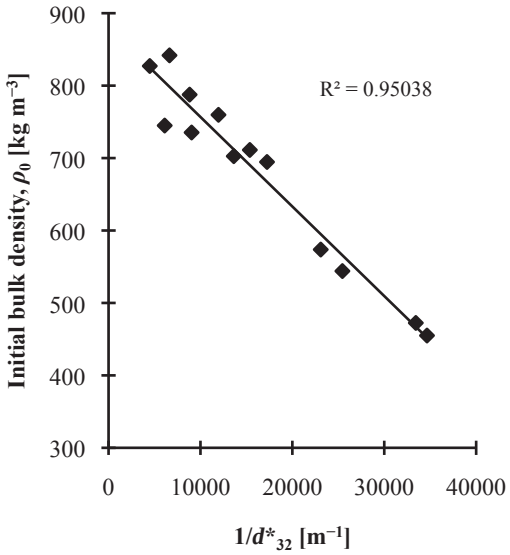

Figure 3.39 Plot of ρ_0 versus $1/d^*_{32}$ for milled lactose powders

$$k_{s,M1} = 1.4721 \times 10^{-5} \frac{1}{d^*_{32}} \tag{3.25}$$

$$k_{s,M2} = 1.3423 \times 10^{-5} \frac{1}{d^*_{32}} \tag{3.26}$$

$$\rho_0 = -0.0124 \frac{1}{d^*_{32}} + 880.3 \tag{3.27}$$

$$\rho^*_B = \left(-1.825 - 1.664 \log \sigma_{pre}\right) \times 10^{-7} \left(\frac{1}{d^*_{32}}\right)^2 + \left(0.01182 \log \sigma_{pre} + 0.00056\right) \frac{1}{d^*_{32}} + 880.3 \tag{3.28}$$

Figure 3.41 shows the ρ_0 of spray-dried lactose powders, sand, and refractory dust plotted against $1/d^*_{32}$. With the limited data sets, the ρ_0 of spray-dried lactose powders seems relatively

constant at 617–656 kg m^{-3}. The ρ_0 of sand is unchanged at ~897 kg m^{-3} up to ~25,000 m^{-1} before decreasing to 858 kg m^{-3}. For refractory dust, ρ_0 ranges from 963–1072 kg m^{-3}; it seems to peak at ~25,000 m^{-1} before dropping to 1048 kg m^{-3}.

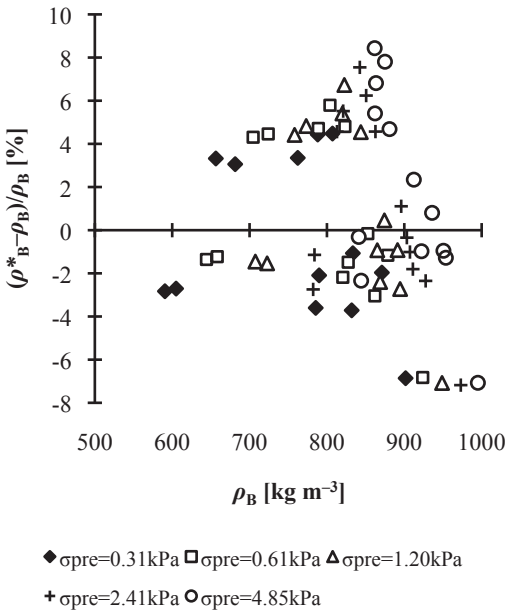

Figure 3.40 Plot of $(\rho^*_B-\rho_B)/\rho_B$ versus ρ_B for milled lactose powders; ρ^*_B is estimated with Equation 3.28

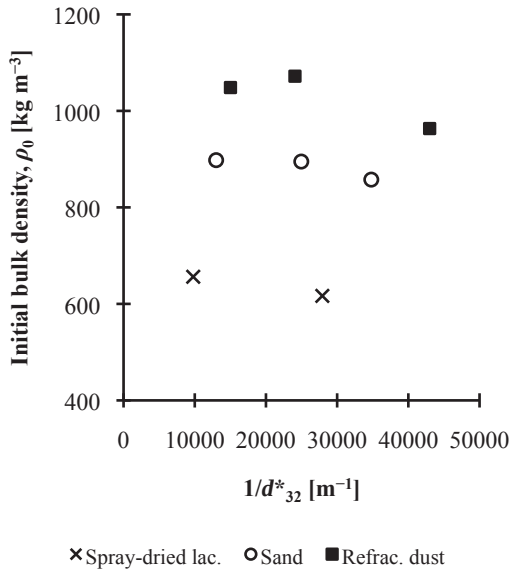

Figure 3.41 Plot of ρ_0 versus $1/d^*_{32}$ for spray-dried lactose powders, sand, and refractory dust

3.5.5 Hopper outlet *B*

Table 3.2 lists the values of δ_e, Φ_w, θ_p, σ_{crit}, $\rho^*_{B,crit}$, $H(\theta_p)$, and B for milled lactose powders. The δ_e values range from ~31–37° and Φ_w from ~23–28°; both ranges are small. The values of θ_p are from 12° to 25°; θ_p is estimated using the Jenike's flow factor charts for conical channels (Jenike, 1964) in Rhodes (1998). For LP4, LM7, LM8, and LM9, the flow factor chart of δ_e=40° and *ff*=~1.4 is used, and for the rest of the powders, the flow factor chart of δ_e=30° and *ff*=~1.8 is used. The values of σ_{crit} are estimated from plots of σ_y or σ_D versus σ_c; the powder flow function of milled lactose powders measured at σ_{pre} of 0.31 kPa, 0.61 kPa, and 1.20 kPa is assumed linear and its intercept with either the *ff*=1.4 or *ff*=1.8 line gives a pair value of (σ_c, σ_{crit}); recall Figure 3.4 and see for example Figure 3.42 for LP4. In cases where the flow function does not intercept with a *ff* line, see for example Figure 3.43 for LM6, backward extrapolation is used. The plots of σ_y or σ_D versus σ_c for the rest of the milled lactose powders are given in Appendix 3.8.

The values of $\rho^*_{B,crit}$ are estimated with Equation 3.29, where the ρ_B of milled lactose powders is modelled as a function of $1/d^*_{32}$ and σ_c. To obtain $\rho^*_{B,crit}$, the value of σ_c that is associated with σ_{crit} is used. Equation 3.29 is derived following similar approach for Equation 3.28 that involves Equation 3.6 and Equation 3.27; further details are given in Appendix 3.9.

With reference to Figure 3.44 which shows $(\rho^*_B-\rho_B)/\rho_B$ plotted against ρ_B, ρ^*_B is within ±8% of ρ_B; ρ_B is the measured bulk density and ρ^*_B is estimated with Equation 3.29.

$$\rho^*_B = \left(-1.383-1.479\log\sigma_c\right)\times 10^{-7}\left(\frac{1}{d^*_{32}}\right)^2+\left(0.0105\log\sigma_c-0.002587\right)\frac{1}{d^*_{32}}+880.3 \qquad (3.29)$$

Table 3.2 Values of δ_e, Φ_w, θ_p, σ_{crit}, $\rho^*_{B,crit}$, $H(\theta_p)$, and B for milled lactose powders

Powders	d^*_{32} [µm]	δ_e [°]	Φ_w [°]	θ_p [°]	σ_{crit} [kPa]	$\rho^*_{B,crit}$ [kg m^{-3}]	$H(\theta_p)$ [-]	B [mm]
Unsieved milled lactose								
LP4	28.9	36.8	28.0	14.0	0.5094	597.3	2.233	194.1
LM1	58.0	35.2	27.6	12.0	0.2678	751.1	2.200	79.9
LP1	150.8	32.7	25.5	19.0	0.1002	810.1	2.317	29.2
Sieved milled lactose								
LM7	29.9	36.9	27.8	15.0	0.3593	583.8	2.250	141.1
LM8	39.3	36.8	27.7	15.0	0.2841	656.3	2.250	99.3
LM9	43.3	36.2	25.3	16.0	0.3615	698.5	2.267	119.6
LM4	65.1	34.7	27.1	13.5	0.2798	770.2	2.225	82.4
LM2	73.4	34.4	22.8	24.0	0.1888	765.2	2.400	60.4
LP2	83.6	32.5	27.1	13.5	0.1850	779.7	2.225	53.8
LM3	110.7	32.9	27.1	13.5	0.1215	791.0	2.225	34.9
LM5	113.4	33.4	22.6	25.0	0.1431	798.9	2.417	44.1
LM6	163.7	32.3	24.6	20.0	0.1264	821.6	2.333	36.6
LP3	223.0	31.1	26.1	16.0	0.0381	814.6	2.267	10.8

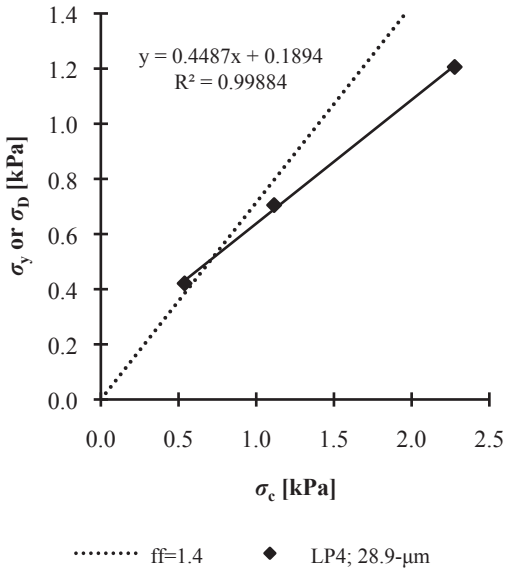

Figure 3.42 Plot of σ_y or σ_D versus σ_c for LP4

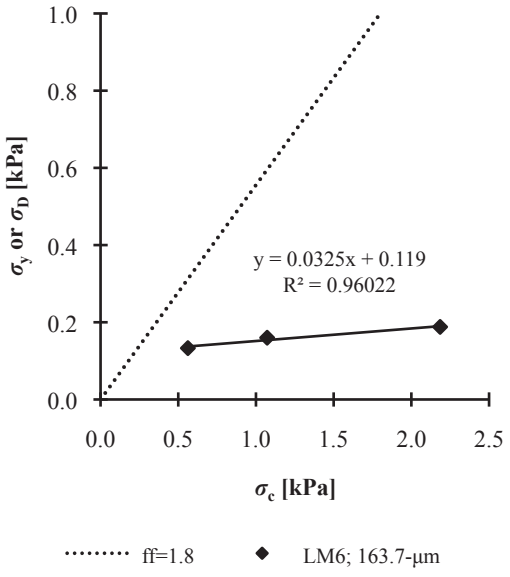

Figure 3.43 Plot of σ_y or σ_D versus σ_c for LM6

Hopper outlet B ranges from ~11 mm to ~194 mm and increases with increasing $1/d^*_{32}$, and a linear trend seems to appear, see Figure 3.45; the trend shown by the unsieved milled lactose powders seems consistent with the trend exhibited by the sieved powders.

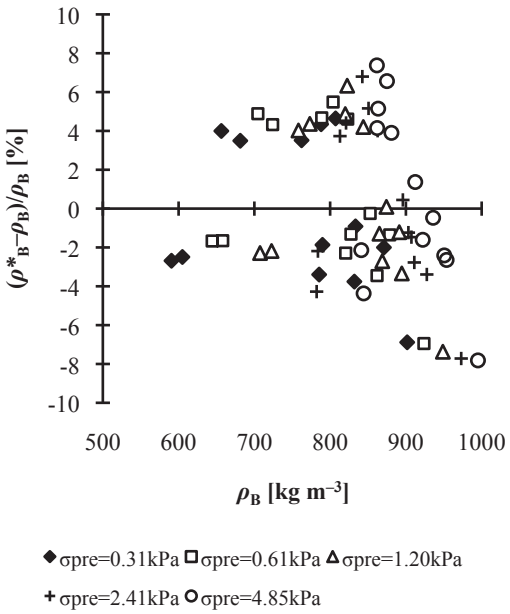

Figure 3.44 Plot of $(\rho^*_B-\rho_B)/\rho_B$ versus ρ_B for milled lactose powders; ρ^*_B is estimated with Equation 3.29

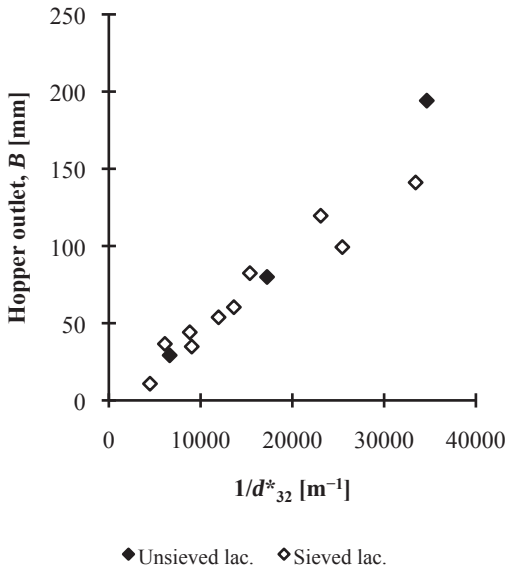

Figure 3.45 Plot of hopper outlet B versus $1/d^*_{32}$ for milled lactose powders

3.6 Discussion

3.6.1 Yield locus and powder flow function

The yield loci for milled and spray-dried lactose powders, sand, and refractory dust exhibit apparent linear trends at σ_{pre} in the range of 0.31–4.85 kPa, recall Figure 3.5. The Coulomb Yield Criterion, Equation 3.2, can therefore be used to fit the data sets and give estimates of C by linear backward extrapolation of yield locus to the ordinate of the σ:τ plot.

Powder flow functions reflect powder strength or cohesiveness, and flowability. Powders that flow well under gravity exhibit an almost flat line relationship between σ_y and σ_c, as demonstrated by powders such as LP3 and LM6 in Figure 3.6 and most of the powders in Figure 3.7. As d^*_{32} decreases, interparticle forces become more dominant and following Jenike's arbitrary powder flow divisions, the flow functions display behaviour changing from *free flowing* ($\sigma_c/\sigma_D>10$) to *easy flowing* ($4<\sigma_c/\sigma_D<10$), and then to *cohesive* ($2<\sigma_c/\sigma_D<4$) and *very cohesive* ($\sigma_c/\sigma_D<2$).

With reference to the milled lactose data sets in Figure 3.6 and considering σ_c of ~2 kPa which corresponds to σ_{pre}=1.2 kPa, the σ_c/σ_y values of the powders at and below this σ_{pre} fall into

either one of the four Jenike's arbitrary powder flow divisions; above σ_{pre}=1.2 kPa the powders are mainly *easy flowing* or *free flowing*. With these observations and hence forward in this thesis, powder flowability according to Jenike's criteria is assigned using σ_c/σ_y at σ_{pre}=1.2 kPa.

3.6.2 Cohesion and Equation 3.21

Equation 3.21 is developed for milled lactose powders following consideration of the physical processes occurring during shearing, which suggest that C is a function of particle surface area per unit volume, $6\rho_B/(\rho_p d^*_{32})$, and dilation force per unit area across the shear zone, represented indirectly by the dimensionless term $(\sigma_{pre}/\sigma_{pre,min})^{0.3}$, recall Section 3.4.4.2. Powders that are *free flowing* at σ_{pre}=1.2 kPa show little change in ρ_B when σ_{pre} is increased from 0.31 kPa to 4.85 kPa; for example the ρ_B of LP3 is from 871 kg m^{-3} to 922 kg m^{-3}, hence little dilation is expected during shear. In contrast, powders that are *very cohesive* such as LP4 with ρ_B of 591–844 kg m^{-3} and *cohesive* such as LM9 with ρ_B of 681–863 kg m^{-3} dilate more significantly when sheared.

Figure 3.46 shows $(C^*–C)/C$ plotted against C for milled lactose powders; C^* is calculated with Equation 3.21 and measured ρ_B values. For the *very cohesive* LP4 and *cohesive* LM7, LM8, LM9, and also LM1, $(C^*–C)/C$ is between –31.6% and +31.1%, indicating reasonable estimates of C. For milled lactose that are *easy flowing* and *free flowing*, $(C^*–C)/C$ is between –18.9% and +356.5%; Equation 3.21 is incapable of estimating accurately the C of *easy* and *free flowing* milled lactose powders preconsolidated and sheared at 0.31–4.85 kPa, and there are two reasons.

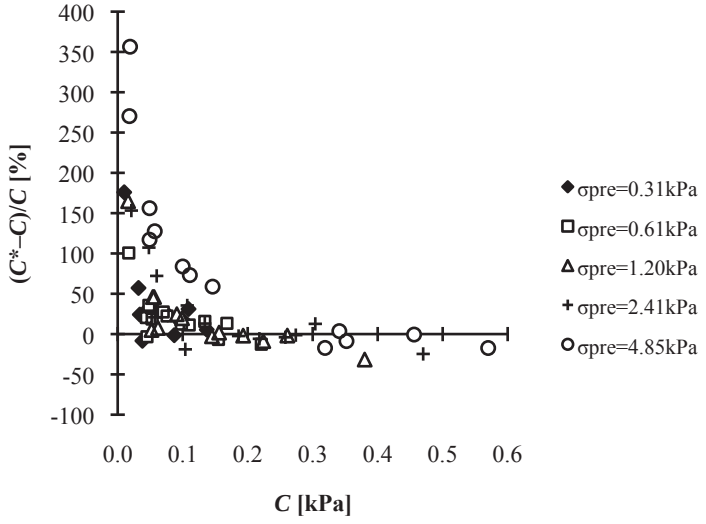

Figure 3.46 Plot of $(C^*–C)/C$ versus C for milled lactose powders; C^* is calculated with Equation 3.21 and measured ρ_B values

i) It is noted that C is expected to have a small nonzero value, C_0, for an unconsolidated powder, i.e. when σ_{pre}=0, recall Figures 3.8, 3.9, 3.10, 3.12, and

3.13. This allowance has not been included in the analysis and development of Equation 3.21; therefore Equation 3.21 in its current form is not refined yet. (C^*–C)/C is expected to decrease with a correlation that takes into account C_0.

ii) With reference to Orband and Geldart (1997), which has been reviewed in Section 3.2.3, there exists a critical d_{32} below which C increases progressively with decreasing particle size and as a function of consolidation stress, and above which C is constant, unaffected by consolidation stress, and fluctuates between 0.1–0.2 kPa; the critical d_{32} for their lactose powders is in the range of 52–60 μm.

The milled lactose data here are consistent with the data of Orband and Geldart (1997). Besides the apparent linearity of the data, the C for *easy* and *free flowing* milled lactose powders are scattered and generally unaffected by σ_{pre} at low $1/d^*_{32}$, see for example the data below 10,000 m^{-1} in Figure 3.47; the C values are also small, consistently below 0.2 kPa. The critical d^*_{32} of the milled lactose powders here is found to be 58 μm, represented by LM1 that sits very closely to the boundary that separates the Jenike's arbitrary *cohesive* flow division from the *easy flowing* division at σ_{pre}=1.2 kPa (σ_c=~2 kPa). In the development of Equation 3.21, the data for *easy* and *free flowing* powders are included, but further analysis on the influence of the scatter of the C data below 0.2 kPa has not been performed because the data seem linear and the R^2 of Equation 3.21 is high at 0.89.

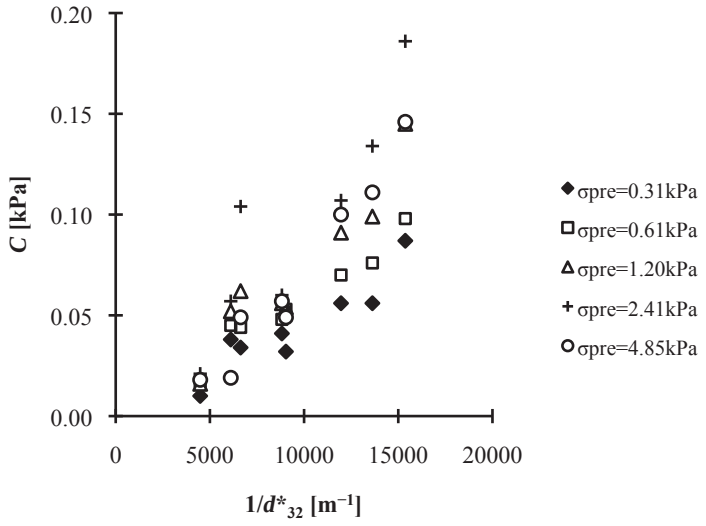

Figure 3.47 Plot of C versus $1/d^*_{32}$ for milled lactose powders that are *easy flowing* and *free flowing* at σ_{pre}=1.2 kPa

Taking into consideration (i) and (ii), re-evaluation of Equation 3.21 is necessary. The critical d^*_{32} of 58 μm can be used as a cut-off point to discard the data of *easy* and *free flowing* milled lactose powders for the development of a more accurate correlation for C that is specific

to *very cohesive* and *cohesive* milled lactose powders. But in doing so, the data of eight powders that are bigger than 58 μm, which constitute ~62% of the data, are omitted; this leaves behind smaller data sets and more data for *very cohesive* and *cohesive* milled lactose powders are desirable. There is at present no supply of milled lactose powders finer than 28.9 μm because these powders are very fine and they cannot be made with the dry sieving method in Section 2.4.1 of Chapter 2.

Nevertheless, the analysis with Equation 3.20 outlined in Section 3.4.4.2 is repeated with the data for *very cohesive* and *cohesive* milled lactose powders. Equation 3.30 with m=10.575 × 10^{-6} kPa m, a=1, b=0.35, and R^2=0.91 is obtained; the correlation error, (C*–C)/C, calculated with measured ρ_B values is between –28.9% and +27.4%. There is a slight improvement when compared with Equation 3.21 that gives an error of approximately ±31%. Equation 3.30 is valid for milled lactose powders with d^*_{32} of ~29–58 μm and preconsolidated at 0.31–4.85 kPa.

$$C^* = 10.575\times10^{-6}\left(\frac{\rho_B}{\rho_p d^*_{32}}\right)\left(\frac{\sigma_{pre}}{\sigma_{pre,min}}\right)^{0.35} \tag{3.30}$$

No further attempt is made to develop another C correlation that accounts for C_0; a primary reason is that there are no measured C_0 values but only estimates determined with the method in Appendix 3.2.

3.6.3 Consolidated bulk density, bulk density correlations, and Equation 3.28

Powder consolidation can be done by tapping, vibration, and mechanical compression; the powders in this work are compressed mechanically in a confined environment during automated shear testing at selected σ_{pre}. When σ_{pre} is applied, the particles are forced to move past one another, rearrange themselves, and fill up the interparticle voids of the powder bed, reducing the bulk volume. It is assumed that no particle deformation occurs to the particles at this range of σ_{pre}, which is below 5 kPa.

The ρ_B data of milled and spray-dried lactose powders, sand, and refractory dust are modelled empirically as a function of σ_{pre}; five straightforward correlations that contain two fitting parameters each, Equations 3.6, 3.8, 3.10, 3.12, and 3.14, are tested and all of them fit the ρ_B data well. The equations are further tested by correlating their fitting parameters with $1/d^*_{32}$. On these grounds, only $k_{s.M1}$ and $k_{s.M2}$ of Equation 3.6 show apparent linear relationships with $1/d^*_{32}$, recall Figures 3.28 and 3.29; hence Equation 3.6 is more convenient for the estimation of ρ_B.

Focusing on milled lactose powders, a_s, k_{N1}, k_{J2}, and k_{G1} relate linearly with $1/d^*_{32}$, see Figures 3.30, 3.31, 3.32, and 3.33; but in relating b_s, k_{N2}, k_{J1}, and k_{G2} to $1/d^*_{32}$, apparent change of

slopes are consistently observed at 15,000–20,000 m^{-1}, see Figures 3.34, 3.35, 3.36, and 3.37. With reference to the powder flow functions in Figure 3.6 and at σ_{pre}=1.2 kPa or σ_c=~2 kPa, the milled lactose powders that are above 20,000 m^{-1} are *very cohesive* (LP4) and *cohesive* (LM7, LM8, and LM9); those below 20,000 m^{-1} are either *easy flowing* or *free flowing*.

Equation 3.28 is derived for milled lactose powders; it is a new correlation that can estimate the consolidated ρ_B of milled lactose powders with d^*_{32} ranging from ~29 μm to 223 μm measured during shear testing in an annular shear cell at σ_{pre} between 0.31 kPa and 4.85 kPa. The correlation error is within ±10% of the measured value; recall Figure 3.40. Note that the use of $1/d^*_{32}$ in Equation 3.28 is consistent with Equation 3.21. Equation 3.28 cannot be applied at σ_{pre}=0, and its validity is expected to be up to 98 kPa following Equation 3.6 (Malave, et al., 1985).

3.6.4 Simultaneous use of Equations 3.21, 3.28, and 3.30

Equations 3.21 and 3.30 each contains a bulk density term, ρ_B, which can be estimated with Equation 3.28 for milled lactose powders consolidated at 0.31–4.85 kPa; simultaneous use of Equations 3.21 or 3.30 and Equation 3.28 can provide quick estimates of cohesion, C^*, for *very cohesive* and *cohesive* milled lactose powders in the d^*_{32} range of ~29–58 μm. With Equations 3.21 and 3.28, the correlation error, $(C^*–C)/C$, is between –32.6% and +27.5%. With Equations 3.28 and 3.30, $(C^*–C)/C$ is between –29.9% and +24.0%, which is lower and expected.

3.6.5 Hopper outlet *B*

Following the suggestion by Jenike (1975) that B can be a measure of powder flowability, and that the general relationships between B, $1/d^*_{32}$, and σ_c/σ_y for powders remain unexplored prior to this work, assessment is made with the milled lactose data. As shown in Figure 3.45, B relates directly to $1/d^*_{32}$ and the trends exhibited by the unsieved and sieved milled lactose powders are consistent. Figure 3.48 shows the relationship between B and σ_c/σ_y at σ_{pre}=1.2 kPa on the logarithmic scale; the plot demonstrates a straightforward connection with high degree of correlation, see Equation 3.31 with R^2>0.97, between B and σ_c/σ_y, which gives powder flowability according to Jenike's criteria.

$$B = 326.67\left[\left(\frac{\sigma_c}{\sigma_y}\right)_{\sigma_{pre}=1.2\text{kPa}}\right]^{-0.933} \tag{3.31}$$

Considering the critical d^*_{32} of 58 μm for *cohesive* milled lactose powders, the corresponding B is ~80 mm, recall Section 3.6.2 and see LM1 in Table 3.2. This implies that when B is 80 mm or smaller, milled lactose powders that are *easy* and *free flowing* at σ_{pre}=1.2 kPa

can generally exhibit mass flow in hoppers with smooth bottom surface made of 304 stainless steel with 2B finish and θ_p ranging from 12° to 25°; refer to Table 3.2. With reference to LP1 in Table 3.2, the critical *B* value for *free flowing* lactose is ~30 mm, and the critical *B* value for the *very cohesive* LP4 is ~190 mm.

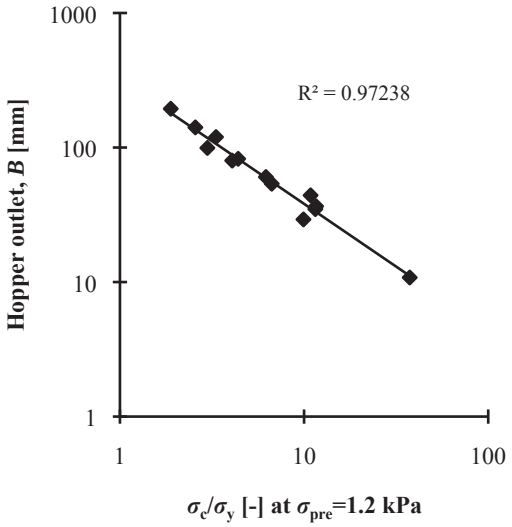

Figure 3.48 Plot of *B* versus σ_c/σ_y at σ_{pre}=1.2 kPa for milled lactose powders

Presented in Table 3.3 is the estimated hopper outlet *B* for milled lactose powders and Jenike's arbitrary powder flow divisions (Jenike, 1964). The table gives a quantitative scale of reference for powder flowability, and the context of this scale is the flow of lactose powders from storage hoppers. The scale can be used as a quick flowability reference, though it is provisional at this stage because the values of *B* are only estimates derived from limited experimental data sets.

Table 3.3 Estimated hopper outlet *B* for milled lactose powders and Jenike's arbitrary powder flow divisions (Jenike, 1964)

Hopper Outlet, *B* [mm]	**Arbitrary Powder Flow Divisions**
$B > 190$	Very cohesive and non-flowing
$80 < B < 190$	Cohesive
$30 < B < 80$	Easy-flowing
$B < 30$	Free-flowing

3.6.6 Effects of room temperature and relative humidity

The effects of room temperature (20–24°C) and relative humidity (35–55%) on the moisture uptake and hence flow properties of the powders used, especially the lactose powders, are assumed insignificant. For instance, Bronlund and Paterson (2004) reported negligible temperature influence on the moisture adsorption by beds of crystalline α-lactose monohydrate

powders when in the range of 12–40°C, and showed that there was very low moisture uptake at equilibrium, ~0.05% weight basis when water activity was between 0.5 and 0.6. Billings, Bronlund and Paterson (2006) demonstrated that significant caking between particles induced by capillary condensation between sugar particles did not occur until the relative humidity of air reached 77%.

3.7 Conclusions

Shear testing was done with samples of milled and spray-dried lactose powders, fine sand, and refractory dust with an annular shear cell at σ_{pre} between 0.31 kPa and 4.85 kPa. The key properties measured and determined include the yield locus, powder flow function, C, δ_e, Φ_w, ρ_B, and B. A summary of key findings is listed below.

When the powders were characterized according to Jenike's arbitrary powder flow divisions, namely *free flowing* ($\sigma_c/\sigma_D>10$), *easy flowing* ($4<\sigma_c/\sigma_D<10$), *cohesive* ($2<\sigma_c/\sigma_D<4$), and *very cohesive* ($\sigma_c/\sigma_D<2$), the spray-dried lactose powders, sand, and refractory dust were in general *easy* and *free flowing* regardless of σ_{pre}. For milled lactose powders, the σ_c/σ_y values at and below σ_{pre}=1.2 kPa indicated that the powders were either *very cohesive*, *cohesive*, *easy flowing*, or *free flowing*, and beyond σ_{pre}=1.2 kPa the powders were mainly *easy* and *free flowing*; the σ_c/σ_y at σ_{pre}=1.2 kPa was therefore chosen to provide flow assessment of milled lactose powders following Jenike's flow divisions.

The powders' yield loci showed apparent linear trends and followed the Coulomb Yield Criterion. C was obtained by linear extrapolation of the yield loci and further correlated with particle surface area per unit volume, $\rho_B/(\rho_p d^*_{32})$, and σ_{pre}. For *easy flowing* and *free flowing* milled and spray-dried lactose powders, sand, and refractory dust, C was scattered and consistently below 0.2 kPa. For *very cohesive* and *cohesive* milled lactose powders, Equation 3.30 has been proposed for the estimation of C; the equation is valid for powders with d^*_{32} of ~29–58 μm and the correlation error is about ±29%.

The ρ_B of powders preconsolidated at 0.31–4.85 kPa was modelled as a function of σ_{pre} with five existing empirical correlations; all the correlations fitted the data well. With the incorporation of d^*_{32}, a new correlation in the form of Equation 3.28 has been proposed for milled lactose powders; this equation can estimate the ρ_B of powders in the d^*_{32} range of ~29–223 μm to within ±10% of the measured ρ_B, but is not applicable to powders in the unconsolidated state. Equation 3.28 can be used to estimate the ρ_B term in Equation 3.30, and the simultaneous use of Equations 3.28 and 3.30 gives estimates of C that are within –30% and +24% of the measured C.

With the milled lactose powders, a straightforward connection between B and σ_c/σ_y at σ_{pre}=1.2 kPa was observed, see Equation 3.31; B can be used as a convenient measure of powder flowability according to Jenike's criteria. The tentative B values and their corresponding Jenike's

arbitrary powder flow divisions are given in Table 3.3; they are specific to milled lactose of d^*_{32} in the range of ~29–223 μm and stored in hoppers with smooth bottom surface made of 304 stainless steel with 2B finish and θ_p between 12^o and 25^o.

Chapter 4 – Powder Compression via Tapping

4.1 Introduction

Powders are compressible; their bulk density can change as a result of intentional or unintentional compression or compaction during handling, processing, and storage. Knowledge of bulk density at different stress levels is useful in tasks like converting volumetric systems to mass systems, determining the filled weight of containers, packaging of materials, and regulating the specification of food powders and pharmaceutical active ingredients and excipients. With regards to powder flowability, bulk density can indicate powder flow behaviour, see for example Abdullah and Geldart (1999). The ratio of tapped density to loose poured bulk density, which is known as Hausner ratio (Grey & Beddow, 1969; Hausner, 1967), has been used as a crude flow index in various investigations involving different powders. When a powder is cohesive and does not flow well, the ratio is generally high; the Hausner ratio for free flowing powders is usually close to unity.

The work reported here included the measurements of loose poured bulk density and tapped bulk density of selected fine powders, modelling of tapped density profiles, and the assessment of how bulk densities and Hausner ratio related to powder physical properties such as particle size distribution. The utility of Hausner ratio as a powder flow indicator for the selected powders was also further explored.

4.2 Literature Review

4.2.1 Loose poured bulk density and tapped density

Bulk density is a measure of particle packing properties; it is the mass of a powder divided by the total volume it occupies including the interparticle and intraparticle voids in the powder bed. Direct measurement of bulk densities to quantify the packing behaviour of powders is necessary in many applications across different industries due to the complexity of powder systems. A powder bed contains a large number of individual particles; each time the powder is filled into a container, the particles pack differently and occupy different spaces than before, and the neighbouring particles are also different. To quantify and predict the packing behaviour of the powder, information on the measured primary properties of the individual particles such as particle size and shape is usually insufficient.

There are two common bulk densities depending on compaction conditions, namely the *loose poured bulk density* and *tapped density*; see the review by Abdullah and Geldart (1999) and Santomaso, Lazzaro and Canu (2003). Loose poured bulk density is the density of a powder that is poured into a container and allowed to settle gently; it is a measure of *random loose packing*.

Tapped density in turn gives a measure of *random dense packing*; it is the density obtained after a loosely packed powder bed is densified by tapping to achieve higher particle packing.

The loose poured bulk density is usually measured by the "free pouring" method. In the review by Santomaso et al. (2003), nine methods were mentioned; they are standard procedures according to the International Organization for Standardization, American Society for Testing and Materials, and European Committee for Standardization. The methods are based on a similar concept – filling a cup of known volume with powder that flows under gravity from a funnel placed on the centre line of the container and at a specified distance above the cup, and measuring the mass of powder that occupies the cup. If powders do not discharge from the funnel, modifications to the method are made; they include changing the size of the funnel outlet, vibrating the funnel, and also the use of other feeding devices.

In the "free pouring" method, variations in loose poured bulk density have been observed, see for example Šmíd, Xuan and Thýn (1993) and Santomaso et al. (2003). The variations occurred because the powder entered the container from a single point source located on the centre line; the highest densities were always observed in the central core of the powder bed. But when the particles that were flowing out of the funnel were impacted and dispersed on a grid distributor or a sieve prior to filling the container, a homogeneous distribution of particles across the bed was achieved; this method was known as the "rainy" filling method as demonstrated by Šmíd et al. (1993).

The U.S. Pharmacopeia recommends the use of a "volumeter" for loose poured bulk density measurement (USP-NF, 2012). The apparatus consists of five components that are arranged in the following order and mounted on a stand: a sieve with 1 mm aperture size, a powder funnel, a loading funnel, a baffle box containing four slanting zigzag baffle plates, and a measuring cup. The function of the sieve is to break up powder agglomerates and it is placed at the top. The powder funnel channels the powder that flows under gravity into the loading funnel, which in turn loads the powder into the baffle box. The powder "slides and bounces" on the baffle plates and through the baffle box before filling the measuring cup at the bottom.

The bulk density of powders can be altered in three ways, *viz* tapping, vibration, and mechanical compression, see for example Malave et al. (1985); the focus of the work in this chapter is limited to tapping only. When a powder bed is tapped, the initial open structure of the bed that is predominantly supported by interparticle forces collapses. The particles are made to 'jump' and lose contact with adjacent particles, and this is possible because the powder is in unconfined conditions. They rearrange themselves and fill up the voids in the powder bed, resulting in lower bulk volume and hence higher particle packing.

The measurement of tapped density usually involves the use of a tapping apparatus; note that in some investigations manual tapping of powders has been practised, see for example Yu and Hall (1994). Many different types of tapping apparatus are available commercially; they can

come in different specifications but their setup is generally similar. A tapping apparatus usually comprises a container or measuring cylinder mounted on a platform that is lifted by a rotating cam connected to a motor via a shaft. The motor-driven cam lifts and drops the platform vertically through a known distance at a specified rotating speed. Depending on the design of the apparatus, the lift-drop distance can be fixed or adjustable within a range; for example the distance was fixed at 3 mm and 25 mm in the work by Abdullah and Geldart (1999), and adjustable between 30 and 250 mm in the work by Malave et al. (1985). The tapping frequency, which is controlled by the rotating speed of the motor, can vary as well; for example the frequencies reported in Abdullah and Geldart (1999) and Santomaso et al. (2003) were ~30 and ~200 taps per min. The lift-drop distance and tapping frequency recommended by the U.S. Pharmacopeia are 3 mm at 250 taps per min, and 14 mm at 300 taps per min; these are consistent with the recommendations by its European and Japanese counterparts (USP-NF, 2012).

The drop height and tapping rate govern the amount of momentum that transfers into a powder bed; together with the initial filling method and total number of taps, they influence the final tapped density of the powder. This has been demonstrated in the work by Abdullah and Geldart (1999).

4.2.2 Tapped density profiles, Hausner ratio, and powder compression correlations

When a powder bed is tapped, the tapped density changes as a function of number of taps. It increases monotonically with increasing taps and then approaches an asymptotic value; this trend has been consistently observed with different types of powder, see for example Malave et al. (1985), Yu and Hall (1994), and Abdullah and Geldart (1999). The asymptotic value is the solid particle density, which is a physical limit; this value is not reached in practice.

The asymptotic tapped density, or a value close to it, has particular significance in the quantification of powder compaction. Hausner (1967) observed that the ratio of tapped density to loose poured bulk density (or *apparent* density as stated in his paper) was a rather "new" and important characteristic of a powder; the ratio was termed Hausner ratio by Grey and Beddow (1969) and has since been used by many authors. Using metal powders of different particle sizes, shapes, and levels of fine particles, Hausner demonstrated that the ratio reflected to some extent the "friction conditions" in powder beds; however the term "friction conditions" was not defined, but was said to be largely affected by factors such as the type of powder, average particle size, particle size distribution, particle shape, specific surface of the powder, and the addition of lubricants. A high ratio indicated high friction, and this was generally observed when the particles were small, and of irregular shape.

The work by Hausner has generated interest in the application of bulk density measurements to powder flow characterization; Hausner ratio has been used as a descriptor to infer flow characteristics, see for example Abdullah and Geldart (1999), and compared or

correlated with the outputs of other flow characterization methods to provide additional information on powder flow, see for example Schüssele and Bauer-Brandl (2003), Santomaso et al. (2003), and Soh, Liew and Heng (2006).

Various empirical correlations have been proposed to model tapped density as a function of number of taps. The correlations are similar to the mathematical equations that express compacted bulk density as a function of compaction stress; recall the review in Section 3.2.4 of Chapter 3 and the work by Kawakita and Lüdde (1971), Malave et al. (1985), Gu et al. (1992), and Yu and Hall (1994). The equations contain fitting parameters that can be obtained by regression analysis. The correlations are mathematically simple and useful prediction tools that can generally model the tapped density data of different types of powder accurately despite the lack of theoretical and fundamental basis for their use and form. For the sake of convenience, accuracy, and simplicity, the compromise is generally accepted.

The two correlations used in this chapter are Equation 4.1 and Equation 4.2; their selection was motivated by the work by Malave et al. (1985) in which their accuracy was demonstrated with food powders. The correlations are simple and each contains only two fitting parameters.

$$\frac{\rho_{\text{tap}} - \rho_0}{\rho_{\text{tap}}} = \frac{a_{\text{t}} b_{\text{t}} N}{1 + b_{\text{t}} N} \tag{4.1}$$

$$\frac{\rho_{\text{tap}} - \rho_0}{\rho_0} = k_{\text{t,M1}} + k_{\text{t,M2}} \log N \tag{4.2}$$

where parameter ρ_{tap} is tapped density [kg m^{-3}]; ρ_0 is initial or loose poured bulk density [kg m^{-3}]; N is the number of taps [-]; a_{t}, b_{t}, $k_{\text{t,M1}}$, and $k_{\text{t,M2}}$ are fitting parameters.

Equation 4.1 is commonly known as the Kawakita equation; it is applicable to the results obtained from the tapping of metallic and pharmaceutical powders (Kawakita & Lüdde, 1971), and at a low number of taps (Yamashiro, Yuasa, & Kawakita, 1983). The Kawakita equation is termed “Sone’s model” by Malave et al. (1985) in their work with food powders. According to the review by Malave et al. (1985), the equation can describe successfully a variety of totally unrelated physical and physicochemical phenomena, *e.g.* mechanical stress relaxation and biochemical reaction kinetics, even though its derivation is not obtained from any kinetic consideration. The authors further demonstrated the capability of Equation 4.1 in capturing the compaction profiles of selected food powders by vibration, tapping, and mechanical compression.

Parameters a_t and b_t are fitting parameters that can be determined by plotting $[\rho_{tap}N/(\rho_{tap}-\rho_0)]$ against N; the slope of the straight line is $1/a_t$ and the intercept is $1/a_tb_t$. When N approaches zero, Equation 4.1 returns a value of initial or loose poured bulk density. When N approaches infinity, parameter a_t represents the asymptotic value of $[(\rho_{tap}-\rho_0)/\rho_{tap}]$ and equals $[1-(1/H_R)]$, where H_R is the Hausner ratio. Yu and Hall (1994) proposed a correlation of the form of Equation 4.3 using the tapped density data of alumina and silicon carbide powders. Parameter b_t is a parameter that could relate to the cohesion of powders, see for example Kawakita and Lüdde (1971) and Yamashiro et al. (1983), but their findings were not conclusive. Yu and Hall (1994) showed that the b_t data of alumina and silicon carbide powders related empirically to Hausner ratio in the form of Equation 4.4.

$$a_t = 1.435\left(1-\frac{1}{H_R}\right)^{1.092} \tag{4.3}$$

$$b_t = 6.244\times10^{-1.762H_R} \tag{4.4}$$

Equation 4.2 is a correlation that has been used on food powders, see for example Malave et al. (1985). Equation 4.2 follows Equation 3.7, recall Section 3.2.4 of Chapter 3, and Equation 3.7 was demonstrated by regression analysis to fit the compacted bulk density of food powders that were subjected to applied pressure in the range of ~4–6 kPa (Peleg & Mannheim, 1973; Peleg, Mannheim, & Passy, 1973). In his review paper, Peleg (1978) plotted the compressibility, k_2, of selected food powders against cohesion measured by shear testing; he demonstrated that a straight line fitted the data well and further suggested that compressibility could be used as a parameter to indicate the flowability of powders.

In Equation 4.2, the difference between tapped density and initial bulk density is normalized with the initial bulk density, $[(\rho_{tap}-\rho_0)/\rho_0]$ (Malave, et al., 1985); the plot of $[(\rho_{tap}-\rho_0)/\rho_0]$ against log N gives a straight line with intercept $k_{t,M1}$ and slope $k_{t,M2}$. Parameter $k_{t,M1}$ is the value of $[(\rho_{tap}-\rho_0)/\rho_0]$ at one tap (N=1) and parameter $k_{t,M2}$ is the powder compressibility which represents the "rate" of tapped density changes. Due to its empiricism, Equation 4.2 cannot be applied at N=0; but the correlation is still relevant because the bulk density at N=0 is the loose poured bulk density which can be measured independently.

4.2.3 Hausner ratio in powder flow indication and general powder classifications

Hausner ratio is defined as tapped density divided by loose poured bulk density; it is a useful powder characteristic as demonstrated by Hausner (1967). Over the years, its utility as a powder flow indicator has been explored. The following examples offer evidence that Hausner ratio can

to an extent relate empirically to powder flow characteristics determined by other flow measurement methods.

Grey and Beddow (1969) related the Hausner ratio of copper powders to powder flow time under gravity measured with a funnel flow meter; their findings showed that the flow time increased with increasing Hausner ratio.

Stanley-Wood et al. (1993) correlated the Hausner ratio of different types of powders with the ratio of major consolidation stress to unconfined yield stress, σ_c/σ_y, measured with a Jenike shear cell at an unconfined yield stress of 3 kPa; the stress value was chosen based on the work by Jenike (1964) in which the Jenike's general classification of flowability of solids was proposed. The correlation between Hausner ratio and σ_c/σ_y at 3 kPa showed a "complicated logarithmic relationship"; Hausner ratio seemed to remain constant at a value of 1.25 when powders exhibited the *free flowing* characteristic.

Lindberg et al. (2004) measured the Hausner ratio of selected pharmaceutical powder mixtures and their avalanche activities with a rotating drum; their data indicated that the ease of flow, which was deduced from the mean time between avalanches and the scatter of the avalanche times, decreased with increasing Hausner ratio.

In their assessment of the use of bulk density measurements as powder flow indicators, Abdullah and Geldart (1999) investigated the dependence of loose poured bulk density, tapped density, and Hausner ratio on the surface-volume mean particle diameter of fluid cracking catalyst and aluminium trihydroxide powders of different particle sizes and proportion of small particles. They demonstrated that loose poured bulk density increased with increasing particle diameter and leveled off at ~25 μm; tapped density also increased with increasing particle diameter but showed a gradual decrease beyond ~15 μm. Hausner ratio decreased with increasing particle diameter, and an inverse power law in the form of Equation 4.5 fitted the data well; the values of fitting parameters n_1 and n_2 for fluid cracking catalyst were 2.77 and 0.21 respectively, and the n_1 and n_2 values for aluminium trihydroxide were 2.65 and 0.19 respectively. It was generally concluded that powder flow improved with the increase of particle size, and a critical size range above which powder flow did not show further improvement seemed to occur.

$$H_R = n_1\left(\frac{1}{d_{32}^{\,n_2}}\right) \tag{4.5}$$

The use of Hausner ratio as a flow indicator or property is not without criticism. First, Hausner ratio is purely empirical and its use as a single or universal index to define or describe powder flow lacks theory. Second, Hausner ratio is not a powder intrinsic property; the ratio is dependent on the methods used to measure loose poured and tapped densities, and its level of

accuracy is low. Third, the amount of information that can be inferred from Hausner ratio is very limited because it is a single index obtained at a particular number of taps or stress level.

Nevertheless, for practical reasons, Hausner ratio is still considered a convenient additional bulk and flow property by many researchers. Compared to other characterization methods such as shear testing, bulk density measurements are more straightforward and easy to make, and tapping devices are relatively cheap. High reproducibility has also been reported by Malave et al. (1985) with food powders.

In terms of general powder classifications, Hausner ratio has been used as a quick index to assess the general behaviour of powders during handling and processing; this has been demonstrated by Geldart et al. (1984) in the gas-fluidization of cohesive powders. The authors first classified 33 powders with flow behaviour ranging from "very free flowing" to "very cohesive" under dry conditions according to the Geldart's powder classification diagram for gas-fluidization under ambient conditions (Geldart, 1973); Group C powders are cohesive and difficult to fluidize, Group A powders are aeratable and show considerable bed expansion, Group B powders fluidize with small bed expansion, and Group D powders show spouting behaviour.

Subsequent correlation between the powders' fluidization characteristics and Hausner ratio measured at 180 taps and a known drop height gave the following classification (Geldart, et al., 1984): powders with Hausner ratio less than 1.25 were certainly Group A powders. Powders with Hausner ratio greater than 1.4 showed distinctly cohesive behaviour and should be considered Group C powders. Powders with Hausner ratio between 1.25 and 1.4 might exhibit some properties of both Groups A and C; these powders were designated "semi-cohesive" Group AC powders in Geldart and Wong (1984).

The classification was used in the work by Geldart, Abdullah, Hassanpour, Nwoke and Wouters (2006); the authors included Groups B and D powders in the group where Hausner ratio was less than 1.25. However, the values of Hausner ratio that could differentiate Groups A, B, and D powders were not reported.

- Hausner ratio < 1.25, Groups A, B, or D
- 1.25 < Hausner ratio < 1.4, Group AC
- Hausner ratio > 1.4, Group C

Another general classification, which was proposed for food powders, is listed in the food engineering data handbook by Hayes (1987). The classification was derived from the correlation between the percentage of powder volume reduction measured by a tapping test, *Novadel Tap Test*, and Hausner ratio; however the context of this classification was not discussed and its methodologies were not fully disclosed. It was noted that loose poured bulk density was measured by inverting a filled measuring cylinder several times and recording the average loose

volume, and tapped density was measured with an *Englesman* tapping machine of unspecified design at 70 taps. The classification, which was called "flowability index", is listed below; the general observation is that powder flow becomes poor with increasing volume reduction and Hausner ratio.

- 1.0 < Hausner ratio < 1.1, free flowing powder
- 1.1 < Hausner ratio < 1.25, medium flowing powder
- 1.25 < Hausner ratio < 1.4, difficult flowing powder (*sic*)
- Hausner ratio > 1.4, very difficult flowing powder (*sic*)

It is noted that the Hausner ratio limits in the classifications by Geldart et al. (1984) and Hayes (1987) are not absolute values. The values are dependent on the methods used to measure bulk densities, especially the influence of filling method, number of taps, and tapping rate. The limits are therefore expected to deviate when a methodology changes; hence caution must be taken in applying such classifications to provide general powder characterization and assessment of handling and flow behaviour. Moreover, each classification was derived and proposed for a particular purpose, *e.g.* gas-fluidization and flow of food powders; its utility can be limited when taken out of context.

4.2.4 Summary of literature review

The measurement of bulk density is straightforward, and bulk density apparatus is usually cheaper than powder flow measuring devices that are more sophisticated. The practicality of using Hausner ratio in general classifications of powders and as a crude flow indicator has been demonstrated with selected methodologies and limited powders; its use under specified conditions has been advocated notwithstanding the fact that it has several unresolved shortcomings. To improve the utility of Hausner ratio, further research is necessary to relate the ratio of different types of powders to their physical properties and flow properties measured by other characterization methods.

4.3 Aims

1. To measure the loose poured bulk density and tapped density of samples of milled lactose powders, spray-dried lactose powders, fine sand, and refractory dust with selected measuring methods, and calculate the Hausner ratio.
2. To model the tapped density profiles of the powder samples with Equations 4.1 and 4.2.
3. To correlate the loose poured bulk density, tapped density, Hausner ratio, and fitting parameters a_t, b_t, $k_{t,M1}$, and $k_{t,M2}$ with d^*_{32}.

4. To correlate Hausner ratio with cohesion and the ratio of major consolidation stress, σ_c, and unconfined yield stress, σ_y, measured with an annular shear cell at preconsolidation stresses below 5 kPa.
5. To explore the utility of Hausner ratio as a general powder flow indicator.

4.4 Materials, Methods and Analysis

4.4.1 Materials

The powders used in this work are those listed in Table 2.1 in Chapter 2. Parameter d^*_{32} is the surface-volume mean diameter calculated with the Mastersizer data using bins equivalent to a full sieve analysis according to BS 410; powder in the range 0–38 μm is grouped together and assigned a mean diameter of 19 μm.

4.4.2 Measurement of loose poured bulk density

Three measurement methods were used to measure initial or loose poured bulk density, ρ_0, and compared. The first two methods were non-standard methods, namely direct filling of powders into a 100 mL and 500 mL cylindrical container respectively with a milk powder plastic spoon; the volume of the spoon was ~14 mL. The excess powder on the container was gently scraped off with a steel ruler, and the mass of powder that filled the container was weighed.

The third method was a modified New Zealand standard; the standard is known as the NZS3111 method (SANZ, 1986). The original NZS3111 method required the pouring of 1 kg of a powder sample vertically into a 500 mL cylindrical container through a funnel of 46.6^o internal angle and 12.7 mm orifice diameter. The funnel was located at the centre line of the container and the distance between the funnel outlet and the container brim was ~70 mm. The powder was first filled into the funnel; the outlet of the funnel was blocked with a finger. The finger was then removed and after all the powder passed through the funnel, excess powder on the container was gently scraped off with a steel ruler and the powder mass was weighed. In the modified NZS3111 method, the sample size was reduced to about 400–500 g for lactose powders and 700 g for mineral powders. In cases where powders did not flow through the funnel, manual stirring was performed with an art brush.

All measurements were done in triplicate, and the average value and standard deviation were calculated.

4.4.3 Measurement of tapped density

The measurement of tapped density, ρ_{tap}, was based on a method for dry dairy powders (Niro, 1978) and the European Pharmacopeia (Schüssele & Bauer-Brandl, 2003). A *Stampfvolumeter* tapping apparatus (STAV 2003, Engelmann, Germany) with a 3 mm drop height and a tapping

rate of ~240 taps min^{-1} was used; the apparatus comprised a 100 mL cylindrical cup of 42.05 mm internal diameter that was extendable by 35 mm in height with a stainless steel extension. With the extension connected, a powder sample was filled to the full and tapping commenced; the number of taps used were 10, 35, 100, 180, 500, 1000, and 1250, and some powders were tapped up to 10,000 times. At each increment, the extension was carefully removed and excess powder on the 100 mL cup was gently scraped off with a steel ruler, and the mass of powder that filled the cup was weighed. This procedure was then repeated with a new batch of sample for each increment in the number of taps. For very fine lactose powders, it was necessary to increase the amount of powder prior to tapping so that the 100 mL cup was fully filled at the end of tapping; a cylindrical cardboard tube of a similar diameter and 100 mm in height was attached to the extended cup to increase the amount of powder. The reproducibility of the measurements was checked with selected powders.

4.4.4 Measurement of flow properties with an annular shear cell

The shear testing procedure used here has been reported in Section 3.4.2 of Chapter 3.

4.4.5 Analysis

Tapped density profiles were modelled following Equations 4.1 and 4.2; modelling was performed for the convenience of the manipulation of primary data. Taking into account constant volume tapped density measurement, Equation 4.1 was rewritten as Equation 4.6, and Equation 4.2 as Equation 4.7, where m_{tap} is the sample mass after N^{th} taps and m_0 is the sample mass in the loose poured state. The values of fitting parameters a_t, b_t, $k_{t,M1}$, and $k_{t,M2}$ were determined by graph fitting; parameter $[m_{tap}N/(m_{tap}–m_0)]$ was plotted against N to give slope $1/a_t$ and intercept $1/a_tb_t$, and $[(m_{tap}–m_0)/m_0]$ was plotted against log N to give intercept $k_{t,M1}$ and slope $k_{t,M2}$. The fitting parameters were then plotted against d^*_{32}.

$$\frac{m_{tap} - m_0}{m_{tap}} = \frac{a_t b_t N}{1 + b_t N} \tag{4.6}$$

$$\frac{m_{tap} - m_0}{m_0} = k_{t,M1} + k_{t,M2} \log N \tag{4.7}$$

Hausner ratio was correlated with cohesion, C, measured at preconsolidation stresses, σ_{pre}, below 5 kPa; C was earlier demonstrated to be a function of powder surface area per unit volume and σ_{pre}, see Section 3.4.4.2 of Chapter 3. Following the work by Stanley-Wood et al. (1993), Hausner ratio was correlated with the ratio of major consolidation stress, σ_c, and

unconfined yield stress, σ_y, in the same stress range. New empirical equations that related Hausner ratio to C, σ_c/σ_y, and σ_{pre} were determined by regression and evaluated.

4.5 Results

4.5.1 Loose poured bulk density

Table 4.1 lists the average ρ_0 and standard deviation of the powders used in this work, which were obtained from the direct filling of powders with a spoon into a 100 mL cup, a 500 mL cup, and the modified NZS3111 funnel method. Also included in Table 4.1 are the flow characteristics of the powders – *Flow* and *No Flow* – through the NZS3111 funnel. By inspection of the average values in Table 4.1, ρ_0 is generally highest with the 100 mL cup method and lowest with the modified NZS3111 method. The standard deviation for all three methods is low, indicating good reproducibility.

From Table 4.1, the critical d^*_{32} below which no flow through the NZS3111 funnel takes place can be estimated. For milled lactose powders, the critical d^*_{32} is ~110 μm. For sand and refractory dust that are by observation more free flowing than the milled lactose powders, the critical d^*_{32} are ~40 μm and ~67 μm respectively.

Figure 4.1 shows ρ_0 measured by the modified NZS3111 method plotted against $1/d^*_{32}$; the trends exhibited by the sieved and unsieved milled lactose powders are different from the spray-dried lactose powders, sand, and refractory dust. The data for milled lactose powders increase linearly with decreasing $1/d^*_{32}$, and the linear regression of both data sets gives Equation 4.8 with R^2=0.96. The ρ_0 for spray-dried lactose powders is relatively constant at ~615–630 kg m^{-3}, and the ρ_0 for sand and refractory dust appears to peak when $1/d^*_{32}$ is in the range of 24,000–25,000 m^{-1}.

$$\rho_{0,\mathrm{mNZS3111}} = -0.0109\frac{1}{d^*_{32}} + 827.61 \qquad (4.8)$$

Table 4.1 Loose poured bulk density and its standard deviation for milled and spray-dried lactose powders, sand, and refractory dust

Powders	d^*_{32} **[µm]**	**Loose poured bulk density [kg m^{-3}]**			**Flow through the**
		Direct filling; 100 mL cup	Direct filling; 500 mL cup	Mod. NZS3111	**NZS3111 funnel**
Unsieved milled lactose					
LP4	28.9	489.6 ± 4.1	485.3 ± 8.0	441.5 ± 3.7	No flow
LM1	58.0	682.3 ± 3.9	677.5 ± 3.7	663.3 ± 2.2	No flow
LP1	150.8	813.6 ± 2.5	808.4 ± 1.7	802.7 ± 1.2	Flow
Sieved milled lactose					
LM7	29.9	489.9 ± 3.5	495.2 ± 10.7	477.0 ± 2.6	No flow
LM8	39.3	– [a]	555.8 ± 1.9	543.4 ± 1.9	No flow
LM9	43.3	583.5 ± 8.8	583.8 ± 6.0	574.3 ± 0.5	No flow
LM4	65.1	682.0 ± 2.0	667.5 ± 1.6	653.7 ± 4.0	No flow
LM2	73.4	683.8 ± 5.8	668.4 ± 1.7	658.4 ± 2.0	No flow
LP2	83.6	734.7 ± 6.8	717.9 ± 2.0	709.9 ± 2.1	No flow
LM3	110.7	–	705.2 ± 0.5	698.1 ± 0.2	Flow
LM5	113.4	742.0 ± 1.5	728.7 ± 1.7	719.9 ± 1.1	Flow
LM6	163.7	734.0 ± 2.4	731.1 ± 0.6	723.4 ± 0.5	Flow
LP3	223.0	– [a]	– [a]	803.1 ± 0.7	Flow
Spray-dried lactose					
LT1	35.8	– [a]	614.9 ± 2.1	– [a]	– [a]
LT2	102.2	– [a]	628.9 ± 1.7	– [a]	– [a]
Sand					
S3	28.7	848.4 ± 6.7	851.3 ± 1.0	855.2 ± 2.6	No flow
S1	40.0	886.9 ± 1.9	885.7 ± 1.9	882.3 ± 2.5	Flow
S2	76.9	869.3 ± 1.2	857.0 ± 1.1	853.3 ± 0.3	Flow
Refractory dust					
RD3	23.3	975.3 ± 1.4	981.5 ± 4.0	963.5 ± 5.3	No flow
RD1	41.5	1082.0 ± 4.0	1060.0 ± 1.0	1027.0 ± 4.9	No flow
RD2	66.6	1033.2 ± 5.7	1014.8 ± 1.1	1000.9 ± 0.5	Flow

[a] Limited powder supply; not possible for measurement

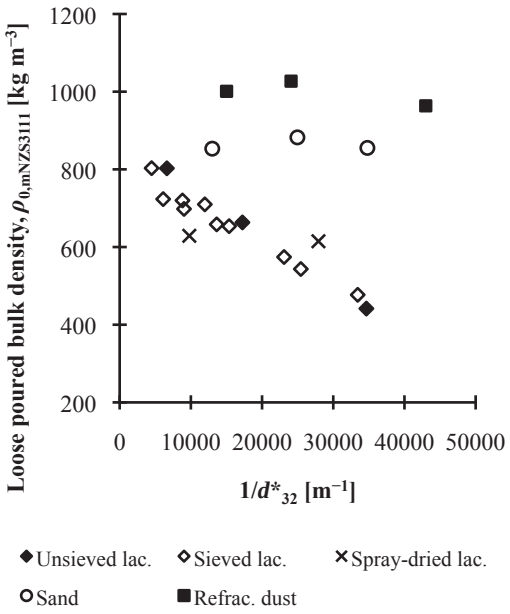

Figure 4.1 Plot of loose poured bulk density measured by modified NZS3111 method versus $1/d^*_{32}$

4.5.2 Tapped density and powder compression correlations

Figure 4.2 shows the ρ_{tap} profiles of powders LP4, LP3, S1, and RD1, which are representative of the trends exhibited by rest of the powders; also demonstrated in Figure 4.2 is the reproducibility of the data. Tapped density increases monotonically with increasing taps and shows signs of leveling off after 500 taps. Powders LM1, LM2, LM3, LM4, LM5, LP1, and LP2 were further tapped up to 10,000 taps; the percentage of increase between ρ_{tap} at 10,000 taps and 1250 taps is small and ranges from 1.09% to 3.48%.

Figure 4.3 shows ρ_{tap} at 1250 taps plotted against $1/d^*_{32}$; the trends exhibited by the sieved and unsieved milled lactose powders are different from the spray-dried lactose powders, sand, and refractory dust. For milled lactose powders and below ~18,000 m^{-1}, ρ_{tap} shows scatter; above ~18,000 m^{-1} ρ_{tap} seems to decrease linearly with increasing $1/d^*_{32}$. The ρ_{tap} for spray-dried lactose, sand, and refractory dust increases with increasing $1/d^*_{32}$; above 24,000 m^{-1} the ρ_{tap} for sand and refractory dust seems to level off.

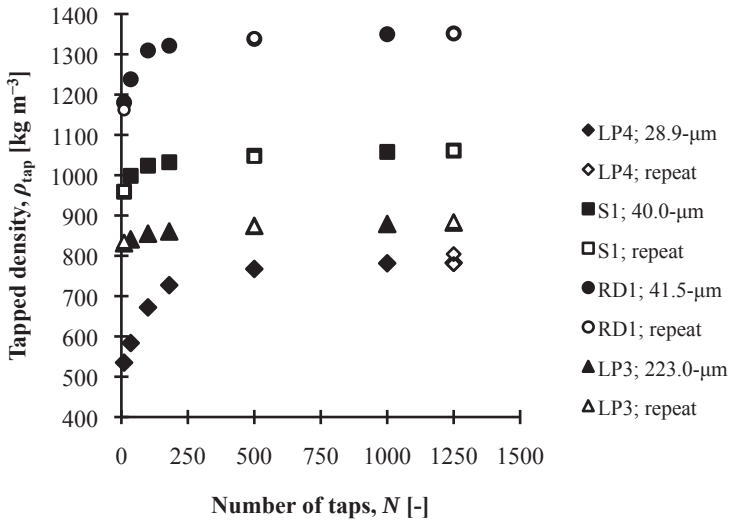

Figure 4.2 Tapped density profiles of powders LP4, LP3, S1, and RD1

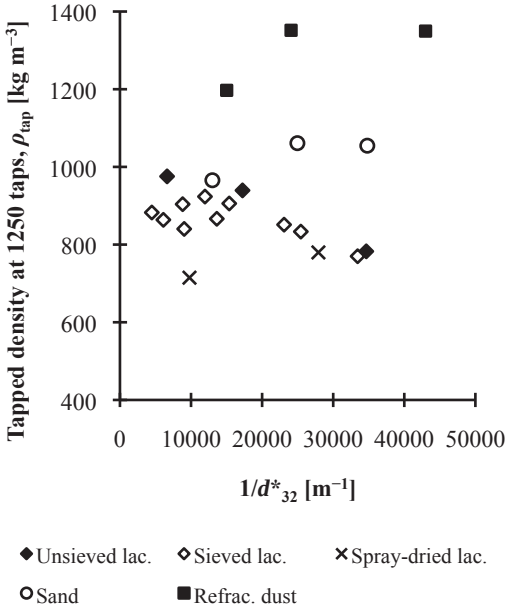

Figure 4.3 Plot of tapped density at 1250 taps versus $1/d^*_{32}$

Figure 4.4 shows the plot of $[m_{tap}N/(m_{tap}–m_0)]$ versus N and Figure 4.5 shows $[(m_{tap}–m_0)/m_0]$ plotted against log N for powders LP4, LP3, S1, and RD1; the trends exhibited by the data of the rest of the powders are similar to those shown in the figures. With reference to both figures, the data are well fitted with straight lines; the values of R^2 are above 0.9. The values of parameters a_t, b_t, $k_{t,M1}$, and $k_{t,M2}$, and R^2 for all the powders are given in Appendix 4.1.

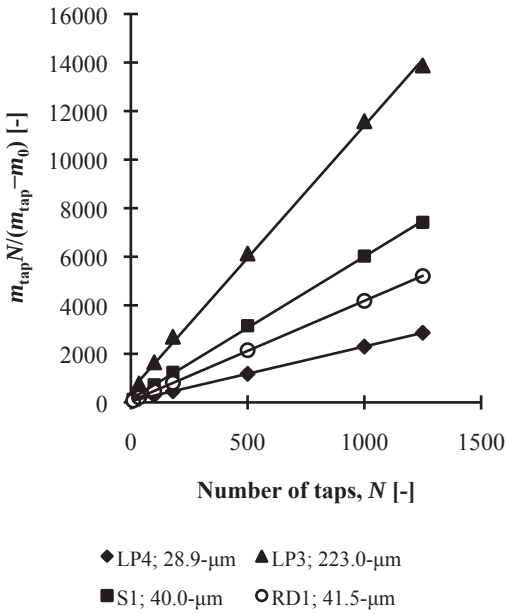

Figure 4.4 Plot of $m_{tap}N/(m_{tap}-m_0)$ versus N

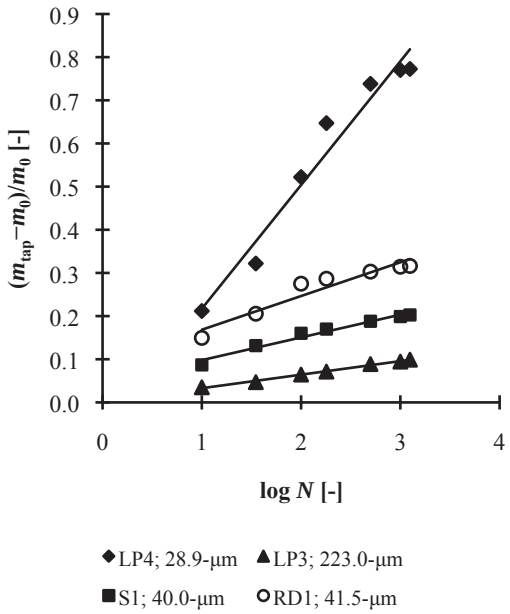

Figure 4.5 Plot of $(m_{tap}-m_0)/m_0$ versus log N

Figure 4.6 and Figure 4.7 plot parameters a_t and b_t against particle size d_{50} respectively. For comparison purposes the data for milled, spray-dried, and agglomerated lactose powders by Soh et al. (2006) and Ilić, Kása Jr., Dreu, Pintye-Hódi and Srčič (2009) are included in both plots; d_{50} is used because d^*_{32} values are not reported in the cited works. By inspection of Figure 4.6, a_t generally increases with decreasing d_{50}; the milled and spray-dried lactose data of this work are consistent with the data by Soh et al. (2006) and Ilić et al. (2009). The trend exhibited by the milled lactose seems different from the rest of the powders; the a_t values for spray-dried and agglomerated lactose powders, sand, and refractory dust are consistently lower.

Referring to Figure 4.7, the b_t values of this work are consistently low, less than 0.08; the average b_t value is 0.0427 with a standard deviation of 0.0153. The spray-dried lactose data are different from Ilić et al. (2009) and the agglomerated lactose powders show a different trend. In general, the b_t data are scattered and there is no clear trend.

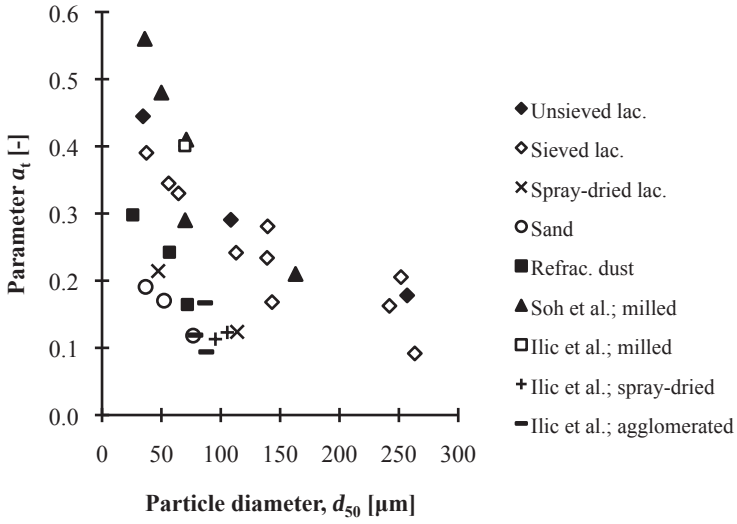

Figure 4.6 Plot of parameter a_t versus d_{50}

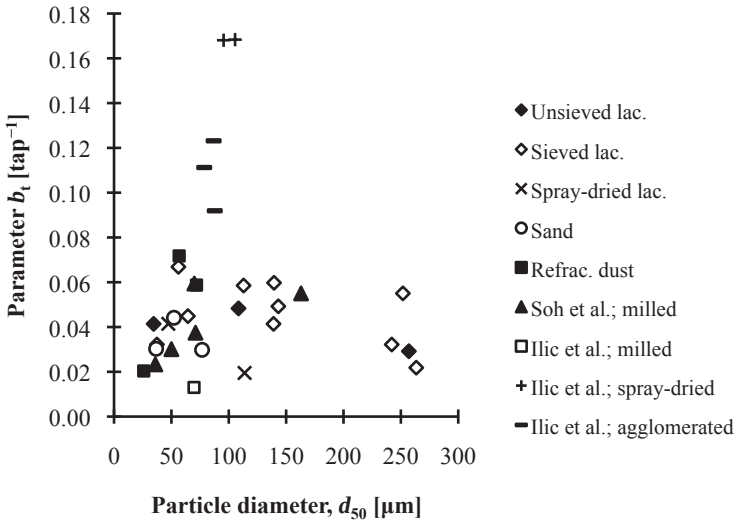

Figure 4.7 Plot of parameter b_t versus d_{50}

Figure 4.8 shows parameter a_t plotted against $1/d^*_{32}$; a_t seems to increase linearly with increasing $1/d^*_{32}$ and the rate of increase is dependent on the type of powder. Figure 4.9 shows b_t plotted against $1/d^*_{32}$; b_t seems to peak between 10,000 and 30,000 m^{-1}.

Figure 4.10 shows parameter $k_{t,M1}$ plotted against $1/d^*_{32}$; $k_{t,M1}$ tends to peak between 10,000 and 30,000 m^{-1}. Figure 4.11 shows $k_{t,M2}$ plotted against $1/d^*_{32}$; $k_{t,M2}$ seems to increase linearly with increasing $1/d^*_{32}$ and the rate of increase is dependent on powder type.

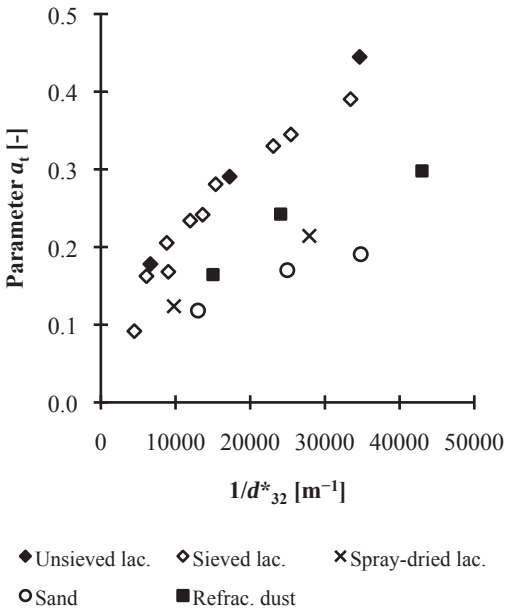

Figure 4.8 Plot of parameter a_t versus $1/d^*_{32}$

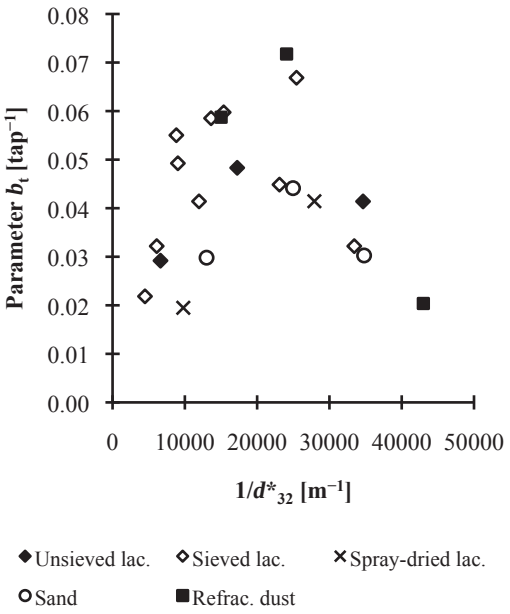

Figure 4.9 Plot of parameter b_t versus $1/d^*_{32}$

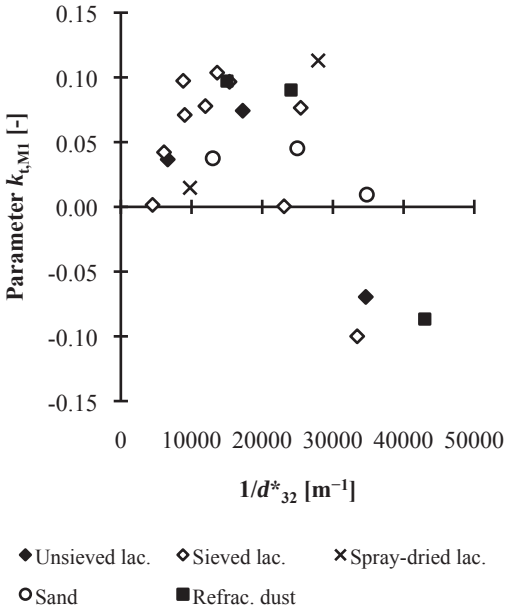

Figure 4.10 Plot of parameter $k_{t,M1}$ versus $1/d^*_{32}$

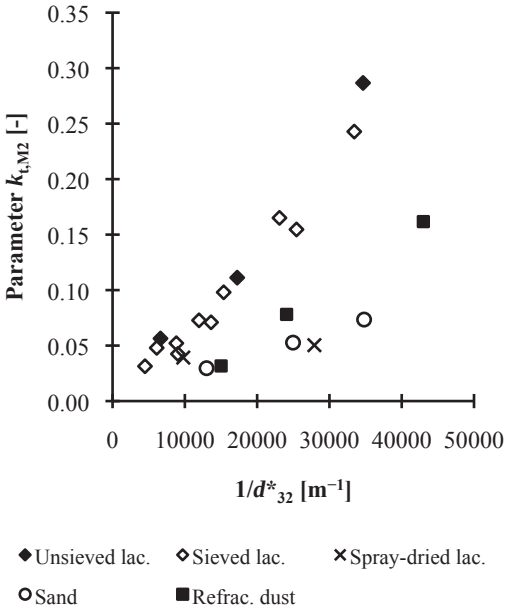

Figure 4.11 Plot of parameter $k_{t,M2}$ versus $1/d^*_{32}$

4.5.3 Hausner ratio

Figure 4.12 plots Hausner ratio at 1250 taps, $H_{R,1250}$, against $1/d^*_{32}$; in the calculation of $H_{R,1250}$, ρ_{tap} at 1250 taps and $\rho_{0,mNZS3111}$ were used. For powders LT1 and LT2, the ρ_0 values by the 500-mL cup direct filling method are used because there was insufficient sample for measurement. With reference to Figure 4.12, $H_{R,1250}$ increases linearly with $1/d^*_{32}$ regardless of powder type; linear regression of each data set shows that the relationship between $H_{R,1250}$ and $1/d^*_{32}$ follows

Equation 4.9 with fitting parameters c_1 and c_2. The values of c_1, c_2, and R^2 are listed in Table 4.2; note that the c_1 and c_2 for unsieved and sieved milled lactose suggest the data follow a similar trend.

$$H_{R,1250} = c_1\left(\frac{1}{d^*_{32}}\right) + c_2 \tag{4.9}$$

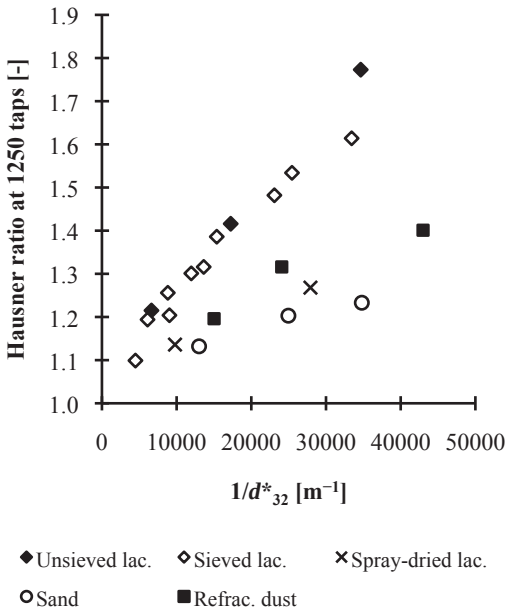

Figure 4.12 Plot of Hausner ratio at 1250 taps versus $1/d^*_{32}$

Table 4.2 Values of fitting parameters c_1 and c_2, and R^2 for milled lactose and spray-dried lactose powders, sand, and refractory dust

Powders	**c_1 x 10^{-6} [m]**	**c_2 [-]**	**R^2**
Unsieved milled lactose	19.973	1.078	0.99
Sieved milled lactose	17.189	1.078	0.96
Milled lactose (combined)	18.537	1.069	0.96
Spray-dried lactose	7.279	1.065	1.00
Sand	4.681	1.076	0.97
Refractory dust	6.895	1.116	0.91

In Figure 4.13, C measured at σ_{pre}=1.20 kPa is plotted against $H_{R,1250}$; the trend displayed by the data is representative of C at 0.31 kPa, 0.61 kPa, 2.41 kPa, and 4.85 kPa plotted respectively against $H_{R,1250}$, see Appendix 4.2. The plot suggests that the data follow one trend regardless of powder types; linear regression gives Equation 4.10, and fitting parameters k_{C1} and k_{C2}. Fitting parameters k_{C1} and k_{C2} are influenced by σ_{pre} as demonstrated in Figure 4.14 and

Figure 4.15; linear regressions of the data give Equation 4.11 and Equation 4.12 with R^2>0.98. Equation 4.13 is obtained when Equations 4.11 and 4.12 are incorporated into Equation 4.10; C^* is estimated cohesion.

$$C = k_{C1} H_{R,1250} + k_{C2} \tag{4.10}$$

$$k_{C1} = 0.6096 \log \sigma_{pre} + 0.4695 \tag{4.11}$$

$$k_{C2} = -0.7250 \log \sigma_{pre} - 0.5180 \tag{4.12}$$

$$C^* = \log\left(\sigma_{pre}^{\,0.6096 H_{R,1250} - 0.7250} \right) + 0.4695 H_{R,1250} - 0.5180 \tag{4.13}$$

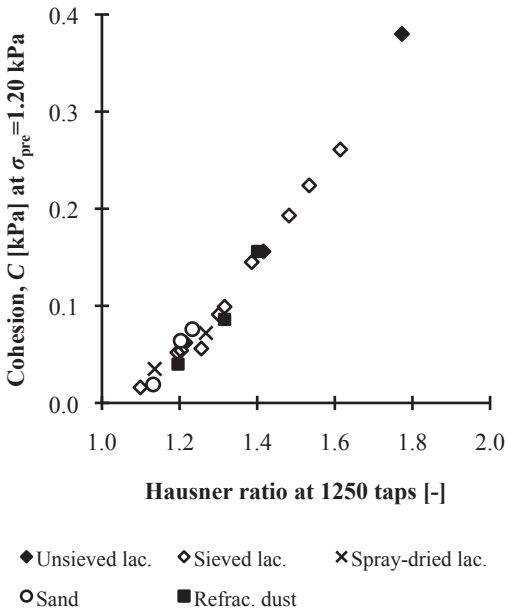

Figure 4.13 Plot of cohesion at σ_{pre}=1.20 kPa versus Hausner ratio at 1250 taps

Figure 4.16 shows σ_c/σ_y at σ_{pre}=1.20 kPa plotted against $H_{R,1250}$; the trend displayed is consistent with how the σ_c/σ_y at other σ_{pre} values relate to $H_{R,1250}$, see Appendix 4.3. By inspection of Figure 4.16, the data suggest a power law relationship; see Equation 4.14 with R^2 from 0.79–0.90.

$$\frac{\sigma_c}{\sigma_y} = k_{F1} H_{R,1250}^{\,-k_{F2}} \tag{4.14}$$

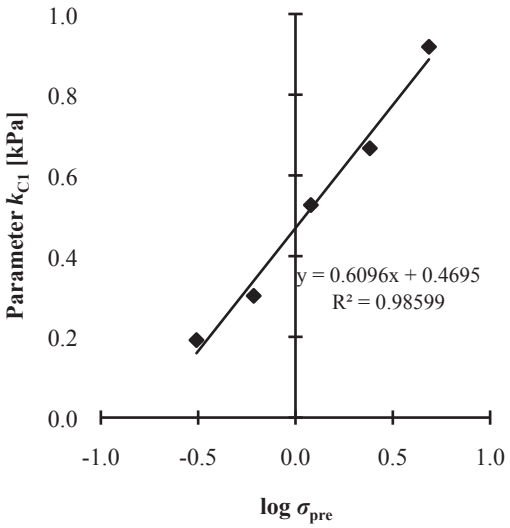

Figure 4.14 Plot of parameter k_{C1} versus log σ_{pre}

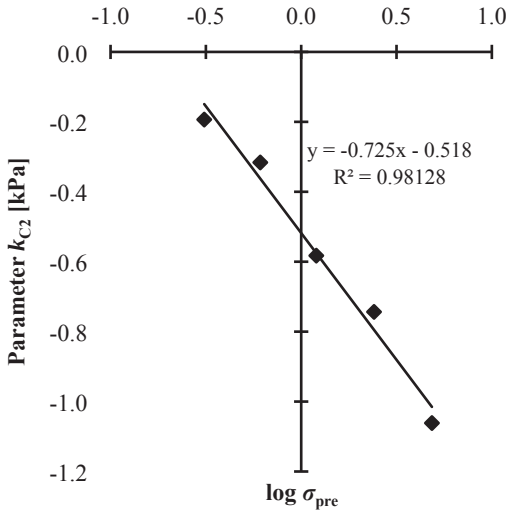

Figure 4.15 Plot of parameter k_{C2} versus log σ_{pre}

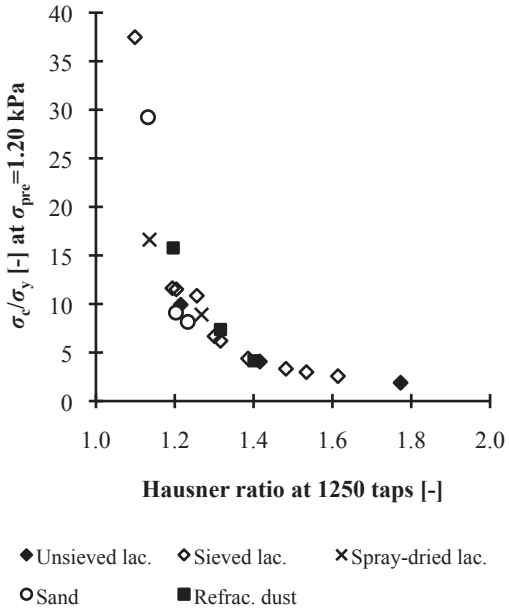

Figure 4.16 Ratio σ_c/σ_y at σ_{pre}=1.20 kPa versus Hausner ratio at 1250 taps

Fitting parameter k_{F1} is plotted against σ_{pre} in Figure 4.17 and k_{F2} is plotted against σ_{pre} in Figure 4.18. Regression of the data in Figure 4.17 gives Equation 4.15, R^2=0.99, and Equation 4.16 is obtained from the regression of the data in Figure 4.18, R^2=0.98. Equation 4.17 is obtained when Equations 4.15 and 4.16 are incorporated into Equation 4.14; σ^*_c/σ^*_y is estimated σ_c/σ_y.

$$k_{F1} = 13.8531\sigma_{pre}^{\ 2} + 9.0954 \qquad (4.15)$$

$$k_{F2} = 0.9678\sigma_{pre} + 4.3098 \tag{4.16}$$

$$\frac{\sigma^*_c}{\sigma^*_y} = \frac{13.8531\sigma_{pre}^{\ 2} + 9.0954}{H_{R,1250}^{\ 0.9678\sigma_{pre}+4.3098}} \tag{4.17}$$

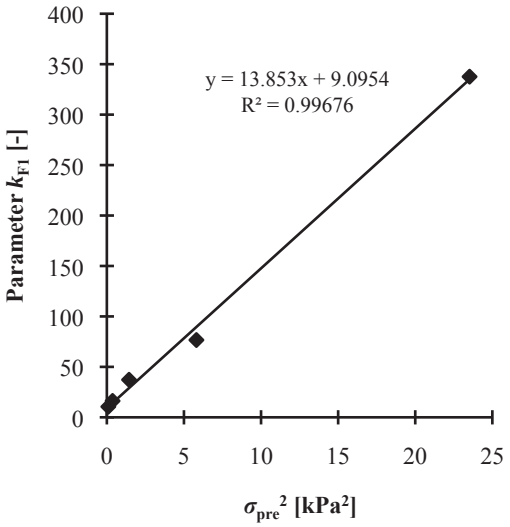

Figure 4.17 Plot of parameter k_{F1} versus σ_{pre}^2

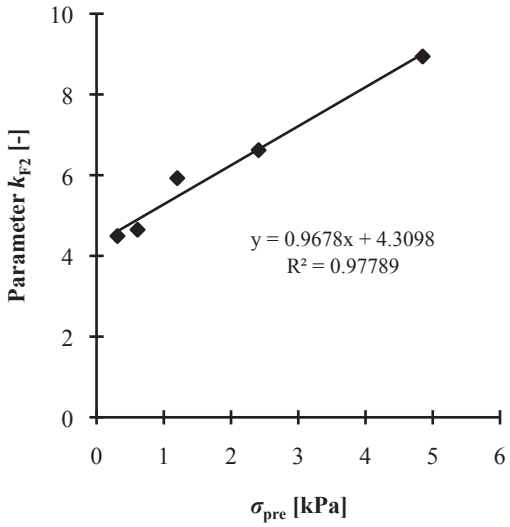

Figure 4.18 Plot of parameter k_{F2} versus σ_{pre}

4.6 Discussion

4.6.1 Loose poured bulk density and tapped density

In this work, the preferred method for ρ_0 measurement was the modified NZS3111 funnel method; the method has been robust, gives relatively lower bulk density values, and its reproducibility has been high. However, comparison between the modified NZS3111 method and other funnel methods, such as measurement with the U.S Pharmacopeia "volumeter", has not been made due to the lack of access to other bulk density apparatuses.

With the modified NZS3111 method, variation in the bulk density of any measured powder bed is expected because the method uses the "free pouring" concept. The density in the central core of the powder bed is always highest because the powder enters the container from the single point source located on the centre line, recall Šmíd et al. (1993).

Figure 4.1 shows that the values of ρ_0 are dependent on powder type. The ρ_0 values of spray-dried lactose powder, sand, and refractory dust are relatively constant because the powders are relatively free flowing. The critical values of d^*_{32} below which no flow through the NZS3111 funnel occurs for sand and refractory dust, which are ~40 μm and ~67 μm respectively, are also lower than the value for milled lactose powder, which is ~110 μm; see Table 1.

For milled lactose powders, the influence of particle size on ρ_0 is significant. When the particle size is small, interparticle forces are dominant; the internal strength of the powder bed is high, resulting in high open structure or bed voidage and low bulk density. The influence of interparticle forces becomes less significant when particle size increases, leading to the decrease in bed voidage and increase in loose poured bulk density.

The *Flow* and *No Flow* characteristics of milled lactose powders, sand, and refractory dust through the NZS3111 funnel are correlated with powder flowability according to Jenike's criteria at σ_{pre}=1.2 kPa; the powders are categorized into four groups – *very cohesive*, *cohesive*, *easy flowing*, and *free flowing* – at this stress level. It is observed that the powders that flow through the funnel without manual stirring are consistently *free flowing* powders, with the exception of sand S1, which is *easy flowing*.

In this work, only the ρ_0 data for milled lactose powders are well correlated with $1/d^*_{32}$, recall Figure 4.1 and Equation 4.8. The use of a general correlation for the prediction of ρ_0 using $1/d^*_{32}$ is not possible with the selected powders; this thus implies the importance of direct measurement of ρ_0.

The measurement of ρ_{tap} at 3 mm drop height, ~250 taps per min, and 1250 taps follows the recommendation by the European Pharmacopoeia, which is consistent with the U.S. and Japanese Pharmacopoeia (Schüssele & Bauer-Brandl, 2003; USP-NF, 2012). This procedure is reproducible and as demonstrated with powders LM1, LM2, LM3, LM4, LM5, LP1, and LP2, the changes in ρ_{tap} beyond 1250 taps are small; the percentage of change between ρ_{tap} at 1250 taps and 10,000 taps is less than 3.5%.

During tapping, the open structure of the bed that is predominantly supported by interparticle forces collapses. The particles are made to 'jump' and lose contacts with adjacent particles; particle rearrangement takes place and the bed voids are filled up, resulting in higher particle packing and bulk density. It is assumed that no particle deformation occurs with the powders used.

With reference to Figure 4.3, the ρ_{tap} data plotted against $1/d^*_{32}$ are relatively scattered. No correlation is proposed for the estimation of ρ_{tap}; hence direct measurement is necessary.

4.6.2 Fitting parameters a_t, b_t, $k_{t,M1}$ and $k_{t,M2}$

Both Equations 4.6 and 4.7 model the ρ_{tap} data well; see Figure 4.4 and Figure 4.5. Parameter a_t of Equation 4.6 represents the asymptotic value of $[(\rho_{tap}-\rho_0)/\rho_{tap}]$ and equals $[1-(1/H_R)]$, see Malave et al. (1985) and Yu and Hall (1994). Figure 4.19 shows parameter a_t plotted against $[1-(1/H_{R,1250})]$, where $H_{R,1250}$ is Hausner ratio at 1250 taps according to the European Pharmacopoeia. With the powders used in this work a_t equals $[1-(1/H_{R,1250})]$ and hence relates directly to $1/d^*_{32}$ in the form of Equation 4.9.

Figure 4.20 shows the relationship between a_t and a_s of Equation 3.8 of Chapter 3; a_s was determined with the ρ_B data measured with the annular shear cell at σ_{pre} below 5 kPa. In general, there is agreement between both data sets despite the involvement of two different compaction mechanisms; tapping involves unconfined compaction and powder consolidation in the shear cell happens in confined environment. The plot of a_t against a_s for each powder is given in Appendix 4.4.

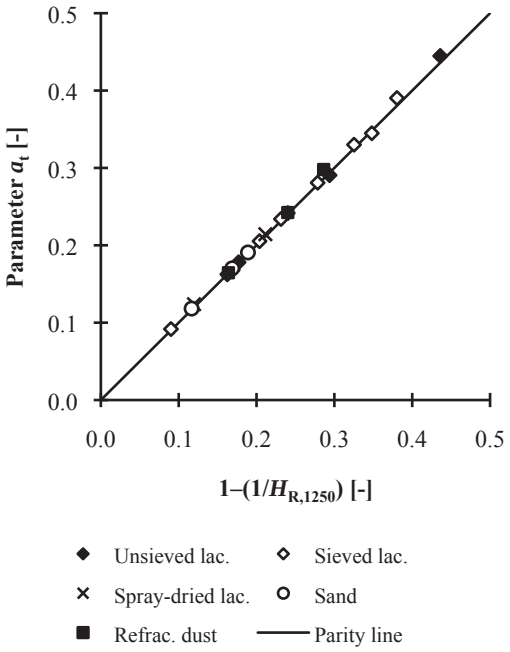

Figure 4.19 Plot of a_t versus 1–(1/$H_{R,1250}$)

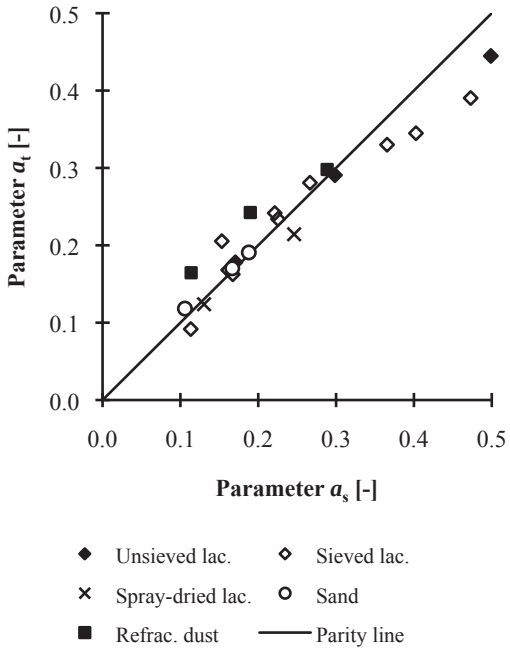

Figure 4.20 Plot of a_t versus a_s of Equation 3.8

With reference to Figure 4.9, b_t is plotted against $1/d^*_{32}$; the b_t data are close to zero, scattered, and there is ambiguity in defining clear trends for the data. Figure 4.21 plots b_t against b_s of Equation 3.8 of Chapter 3 determined with the ρ_B data measured with the annular shear cell at σ_{pre} below 5 kPa; the plot is scattered and no clear trend is observed, demonstrating significant influence of compaction mechanism on both b_t and b_s.

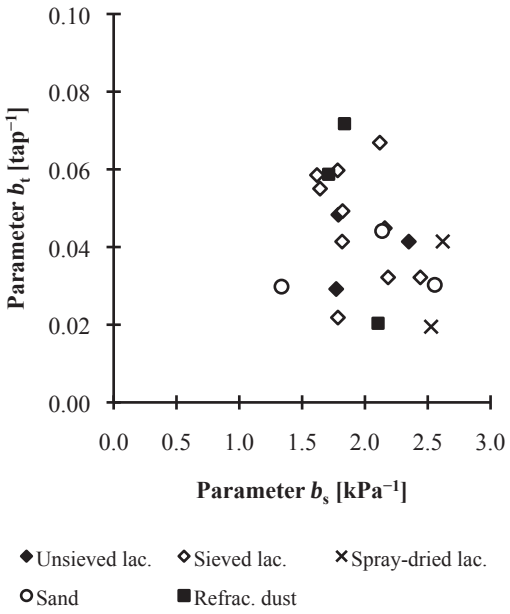

Figure 4.21 Plot of b_t versus b_s of Equation 3.8

Fitting parameter $k_{t,M1}$ of Equation 4.2 is the value of $[(\rho_{tap}-\rho_0)/\rho_0]$ at one tap and $k_{t,M2}$ is powder compressibility, recall Malave et al. (1985). Figure 4.22 shows $k_{t,M1}$ plotted against $k_{s,M1}$ of Equation 3.6 of Chapter 3 determined with the ρ_B data measured with the annular shear cell at σ_{pre} below 5 kPa; parameter $k_{s,M1}$ is the value of $[(\rho_B-\rho_0)/\rho_0]$ at one unit stress. By inspection of Figure 4.22, the plot is scattered and no correlation is found. Also, negative values of $k_{t,M1}$ are obtained with powders LP4, LM7, and RD3, see Appendix 4.1; based on the definition of $k_{t,M1}$ negative values are not possible and their occurrence is very likely attributed to the scatter in the experimental data. Powders LP4, LM7, and RD3 are the most cohesive powders in their respective family of powders; as cohesiveness increases the ρ_{tap} data become more scattered, for example see Figure 4.5 and compare the data of LP4 and LP3, which is free flowing.

Figure 4.23 shows $k_{t,M2}$ plotted against $k_{s,M2}$ of Equation 3.6 of Chapter 3 determined with the ρ_B data measured with the annular shear cell at σ_{pre} below 5 kPa. By inspection of Figure 4.23, the values of $k_{t,M2}$ are generally lower and the slope for each data set is dependent on powder type; powder compressibility is not an intrinsic powder property and as demonstrated, it is influenced by compaction mechanism. The plot of $k_{t,M2}$ against $k_{s,M2}$ for each powder is given in Appendix 4.5.

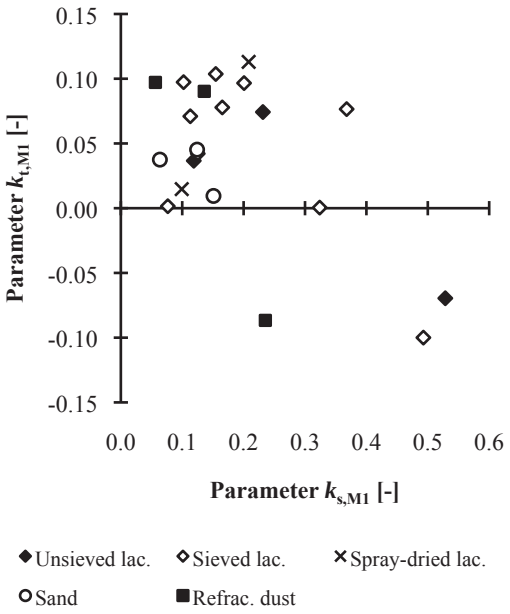

Figure 4.22 Plot of $k_{t,M1}$ versus $k_{s,M1}$ of Equation 3.6

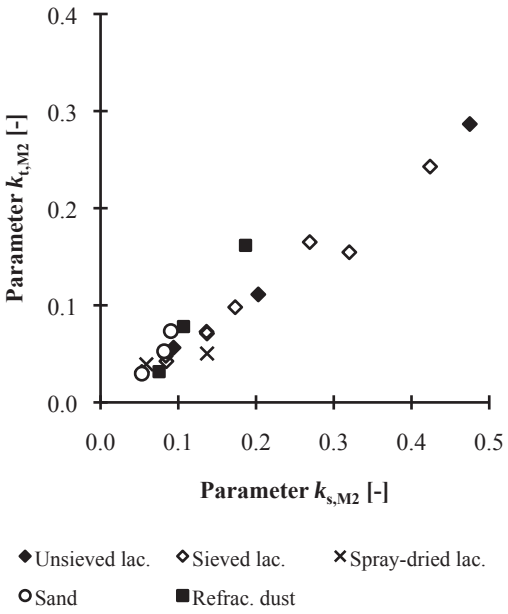

Figure 4.23 Plot of $k_{t,M2}$ versus $k_{s,M2}$ of Equation 3.6

4.6.3 Estimation of loose poured bulk density with Equation 4.1 and Equation 4.2

The accuracy of Equation 4.1 and Equation 4.2 for the estimation of ρ_0 is examined. Figure 4.24 shows $(\rho^*_{0,1}-\rho_{0,mNZS3111})/\rho_{0,mNZS3111}$ plotted against the measured $\rho_{0,mNZS3111}$; $\rho^*_{0,1}$ is the loose poured bulk density estimated with Equation 4.1 and the values of a_t and b_t in Appendix 4.1. The estimated value is within –0.2% and +1.2% of the measured $\rho_{0,mNZS3111}$.

Figure 4.25 shows $(\rho^*_{0,2}-\rho_{0,mNZS3111})/\rho_{0,mNZS3111}$ plotted against the measured $\rho_{0,mNZS3111}$; $\rho^*_{0,2}$ is the loose poured bulk density estimated with Equation 4.1, the values of a_t in Appendix 4.1, and the average b_t value determined with the data of milled and spray-dried lactose powders, sand, and refractory dust, which is 0.0427 ± 0.0153. The use of an average value is possible because the b_t values are consistently small; recall Figure 4.9. The estimated $\rho^*_{0,2}$ is within –1.0% and +1.5% of the measured $\rho_{0,mNZS3111}$.

Figure 4.26 shows $(\rho^*_{0,3}-\rho_{0,mNZS3111})/\rho_{0,mNZS3111}$ plotted against the measured $\rho_{0,mNZS3111}$; $\rho^*_{0,3}$ is the loose poured bulk density estimated with Equation 4.2 and the values of $k_{t,M1}$ and $k_{t,M2}$ in Appendix 4.1. The figure shows that the predicted value is within –2.5% and +0.5% of the measured $\rho_{0,mNZS3111}$.

Using the data sets in this work to compare Equations 4.1 and 4.2, Equation 4.1 is a more convenient tool for the estimation of ρ_0 of milled and spray-dried lactose powders, sand, and refractory dust because b_t is essentially constant at 0.0427; hence Equation 4.1 is reduced to only one fitting parameter, see Equation 4.18.

$$\frac{\rho_{\text{tap}} - \rho_0}{\rho_{\text{tap}}} = \frac{0.0427 a_t N}{1 + 0.0427 N} \tag{4.18}$$

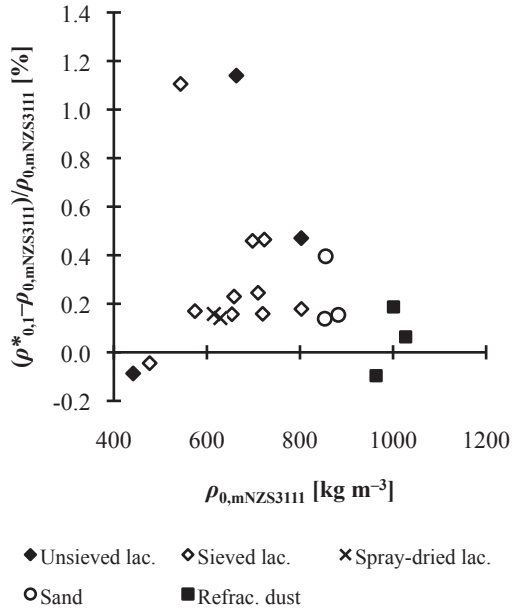

Figure 4.24 Plot of $(\rho^*_{0,1}-\rho_{0,\text{mNZS3111}})/\rho_{0,\text{mNZS3111}}$ versus $\rho_{0,\text{mNZS3111}}$

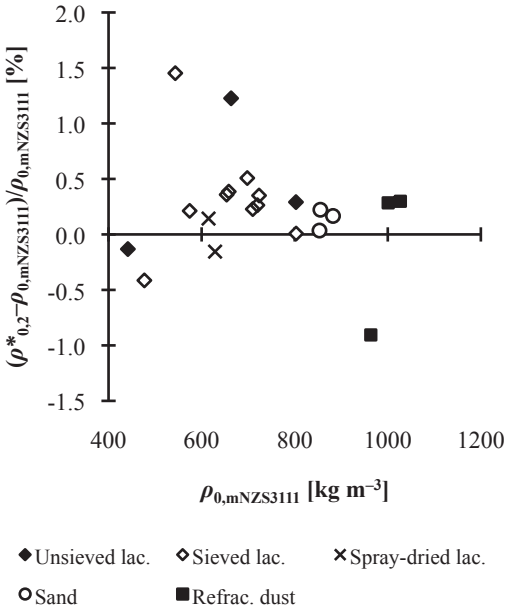

Figure 4.25 Plot of $(\rho^*_{0,2}-\rho_{0,\text{mNZS3111}})/\rho_{0,\text{mNZS3111}}$ versus $\rho_{0,\text{mNZS3111}}$

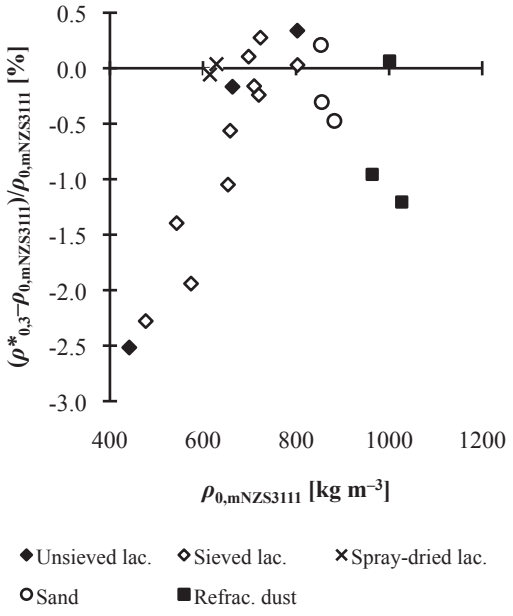

Figure 4.26 Plot of $(\rho^*_{0,3}-\rho_{0,\text{mNZS3111}})/\rho_{0,\text{mNZS3111}}$ versus $\rho_{0,\text{mNZS3111}}$

4.6.4 Hausner ratio, cohesion, and the ratio of major consolidation stress and unconfined yield stress

Hausner ratio is an empirical index that depends significantly on the measurement of bulk densities; it lacks scientific theory but for practical reasons has been considered a convenient additional bulk and flow property, recall the review in Section 4.2.3. In this work, the utility of $H_{R,1250}$, which is a standard powder and flow property according to the European, U.S., and Japanese Pharmacopeias, is further expanded through direct correlations with $1/d^*_{32}$, C, and σ_c/σ_y measured at σ_{pre} below 5 kPa. The incentive for such expansion is that in cases where the facilities for shear testing are not available, the ratio of bulk densities can provide a quick assessment of powder flowability within the stress range investigated. Moreover, the measurement of bulk densities is straightforward and tapping devices are usually cheaper than shear cells.

With reference to Figure 4.12 and Equation 4.9, the relationship between $H_{R,1250}$ and $1/d^*_{32}$ is straightforward and shows dependence on powder type. Equation 4.9 and its fitting parameters listed in Table 4.2 can be used in the estimation of $H_{R,1250}$ and hence bulk densities for powders similar to those used in this work and within similar d^*_{32} range.

Figure 4.27 shows $(H^*_{R,1250}-H_{R,1250})/H_{R,1250}$ plotted against $H_{R,1250}$; $H^*_{R,1250}$ is the Hausner ratio estimated with Equation 4.9 and the c_1 and c_2 values in Table 4.2. The estimated $H^*_{R,1250}$ is within –4% and +5% of the measured $H_{R,1250}$.

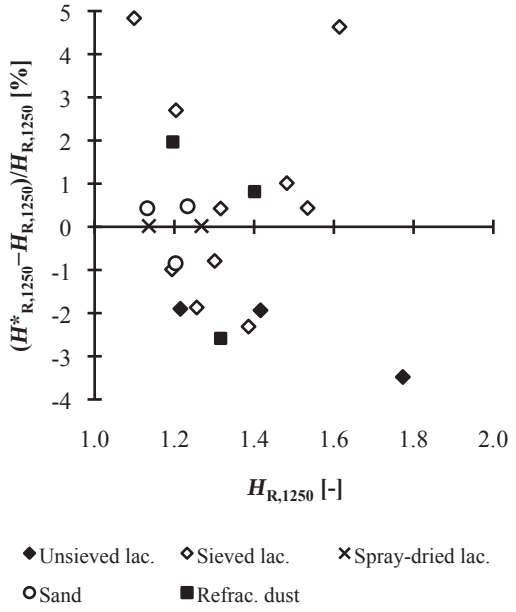

Figure 4.27 Plot of $(H^*_{R,1250}-H_{R,1250})/H_{R,1250}$ versus $H_{R,1250}$

With reference to Figure 4.13, which plots C against $H_{R,1250}$, a linear relationship is observed, recall Equations 4.10, 4.11, and 4.12. Equation 4.13 is an empirical correlation for the estimation of C^* with $H_{R,1250}$ and σ_{pre} between 0.31 kPa and 4.85 kPa.

Figure 4.28 shows $(C^*-C)/C$ plotted against C for lactose LP4 that is *very cohesive* at σ_{pre}=1.2 kPa; C^* was estimated with Equation 4.13 and $H^*_{R,1250}$ was estimated with Equation 4.9 and c_1 and c_2 values in Table 4.2. C^* is within about –18.3% and –1.7% of the measured C. Referring to Figure 4.29, the C^* for powders that are *cohesive* at σ_{pre}=1.2 kPa is within about –11.0% and +28.7% of C. The C^* for powders that are *easy flowing* is generally within –34.0% and +42.1% of C with two potential outliers, which give $(C^*-C)/C$ values of 83.4% and 90.4% respectively; see Figure 4.30. With reference to Figure 4.31, it is deduced that Equation 4.13 is not capable of estimating C^* of *free flowing* powders.

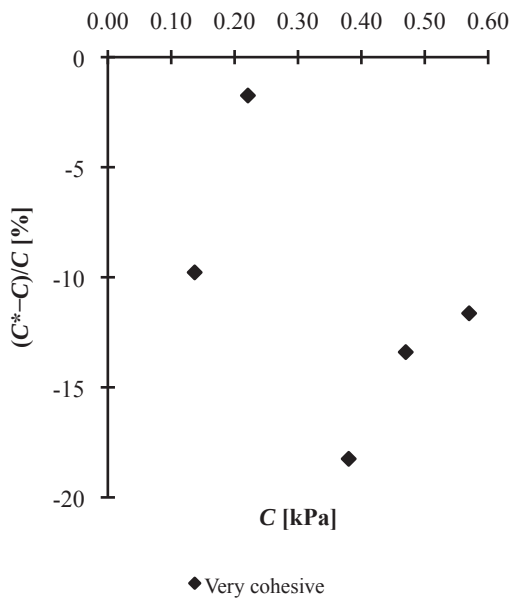

Figure 4.28 Plot of $(C^*-C)/C$ versus C for lactose LP4 that is *very cohesive* at σ_{pre}=1.2 kPa

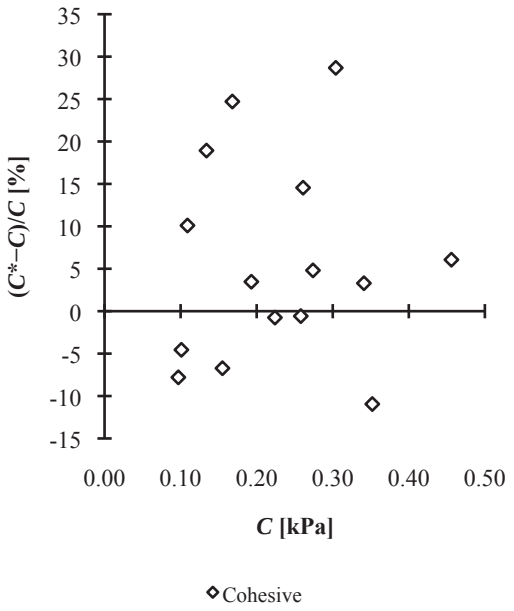

Figure 4.29 Plot of $(C^*-C)/C$ versus C for powders that are *cohesive* at σ_{pre}=1.2 kPa

The correlation between σ_c/σ_y and $H_{R,1250}$ follows a power law relationship, recall Equation 4.14, and its fitting parameters are functions of σ_{pre}, recall Equations 4.15 and 4.16. Figure 4.32 shows $[(\sigma^*_c/\sigma^*_y)-(\sigma_c/\sigma_y)]/(\sigma_c/\sigma_y)$ plotted against σ_c/σ_y for *very cohesive* LP4 at σ_{pre}=1.2 kPa; σ^*_c/σ^*_y was estimated with Equation 4.17 and $H^*_{R,1250}$ was estimated with Equation 4.9. With reference to Figure 4.32, the difference between σ^*_c/σ^*_y and σ_c/σ_y is within –39.5% and –9.3%. The difference between σ^*_c/σ^*_y and σ_c/σ_y for *cohesive* powders at σ_{pre}=1.2 kPa is within –45.9% and +26.7%, see Figure 4.33. Referring to Figure 4.34, the $[(\sigma^*_c/\sigma^*_y)-(\sigma_c/\sigma_y)]/(\sigma_c/\sigma_y)$ for *easy flowing* powders data saturate between –13.6% and +127.2%, and in Figure 4.35,

$[(\sigma^*_c/\sigma^*_y)-(\sigma_c/\sigma_y)]/(\sigma_c/\sigma_y)$ is between –76.7% and +134.9% for powders that are *free flowing* at σ_{pre}=1.2 kPa.

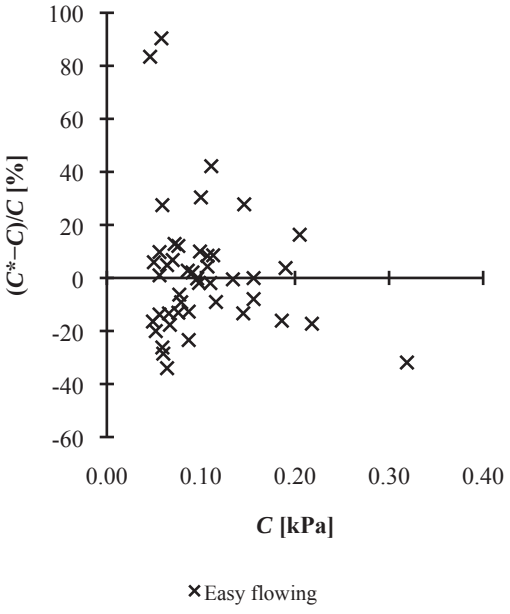

Figure 4.30 Plot of $(C^*-C)/C$ versus C for powders that are *easy flowing* at σ_{pre}=1.2 kPa

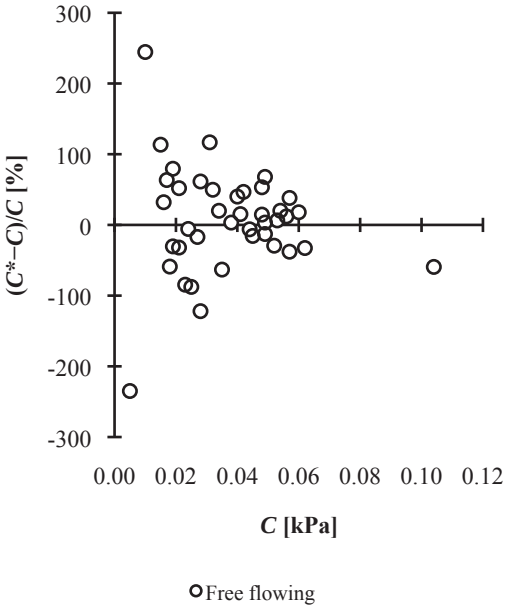

Figure 4.31 Plot of $(C^*-C)/C$ versus C for powders that are *free flowing* at σ_{pre}=1.2 kPa

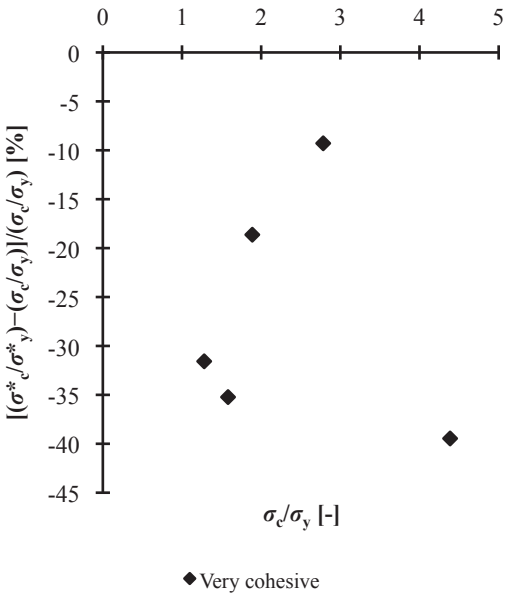

Figure 4.32 Plot of $[(\sigma^*_c/\sigma^*_y)-(\sigma_c/\sigma_y)]/(\sigma_c/\sigma_y)$ versus σ_c/σ_y for lactose LP4 that is *very cohesive* at σ_{pre}=1.2 kPa

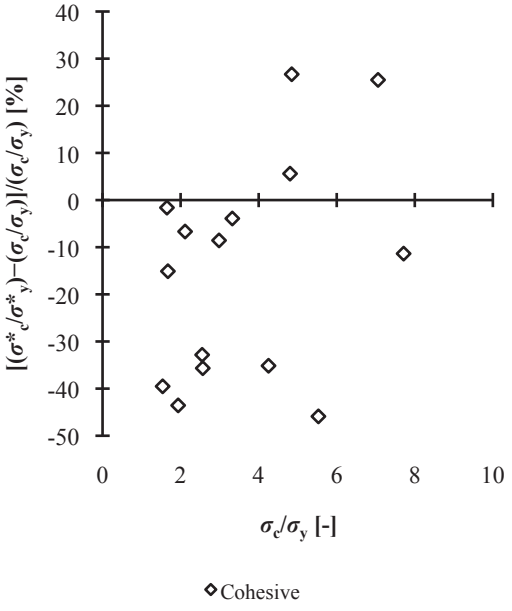

Figure 4.33 Plot of $[(\sigma^*_c/\sigma^*_y)-(\sigma_c/\sigma_y)]/(\sigma_c/\sigma_y)$ versus σ_c/σ_y for powders that are *cohesive* at σ_{pre}=1.2 kPa

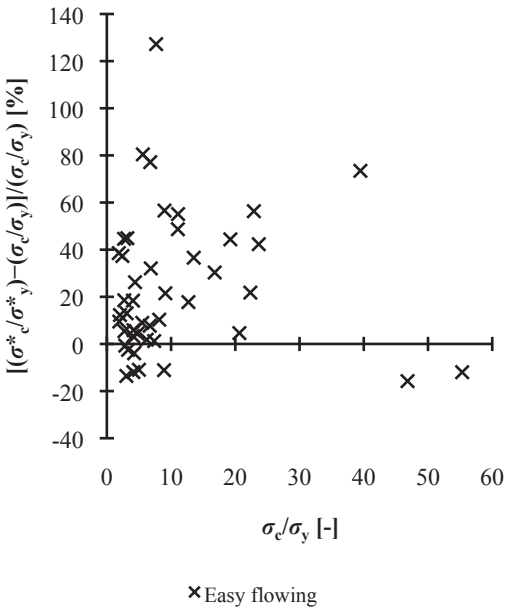

Figure 4.34 Plot of $[(\sigma^*_c/\sigma^*_y)-(\sigma_c/\sigma_y)]/(\sigma_c/\sigma_y)$ versus σ_c/σ_y for powders that are *easy flowing* at σ_{pre}=1.2 kPa

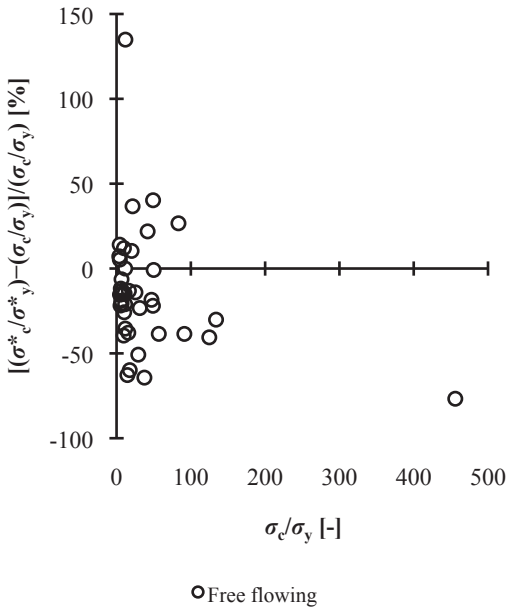

Figure 4.35 Plot of $[(\sigma^*_c/\sigma^*_y)-(\sigma_c/\sigma_y)]/(\sigma_c/\sigma_y)$ versus σ_c/σ_y for powders that are *free flowing* at σ_{pre}=1.2 kPa

The analysis here – the derivation of correlations for the estimation of C and σ_c/σ_y with Hausner ratio at 1250 taps – has been inspired by and serves to expand the work by Stanley-Wood et al. (1993), where the relationships between the outputs of powder tapping and shear testing were examined empirically but no mathematical correlations were proposed. As demonstrated in this work, the variability of C^* and σ^*_c/σ^*_y is high, and their values are underestimated or overestimated. Therefore, the use of Equation 4.13 and Equation 4.17, though appealing, is unfortunately not recommended.

In Section 4.2.3, two general powder classifications are given and reviewed. The first classification (Geldart, et al., 1984; Geldart & Wong, 1984) relates Hausner ratio to Geldart Groups C, A, B, and D powders (Geldart, 1973). The Hausner ratio data of this work have been correlated with the fluidization characteristics of the powders used; the results are presented and discussed in the next chapter, which is on gas-fluidization.

The second classification is for food powders (Hayes, 1987), which was derived based on Hausner ratio and the percentage of powder volume reduction measured by a specific tapping test. Since the context of this classification is unclear and the methodologies used were not fully disclosed and hence not repeatable, no attempt was made to compare the data of this work with the classification.

4.7 Conclusions

The ρ_0 and ρ_{tap} of milled and spray-dried lactose powders, sand, and refractory dust were measured with selected standard methodologies and $H_{R,1250}$ was calculated. The ρ_{tap} profiles were modelled with Equation 4.1 and Equation 4.2 and it was demonstrated that both models fitted the experimental data well; hence Equations 4.1 and 4.2 could be used as tools for bulk density estimation. The use of Equation 4.1 was more convenient because fitting parameter b_t was essentially constant; Equation 4.1 was reduced to Equation 4.18. Parameter a_t equaled to $[1-(1/H_{R,1250})]$ and $H_{R,1250}$ was a linear function of $1/d^*_{32}$ for milled and spray-dried lactose powders, sand, and refractory dust, see Equation 4.9.

Cohesion and σ_c/σ_y measured by shear testing were correlated with $H_{R,1250}$. The motivation was that when facilities like shear cells were not available, bulk densities ratio could provide quick assessments of powder flowability within the σ_{pre} range investigated, which was below 5 kPa. Tapping devices are also cheaper than shear cells, and the measurement of bulk densities is relatively straightforward. Two empirical equations that correlated C and σ_c/σ_y respectively with σ_{pre} and $H_{R,1250}$ were derived, see Equation 4.13 and Equation 4.17. Equations 4.13 and 4.17 looked promising, but it was shown that both equations generally underestimated or overestimated the values of C and σ_c/σ_y. Therefore, recommendations on the use of Equations 4.13 and 4.17 to potentially expand the utility of $H_{R,1250}$ as powder flow indicators could not be done. It was also noted that more precise values of C and σ_c/σ_y could only be obtained experimentally, at least within this work.

Chapter 5 – Gas-Fluidization

5.1 Introduction

There is interest in the gas-fluidization of powders because there is similarity between powder bed expansion and collapse in fluidized systems and powder dilation and avalanche in rotating drums. When a bed of fine powder is fluidized, the powder bed expands with increasing fluidizing gas and collapses upon the termination of the fluidizing gas, see for example Geldart and Wong (1984, 1985). When the fine powder is rotated in a rotating drum, the powder bed goes through a sequence of "tumbling and reshuffling" (Rietema, 1984) or dilation and avalanche, see for example Alexander et al. (2006), Faqih et al. (2006) and Faqih, Chaudhuri, Alexander et al. (2006). The similarity between bed dilation-avalanche and expansion-collapse has been demonstrated in the work by Castellanos, Valverde and Quintanilla (2002) and Huang, Zhang and Zhu (2009, 2010).

This chapter reports the design and assembly of an in-house fluidized bed apparatus, the measurement of minimum fluidizing velocity and minimum bubbling velocity, the tracking of fluidization regimes and transitions with measurements of pressure fluctuations, the classification of selected powders into Groups C, A, and B according to Geldart's Fluidization Diagram (Geldart, 1973), the investigation of powder bed expansion and bed collapse of selected fine powders, and the correlations of fluidization results with selected results obtained by shear testing in Chapter 3 and powder tapping in Chapter 4.

5.2 Literature Review

5.2.1 Gas-fluidization phenomenon

Gas-fluidization is the use of gas to suspend solid particles in order to promote a fluid-like state. A gas is passed through a bed of powder in a column in the upward direction via a gas distributor at the bottom of the column. At low gas flow, the gas merely passes through the void spaces between stationary particles; the powder bed remains as a fixed or packed bed. With increasing gas flow, a point is reached where the upward drag force exerted by the gas on the particles – the frictional force between particles and gas – equals the apparent weight of the particles. At this point and for an ideal system, the pressure drop through any section of the bed equals the weight of the gas and particles in that section; fluidization initiates and the bed of particles is incipiently fluidized. The bed is at minimum fluidization and the superficial velocity at this point is the minimum fluidizing velocity, U_{mf}, see Richardson (1971) and Kunii and Levenspiel (1991).

The minimum fluidizing velocity is obtained graphically from the plot of measured bed pressure drop, ΔP_b, against superficial gas velocity, U; Figure 5.1 shows three typical plots of ΔP_b against U. Figure 5.1 (a) shows an ideal plot of U:ΔP_b. The packed bed region in which ΔP_b

increases linearly with U is represented by line X, and the fluidized region by line Y; the intersect of the lines gives a measure of U_{mf} (Richardson, 1971).

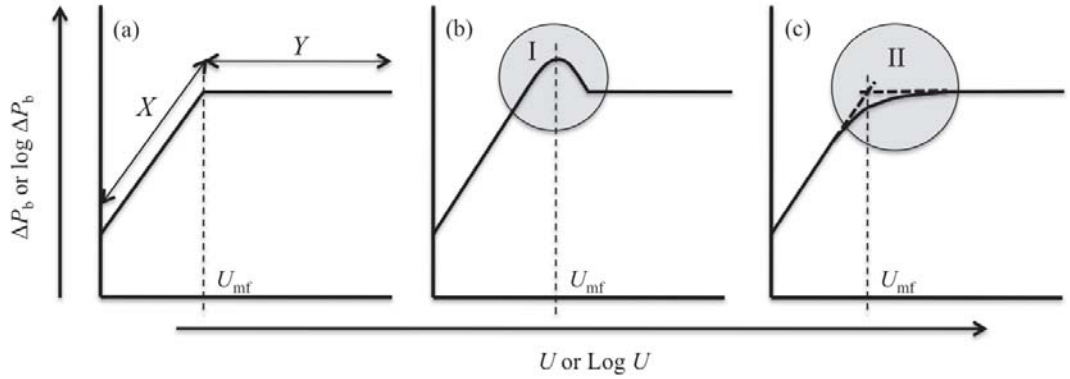

Figure 5.1 Three typical plots of bed pressure drop versus superficial gas velocity in the fluidization of powders, adapted from Richardson (1971)

In Figure 5.1 (b), there is an excess in pressure drop as shown in the form of a small characteristic "hump" in the marked area I. This "hump" shows a gradual transition between the packed bed and fluidized bed regions; it is caused by local permeability variations in a randomly packed bed (Richardson, 1971). The plot is typical for beds of fine powders that are highly consolidated or compacted to some extent prior to fluidization, see for example Valverde, Ramos, Castellanos and Watson (1998). The excess in pressure drop is associated with the extra force needed to overcome interparticle forces and the frictional forces exerted by container walls in beds with small diameter (Richardson, 1971).

Figure 5.1 (c) shows pressure drop deficiency at the point of minimum fluidization, see marked area II; this is a direct result of the presence of non-fluidized regions in the bed of particles. Non-fluidized regions exist when the bed structure is not uniform. The fluidizing gas flows preferentially across the bed and part of the apparent weight of the bed is still supported by the bed distributor; hence the pressure drop is smaller than the expected value (Richardson, 1971). This anomalous U:ΔP_b plot is generally observed with very fine powders, for example those below 38 μm. Also due to significant interparticle forces, channeling, and plugging during fluidization, the point of incipient fluidization can be unclear and the ΔP_b irreproducible, see for example Dry et al. (1983) and Wang, Kwauk and Li (1998).

A further increase in gas flow leads to excess gas flowing through the bed as bubbles; the bed of powder begins to bubble in a manner similar to that of boiling water. The superficial gas velocity at which the first bubble occurs and breaks through the surface of the powder bed is termed the minimum bubbling velocity, U_{mb}; it can also be taken as the gas velocity at which bubbling ceases when gas flow is decreased, see for example Geldart and Wong (1984).

5.2.2 Powder bed expansion

When a powder is fluidized with increasing superficial gas velocity beyond U_{mf}, the powder bed expands and then bubbles. Powders, which naturally possess different mean particle diameter and particle density, exhibit different bed expansion characteristics. Geldart (1973) proposed a general classification for powder fluidization based on the bed expansion of powders at ambient conditions and the difference between particle density and gas density, $\rho_p - \rho_g$, and surface-volume mean particle diameter, d_{32}; see Figure 5.2. In this classification, powders are categorized into 4 distinct groups; each group is termed Geldart Group C, A, B, and D respectively.

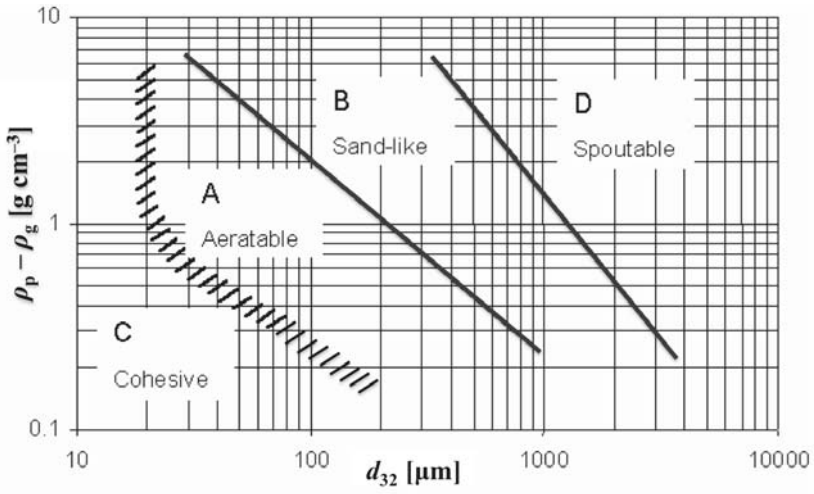

Figure 5.2 Powder classification diagram for fluidization by air under ambient conditions (Geldart, 1973)

5.2.2.1 Geldart Group A powders

Geldart Group A powders have a small d_{32} or a low ρ_p, less than ~1,400 kg m^{-3}, or both; fluid cracking catalysts are typical examples. The powders are aeratable and show considerable homogeneous bed expansion beyond incipient fluidization and before the occurrence of the first bubble (Geldart, 1973). The bed expansion is primarily attributed to the nucleation and growth of microcavities that increase with increasing U, see for example Geldart and Wong (1984). When the powder bed is bubbling, the fluidized particles move around the rising bubbles and the bed expansion is sustained by bubble holdup. It has been observed that bed expansion generally decreases above U_{mb}, see for example Abrahamsen and Geldart (1980a) and Geldart and Wong (1984); the rising bubbles continuously disrupt the interparticle contact in the bed, resulting in the reduction of the voids in the fluidized bed (Geldart & Wong, 1984; Rietema, 1984).

5.2.2.2 Geldart Group B powders

Geldart Group B powders are sand-like; the d_{32} is between 40 μm and 500 μm, and ρ_p ranges from 1,400 kg m^{-3} to 4,000 kg m^{-3}. When fluidized, bubbles form at or slightly above minimum

fluidization, and bed expansion is small, predominantly caused by particles being held up by rising bubbles (Geldart, 1973).

5.2.2.3 Geldart Group C powders

Geldart Group C powders are fine particles that are cohesive; they are distinguished by their extreme fluidization behaviour. In general, the powders do not fluidize or are hard to fluidize due to the presence and dominant effect of interparticle forces, and also the adhesion between the powders and contacting surfaces. The interparticle forces are greater than the forces exerted by the fluidizing gas on the particles; as a consequence phenomena such as the formation of channels in the powder bed through which the fluidizing gas escapes, and the lifting of the powder bed as a plug in small diameter columns upon incipient fluidization can take place (Chaouki, Chavarie, & Klvana, 1985; Geldart, 1973; Wang, et al., 1998). The interparticle forces cause the particles to agglomerate or form clusters, and this has been observed to result in four distinct fluidization behaviours, namely channeling, homogeneous expansion, small expansion, and transitional fluidization, see for example Chaouki et al. (1985), Dry et al. (1983), Iyer and Drzal (1989), and Wang et al. (1998).

a) Channeling

Channeling in Geldart Group C powder beds can come in two forms. Firstly, fractures or cracks that are sloping or more or less horizontal can form next to the wall of fluidized bed columns; these fractures or cracks are usually connected by irregular vertical channels through which the fluidizing gas flow upwards (Geldart & Wong, 1985; Rietema, 1984; Wang, et al., 1998). Iyer and Drzal (1989) noted that the cracks could appear in different orientations, lengths, and tortuosities. Secondly, vertical channels like large “rat holes” can form in the powder beds (Wang, et al., 1998); the “rat holes” usually extend from the gas distributor to the bed surface (Geldart, 1973).

During channeling, the powder bed hardly moves (Rietema, 1984). At the initial stage of fluidization, the spouting of particles and the formation of winding channels can be observed; the bed pressure drop also fluctuates (Chaouki, et al., 1985; Wang, et al., 1998). When the superficial gas velocity increases, the powder bed disrupts randomly and regionally. The phenomena that follow can include the progressive increase in bed pressure drop, the alternation between fixed bed regions and fluidized regions, bubbling, slow bed expansion, and the occurrence of an unstable bed surface. Observation at the microscopic scale has revealed that the particles appear as agglomerates of uniform size (Wang, et al., 1998).

b) Homogeneous bed expansion

This behaviour is similar to that of Geldart Group A powder bed expansion. The particles fluidized smoothly as agglomerates due to particle agglomeration caused by interparticle forces; the agglomerates are non-spherical and they have different sizes ranging from tens of micrometer to one millimeter (Chaouki, et al., 1985; Wang, et al., 1998). Depending on the type of powder, the size of the agglomerates can increase from the top of the powder bed to the bottom, and distribute well radially (Wang, et al., 1998); they can also be reasonably uniform throughout the bed (Chaouki, et al., 1985).

It has been observed that with increasing superficial gas velocity, a Group C powder bed can expand appreciably and continuously between U_{mf} and U_{mb} with a stepwise increase in bed pressure drop. The bed can also expand abruptly at a certain superficial gas velocity prior to homogeneous fluidization with a sharp rise in pressure drop before a constant pressure drop is reached (Chaouki, et al., 1985; Wang, et al., 1998). The bubbles that form in Group C powder beds are generally small (Geldart & Wong, 1984; Wang, et al., 1998), and slugging can take place at higher superficial velocities as well (Wang, et al., 1998).

c) Small bed expansion

This characteristic is similar to that of Geldart Groups B and D powders. In the work by Wang et al. (1998), cohesive powders, which were generally very high in ρ_p of up to 8,500 kg m^{-3}, were observed to show small bed expansion when fluidized. A connection of cohesive structure was seen in the powder bed; they formed unstable and high-density fluidized agglomerates of sizes up to 3 mm. At low superficial gas velocity, channels formed in the bed and the bed pressure drop fluctuated. When the superficial velocity increased, the bed height remained almost constant.

d) Transitional fluidization

Transitional fluidization can be elucidated by the occurrence of two or three regions in a fluidized bed, depending on the type of cohesive powder. Iyer and Drzal (1989) demonstrated the existence of two regions, which comprised a de-fluidized or fixed bed region with cracks and vertical channels formed above the gas distributor, and a bubbling region above the fixed bed region. Wang et al. (1998) showed that the three regions consisted of a fixed bed of large agglomerates above the distributor, a fluidized region of small agglomerates above the fixed bed, and a dilute phase of small agglomerates.

In the two-region fluidization, there is no true fluidization in the fixed bed region due to channeling and the formation of cracks. Above the fixed bed, bubbles form and increase in size as they move up the powder bed. The bubbles play a crucial role in disrupting the cracks and channels, providing a stable fluidized state. Below a certain superficial gas velocity, the two-region profile is unstable over time because the fixed bed region will traverse the entire bed

height; vertical channeling will prevail and continuous changes in the fixed bed height will cause scatter in the bed pressure drop. Sustained fluidization will transpire when a certain superficial velocity is reached and exceeded. When particle size increases slightly, ~5 μm, sustained fluidization can be achieved at a lower superficial, accompanied by higher fluctuation in the fixed bed height, greater scatter in pressure drop, and lower bed expansion (Iyer & Drzal, 1989).

In the three-region fluidization, plugging generally takes place prior to channeling, causing the bed pressure drop to be higher than the apparent weight of the bed. At higher superficial velocities, the plug splits and channeling proceeds with a sudden decrease in pressure drop. An increase in superficial velocity sees the formation of bubbles, increase in pressure drop, disruption of the powder bed, and suspension of particles. With further increase in superficial velocity, the powder bed expands progressively with essentially constant pressure drop. The powder in the bed appears as fluidized agglomerates. For some powders, the height of the fixed bed of agglomerates increases with increasing superficial velocity before the agglomerates break into smaller agglomerates in the fluidized region. The smaller agglomerates then further fragment into even smaller agglomerates or down to single particles before elutriating out of the fluidized bed. At higher superficial velocities, some powders display slugging behaviour (Wang, et al., 1998).

5.2.2.4 Geldart Group D powders

Geldart Group D powders have either a large surface-volume mean particle diameter or a very high particle density, or both. When fluidized, the bed expansion is small. At high superficial gas velocities, Group D powders display spouting or erupting ability; excess gas escapes through vertical channels formed in the bed, and the particles are swept upwards through these channels before returning to the bed (Geldart, 1973).

5.2.2.5 Geldart C/A, A/B, and B/D boundary powders

There are powders that sit on the C/A, A/B, and B/D arbitrary boundaries of the Geldart's Fluidization Diagram; the powders may show characteristics comparable to those of Groups C or A, Groups A or B, and Groups B or D respectively, or behaviour that is transitional or distinct. For example, Dry et al. (1983) fluidized Geldart C/A powders with average particle sizes of 12–67 μm and ρ_p of 1,300–5,200 kg m^{-3}; they observed the absence of a meaningful minimum fluidization point and the disappearance of powder bed contraction or reduction in bed height when bubbles first passed through. They also proposed the measurement and use of a *full support velocity* instead of U_{mf} because of anomalous bed pressure drop plots; the full support velocity is the superficial gas velocity at which the constant bed pressure drop of a fully fluidized bed first decreases when the gas flow is gradually reduced.

5.2.3 Pressure fluctuations and transitions in fluidized beds

When a gas flows through a powder bed, the pressure drop across the bed fluctuates about a mean value; the magnitude of the measured pressure drop and its fluctuations and frequencies are influenced by U and bed structure. Pressure fluctuations have been recognized as having utility in the investigation of the hydrodynamic conditions of fluidized beds. Punčochář, Drahoš, Čermák and Selucký (1985) and Wilkinson (1995) used plots of the standard deviation, σ, of bed pressure drop against U to determine U_{mf}; the formula for σ is as Equation 5.1. The measured values of σ were initially close to zero when the bed was not fluidized and the values increased rapidly with increasing U upon incipient fluidization; estimates of U_{mf} were obtained by extrapolation to the abscissa. It was later pointed out by Davies, Carroll and Flemmer (2008) that the method by Punčochář et al. (1985) and Wilkinson (1995) gave estimates of U_{mb} and not U_{mf} because the powders of investigation were Geldart Groups B and D particles; the U_{mf} and U_{mb} of these powders were similar, recall Geldart (1973).

In the work by Davies, Krouse and Carroll (2010), a statistical tool known as the von Neumann ratio, T, was used in addition to σ to analyze the bed pressure data for batches of silica sand that were nominally Geldart Group B particles; the reciprocal of T is given by Equation 5.2. The variations of T^{-1} and σ with U were compared, and it was observed that T^{-1} peaked at or close to U_{mf}. However, comments on the relationships between T and the onset of bubbling were restricted because information on visual estimates of U_{mb} was not available.

$$\sigma = \sqrt{\frac{\sum_{i=1-n}\left(x_i - \bar{x}\right)^2}{n-1}} \tag{5.1}$$

$$T^{-1} = \frac{\sum_{i=1-n}\left(x_i - \bar{x}\right)^2}{\sum_{i=2-n}\left(x_i - x_{i-1}\right)^2} \tag{5.2}$$

where σ is standard deviation [Pa]; T is von Neumann ratio [-]; i is label for data point [-]; n is number of data points [-]; x is sample variable, which in this case is bed pressure drop [Pa].

With reference to the framework provided by Geldart (1973), U_{mb} is a defining criterion in the classification of Group A powders; therefore the onset of bubbling continues to be of practical and theoretical interest. However, the determination of U_{mb} through visual observation is operator bias and can introduce subjectivity to the data. Moreover, it is labour intensive and can present practical challenges when fluidization is done at elevated temperatures and pressures.

Hence, a route forward to reduce or eliminate these drawbacks in the determination of U_{mb} is the use and manipulation of the information contained in the bed pressure drop fluctuations measured at different values of U. For this reason, a part of the work in this chapter has been devoted to extending the investigation by Davies et al. (2010).

5.2.4 Powder bed collapse

Powder bed collapse is first proposed by Rietema (1967) as a method for the measurement of dense phase or emulsion phase properties of aerated powders, such as the bubble-free bed height and dense phase superficial gas velocity. The fluidizing gas is abruptly interrupted or shut off at a superficial velocity higher than U_{mf}, and the fluidized powder bed is allowed to de-aerate and collapse. Upon the abrupt termination of gas, the bed height is measured as a function of time as the powder bed collapses; the extrapolation of the bed collapse curve to time zero measured from the time the gas is interrupted yields the bubble-free bed height or volume, and the bed collapse rate is taken as the dense phase gas velocity, see for example Abrahamsen and Geldart (1980b), Tung and Kwauk (1982), Geldart and Wong (1985), and Grace (1992). The bed pressure drop profile during bed collapse can also be used to obtain the bubble-free bed height and dense phase superficial gas velocity, see for example Xie (1997) and Lorences et al. (2003).

Geldart Groups of powders exhibit different bed collapse characteristics due to their different fluidization behaviours. According to Grace (1992), the bed collapse method has been used as a tool in the industry to appraise the relative fluidization behaviours of different particulate systems.

5.2.4.1 Bed collapse curves for Geldart Groups of powders

Bed collapse curves for Geldart Groups B, A, and C powders are presented in Figure 5.3. When Group B powders are fluidized, the bed expansion is very small; the powder bed collapses very rapidly when the fluidizing gas is abruptly shut off (Grace, 1992; Tung & Kwauk, 1982), see Figure 5.3 (a).

With reference to Figure 5.3 (b), the bed collapse of Group A powders involves three successive stages, namely *bubble escape*, *hindered settling*, and *solids consolidation*, see for example Tung and Kwauk (1982) and Geldart and Wong (1985). Bubble escape is the initial stage; it is a short period in which the excess gas in the fluidized bed escapes as bubbles when the gas supply is instantaneously interrupted. In the second stage, the remaining gas in the powder bed is exhausted steadily. The particles that are aerated and have little or no interparticle contact begin to move closer to each other and the surface of the powder bed moves at a constant velocity downwards as a result of particle sedimentation; the particles at the bottom of the bed begin to accumulate and pile up. A visible interface between the particles that have settled and those that are still aerated has been observed, see for example Geldart and Wong (1985), and the

interface gradually rises to meet the bed surface. In the third stage, solids consolidation, the interface meets the bed surface and the layer of aerated powder disappears; the whole bed settles a little further by consolidation and ceases to move when a packed bed is reached (Geldart & Wong, 1985; Grace, 1992; Tung & Kwauk, 1982).

Group C powders that can be fluidized exhibit an exponential bed collapse curve; see Figure 5.3 (c). As bed expansion is usually accompanied by channels, cavities, and cracks, the bed collapses rapidly in the initial stage due to the closure of cavities and cracks; the whole bed subsequently settles by consolidation, a manner that is similar to that of solids consolidation for Group A powders (Geldart & Wong, 1985; Tung & Kwauk, 1982).

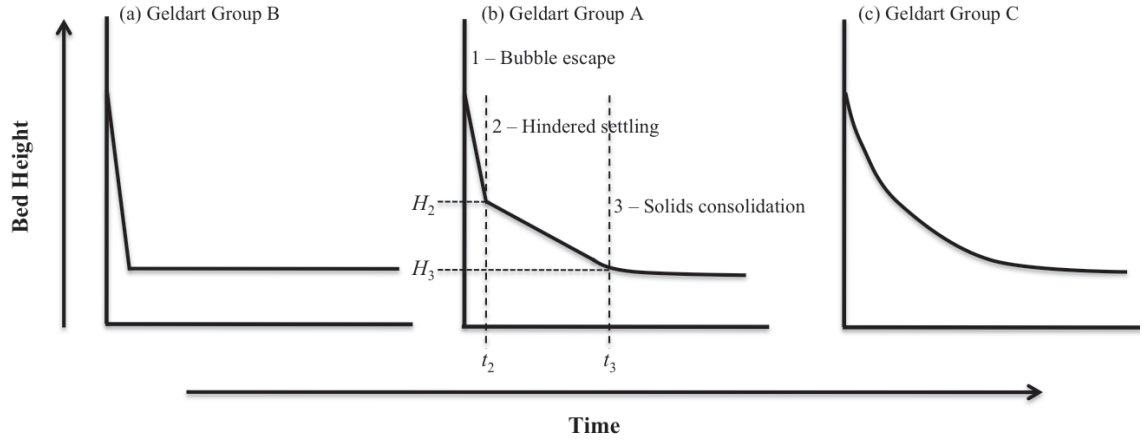

Figure 5.3 Bed collapse curves for Geldart (a) Group B, (b) Group A, and (c) Group C powders; adapted from Tung and Kwauk (1982) and Geldart and Wong (1985)

The bed collapse characteristics of Geldart Groups B, A, and C powders are primarily dependent on the intrinsic properties of powders, namely d_{32} and ρ_p. But strictly speaking, the use of bed collapse method to appraise and quantify the fluidization behaviours of powders is limited to Groups A, A/C, and C powders that can be fluidized due to the rapid collapse of Group B powders.

5.2.4.2 Type of bed collapse system

There are three types of bed collapse system, namely the single-drainage system, the double-drainage system, and the controlled double-drainage system. The design and setup of each system take into consideration factors such as the venting of excess gas from the plenum chamber (Grace, 1992; Lorences, et al., 2003), the volume of the plenum chamber (Abrahamsen & Geldart, 1980b; Grace, 1992; Park, Park, Chang, Kim, & Choi, 1991), and the pressure drop across the gas distributor (Abrahamsen & Geldart, 1980b; Cherntongchai & Brandani, 2005; Park, et al., 1991).

a) Single-drainage system

This system involves abrupt interruption of the fluidizing gas supply, usually with a solenoid valve installed at the inlet gas supply, right before the plenum chamber of the fluidized bed. The excess gas that flows upwards during bed collapse includes the gas in the powder bed, plenum chamber, and any piping downstream of the solenoid valve, see for example Grace (1992) and Lorences et al. (2003). The excess gas results in a slower bed collapse and a higher bed collapse curve; the slower curve leads to an underestimation of the dense phase gas velocity, and the higher curve leads to an overestimation of the dense phase bed height when extrapolation back to time zero is done (Cherntongchai & Brandani, 2005; Grace, 1992). The single-drainage system gives inaccurate measures of dense phase properties, but nevertheless the shapes of the bed collapse curves are consistent with the double-drainage and controlled double-drainage systems.

Two factors that influence the bed collapse of powders in the single-drainage system are the volume of the plenum chamber and the use of gas distributors with pressure drop higher than the powder bed pressure drop; in both cases, a larger amount of excess gas is available and allowed to escape through the powder bed (Abrahamsen & Geldart, 1980b; Cherntongchai & Brandani, 2005; Grace, 1992; Park, et al., 1991). The excess gas can be accounted for by mathematical equations to partially correct for the excess gas, see for example Tung and Kwauk (1982) and Geldart and Wong (1985), or reduced with the use of gas distributors with low pressure drops and plenum chambers with a small volume, see for example Abrahamsen and Geldart (1980b) and Grace (1992). Grace (1992) noted that when the size of the plenum chamber was reduced, the results from the single-drainage system were closer to the controlled double drainage system; in the limit of zero plenum chamber volume, which was impossible to achieve, both results should be identical.

b) Double-drainage system

This system involves simultaneous abrupt interruption of the gas supply as in the single-drainage system, and opening the plenum chamber to atmospheric pressure using a second solenoid valve installed at the plenum chamber; the excess gas in the plenum chamber and any piping downstream of the first solenoid valve is drained instantly as bed collapse initiates (Grace, 1992; Lorences, et al., 2003; Park, et al., 1991). The setback of this system is the over drainage of the plenum chamber, leading to an under-pressure situation in the chamber. Consequently, the excess gas in the powder bed flows reversely and downwards through the gas distributor into the plenum chamber due to higher bed pressure drop and escapes through the second solenoid valve; this results in a faster and lower bed collapse curve, overestimation of dense phase gas velocity, and underestimation of dense phase bed height (Cherntongchai & Brandani, 2005; Grace, 1992; Lorences, et al., 2003).

To prevent reverse gas flow during bed collapse, the use of gas distributors with a pressure drop higher than the powder bed pressure drop has been suggested, see for example Cherntongchai and Brandani (2005). The choice of distributors can include porous plate (Abrahamsen & Geldart, 1980b), thick papers supported by a perforated zinc plate (Geldart & Wong, 1985), filter papers supported by a porous plate (Park, et al., 1991), and glass frit (Lorences, et al., 2003); the pressure drop of such gas distributors are ~300 to 30,500 Pa at U=0.01 m s^{-1}. It has been demonstrated by Park et al. (1991) that the effect of plenum chamber volume on powder bed collapse is insignificant in the double-drainage system.

c) Controlled double-drainage system

This system improves the double-drainage system by controlling the rate at which excess gas is vented from the plenum chamber during bed collapse via a valve that is installed at the venting line of the plenum chamber, see for example Grace (1992) and Lorences et al. (2003). The degree of opening of the valve is adjusted by trial and error to maintain a value of gas distributor pressure drop that is close to zero, hence to ensure negligible upward and downward gas flow across the distributor during bed collapse. It has been further demonstrated by Grace (1992) and Lorences et al. (2003) that the bed collapse curve for this system comes as an intermediate to the curves obtained with the single-drainage and double-drainage systems; the dense phase properties measured are also reported to be more accurate.

5.2.4.3 Standardized collapse time

Geldart and Wong (1985) proposed an index known as the standardized collapse time, t_c/H_{mf}, to quantify the bed collapse of Geldart Group A powders; t_c is time [s] required for hindered settling, H_{mf} is bed height [m] at incipient fluidization, μ is gas viscosity [N s m^{-2}], and g is gravitational acceleration [m s^{-2}]. With nine Group A powders of d_{32} between 28 μm and 125 μm and ρ_p from 364–3,970 kg m^{-3}, three Group A/C powders of 23–30 μm and 3,970 kg m^{-3}, and the single-drainage system, Equation 5.3 was derived. It was noted that Equation 5.3 was "*helpful in indicating the relative influence of the variables on the behaviour of Group A systems*", but due to limited powders of investigation and also large scatter of the data, Equation 5.3 was not recommended for predictive purposes. With reference to Equation 5.3, t_c/H_{mf} is inversely proportional to $[d_{32}]^{1.2}$ and $[\rho_p-\rho_g]^{1.4}$, and directly proportional to exp(1.074 F_{45}). Geldart and Wong (1985) further noted that the lowest d_{32} value was ~30 μm because below this the powders transitioned into the Group C region.

$$\frac{t_c}{H_{mf}} = \frac{1.27\times10^6 \rho_g^{0.19} \mu^{0.785} \exp\left(1.074F_{45}\right)}{d_{32}^{1.2} g^{1.4} \left(\rho_p - \rho_g\right)^{1.4}} \tag{5.3}$$

5.2.5 Fluidization, powder characterization and other flowability characterization methods

Khoe et al. (1991) advocated a multi-disciplinary approach involving fluidization, particle characterization, and shear testing as being potentially rewarding in understanding the complex behaviour of powder systems. The authors found apparent correlation between $(\varepsilon_{mb}-\varepsilon_{mf})/\varepsilon_{mf}$ and adhesive force per particle calculated from shear cell measurements following the methods of Molerus (1975, 1978); ε_{mb} is bed voidage at bubbling onset and ε_{mf} is bed voidage at incipient fluidization. The data correlated well with d_{32} when size distributions were narrow. The authors also cautioned that because of the complexity of powders, more than one parameter or mean particle diameter was required in the correlation of experimental results.

Bruni et al. (2007) investigated the role of interparticle forces on the fluidization of fine alumina powders. Their bed collapse experiments showed that small changes in fines level caused significant changes in t_c/H_{mf}; the powder that contained higher level of fines smaller than 25 μm was observed to give greater t_c/H_{mf} than the powder with higher level of fines of 25–45 μm. The authors also discussed qualitative links between fluidization and flow properties measured by shear testing, suggesting that cohesion could explain bed collapse results.

A general powder classification involving the fluidization of cohesive powders and Hausner ratio measured at 180 taps and a known tap height has been reviewed in Section 4.2.3 in Chapter 4. With 33 dry powders of flow behaviour ranging from "very free flowing" to "very cohesive", the following classification was proposed; the classification was used in the work by Geldart et al. (2006).

- Hausner ratio < 1.25, Groups A, B, or D
- 1.25 < Hausner ratio < 1.4, Group AC
- Hausner ratio > 1.4, Group C

Webster and Davies (2006) investigated the avalanche activity of a Geldart Group C agricultural lime powder, a Group A fluid cracking catalyst, a Group B sand, and a Group D plastic pellets with the rotating drum developed by Davies et al. (2004). Plots of variance of load cell signal versus drum rotation speed were presented; the load cell signal gave indication of avalanche activity. Four characteristic plots were observed, hence showing distinct avalanche behaviours and suggesting correlation between Geldart's Powder Groups and avalanching behaviour. Investigations involving the rotating drum (Davies, et al., 2004; Webster & Davies, 2006) and powder tumbling will be further reviewed and explored in Chapter 6.

5.2.6 Summary of literature review

There is similarity between the behaviour of powders in fluidization and powder tumbling; information on bed expansion and collapse of powders from different Geldart Groups is useful to understanding and providing insights to avalanche activity of different powder systems in rotating drums. With reference to Geldart Classification Diagram (Figure 5.2), powders can be conveniently classified into Geldart Groups C, A, B, and D based on particle properties d_{32} and ρ_p. A more accurate way to classify powders includes direct measurements of fluidizing velocities U_{mf} and U_{mb} under ambient conditions, calculation of U_{mb}/U_{mf}, and measurements and observation of powder bed expansion and collapse characteristics.

With regards to measurement of U_{mb}, the general practice is by visual observation; this method is laborious and can be operator bias and impractical under high-temperature and high-pressure fluidization. A potential new route to tracking the onset of bubbling is the application of bed pressure drop fluctuations measured in a range of superficial velocity where powder beds transition from packed bed to incipient fluidization and to bubbling. The use of statistical tools such as Equations 5.1 and 5.2 can assist in the quantification of bed pressure data; however more experimental validation is necessary.

It has been demonstrated by various authors and with limited data sets that correlations exist between particle properties, flow properties measured by shear testing and powder tapping, fluidization behaviours of powders, and avalanche activity in powder tumbling; recall Section 5.2.5. Therefore, experimental works on fluidization are key to this thesis.

5.3 Aims

1. To measure the minimum fluidizing velocity and minimum bubbling velocity of samples of milled lactose powders, spray-dried lactose powders, sand, refractory dust, and glass beads.
2. To classify the selected powders into Groups C, A, and B according to Geldart Fluidization Diagram.
3. To track the regimes and transitions in fluidization with measurements of powder bed pressure fluctuations.
4. To measure and investigate bed expansion and bed collapse of the selected powders.
5. To correlate fluidization results with d^*_{32}, C_0 obtained by shear testing and $H_{R,1250}$ by powder tapping.

5.4 Materials, Methods and Analysis

5.4.1 Materials

The powders used were samples of milled and spray-dried lactose powders, sand, refractory dust, and glass beads as listed in Table 5.1. Diameter d^*_{32} is the surface-volume mean diameter calculated with the Mastersizer data using bins equivalent to a full sieve analysis according to BS 410; powder in the range 0–38 μm is grouped together and assigned a mean diameter of 19 μm.

5.4.2 Experimental setup

Figure 5.4 shows the fluidized bed setup, which was built and assembled in-house. The fluidizing air was from the laboratory mains supply; the relative humidity of the air was ~11%. The gas flow into the bed was controlled manually with a rotameter and metered with a hot-wire anemometer. Three rotameters (Key Instruments, USA) were used and their selection depended on the fluidization behaviour of the powders; the ranges of gas flow were 0–5 L min^{-1}, 0–10 L min^{-1}, and 0–15 L min^{-1} respectively. The hot-wire anemometer was developed in-house and calibrated with a soap film flowmeter (Model 311-1000, SKC, USA). Further details of the rotameters and anemometer are given in Appendix 5.1.

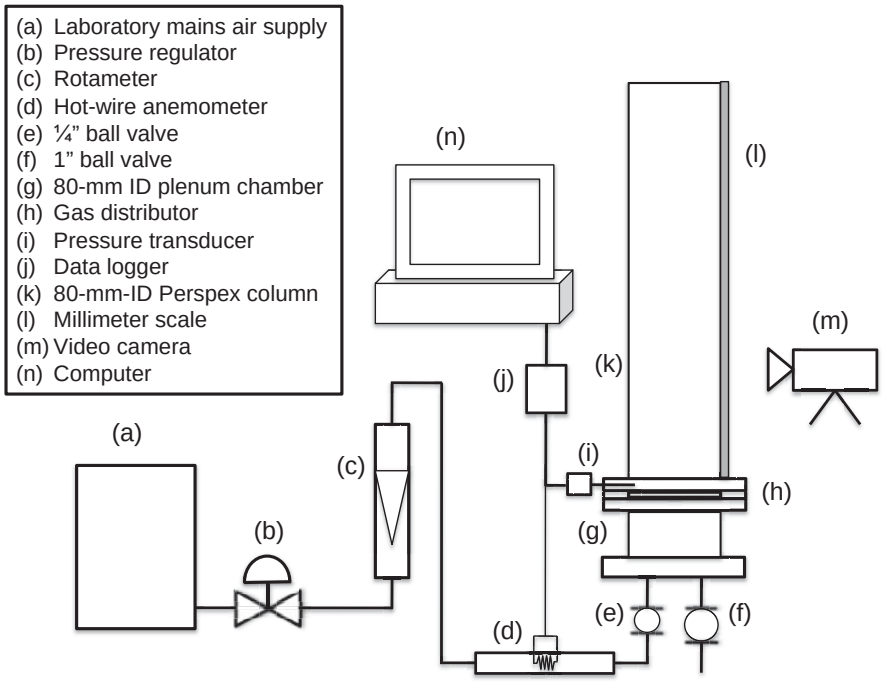

Figure 5.4 Schematic diagram of fluidized bed setup (not to scale)

The plenum chamber was cylindrical and made from Perspex; the inner diameter and height were both 80 mm. The chamber was packed with marbles for even gas distribution. At the bottom of the chamber were a ¼" opening and a 1" opening. A ¼" ball valve was installed close

to the ¼" opening, and a 1" ball valve close to the other opening; the ¼" valve was used to control inlet gas flow and the 1" valve to vent gas from the chamber during bed collapse experiments. The valves were connected physically with a chain and their opening and closing synchronized; when one was fully open, the other was fully closed. A lever was used to control the degree of valve opening. When the ¼" valve was fully closed, the lever touched a mini-switch which turned on a red light-emitting diode (LED); likewise the lever touched another mini-switch which turned on a green LED when the 1" valve was fully opened. The red and green LEDs were used to indicate the opening and closing of the valves for video recording of bed collapse experiments.

A Motorola MPX10DP pressure transducer, which was calibrated with a Baratron® pressure transducer (Type 220D, MKS Instruments, USA), was used to measure powder bed pressure drop, ΔP_b; pressure tapping was through the side of the column, ~2 mm above the gas distributor. The transducer was connected to a National Instruments data acquisition unit and a laptop computer. The transducer was sensitive to temperature increase during measurement; Appendix 5.2 gives details on its pressure offset and how corrected ΔP_b values were obtained.

The gas distributor was made of 16 layers of Whatman filter paper No. 3 stacked and held tightly around the edges by two cylindrical mild steel rings that were screwed together; the distributor pressure drop, ΔP_d, was ~5.6 kPa at U=0.01 m s^{-1}, see Appendix 5.3 for the plot of ΔP_d against U.

The fluidization column was a cylindrical Perspex column with an inner diameter of 80 mm and the column height was 500 mm. A millimeter scale was glued to the outside of the column to enable measurement of bed height. A video camera (DMC-TZ20, LUMIX, Japan) was used to record powder bed height read against the millimeter scale.

5.4.3 Measurement of bed pressure drop, bed height, and onset of bubbling

Five hundred grams of powders were loaded into the fluidization column, fluidized vigorously for ~5 min, and allowed to collapse to a reproducible bed height by turning off the air supply. Measurements were first made with increasing superficial velocities, and then decreasing velocities, both at ambient conditions (16–25^{o}C). At each increment, the bed was left to equilibrate for ~5 min. Ten thousands pressure data points were sampled at 50 Hz with the data acquisition unit and computer. The bed condition was observed visually from the top and sides, and noted. Bed height was read against the millimeter scale; in cases where the bed surface was uneven, the maximum and minimum were noted and an arithmetic mean was calculated. For sand SB and glass beads B8, 800 g of powders were used.

5.4.4 Measurement of bed collapse

Five hundred grams of powders were fluidized vigorously for ~5 min under ambient conditions.

The superficial velocity was then set to ~2 times the minimum bubbling velocity. Bed collapse began when the ¼" and 1" ball valves were respectively closed and opened to the maximum simultaneously and instantly. Change in bed height was recorded with the camera at 30 frames per second and read against the millimeter scale. With refractory dust RD2, the experiments were done with the single-drainage and double-drainage systems and at 1.5, 2, and 3 times the minimum bubbling velocity.

5.4.5 Analysis

5.4.5.1 Transition velocities and regimes in fluidization

The following superficial velocities were used in this analysis:

- **Minimum fluidizing velocity, U_{mf}** – The velocity at which the bed became incipiently fluidized, determined from the plot of bed pressure drop, ΔP_b, versus U, recall Figure 5.1; the value of ΔP_b used was the mean of the 10,000 pressure data points sampled at 50 Hz.
- **Experimental minimum bubbling velocity, $U_{mb,v}$** – The velocity at which bubbles first appeared for increasing superficial velocities, and the velocity at which bubbles were last seen for decreasing velocities, detected by visual inspection of the bed surface.
- **Estimated minimum bubbling velocity, $U_{mb,\sigma}$** – The velocity estimated using the plot of σ:U and determining U for σ=0 by extrapolation (Punčochář, et al., 1985).
- **Minimum vigorous bubbling velocity, U_{bv}** – The velocity at which vigorous bubbling without channels and cracks began, detected by visual inspection of the bed.

The values of σ and T^{-1} (Equation 5.2) were computed using Microsoft Excel. Following Davies et al. (2010), composite plots of normalized ΔP_b, bed height, H, σ and T^{-1} against normalized U were constructed; each parameter was normalized with respect to the maximum in its data set, and U were normalized with U_{mf} and $U_{mb,v}$.

5.4.5.2 Bed collapse

Bed collapse videos were analyzed frame by frame with computer software (QuickTime Player version 7.6.9). The videos showed that bed surface was relatively flat; bed height was plotted against time. The time needed for linear bed collapse, the hindered settling zone, was determined graphically, and t_c/H_{mf} was calculated. The relationships between t_c/H_{mf}, d^*_{32}, and C_0, cohesion [Pa] at zero preconsolidation stress estimated by shear testing, were investigated.

5.5 Results

5.5.1 Transition velocities

The transition velocities for the powders measured at increasing and decreasing U are tabulated in Table 5.1; also included in the table are the values of ρ_p and d_{32}, and the powders' Geldart groupings. In general, the superficial velocities measured with increasing gas flow order are lower than those measured with decreasing gas flow order. The values of $U_{mb,\sigma}$ are higher than $U_{mb,v}$, see the ratio of $U_{mb,\sigma}/U_{mb,v}$ which ranges from 1 to 2, and U_{bv} is greater than $U_{mb,\sigma}$ and $U_{mb,v}$. For powders LM2, LT1 (decreasing gas flow), and RD1, $U_{mb,\sigma}$ cannot be estimated because the data sets deviate from the normal trend.

Table 5.1 Transition velocities of powders

Powder	ρ_p	d^*_{32}	Gas flow order	U_{mf}	$U_{mb,v}$	$U_{mb,\sigma}$	U_{bv}	$U_{mb,v}/U_{mf}$	$U_{mb,\sigma}/U_{mf}$	$U_{mb,\sigma}/U_{mb,v}$	U_{bv}/U_{mf}	Geldart Group
	[kg m^{-3}]	[μm]		[m s^{-1}]					[-]			
LM2	~1,540	73.4	Increasing	0.00478	0.00591	– [a]	0.01348	1.24	–	–	2.82	A
			Decreasing	0.00478	0.00591	– [a]	0.01526	1.24	–	–	3.19	
LP2	~1,540	83.6	Increasing	0.00620	0.00734	0.00972	0.01724	1.18	1.57	1.32	2.78	A
			Decreasing	0.00700	0.01103	0.01414	0.02024	1.58	2.02	1.28	2.89	
LM3	~1,540	110.7	Increasing	0.00570	0.00733	0.01305	0.01628	1.29	2.29	1.78	2.86	A
			Decreasing	0.00733	0.00895	0.01302	0.01710	1.22	1.78	1.46	2.33	
LM6	~1,540	163.7	Increasing	0.01465	0.01628	0.02430	0.02768	1.11	1.66	1.49	1.89	A/B
			Decreasing	0.01700	0.01791	0.02510	0.02768	1.05	1.48	1.40	1.63	
LP3	~1,540	223.0	Increasing	0.02321	0.02321	0.02810	0.02818	1.00	1.21	1.21	1.21	B
			Decreasing	0.02600	0.02652	0.02943	0.02984	1.02	1.13	1.11	1.15	
LT1	~1,540	35.8	Increasing	0.00204	0.00330	0.00320	0.00788	1.62	1.57	0.97	3.86	A
			Decreasing	0.00280	0.00319	– [a]	0.01229	1.14	–	–	4.39	
LT2	~1,540	102.2	Increasing	0.00645	0.01101	0.01343	0.01489	1.71	2.08	1.22	2.31	A
			Decreasing	0.00900	0.01516	0.01511	0.01997	1.68	1.68	1.00	2.22	
S3	~2,470	28.7	Increasing	0.00138	0.00265	– [b]	– [b]	1.92	–	–	–	A
			Decreasing	– [b]	– [b]	– [b]	– [b]	–	–	–	–	
S1	~2,120	40.1	Increasing	0.00190	0.00282	0.00558	0.00912	1.48	2.94	1.98	4.80	A
			Decreasing	0.00200	0.00291	0.00517	0.00914	1.46	2.59	1.78	4.57	
S2	~2,130	76.9	Increasing	0.00326	0.00596	0.00584	0.00947	1.83	1.79	0.98	2.91	A
			Decreasing	0.00300	0.00592	0.00607	0.00958	1.97	2.02	1.03	3.19	
SB	~2,710	159.5 [c]	Increasing	0.02768	0.02768	0.03229	0.03582	1.00	1.17	1.17	1.29	B
			Decreasing	0.03000	0.03093	0.03242	0.03582	1.03	1.08	1.05	1.19	
RD1	~3,010	41.5	Increasing	0.00139	0.00179	– [a]	0.00828	1.29	–	–	5.96	A
			Decreasing	0.00140	0.00143	– [a]	0.00830	1.02	–	–	5.93	
RD2	~2,750	66.6	Increasing	0.00360	0.00561	0.00841	0.01160	1.56	2.34	1.50	3.22	A
			Decreasing	0.00380	0.00510	0.00894	0.01137	1.34	2.35	1.75	2.99	
B8	~2,460	193.0 [c]	Increasing	0.02900	0.02984	0.03053	0.03315	1.03	1.05	1.02	1.14	B
			Decreasing	0.02984	0.02984	0.03053	0.03315	1.00	1.02	1.02	1.11	

[a] Cannot be estimated due to scatters in data sets; [b] Not measured; [c] Measured by sieve analysis

5.5.2 Fluidization behaviour and pressure fluctuations

There are three general distinct states in the fluidization of the Geldart Group A powders of this work; the fluidization states are differentiable according to U, as described below:

- **State 1; $U<U_{mb,v}$** – The powder is in a packed bed state, and the bed surface is usually even. The bed becomes incipiently fluidized at a velocity below $U_{mb,v}$.
- **State 2; $U_{mb,v}\leq U<U_{bv}$** – This is a transitional state. Small bubbles occur with channels and cracks. Channels usually form in the middle of the bed; cracks can be seen at the sides. The bubbles, channels and cracks can disappear and reappear randomly at different locations. Bubble size and frequency increase with increasing velocity. The bed surface fluctuates and is uneven.
- **State 3; $U_{bv}\leq U$** – The bed bubbles vigorously without channels and cracks. The bubbles are relatively big. The bed surface fluctuates.

For Geldart Group B powders, the transitional State 2 is not significant; onset of bubbling happens at or close to incipient fluidization, and $U_{mb,v}$ and U_{bv} are close to each other.

Figure 5.5 shows the bed pressure fluctuations for lactose LP2 at U_{mf}, $U_{mb,v}$, and U_{bv}; the fluctuations are representative of the rest of the powders. The fluctuations show different qualitative trends indicative of changes in the internal state of the fluidized bed, and increase in amplitude with increasing U.

Figure 5.6 shows the plot of normalized ΔP_b, H, σ, and T^{-1} against U normalized with U_{mf} for lactose LP2 and increasing U; ΔP_b is maximum and H begins to increase at U_{mf}, and σ and T^{-1} peak near U_{mf}, but with decreasing U, σ and T^{-1} do not peak close to incipient, see Figure 5.7. The composite plots for the other powders are given in Appendix 5.4.

Figure 5.8 shows the trends for σ and T^{-1} with respect to U_{mf}, $U_{mb,v}$, $U_{mb,\sigma}$, and U_{bv} for lactose LP2 and increasing U. Both σ and T^{-1} exhibit distinct peaks at $U_{mb,v}$. The values of σ and T^{-1} decrease between $U_{mb,v}$ and U_{bv}. At and beyond U_{bv}, σ increases linearly and T^{-1} levels off at about 0.4–0.5. Note that the data show a peak value for T^{-1} at $U_{mb,v}$ and not U_{mf}, though there is a change in slope at or close to U_{mf}. With reference to Figure 5.9, similar trend is observed with decreasing U for the same powder. The trends for T^{-1} are reproducible; see Appendix 5.5 for the plots for lactose LP2 (repeat) and the rest of the powders.

Figure 5.10 shows the σ and T^{-1} trends for Group B lactose LP3 and increasing U, and Figure 5.11 for decreasing U; T^{-1} peaks at $U_{mb,v}$ and the trend for σ is less distinct though there is a discernible change close to $U_{mb,v}$. For this powder, $U_{mb,\sigma}$ and U_{bv} are similar, and as expected U_{mf} and $U_{mb,v}$ are close.

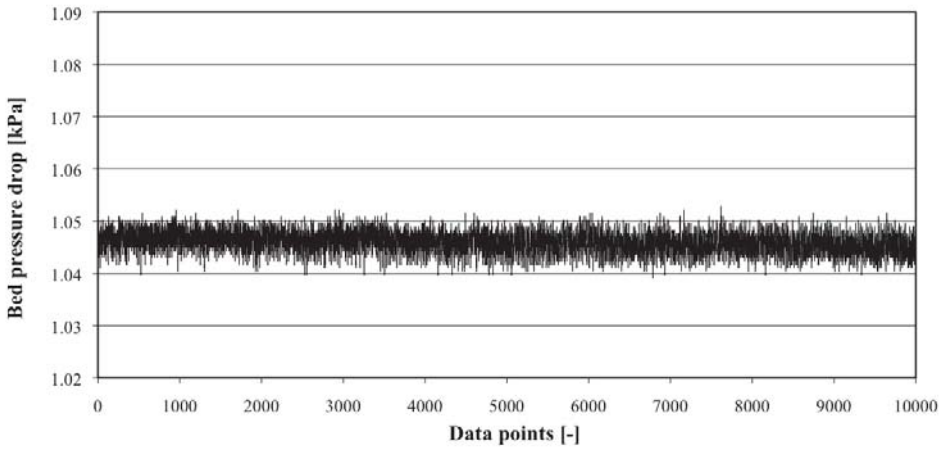

(a) $U=U_{mf}=0.00620$ m s^{-1}

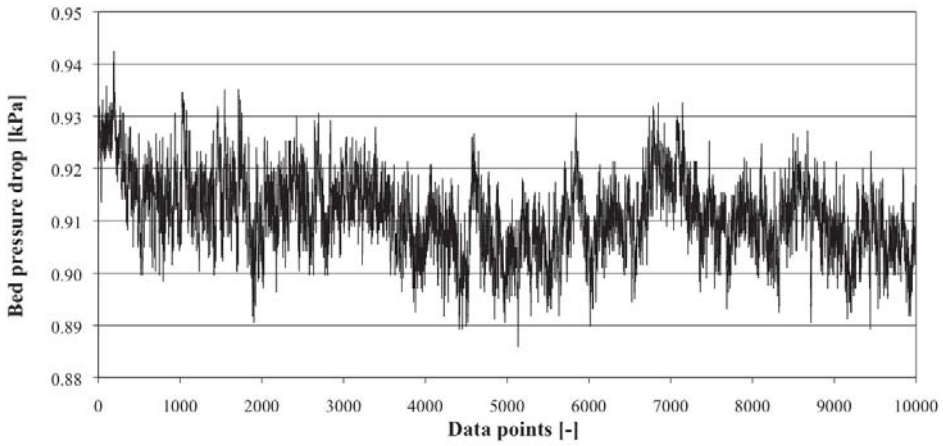

(b) $U=U_{mb,v}=0.00734$ m s^{-1}

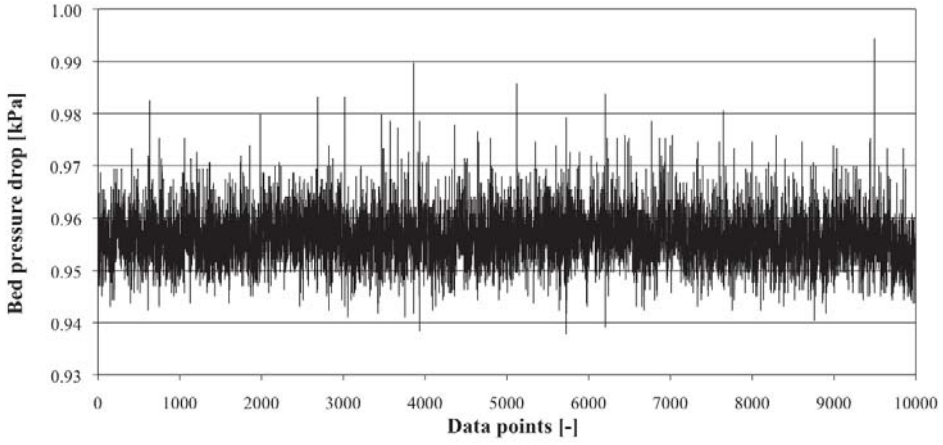

(c) $U=U_{bv}=0.00972$ m s^{-1}

Figure 5.5 Bed pressure fluctuations for lactose LP2 at U_{mf}, $U_{mb,v}$, and U_{bv} for increasing gas flow

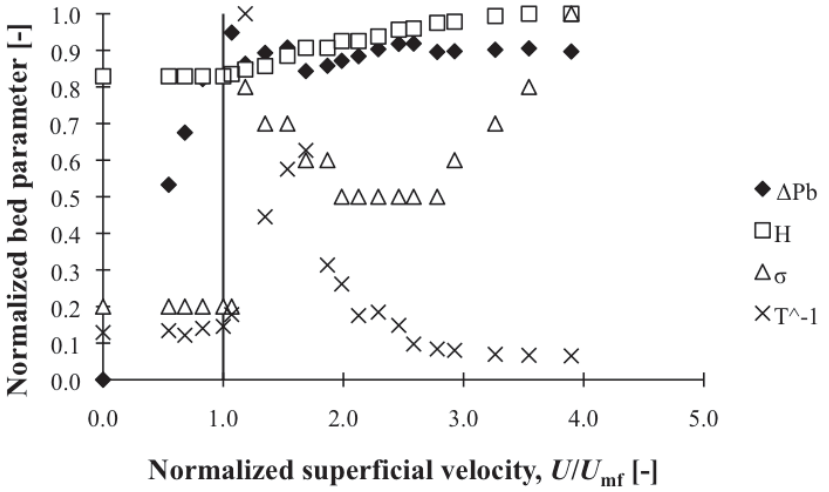

Figure 5.6 Plot of normalized bed parameters versus normalized superficial velocity, U/U_{mf}, for lactose LP2 and increasing U

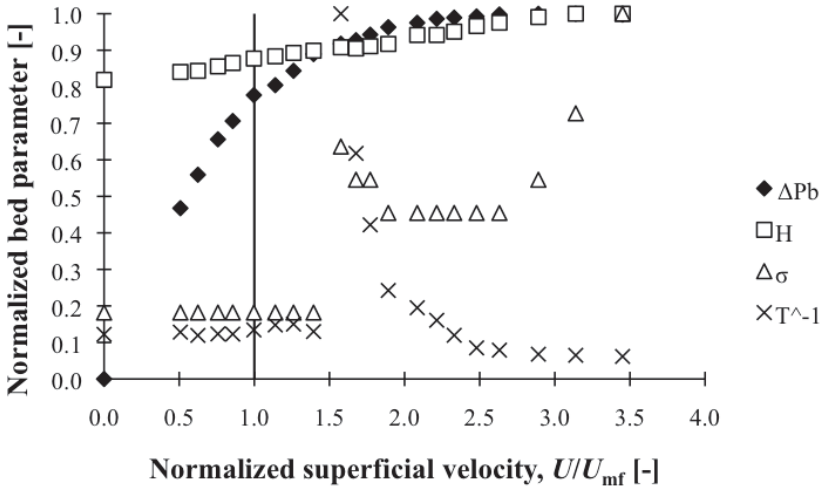

Figure 5.7 Plot of normalized bed parameters versus normalized superficial velocity, U/U_{mf}, for lactose LP2 and decreasing U

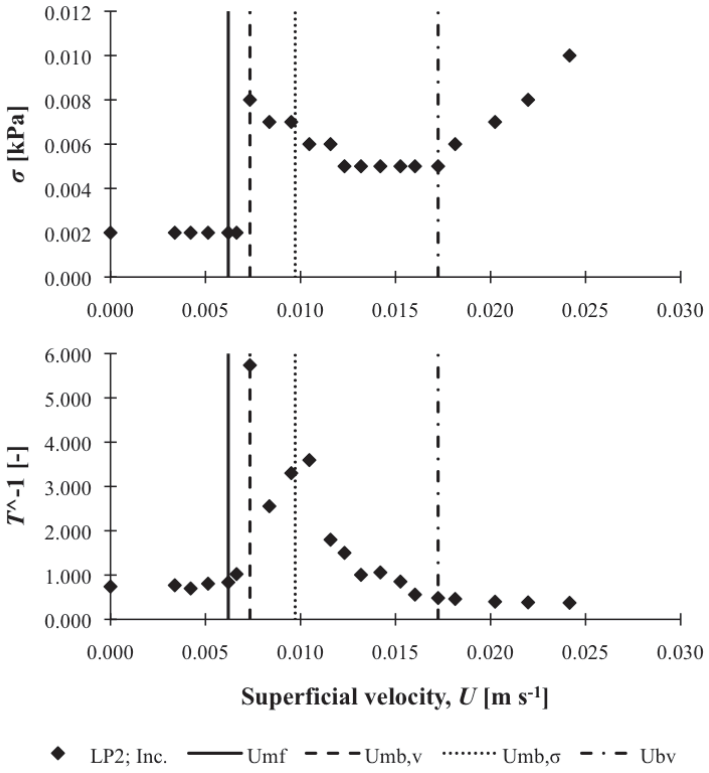

Figure 5.8 Plots of σ and T^{-1} versus U for lactose LP2 and increasing U

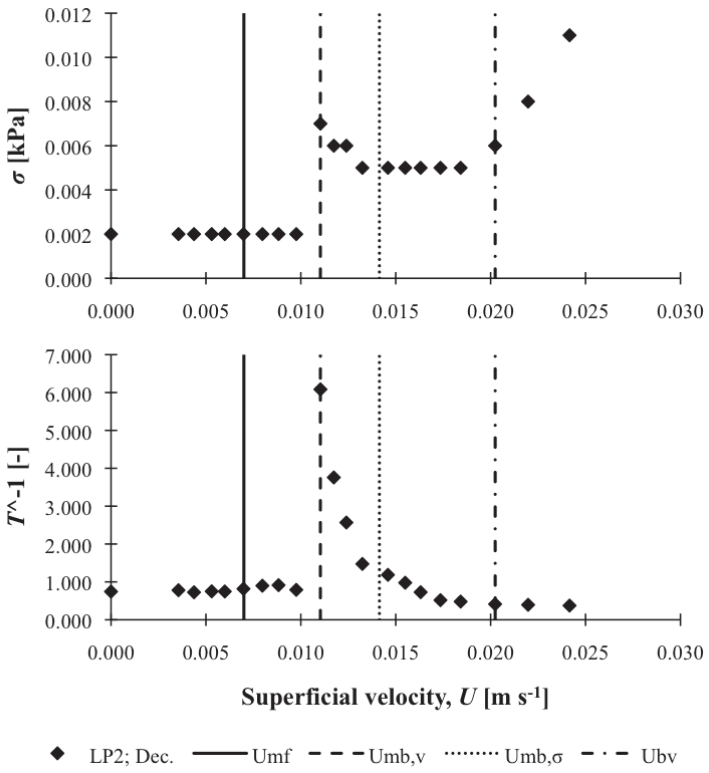

Figure 5.9 Plots of σ and T^{-1} versus U for lactose LP2 and decreasing U

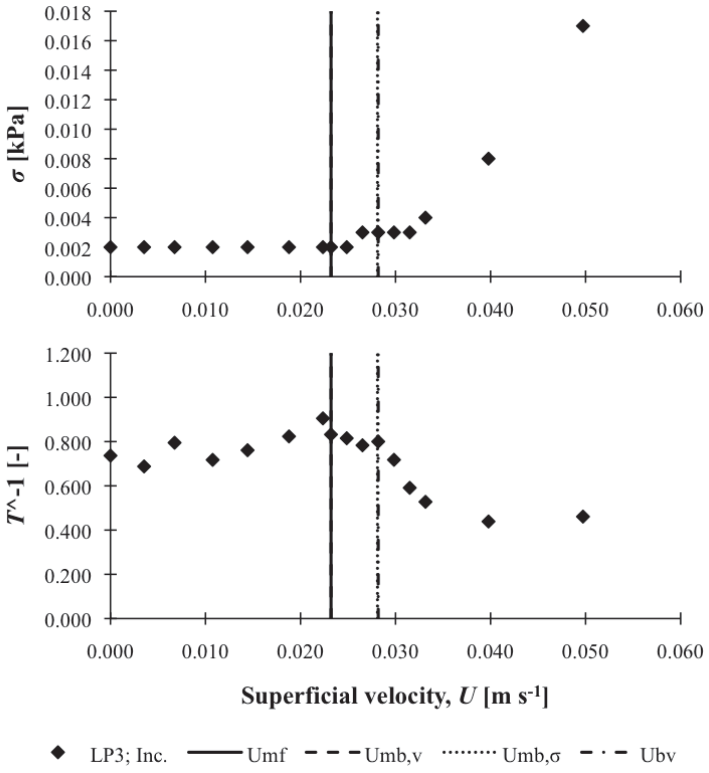

Figure 5.10 Plots of σ and T^{-1} versus U for lactose LP3 and increasing U

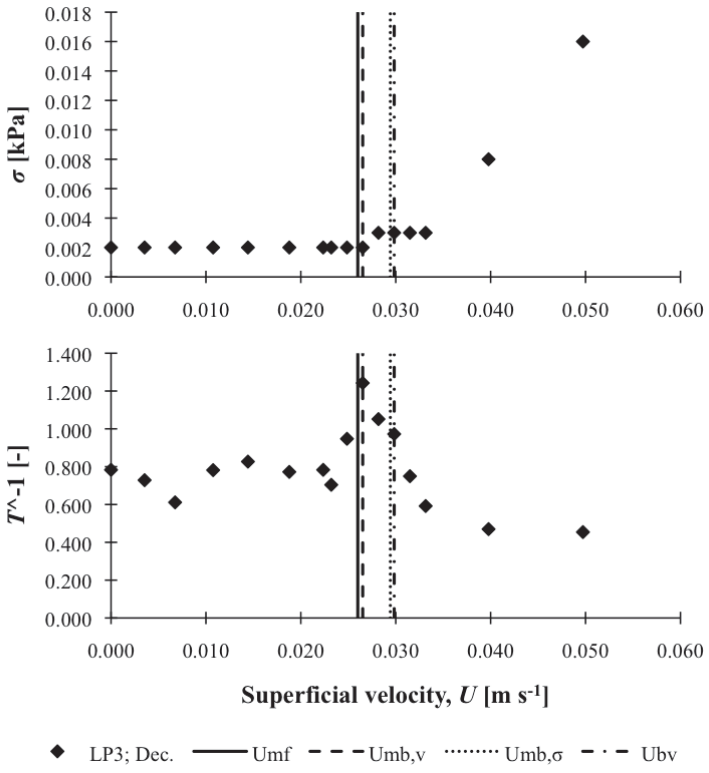

Figure 5.11 Plots of σ and T^{-1} versus U for lactose LP3 and decreasing U

Normalized σ data for increasing and decreasing U are respectively plotted against $U/U_{mb,v}$ in Figure 5.12 and Figure 5.13, and Figure 5.14 and Figure 5.15 each shows T^{-1} data plotted against $U/U_{mb,v}$ for increasing and decreasing U; these plots were constructed to show the σ and T^{-1} trends. With reference to Figures 5.12 and 5.13, σ/σ_{max} abruptly changes from a steady value at or close to $[U/U_{mb,v}]=1$. As $U/U_{mb,v}$ increases beyond 1, variation in σ/σ_{max} is first observed, and σ/σ_{max} proceeds to increase steadily with further increase in $U/U_{mb,v}$. Referring to Figure 5.14 and Figure 5.15, T^{-1}/T^{-1}_{max} rises rapidly to its peak value at or close to $[U/U_{mb,v}]=1$; for increasing U, 8 data points peak at $[U/U_{mb,v}]=1$ and 6 points close to $[U/U_{mb,v}]=1$, and for decreasing U, 9 data points at $[U/U_{mb,v}]=1$ and 5 points close to $[U/U_{mb,v}]=1$. When $U/U_{mb,v}$ continues to increase, T^{-1}/T^{-1}_{max} decreases rapidly and then levels off.

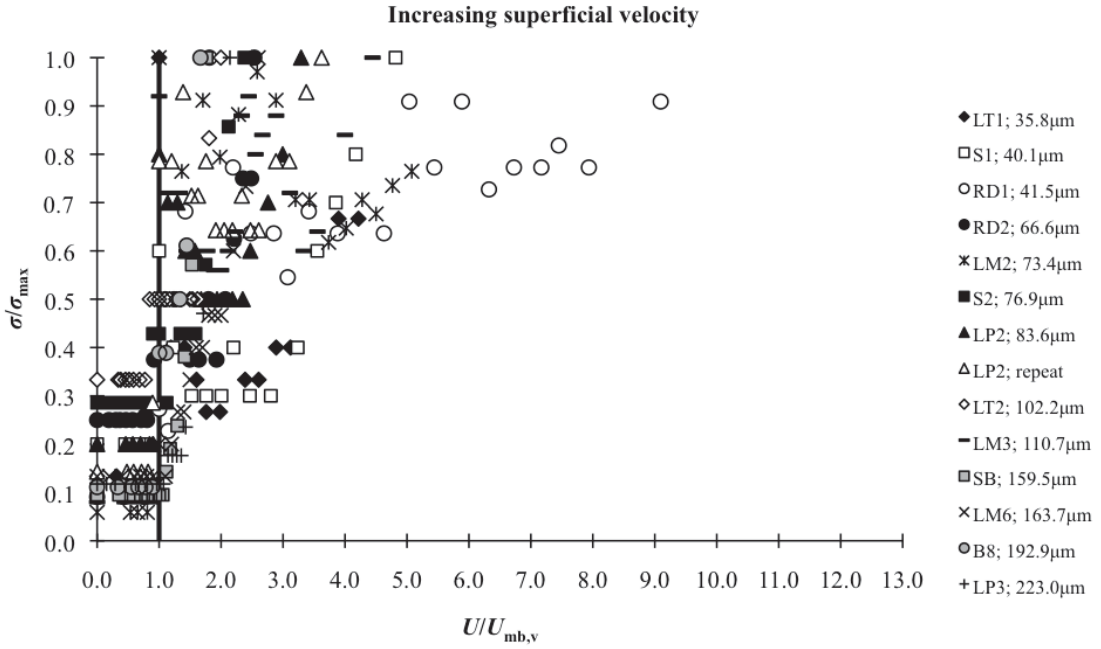

Figure 5.12 Plot of normalized σ versus $U/U_{mb,v}$ for increasing U

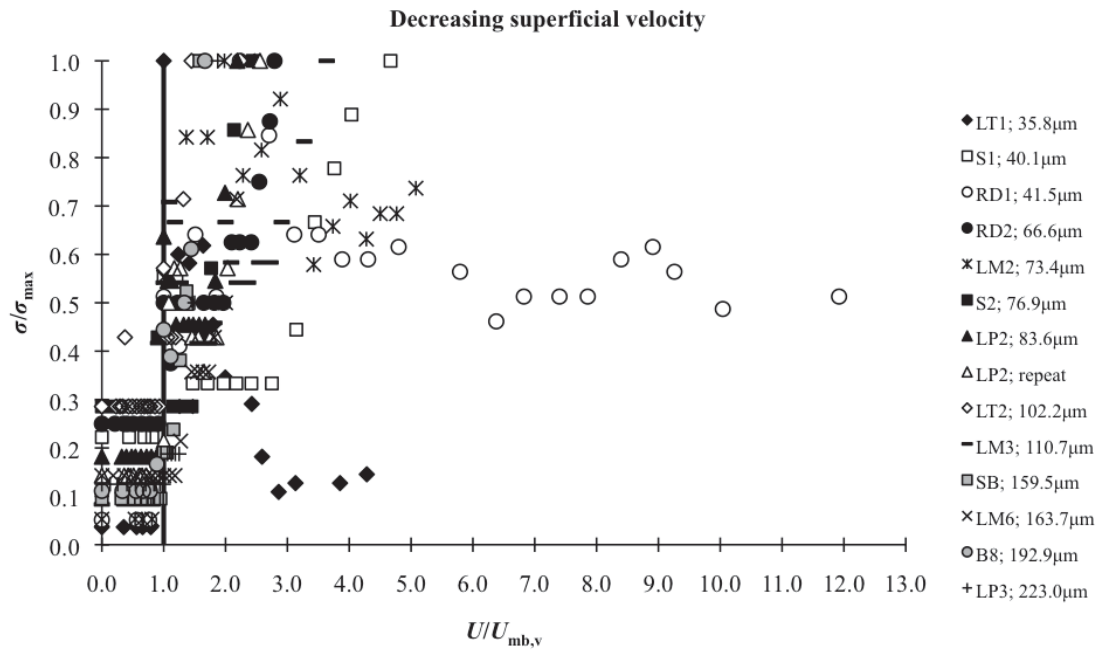

Figure 5.13 Plot of normalized σ versus $U/U_{mb,v}$ for decreasing U

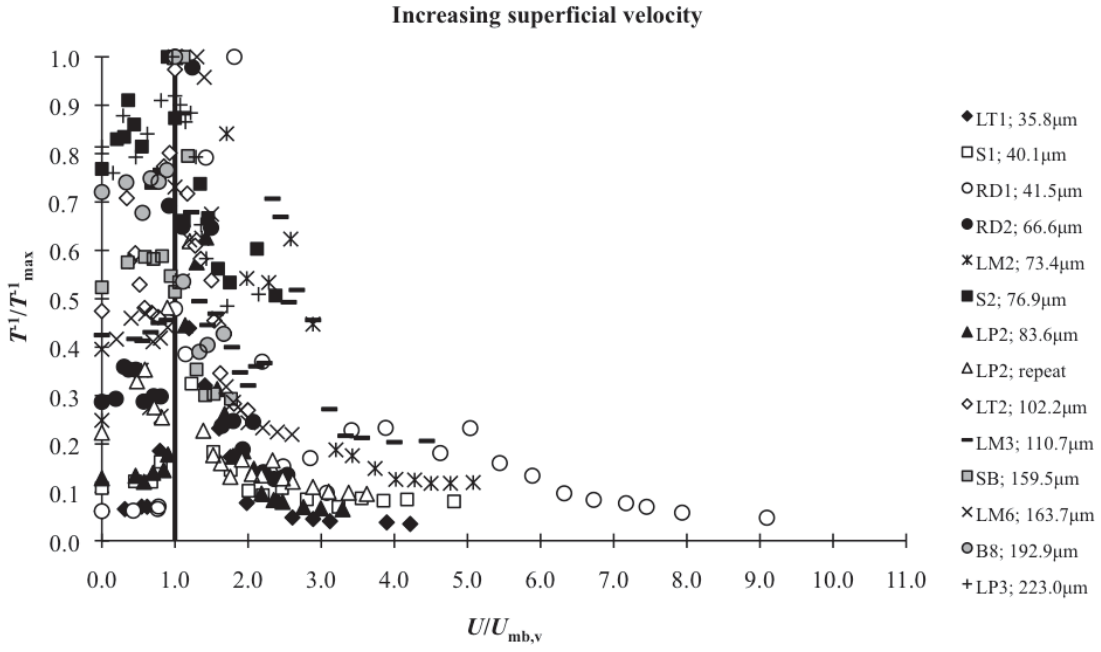

Figure 5.14 Plot of normalized T^{-1} versus $U/U_{mb,v}$ for increasing U

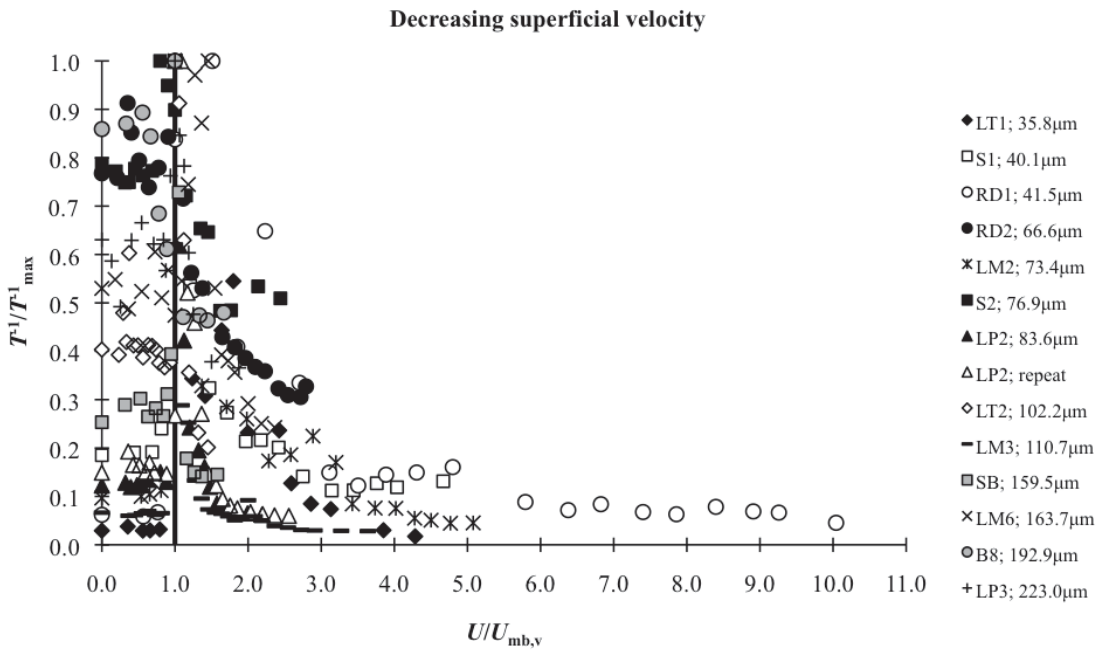

Figure 5.15 Plot of normalized T^{-1} versus $U/U_{mb,v}$ for decreasing U

5.5.3 Bed collapse

Figure 5.16 shows the bed collapse profiles for refractory dust RD2 measured with the single- and double-drainage systems at initial superficial velocity of $1.5U_{mb,v}$, $2U_{mb,v}$, and $3U_{mb,v}$. The bed collapse profiles are typical of Geldart Group A powders. With the single-drainage system, bed height during hindered settling is highest when $U=2U_{mb,v}$, followed by $3U_{mb,v}$ and $1.5U_{mb,v}$. Comparing the single- and double-drainage results, the hindered settling bed height is lower and bed collapse is faster with the double-drainage system; this result is expected. With reference to the double-drainage results, the effect of initial U on hindered settling bed height is insignificant, though there is indication that the measurement at $2U_{mb,v}$ gives slightly higher bed height, consistent with the observation in the single-drainage system.

Figure 5.17 shows the bed collapse profiles for powders RD2, LM2, S2, LP2, LT2, LM3, LM6, and LP3; the bed height is normalized with bed height at which hindered settling initiates. With reference to RD2, LM2, S2, LP2, LT2, and LM3, which are Geldart Group A powders, hindered settling happens within 2–3 s. Both Group A/B LM6 and Group B LP3 exhibit rapid de-aeration; bed collapse happens within 1 s.

In Figure 5.18, the normalized bed height for powders S3, LT1, S1, and RD1 are plotted against time. For S3, LT1, and S1, hindered settling requires about 8 s to 13 s. Interestingly, when RD1 and S1 are compared, RD1 has smaller bed expansion and collapses faster even though the values of d^*_{32} are similar.

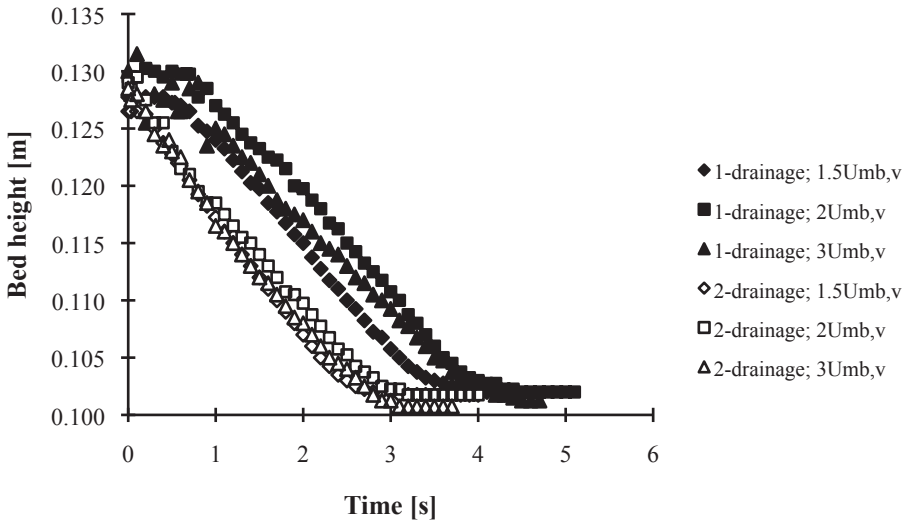

Figure 5.16 Bed collapse profiles of refractory dust RD2 measured with single-drainage and double-drainage systems and at initial superficial velocity of $1.5U_{mb,v}$, $2U_{mb,v}$, and $3U_{mb,v}$

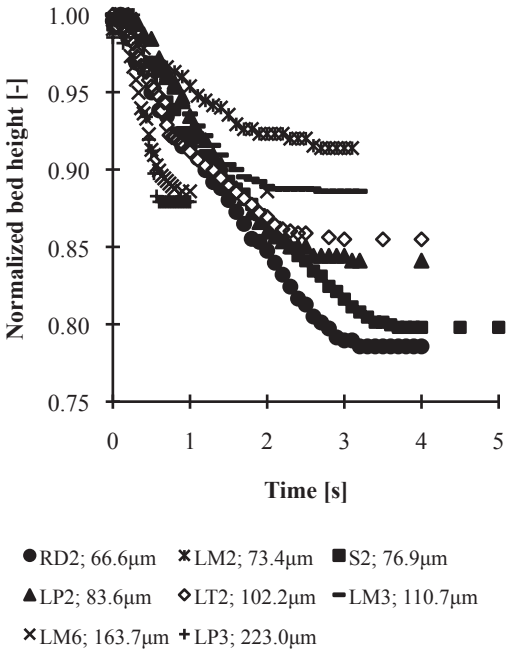

Figure 5.17 Plot of normalized bed height versus time for powders RD2, LM2, S2, LP2, LT2, LM3, LM6, and LP3

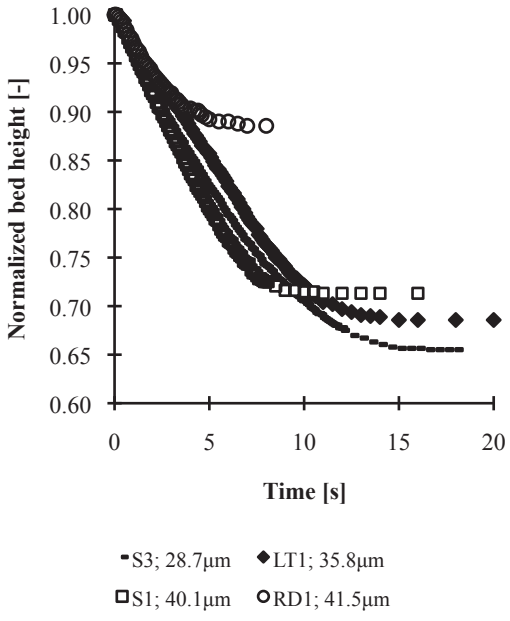

Figure 5.18 Plot of normalized bed height versus time for powders S3, LT1, S1, and RD1

Figure 5.19 shows a plot of t_c/H_{mf} against d^*_{32}; t_c/H_{mf} decreases rapidly showing apparent inverse proportionality with d^*_{32}. When t_c/H_{mf} is correlated with C_0 as in Figure 5.20, the data appear to fall into two groupings. The first group comprises the milled lactose powders and the other comprises the other test powders; scatters are observed in both groupings.

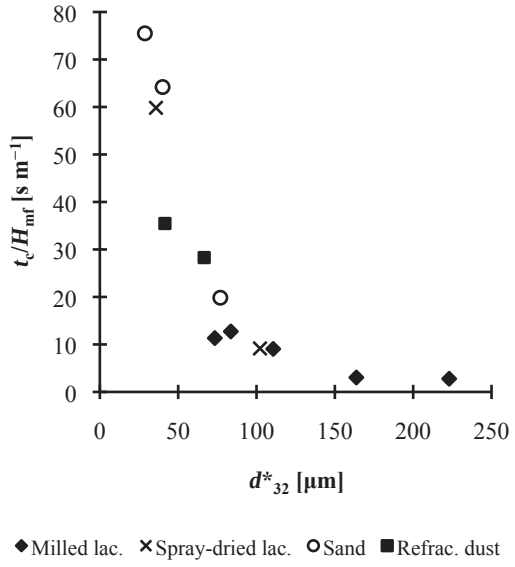

Figure 5.19 Plot of t_c/H_{mf} against d^*_{32}

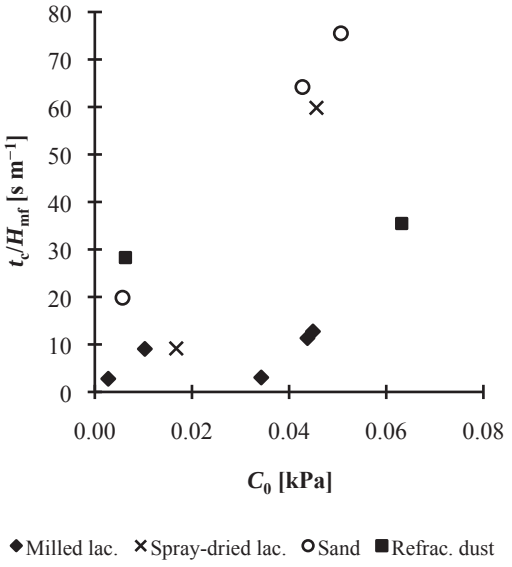

Figure 5.20 Plot of t_c/H_{mf} against C_0

5.6 Discussion

5.6.1 Superficial velocities, transitions and pressure fluctuations in fluidized beds

The transition velocities of the powders were measured with the custom built and calibrated hot-wire anemometer and very small changes in U; this was deliberate in order to measure minute changes in U and its influence on the internal state of fluidized beds. With the small changes in U, three internal states were identified visually, namely the packed bed state, $U<U_{mb,v}$, the transitional state, $U_{mb,v}\leq U<U_{bv}$, and the fully bubbling state, $U_{bv}\leq U$.

Referring to Table 5.1, the values of $U_{mb,\sigma}$ are consistently higher than $U_{mb,v}$; the ratio of $U_{mb,\sigma}/U_{mb,v}$ ranges from 1 to 2. The results show that the method by Punčochář et al. (1985), which was used by Davies et al. (2010) to estimate the U_{mb} of nominally Geldart Group A and A/B sand fractions, is not suitable for powders from the aforementioned groups. Moreover, it is demonstrated that there can be situations where $U_{mb,\sigma}$ can not be estimated due to scatters in the data sets; this is true for powders LM2 and LT1 for decreasing gas flow order, and also RD1.

With reference to Figure 5.5, the pressure fluctuations of the powders here are consistent with the pressure fluctuations of sand fractions (Davies, Krouse, & Carroll, 2007). The utility of σ and T is then compared for the identification and determination of transitions in fluidized beds using pressure fluctuations data. With the data sets available, T is observed to be more sensitive to changes in the internal state of fluidized beds than σ; distinct and abrupt changes in T occur at U consistent with $U_{mb,v}$ determined by visual observation, which is the conventional method, recall Figures 5.14 and 5.15. The findings here provide further support for the use of T as an indicator for transitions in powder fluidization particularly the onset of bubbling, an approach first advocated by Davies et al. (2010) but not fully substantiated due to missing data for $U_{mb,v}$.

5.6.2 Powder bed collapse, standardized collapse time and cohesion

The bed collapse profiles of the powders used in this work, recall Figures 5.16, 5.17, and 5.18, are consistent with findings in the literature, see for example Tung and Kwauk (1982), Geldart and Wong (1985), and Grace (1992). With reference to Figure 5.16, the bed height and rate of bed collapse obtained with the single-drainage system are respectively higher and slower because excess gas in the plenum chamber was not vented; the gas therefore flowed upward into the collapsing bed. In the double-drainage system, the pressure drop across the gas distributor was set high at ~5.6 kPa at U=0.01 m s^{-1}; this ensured no reverse gas flow into the vented plenum chamber during bed collapse. Note that the shapes of the bed collapse profile remain consistent regardless of drainage system; powder bed collapse is a useful tool to assess the fluidization characteristics of powders particularly Geldart Groups A, A/B, and also B powders.

The standardized collapse time, t_c/H_{mf}, is a convenient index to quantify the bed collapse of Group A powders. As pointed out by Geldart and Wong (1985), t_c/H_{mf} is helpful in indicating the influence of d_{32}, ρ_p, and F_{45}, refer to Equation 5.3, but limited in predictive purposes; t_c/H_{mf} is also not suitable for Geldart Group C powders and the threshold for its use is d_{32}= ~30 μm. Referring to Figure 5.19, an apparent linear relationship between t_c/H_{mf} and d^*_{32} is observed when d^*_{32} is ~29–110 μm; the powders are Group A materials in this size range, hence there is in general consistency between the findings here and the work by Geldart and Wong (1985).

The relationship between t_c/H_{mf} and C_0 is shown in Figure 5.20; C_0 is effectively a bulk measure of interparticle adhesive forces of unconsolidated powder beds. With the data sets here, two groupings with scatters are observed, suggesting the existence of other factors that are not accounted for. Considering again Equation 5.3, the work by Khoe et al. (1991) in which a correlation between $(\varepsilon_{mb}-\varepsilon_{mf})/\varepsilon_{mf}$ and adhesive force per particle was demonstrated for selected powders with narrow size distributions, the work by Bruni et al. (2007) in which inconclusive qualitative links between fluidization and cohesion was presented, and the crude dependence of C_0 on $\rho_0/(\rho_p d^*_{32})$ as presented in Figure 3.13 of Chapter 3 and where ρ_0/ρ_p implies a voidage term, an expression in the form of Equation 5.4 is suggested. Clearly, Equation 5.4 is complex and empirical inspection of the data alone as used here is insufficient to elucidate the relationships between t_c/H_{mf}, d^*_{32}, and C_0.

$$\frac{t_c}{H_{mf}} \propto f\left\{C_0\left[\, f\left(\text{size distribution and fines content}\right), f\left(\text{voidage}\right), f\left(\text{particle density}\right)\right]\right\} \qquad (5.4)$$

5.6.3 Geldart Powder Groups and Hausner ratio at 1,250 taps

According to Geldart et al. (2006), powders from Groups A, B, or D give values of Hausner ratio less than 1.25, and Hausner ratio is between 1.25 and 1.4 for Group AC powders. With the limited powders here and Hausner ratio measured at 1,250 taps, $H_{R,1250}$, according to the

protocols listed in Sections 4.4.2 and 4.4.3 of Chapter 4, the following is observed for milled lactose powders:

- $H_{R,1250} < 1.10$, Group B
- $1.10 < H_{R,1250} < 1.19$, Group A/B
- $1.20 < H_{R,1250} < 1.32$, Group A

For the Group A spray-dried lactose powders, sand, and refractory dust, the $H_{R,1250}$ range is from ~1.14 to 1.32; this range is slightly broader than but consistent with the one for milled lactose powders.

5.7 Conclusions

Selected samples of milled and spray-dried lactose powders, sand, refractory dust, and glass beads were fluidized under ambient conditions in a custom made fluidized bed equipped with a hot-wire anemometer for measurement of minute changes in superficial gas velocity, a pressure transducer for bed pressure drop and pressure fluctuations measurements, and a double-drainage system for bed collapse experiments. The measured superficial velocities were U_{mf}, $U_{mb,v}$, $U_{mb,\sigma}$, and U_{bv}, and the powders were classified into Groups A, A/B and B according to Geldart Fluidization Diagram and based on the ratio of $U_{mb,v}/U_{mf}$.

Using a combination of visual inspection, the values of U_{mf}, $U_{mb,v}$, and U_{bv}, and pressure fluctuations data, three internal states of powder beds were identified; they were the packed bed state, $U<U_{mb,v}$, the transitional state, $U_{mb,v}\leq U<U_{bv}$, and the fully bubbling state, $U_{bv}\leq U$. When statistical tools σ and T^{-1} were applied on the pressure fluctuations data and subsequently correlated with U_{mf}, $U_{mb,v}$, $U_{mb,\sigma}$, and U_{bv}, T^{-1} was found to peak at or close to $U_{mb,v}$; it was concluded that T is a useful indicator for the identification of onset of bubbling in fluidized beds.

Powder bed collapse was used as a tool to assess the fluidization quality of the Groups A, A/B, and B powders; the t_c/H_{mf} data for milled lactose powders showed a trend different from the rest of the powders. The combined influence of particle size distribution, fines content, bed voidage, and particle density on t_c/H_{mf} remains inconclusive.

In correlating $H_{R,1250}$ with Geldart groupings, the following were found for milled lactose powders: $H_{R,1250} < 1.10$ for Group B, $1.10 < H_{R,1250} < 1.19$ for Group A/B, and $1.20 < H_{R,1250} < 1.32$ for Group A. For Group A spray-dried lactose powders, sand, and refractory dust, the $H_{R,1250}$ range was ~1.14–1.32.

Chapter 6 – Powder Tumbling

6.1 Introduction

Rotating drums are commonly used in industry to aerate and flow powders through a sequence of tumbling or "reshuffling" (Rietema, 1984) and in operations such as mixing, heat and mass transfer, and granulation. Powder tumbling also has a growing role in the characterization of flowability under controlled and dynamic conditions. In this work, powder tumbling was performed in a Gravitational Displacement Rheometer (GDR); the GDR is a novel apparatus that measures the avalanche activity of powders that move under their own weight when rotated in a cylindrical drum at varying drum speeds. The use of powder tumbling in a very short rotating cylinder to characterize powder flowability was pioneered by Kaye and co-workers (Kaye, 1997; Kaye, et al., 1995). Subsequently, the concept of the GDR was proposed and developed by Davies and co-workers (Davies, et al., 2002; Davies, et al., 2004). The application of the GDR to flowability characterization has been reported in the work by Muzzio and co-workers, see for example A. M. Faqih, Chaudhuri, Alexander, et al. (2006), Faqih, Chaudhuri, Muzzio, et al. (2006), and Alexander et al. (2006).

Powder tumbling was done with selected lactose powders, sand, refractory dust, and glass beads at drum speeds of 5–30 rotations per minute, RPM. The effect of drum fill level on avalanche activity, and the relationship between avalanche activity and surface-volume mean particle diameter, d^*_{32}, and Geldart Powder Classification (Geldart, 1973) were investigated and discussed, taking into consideration the flow data and findings from shear testing in Chapter 3 and powder fluidization and bed collapse in Chapter 5.

6.2 Literature Review

6.2.1 Flow regimes of powders in rotating drums

Henein, Brimacombe and Watkinson (1983) identified and proposed six forms of transverse motion for coarse solids in rotating drums; the six forms were *sliding*, *slumping*, *rolling*, *cascading*, *cataracting*, and *centrifuging*, and the coarse particles were Geldart Groups B and D materials, recall Section 5.2.2 of Chapter 5 for Geldart Powder Classification (Geldart, 1973). The flow modes were extended to seven by Mellmann (2001). According to Mellmann, the three basic forms are the slipping, cascading, and cataracting motions. The slipping motion comprises two subtypes, namely sliding and *surging*; note that surging was not reported by Henein et al. (1983). The cascading motion comprises three subtypes; they are slumping, rolling, and cascading. Under the cataracting motion are cataracting and centrifuging.

Flow regimes for fine powders were reported by Castellanos, Valverde and Quintanilla (2002) and Huang, Zhang and Zhu (2009, 2010); the fine powders were Geldart Groups C and A

powders. Figure 6.1 shows the flow characteristics of fine and coarse powders in rotating drums defined by Huang et al. (2010); ω is the angular velocity [rad s^{-1}], θ_s is the minimum angle which triggers powders to slip [degrees], and θ_a is the minimum angle for which avalanches are observed [degrees]. There are differences in the flow regimes observed for fine and coarse powders.

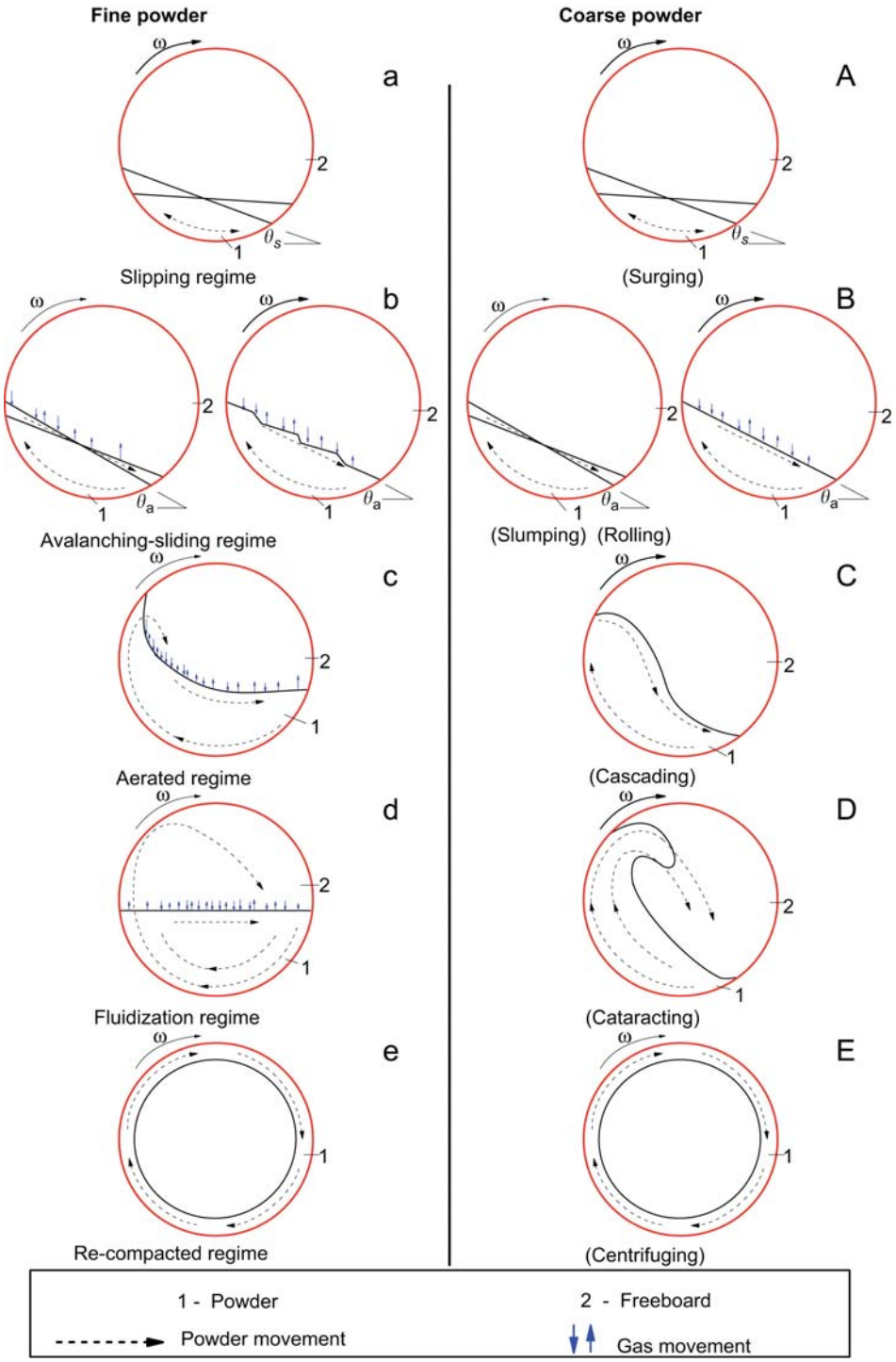

Figure 6.1 Flow characteristics of fine and coarse powders in rotating drums by Huang et al. (2010); used with permission (see Appendix 6.1 for permission)

With reference to Figure 6.1, the flow regimes for fine and coarse powders are similar at low rotational speeds, slipping for fine powder, see Figure 6.1 (a), and surging for coarse powders, see Figure 6.1 (A). With increasing drum speeds, fine powders show an *avalanching-sliding* mode, see Figure 6.1 (b), as opposed to the slumping and rolling motions observed with coarse powders, see Figure 6.1 (B). The observed flow motions between fine and coarse powders become more distinct at higher drum speeds; fine powders become aerated, see Figure 6.1 (c), and coarse powders flow in the cascading mode with a characteristic '*S*' profile, see Figure 6.1 (C). A further increase in drum speed leads to fine powders being fluidized, where the bed profile becomes flat because of the entrainment of gas, see Figure 6.1 (d), and coarse powders cataracting, see Figure 6.1 (D). At higher speed still, fine powders are "compacted" to the drum wall, see Figure 6.1 (e); this is the equivalent to the centrifuging motion of coarse powders at similar drum speeds, see Figure 6.1 (E).

6.2.2 Characterizing powder flowability with a rotating disc

Kaye et al. (1995) pioneered the use of a very short rotating cylinder or hollow disc for the characterization of powder flowability under low compaction and dynamic conditions. The concept was to monitor powder motion and deduce flow information from the motion. The rotating disc apparatus by Kaye et al. (1995) was commercialized as Aero-Flow™ (TSI, 2005). To analyze powder flowability with this apparatus, a powder sample was partially filled into the disc and rotated at specified drum speeds, and a photosensor array was used to detect the passage of powder avalanches. The size and frequency were plotted in discrete phase-space maps that gave scatter pattern of lines; the phase-space map was constructed by joining the points defined by the time between a set of avalanches, (t_n, t_{n+1}), and similar subsequent events, (t_{n+2}, t_{n+3}). The centroid or attractor point of the phase-space map was defined as the *mean time to avalanche* (MTA) or *flowability index*, and the scatter of the plot in the *x*-direction and *y*-direction indicated the time scatter of the avalanches and gave a *cohesivity index* (CI). The MTA and CI have been used as flow indices to reflect powder flowability, see for example Lee et al. (2000), Lavoie et al. (2002), and Lindberg et al. (2004); low MTA represented good flowability and low CI indicated low cohesivity.

6.2.3 Modification of the rotating disc apparatus

Davies et al. (2002; 2004) sought a more direct approach to monitoring and quantifying the avalanche activity of powders in rotating drums. A rotating apparatus with a roller system and a cylinder 150 mm in diameter and 300 mm in length, and another apparatus with a direct drive and a hollow disc 130 mm in diameter and 25.4 mm deep, which was the same to that of Kaye et al. (1995) in terms of disc geometry, were built and developed by Davies et al. (2002). The setup for each apparatus was that the cylinder or disc was mounted on a pivoted framework, and a load

cell was positioned under the cylinder centre line. The cylinder and the narrow disc were filled at different fill levels with sago particles of weight mean diameter of ~2.4 mm and rotated between ~0.6 and 25 RPM. When rotated, the material centre of mass changed position and caused a countering moment at the distance from the pivot to the load cell. The load cell continuously detected the resulting force and the variance of the force provided information on avalanche activity. A simple mathematical model was presented and used to interpret the load cell signal in terms of the movement of particles in the rotating cylinder.

The scalability of the work by Davies et al. (2002; 2004) was tested by Davies, Jones, Hussein, Fievez and Tallon (2006). An apparatus comprising a drum 1 m in diameter was constructed with the same design basis as the 130 mm characterization device. Using silica sand with a d_{32} of 150 μm rotated at ~0.2–5.9 RPM and 20% fill level by volume, it was found that decreasing variance of the load cell signal was associated with decreasing avalanching activity. Bed profiles obtained from digital video images were consistent with the observed flow regimes (Davies, et al., 2006).

The term *Gravitational Displacement Rheometer* (GDR) was coined by Muzzio for a version of rotating apparatus built and developed by Davies et al. (2002) (C. E. Davies, personal communication, 29 January 2015); this version of the apparatus comprised a cylindrical drum that was ~250 mm in diameter and ~300 mm in length. The application of the GDR to flowability characterization is given in Alexander et al. (2006), A. M. Faqih, Chaudhuri, Alexander et al. (2006), and A. M. Faqih, Chaudhuri, Muzzio et al. (2006).

6.2.4 Significant findings on powder flowability with rotating drum apparatuses

6.2.4.1 Identification of flow regimes and regime transitions

Davies et al. (2002) demonstrated with their first rotating apparatus that the flow regime transitions of the sago particles identified by visual inspection using video footage of particle motion at drum end walls correlated with the turning points on the plot of variance of the load cell signal against rotation speed; the onset of slumping occurred as the variance peaked and the transition to rolling was consistent with the variance leveling off, regardless of drum fill level. Consistent trends were observed with the rotating disc apparatus; the variance reached a maximum at the surging/slumping transition, ~1 RPM, and reduced to a steady value at the slumping/rolling transition, ~2 RPM.

Using lactose powder with a weight mean diameter of 206 μm and at 20% fill level in the rotating disc apparatus, Davies et al. (2004) reported qualitative and quantitative differences between the variance of the load cell signal of lactose powders and the sago particles in earlier work (Davies, et al., 2002). Partial surging and powder consolidation were observed at very low rotation rates and the variance increased to a maximum at ~10 RPM; video footage indicated

powder slumping at this drum speed. The lactose was still slumping at ~15 RPM and judged to have progressed beyond rolling at ~23 RPM; it was suggested that the rate of change of variance tended from a negative value to zero with respect to drum speed.

Davies et al. (2004) also pointed out that avalanche activity in real systems was not ideal, evidenced by their sago and lactose data and video footages; the departure from ideality and its influence on the analysis of flow regimes and transitions remained unclear and it was noted by Davies et al. (2004) that "*a single model of the genesis and transit of real avalanches is unlikely to be adequate for all materials*". Further evaluation showed that for each avalanche, the time of first material movement, the time at which the avalanche achieved its furthest displacement relative to a fixed frame of reference against the frontal plane of the drum, the time for gross material movement began, and the time at which material motion in an avalanche relative to the material bed in the drum ceased as identified by video footage frame-by-frame inspection, could be synchronized with the load cell time series data.

6.2.4.2 Identification of behaviour of Geldart Powder Groups

Webster and Davies (2006) observed four distinct shapes in the plot of load cell signal variance against rotation speed up to ~23 RPM for four different materials which included an agricultural lime sample judged to be a Geldart Group C or A/C powder, a Group A fluid cracking catalyst (FCC), a Group B sand, and Group D plastic pellets; experiments were done using the same rotating disc apparatus previously used by Davies et al. (2004). The Group B sand and Group D plastic pellets were characterized by high variance at low drum speed; the variance decreased with increasing rotation speed, before leveling off for the sand sample and increasing again for the plastic pellets. For the Group A FCC, the variance was low at low rotation speed and increased to a maximum with increasing drum speed before dropping off again as rotation rate increased further. For the Group C lime sample, the variance was also low at low rotation speeds but increased continuously within the drum speed range tested. Power spectral density analysis revealed that most avalanche activity happened and spread fairly uniformly below 5 RPM for the Group B sand and Group D plastic pellets. For the Group A FCC and Group C lime sample, significant avalanching occurred at drum speeds beyond 5 RPM; composite plots of power, slumping or mean avalanching frequency, and rotation speed are given in Webster and Davies (2010).

6.2.4.3 Flow Index as indicator for cohesivity and flowability

In the work by A. M. Faqih, Chaudhuri, Alexander et al. (2006), experiments with the GDR were performed in a cylinder ~200 mm in diameter and ~254 mm in length, and approximately 40% fill level. The only information given regarding the powder systems used is as follows: spherical lactose powder with mean particle size of ~100 μm, two samples of needle-shaped

microcrystalline cellulose powders, one ~90 μm and the other ~60 μm, and a sample of irregularly shaped milled lactose of ~50 μm. Plots of load cell standard deviation, σ_{ws}, versus drum rotation in the range of 5–30 RPM showed that firstly, σ_{ws} values were higher as particle size decreased and secondly, σ_{ws} increased with rotation rate; the size of avalanches increased because of the effect of centrifugal forces in addition to the interparticle or frictional-cohesive forces that resisted the onset of avalanching. For the more cohesive ~50 μm milled lactose powder, σ_{ws} reached a maximum at 20 RPM and decreased thereafter; this was attributed to the overlapping of simultaneous avalanches.

A. M. Faqih, Chaudhuri, Alexander et al. (2006) noted that the essential assumption behind the GDR method to characterize powder flowability was that σ_{ws} would be proportional to the "intensity of cohesive interparticle forces", but verification cannot be done experimentally due to a lack of an independent method for direct measurement of cohesion under relevant dilated conditions. However, the authors tested the assumption using a computational model and simulation, and demonstrated a monotonic relationship between cohesive stress and standard deviation of the moment of inertia of their simulated particle assemblies, provided drum rotation was sufficiently slow to allow individual avalanches to flow independently from one another. Hence, the authors inferred that σ_{ws} was proportional to cohesion. Based on this finding, a Flow Index in the form of Equation 6.1 was proposed; $\sigma_{ws,5RPM}$, $\sigma_{ws,10RPM}$, $\sigma_{ws,15RPM}$, and $\sigma_{ws,20RPM}$ are the standard deviation of load cell signal at sufficient low drum speeds, namely 5 RPM, 10 RPM, 15 RPM, and 20 RPM respectively. Equation 6.1 was said to be a quantitative flow index that could provide "*a convenient, sensitive, and practical single-number quantifier of powder flow properties under dilated conditions*" (A. M. Faqih, Chaudhuri, Alexander, et al., 2006).

$$\text{Flow Index} = \frac{\sigma_{ws,5RPM} + \sigma_{ws,10RPM} + \sigma_{ws,15RPM} + \sigma_{ws,20RPM}}{4} \quad (6.1)$$

A. M. Faqih, Chaudhuri, Alexander et al. (2006) correlated Equation 6.1 with the flow behaviours of powders – *funnel flow*, *mass flow*, *intermittent flow* (caused by steady vibration), and *no flow* – through a set of hoppers made of Plexiglas and with angles of 35°, 45°, 55°, 65°, and 75° to simulate industrial conditions; results showed that flow through the hoppers changed from funnel flow to mass flow, mass flow to intermittent flow, and intermittent flow to no flow as Flow Index increased. Using lactose, microcrystalline cellulose, and mixtures of lactose and microcrystalline cellulose powders, A. N. Faqih et al. (2007) reported consistent findings; a plot of Flow Index against increasing hopper angle was proposed for the prediction of the shallowest angle required by a powder to flow through a hopper.

Using selected pharmaceutical blends, Vasilenko et al. (2011) correlated Equation 6.1 with cohesion, *C*, measured at 3–15 kPa with a rotational shear cell. A linear relationship was

observed and the slope of the straight line was influenced by the composition of the pharmaceutical blends. Extending the work with selected catalyst powders and over a lower consolidation stress range, 0.5–3 kPa, Vasilenko et al. (2013) observed similar and consistent findings; *C* was a linear function of Flow Index and the slope of the straight line was dependent on the consolidation stress value. As already critiqued in Section 3.2.3 in Chapter 3, the approach used by Vasilenko et al. (2011; 2013) is empirical; however they have shown correlations between *C* measured under confined and consolidated conditions and Flow Index measured under unconfined conditions. There has not been evaluation and discussion on correlations between C_0, the cohesion under zero consolidation stress that has to be overcome for the initiation of powder flow under unconfined conditions, and Equation 6.1; evaluation and discussion are given in this chapter with selected powders.

6.2.4.4 Powder dilation as indicator for cohesivity and flowability

Using the model powders as in A. M. Faqih, Chaudhuri, Alexander et al. (2006) and applying discrete element simulations, A. M. Faqih, Chaudhuri, Muzzio et al. (2006) investigated powder dilation induced by powder flow in the GDR. The behaviour of powders at 50% fill level and 7 RPM, 16 RPM, and 29 RPM was recorded with a video camera and video footage was analyzed with a pixel-counting computer program to determine the relative volume of powder to bed void. Equation 6.2 was used to calculate powder dilation; V_{Initial} was the initial volume of powder bed after the powder in the GDR was shaken horizontally and vertically for an unreported fixed number of times and allowed to settle under its own weight, and V_{New} was the volume of powder measured at the first 11 revolutions.

$$\text{Powder dilation} = \frac{V_{\text{New}} - V_{\text{Initial}}}{V_{\text{Initial}}} \times 100\% \qquad (6.2)$$

It was observed that radical increase in dilation occurred between 1–2 revolutions before the powders reached a steady state (A. M. Faqih, Chaudhuri, Muzzio, et al., 2006). Dilation increased with increasing cohesiveness, and an excellent correlation between Flow Index and powder dilation (Eq. 6.2) was demonstrated. Drum speeds caused short-term variability in dilation regardless of the powders used, and the speed effect generally became insignificant once steady state was reached. For cohesive powders, such as the ~60 μm microcrystalline cellulose and ~50 μm milled lactose powders, higher drum speeds led to a higher frequency of avalanches without significantly changing the dynamics of flow. For the more free-flowing ~100 μm spherical lactose powder, dilation increased with increasing rotation rate at steady state; continuous powder flow, avalanches that were neither discrete nor separated, and aperiodic cascading of the bed surface were seen. At higher rotation rates, the powder became airborne at

the top of the flowing layer. With regards to the effect of cylinder diameter (A. M. Faqih, Chaudhuri, Muzzio, et al., 2006), dilation decreased monotonically when the diameter of the cylinder was between ~50 mm and ~200 mm, and a sharp rise was observed when the diameter increased from ~200 mm to ~254 mm. The monotonic decrease was attributed to less constrained flow and increase in shear that caused powder agglomerates to break up, allowing more powders to move as individual particles. In the ~254 mm drum, although powder flowed freely, avalanches would cease before reaching the end wall of the cylinder. The authors stated that shear was insufficient to break up powder agglomerates and allow the powders to cascade down the cylinder; hence powder dilation remained high (A. M. Faqih, Chaudhuri, Muzzio, et al., 2006).

Results from discrete element simulations were consistent with experimental data (Alexander, et al., 2006; A. M. Faqih, Chaudhuri, Muzzio, et al., 2006). It was further noted by A. M. Faqih, Chaudhuri, Muzzio et al. (2006) that air entrainment was a consequence of powder dilation at low drum rotations and not a root cause because the influence of interstitial air was neglected in the simulations.

6.2.5 Summary of literature review

Powder tumbling is common in the handling and processing of powder systems. The GDR has been built and developed to measure the avalanche activity of powders that move under their own weight when rotated in a cylindrical drum; manipulation of the avalanche data gives information on powder flowability. With limited experimental data from selected powder systems, the GDR has shown promise as a robust tool for flowability characterization; the utility of the GDR has included the identification of powder flow regimes at different drum speeds, identification of transitions between flow regimes, and comparison of avalanche activity of powders from different Geldart Groups. Two flow indices, namely the Flow Index, Equation 6.1, and powder dilation, Equation 6.2, have been proposed as indicators to powder flowability and cohesivity; there has been consistency between experimental results and computer simulations.

6.3 Aims

1. To measure the avalanche activity of samples of milled lactose powders, sand, refractory dust, and glass beads.
2. To investigate the influence of drum fill level and d^*_{32} on the avalanche activity of the selected powders.
3. To investigate the relationships between avalanche activity, cohesion measured by shear testing, and powder bed collapse measured by fluidization for the selected powders.
4. To assess the relationship between avalanche activity and Geldart Powder Classification.

6.4 Materials, Methods and Analysis

6.4.1 Materials

The powders used were samples of milled lactose LP4, LM1 and LP1, sand S1, refractory dust RD1, and glass beads B8; Table 6.1 gives information on the d^*_{32}, span, t_c/H_{mf}, C_0, and Geldart Classification (Geldart, 1973) for the powders. LP4 was a Group C powder, LM1, S1, and RD1 were Group A powders, and LP1 was a A/B boundary powder. B8 was a Group B powder; its d_{32} was measured by sieve analysis.

Table 6.1 Information on d^*_{32}, span, t_c/H_{mf}, C_0, and Geldart Classification for lactose LP4, sand S1, refractory dust RD1, lactose LM1, lactose LP1, and glass beads B8

Powders	d^*_{32} [µm]	Span [-]	t_c/H_{mf} [s m^{-1}]	C_0 [kPa]	Geldart Classification
LP4	28.9	2.26	–	0.0534	C
S1	40.1	1.43	64.20	0.0427	A
RD1	41.5	1.57	35.47	0.0632	A
LM1	58.0	2.23	–	0.0527	A
LP1	150.8	1.75	–	0.0245	A/B
B8	193.0	0.15	–	–	B

6.4.2 Experimental setup

Figure 6.2 is a front view photo of the GDR. The cylindrical drum was made of Perspex. One end of the drum was permanently closed by a Perspex disc and the other end was fitted with a snug-fit Perspex lid; the internal diameter and length were respectively 192.5 mm and 292.5 mm. The GDR included a drive system that consisted of a motor, a drive pulley, a pivot plate, four support rollers on which the drum was mounted, a built-in load cell positioned at the drum centre line and under the pivot plate, and a control panel that comprised, from left to right, an on/off switch, a drum directional control switch, a dial that controlled the drum speed, and a L.E.D. drum speed indicator. The drive pulley transferred power from the motor and drove the rotation of the support rollers and drum. The pivot plate held the drum atop the load cell, and the position of the pivot plate – lifted up or touching the load cell – was controlled by a lever. The load cell was connected to a data acquisition system and a computer equipped with custom software. Schematic diagrams of a similar GDR are given in Davies et al. (2002).

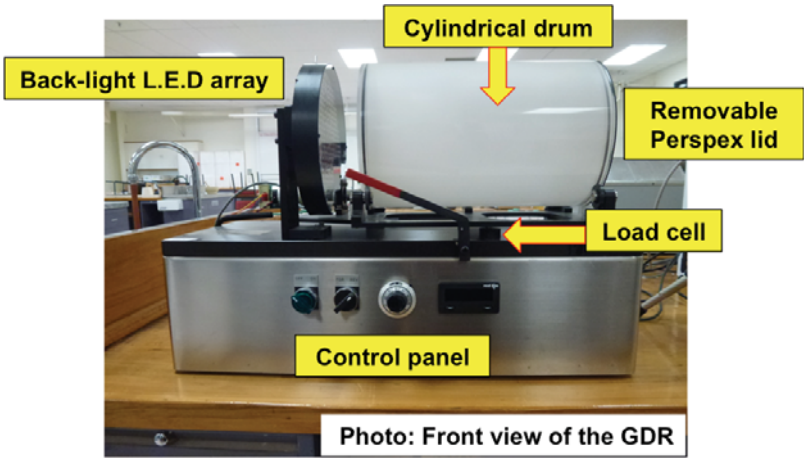

Figure 6.2 A photo of the Gravitational Displacement Rheometer

6.4.3 Setup and operation of GDR

The setting up and operation of the GDR were based on the operator's guide by Pingali and Kick (2013); the operator's guide contains information on setting up of the GDR, understanding the *Graphical User Interface* in the custom software, and step-by-step instructions on operating the GDR, which included imaging setup, load cell calibration, powder installation, and Flow Index experimentation.

Drum rotation rates were measured by visual observation and with a stopwatch; the number displayed on the L.E.D. drum speed indicator was used as a guide.

Circularity, irregularity, and dimensional tolerances of the cylindrical drum, which could cause wobble, were checked prior to experiments. The empty drum was rotated between ~5 RPM and ~30 RPM, and the load cell signal at each incremental drum speed was recorded at a sampling rate of 30 Hz; 1,800 data points were collected and the standard deviation of drum weight shift, σ_{ws}, at each incremental drum speed was determined. The plot of σ_{ws} data versus drum speed was shown in Figure A6.1 in Appendix 6.2; σ_{ws} increased with increasing drum speed, see the *filled diamond* data points with the label *Initial drum*, and σ_{ws} ranged from 0.0223–0.0315 kg, indicating wobble caused by the cylindrical drum. A new cylindrical drum of the same dimensions was made and its wobble was checked. The σ_{ws} data were relatively constant within the range of drum speeds used, see Figure A6.1; the values of σ_{ws} were 0.0204–0.0247 kg in Run 1, 0.0217–0.0240 kg in Run 2, 0.0179–0.0218 kg in Run 3, and 0.0211–0.0252 kg in Run 4. The new drum gave significant improvement and was subsequently used for experiments.

Avalanche activity was measured at 5 RPM, 10 RPM, 15 RPM, 20 RPM, 25 RPM, and 30 RPM; 1,800 data points were sampled at 30 Hz, σ_{ws} was determined, and Flow Index was calculated following Equation 6.1. All powder samples were initialized before the experiments; this was done by rotating the powders at 15 RPM for ~2 minutes prior to avalanche activity measurement. In the investigation on the effect of drum fill level, the fill levels were set at 20%, 30%, 40%, and 50% on a volume basis; loose poured bulk density measured by the modified

NZS3111 method, $\rho_{0,mNZS3111}$, see Section 4.4.2 and Table 4.1 in Chapter 4, was used to calculate the sample mass required for each fill level. An infrared video camera that was connected to the computer and controlled by the custom software was used to capture random images of powder bed surface during tumbling; the 'Print Screen' function was used as the function of the video camera was limited to powder dilation measurement and not video recording. All experiments were repeated once or twice, and the average σ_{ws} was calculated.

6.4.4 Analysis

Plots of standard deviation of drum weight shift, σ_{ws}, versus drum speed were constructed. Interpretation of the data was done taking into consideration d^*_{32}, C_0, Geldart Powder Classification, and powder bed collapse and t_c/H_{mf}; see respectively Section 2.5.1 of Chapter 2, Section 3.5.3 of Chapter 3, Section 5.2.2 of Chapter 5, and Section 5.5.3 of Chapter 5.

6.5 Results

6.5.1 Effect of drum fill level on avalanche activity

Figure 6.3 is a plot of σ_{ws} versus drum speed for Geldart Group C lactose LP4 at fill levels between 20% and 50%; σ_{ws} increases with increasing fill level. Figure 6.4 is a plot of σ_{ws} versus drum speed for Geldart Group A sand S1, and Figure 6.5 shows σ_{ws} plotted against drum speed for Geldart Group A refractory dust RD1. At 20% and 30% fill levels, the trends for σ_{ws} are similar for both S1 and RD1; σ_{ws} seems to increase linearly with drum speed. Distinct trends are observed at 50% fill level for S1, and at 40% and 50% fill levels for RD1. In Figure 6.6, which plots σ_{ws} versus drum speed for lactose Geldart Group A lactose LM1, σ_{ws} fluctuates between 0.04 kg and 0.12 kg from 5 RPM to 30 RPM, and is relatively constant, 0.04–0.06 kg, at 50% fill level.

Comparing Figure 6.3 with Figures 6.4, 6.5, and 6.6, the opposite trend is observed. The σ_{ws} for Group C lactose LP4 increases with increasing fill level, see Figure 6.3, but the trend is reversed with Group A sand S1, refractory dust RD1, and lactose LM1, see Figures 6.4, 6.5, and 6.6.

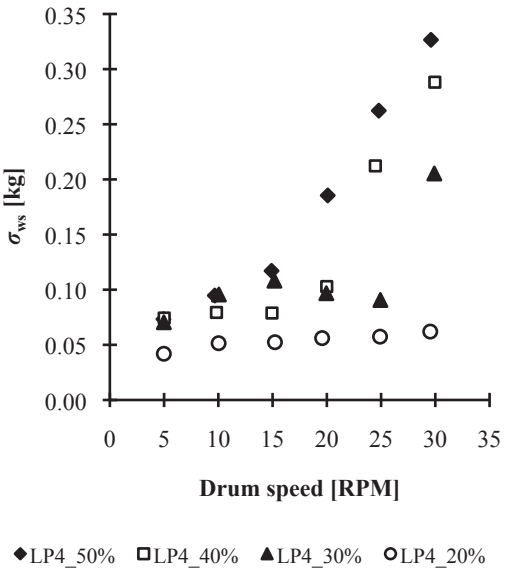

Figure 6.3 Plot of σ_{ws} against drum speed for lactose LP4 at 20–50% fill level

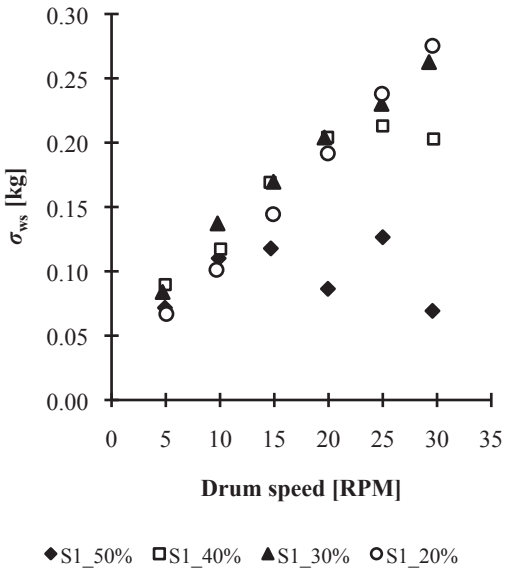

Figure 6.4 Plot of σ_{ws} against drum speed for sand S1 at 20–50% fill level

Figure 6.7 is a plot of σ_{ws} versus drum speed for Geldart Group A/B lactose LP1 at 10% to 50% fill levels. In general, σ_{ws} seems to decrease with increasing fill level, similar to that of the Geldart Group A powders used, see Figures 6.4, 6.5, and 6.6. It is also observed that σ_{ws} at 30%, 40%, and 50% fill levels seem similar. Figure 6.8 shows σ_{ws} versus drum speed for Geldart Group B glass beads B8 at 20% to 50% fill levels; σ_{ws} increases with increasing fill level, similar to the trend of Group C lactose LP4 in Figure 6.3.

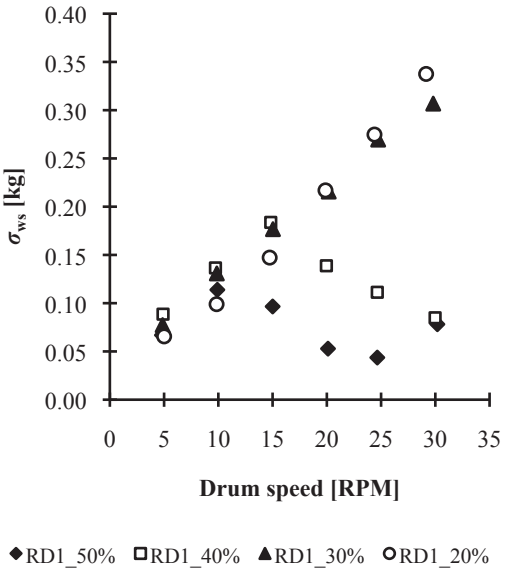

Figure 6.5 Plot of σ_{ws} against drum speed for refractory dust RD1 at 20–50% fill level

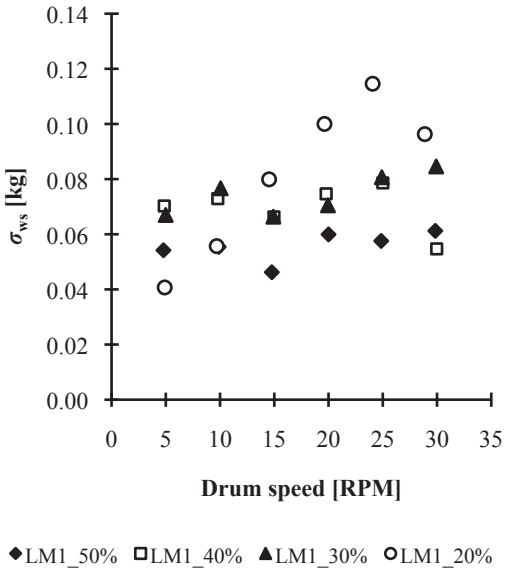

Figure 6.6 Plot of σ_{ws} against drum speed for lactose LM1 at 20–50% fill level

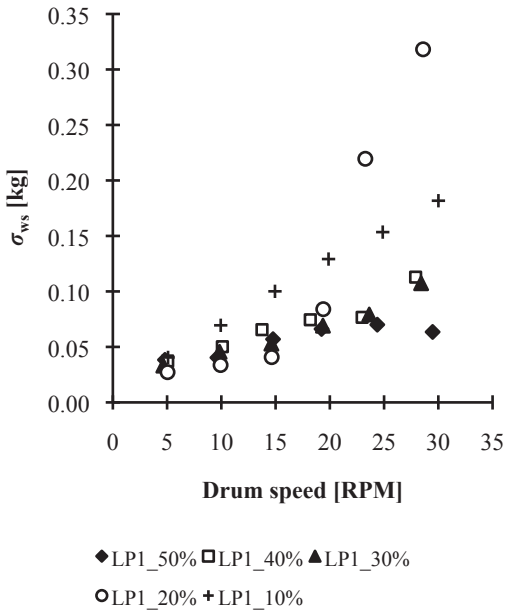

Figure 6.7 Plot of σ_{ws} against drum speed for lactose LP1 at 10–50% fill level

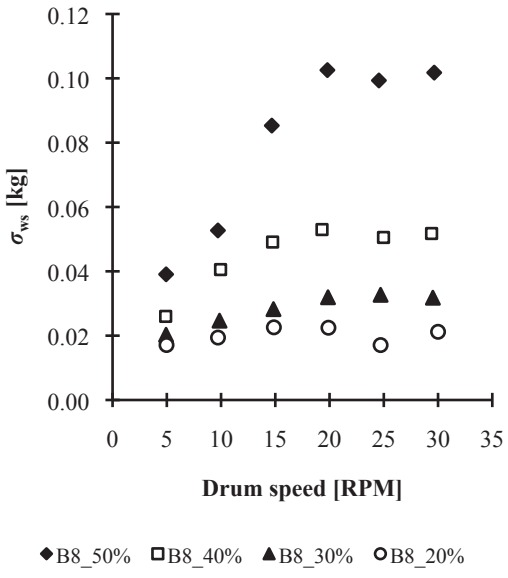

Figure 6.8 Plot of σ_{ws} against drum speed for glass beads B8 at 20–50% fill level

6.5.2 Avalanche activity and Geldart Powder Classification

The avalanche activity of Geldart Groups A, C, A/B, and B powders is examined in this section. Figure 6.9 is a plot of σ_{ws} against drum speed for Group A powders sand S1, refractory dust RD1, and lactose LM1 at 50% fill level, and Figure 6.10 plots the σ_{ws} data of Group C lactose LP4, Group A/B lactose LP1, and Group B glass beads B8 at 50% fill level against drum speed. By observation of both Figures 6.9 and 6.10, σ_{ws} shows differences between 10 RPM and 15 RPM.

With reference to Figure 6.9 and comparing S1 and RD1, the σ_{ws} for S1 is higher at 15–25 RPM; the σ_{ws} data at 5, 10, and 30 RPM are similar. As for LM1, the σ_{ws} values are lower and fairly constant. Referring to Figure 6.10, σ_{ws} is highest with LP4, followed by B8 and then LP1. The σ_{ws} for LP4 increases with increasing drum speed, and a change in slope is observed at 15 RPM. For B8 and LP1, σ_{ws} increases from 5 RPM to ~20 RPM and subsequently begins to level off.

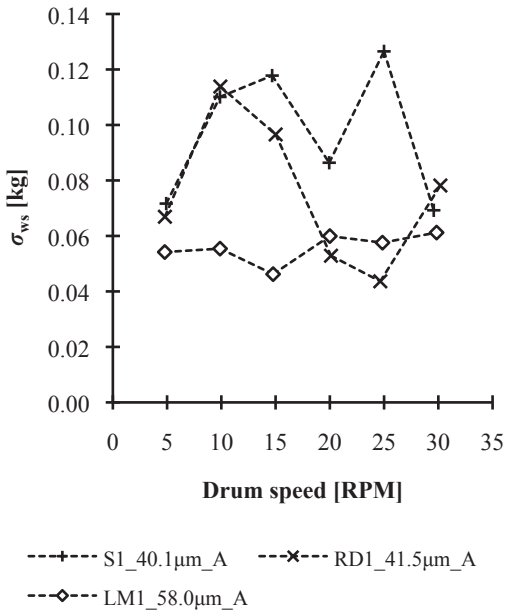

Figure 6.9 Plot of σ_{ws} against drum speed for Geldart Group A sand S1, refractory dust RD1, and lactose LM1 at 50% fill level

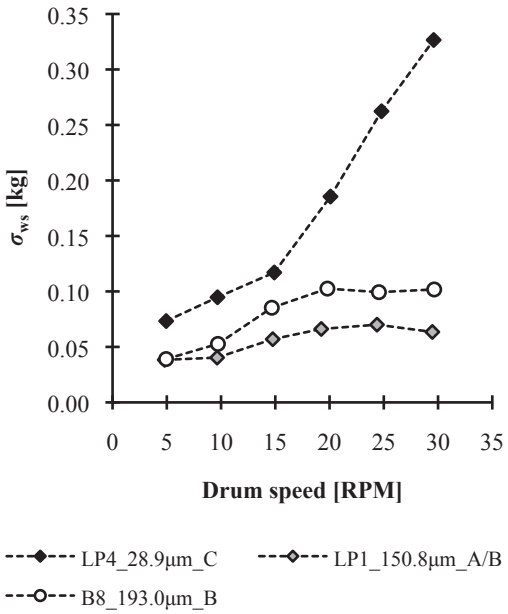

Figure 6.10 Plot of σ_{ws} against drum speed for Geldart Group C lactose LP4, Group A/B lactose LP1, and Group B glass beads B8 at 50% fill level

6.5.3 Avalanche activity and d^*_{32}

Parameter d^*_{32} has dominant influence on powder avalanche activity. Figure 6.11 shows σ_{ws} at 5 RPM for all the drum test powders and 50% fill level versus $1/d^*_{32}$; the data display a linear trend. In Figure 6.12, σ_{ws} at 10 RPM and 50% fill level is plotted against $1/d^*_{32}$. Figure 6.13 shows σ_{ws} at 15 RPM and 50% fill level versus $1/d^*_{32}$. Figure 6.14 shows σ_{ws} at 20 RPM and 50% fill level plotted against $1/d^*_{32}$. In Figure 6.15, σ_{ws} at 25 RPM and 50% fill level is plotted against $1/d^*_{32}$. Figure 6.16 shows σ_{ws} at 30 RPM and 50% fill level versus $1/d^*_{32}$. With reference to Figures 6.12 to 6.16, consistent scatter is observed.

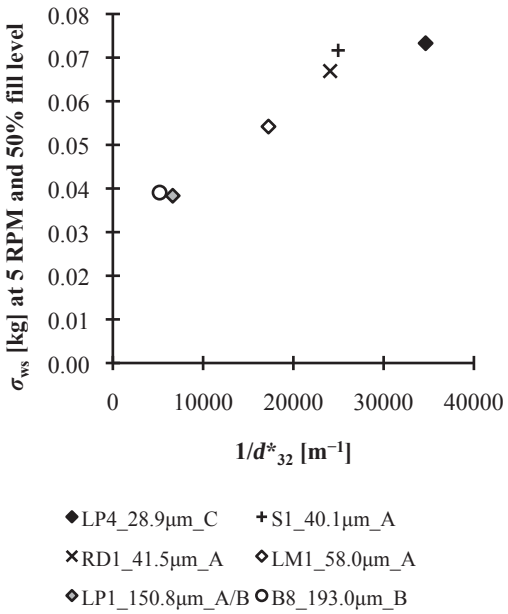

Figure 6.11 Plot of σ_{ws} at 5 RPM and 50% fill level against $1/d^*_{32}$

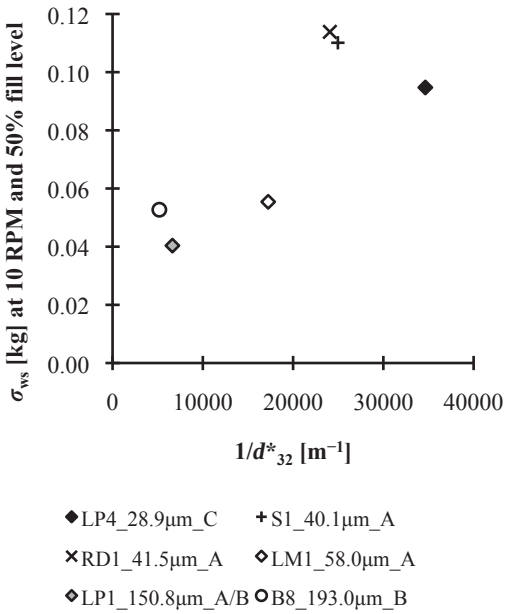

Figure 6.12 Plot of σ_{ws} at 10 RPM and 50% fill level against $1/d^*_{32}$

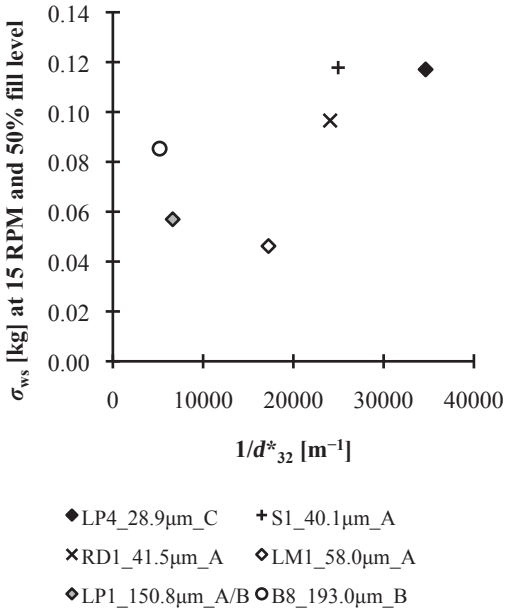

Figure 6.13 Plot of σ_{ws} at 15 RPM and 50% fill level against $1/d^*_{32}$

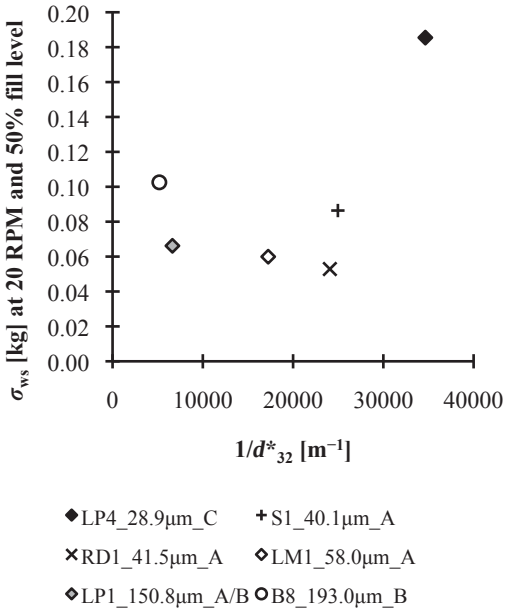

Figure 6.14 Plot of σ_{ws} at 20 RPM and 50% fill level against $1/d^*_{32}$

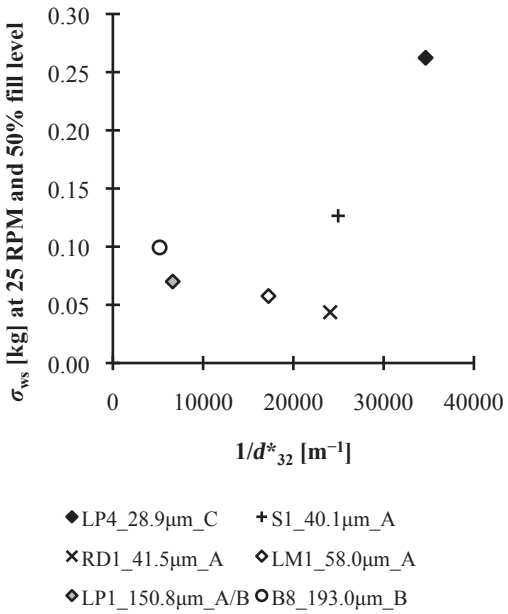

Figure 6.15 Plot of σ_{ws} at 25 RPM and 50% fill level against $1/d^*_{32}$

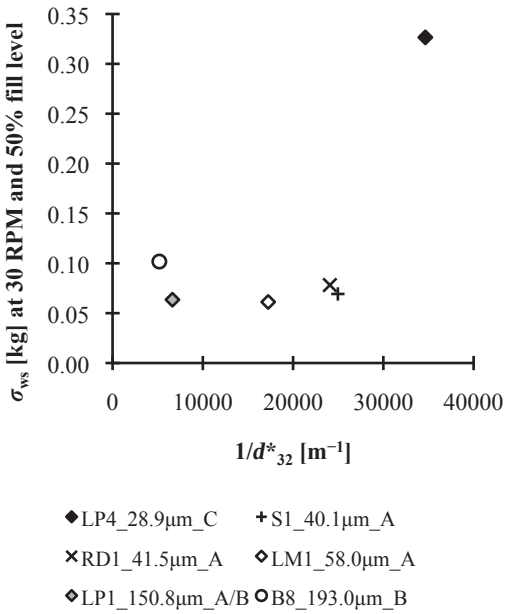

Figure 6.16 Plot of σ_{ws} at 30 RPM and 50% fill level against $1/d^*_{32}$

6.6 Discussion

6.6.1 Avalanche activity and influence of drum fill level

The influence of drum fill level, 20%, 30%, 40%, and 50% on a volume basis, on σ_{ws} is shown in Figures 6.3 to 6.8; the internal diameter of the cylinder used was 192.5 mm. The influence of fill level was investigated because the amount of powder has to be sufficient for avalanching to take place and to prevent the slipping of powders in the cylinder. It is demonstrated with Geldart Group C lactose LP4, see Figure 6.3, and Geldart Group B glass beads B8, see Figure 6.8, that σ_{ws} increases with increasing fill level. In contrast, σ_{ws} generally decreases with increasing fill level for Geldart Group A powders – sand S1, refractory dust RD1, and lactose LM1 – see Figures 6.4, 6.5, and 6.6, and also Geldart Group A/B lactose LP1, see Figure 6.7. It is noted that the data were obtained with limited powder systems; there is a need for caution in the selection of drum fill level.

Note that in the work by Davies et al. (2002; 2004) involving a narrow cylinder of 130 mm in diameter and 25.4 mm in length, 20% fill level was sufficient for avalanche activity to be observed and measured. In later work (Webster & Davies, 2006, 2010), a layer of silica sand, –355 µm +250 µm, was glued to the curved wall of the narrow cylinder to prevent the slipping of powders during rotation. In the work by A. M. Faqih, Chaudhuri, Alexander et al. (2006), the fill level was ~40% by mass in a cylinder of ~200 mm in diameter and ~254 mm in length. In the work by A. M. Faqih, Chaudhuri, Muzzio et al. (2006), the fill level was 50% by volume in cylinders with diameter ranging from ~50 mm to ~254 mm and drum length up to ~300 mm.

Faqih and colleagues have not given any explanation as to why and how they selected the particular fill levels they used.

6.6.2 Avalanche activity and Geldart Groups C, A, A/B and B powders

With reference to Figure 6.9 and Figure 6.10, the selected powders, which are from different Geldart Groups, exhibit different characteristic drum speed:σ_{ws} profiles at 50% fill level. For a full understanding and interpretation of the avalanche activity profiles, additional information such as tumbling bed profile, d^*_{32}, span, C_0 measured by shear testing, and t_c/H_{mf} measured by bed collapse are necessary. Figure 6.17 shows the tumbling bed profiles for Geldart Group A refractory dust RD1, sand S1 and lactose LM1. Figure 6.18 shows the tumbling bed profiles for Geldart Group C milled lactose LP4; three random shots at each drum speed are shown. Figure 6.19 shows the tumbling bed profiles for Geldart Group A/B milled lactose LP1 and Group B glass beads B8.

With reference to Figure 6.9, Table 6.1, and Figure 6.17, the Geldart Group A powders are first discussed. The σ_{ws} values for sand S1 at 15 RPM, 20 RPM, and 25 RPM are higher than refractory dust RD1. The d^*_{32} and span of S1 and RD1 are similar; this suggests the differences in σ_{ws} are mainly attributed to t_c/H_{mf} and C_0. As shown in Figure 6.17, horizontal bed surface is observed for both S1 and RD1; the powders are fluidized when drum speed is beyond 15 RPM. But S1 is less cohesive, C_0=0.0427 kPa, and its ability to retain air is higher, t_c/H_{mf}=64.20 s m^{-1}; note that the bed expansion of S1 is also higher, see Figure 6.20 and also recall Section 5.5.3 of Chapter 5. For lactose LM1, σ_{ws} is relatively constant, which is consistent with its tumbling bed profiles in Figure 6.17. The absence of a horizontal bed surface shows lack of aeration and this has been independently checked by fluidizing LM1 in the fluidized bed; segregation of powders has been observed and this has been attributed to the relatively wide particle size distribution of LM1, which has a span of 2.23.

Referring to Figure 6.10, the σ_{ws} for lactose LP4 is highest; d^*_{32} is lowest among the test powders and LP4 cannot be fluidized, typical of Geldart Group C powders. Its bed profiles in Figure 6.18 show that LP4 moves as agglomerates when tumbled; it has been observed visually that the powder movement is random.

When Geldart Group A/B lactose LP1 and Group B glass beads B8 are compared, see Figure 6.10, the σ_{ws} for LP1 is lower. This can be attributed to a combination of factors such as the higher presence of smaller particles in LP1, which is reflected by a lower d^*_{32}, wider size distribution, and the difference in tumbling bed profiles, see Figure 6.19.

With reference to the tumbling bed profiles of B8 in Figure 6.19, horizontal bed surface is observed between 10 RPM and 30 RPM. The phenomenon is attributed to a mechanism different from powder aeration that occurs in Geldart Group A powders because B8 will not hold any air; B8 is a Geldart Group B material and its bed collapse is expected to be virtually

instantaneous, t_c/H_{mf} is very close to zero. The possible mechanism may involve rapid rearrangement of the particles in response to the rapid drum rotations, and the extreme free flowing nature of the particles.

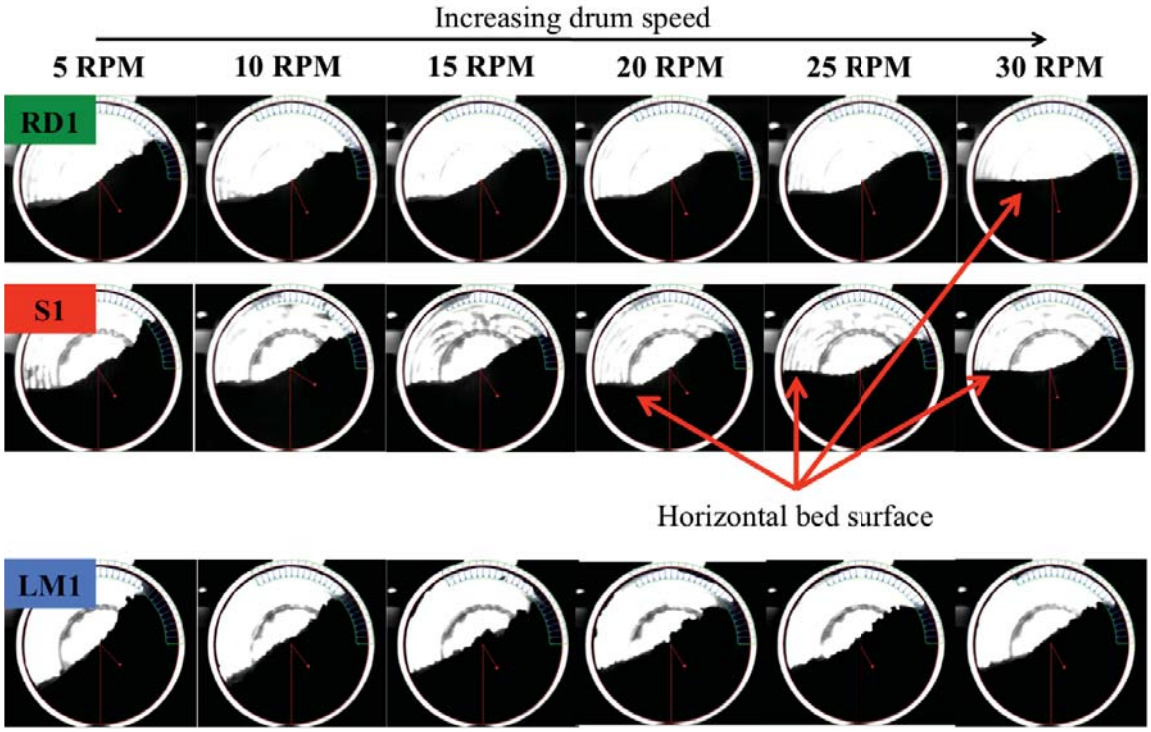

Figure 6.17 Tumbling bed profiles for Geldart Group A refractory dust RD1, sand S1 and milled lactose LM1

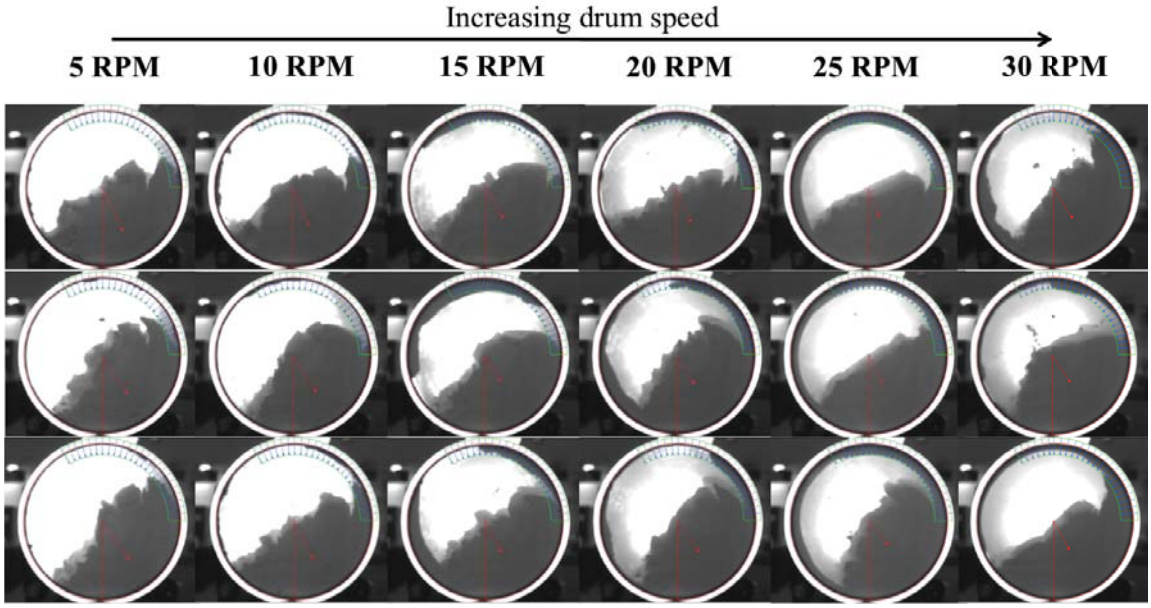

Figure 6.18 Tumbling bed profiles for Geldart Group C milled lactose LP4; there are three random shots at each drum speed

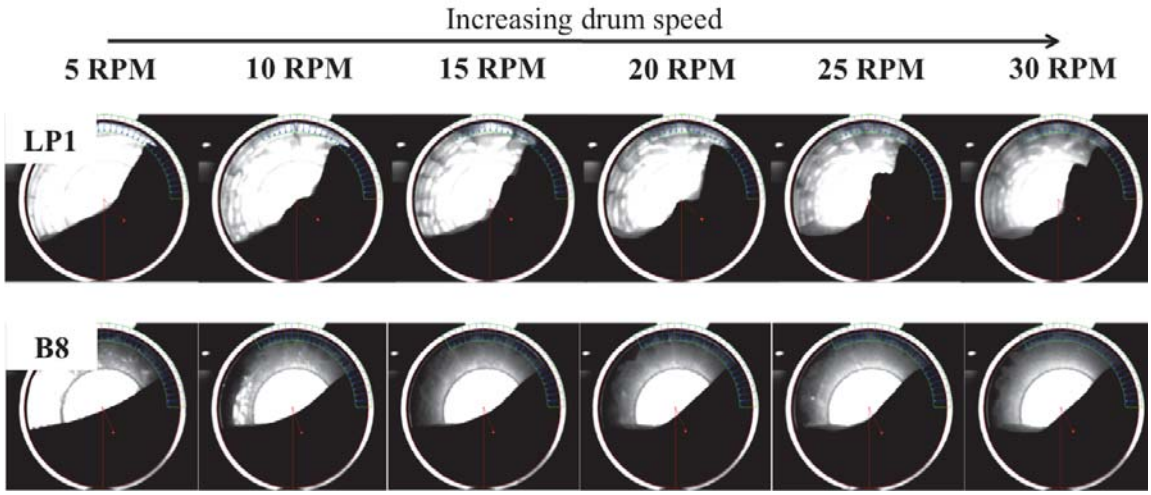

Figure 6.19 Tumbling bed profiles for Geldart Group A/B milled lactose LP1 and Group B glass beads B8

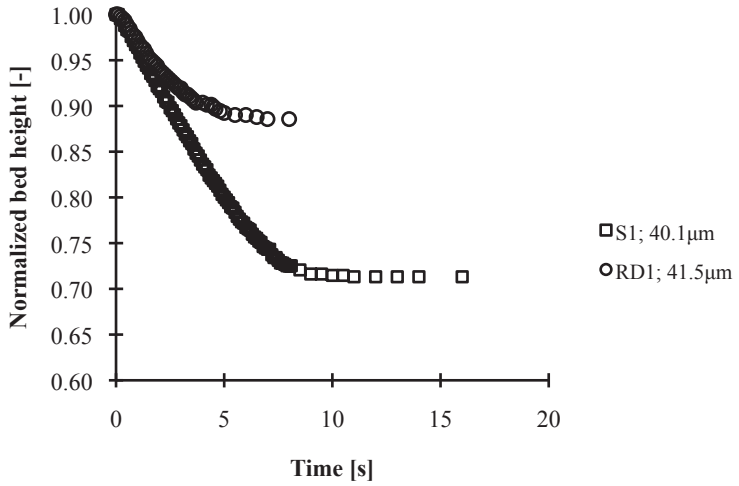

Figure 6.20 Plot of normalized bed height against time; bed collapse profiles for Geldart Group A sand S1 and refractory dust RD1

6.6.3 Avalanche activity, Flow Index and $1/d^*_{32}$

With reference to Figure 6.11, σ_{ws} at 5 RPM seems to increase linearly with $1/d^*_{32}$; scatter of data is observed as drum speed increases, recall Figures 6.12 to 6.16. The scatter is very likely caused by the powders themselves, which are very different by nature. Besides that, the scatter could partly be caused by the construction and imperfection of the GDR; the GDR comprises a cylindrical drum that is mounted on a roller system and there is a small degree of wobble arising from the circularity, irregularity, and dimensional tolerances of the cylindrical drum, as previously noted in Section 6.4.3. For this reason, Davies et al. (2002; 2004) and Webster and Davies (2006, 2010) have put much emphasis on an apparatus with a smaller cylinder that is directly driven by a shaft connected to a motor.

Figure 6.21 shows Flow Index plotted against $1/d^*_{32}$; the trend exhibited in Figure 6.21 seems consistent with those in Figures 6.12 to 6.16. Comparing Figure 6.11 and Figure 6.21, the trend in Figure 6.11 is neater; this suggests that measurement of σ_{ws} at 5 RPM may be a more practical way forward in the context of rapid flowability characterization.

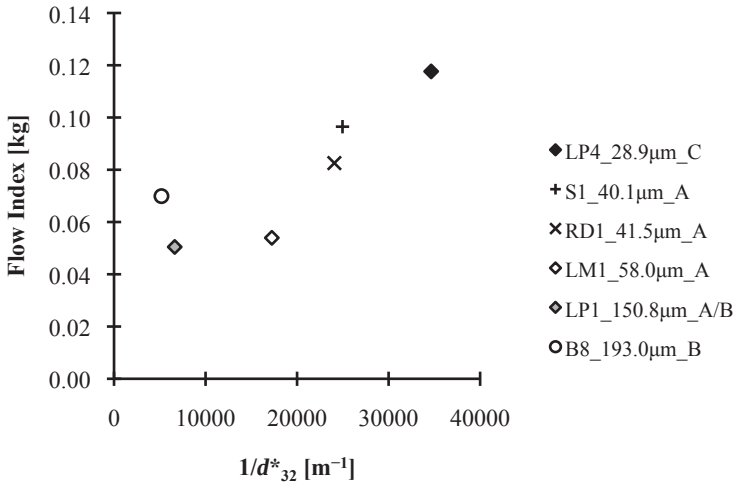

Figure 6.21 Plot of Flow Index, Equation 6.1, against $1/d^*_{32}$

6.6.4 Avalanche activity and powder dilation

The work in this chapter has not included experiments on powder dilation. This is because there are discrepancies between the GDR's pixel-counting computer program and procedures used by Faqih and colleagues (A. M. Faqih, Chaudhuri, Alexander, et al., 2006; A. M. Faqih, Chaudhuri, Muzzio, et al., 2006), and the GDR system in this work; the custom software of the present GDR and its operating procedures have been revised by Pingali and Kick (2013). In the earlier work, powder dilation was measured after the initialization of powder, see Section 6.2.4.4; the powder in the cylinder was shaken horizontally and vertically for an unreported fixed number of times and allowed to settle under its own weight (A. M. Faqih, Chaudhuri, Muzzio, et al., 2006). In the procedure by Pingali and Kick (2013), the tapping of powder up to 1,000 taps with a tapping apparatus is required after a powder is filled into the cylinder; powder dilation is then calculated with a revised pixel-counting program that incorporates the tapped volume and not the $V_{Initial}$ of Equation 6.2.

6.7 Conclusions

The flowability of powders under controlled and unconfined conditions was assessed by measurement and characterization of powder motion in a Gravitational Displacement Rheometer, GDR, which comprised a cylindrical drum of 192.5 mm internal diameter and 292.5 mm drum length. Avalanche activity of Geldart Group C lactose LP4, Group A sand S1, Group A

refractory dust RD1, Group A lactose LM1, Group A/B lactose LP1, and Group B glass beads B8 was measured at drum speeds in the range 5 RPM to 30 RPM, and plots of standard deviation, σ_{ws}, of the GDR load cell signal versus drum speed were used to represent avalanche activity. In investigating the influence of drum fill level, 20–50% on a volume basis, on avalanche activity, it was observed that σ_{ws} increased with increasing fill level for Geldart Groups C and B powders, and the opposite trend occurred with Group A powders. The σ_{ws} data at 50% fill level were different from the data at the other fill levels; further observation of the σ_{ws} profile at 50% fill level for each powder revealed that σ_{ws} consistently showed changes between 10 RPM and 15 RPM.

To explain and interpret σ_{ws}, information on d^*_{32}, span of particle size distribution, C_0 measured by shear testing, t_c/H_{mf} measured by fluidization and bed collapse, and powder bed profiles during tumbling in the GDR were taken into account. When the σ_{ws} profiles of sand S1 and refractory dust RD1, which had similar d^*_{32} and span, were compared, the σ_{ws} for sand S1 at 15–25 RPM was higher; C_0 was lower and t_c/H_{mf} was higher for S1. For lactose LM1, σ_{ws} was relatively low and constant, and the absence of a horizontal bed surface during tumbling was also observed, indicating lack of powder aeration; LM1 had a higher span and showed segregation when fluidized in a 80 mm inner diameter cylindrical fluid bed. The σ_{ws} values for lactose LP4, which was most cohesive among the test materials, were highest; the powder moved as agglomerates when tumbled. In contrast, the σ_{ws} for glass beads B8 was lower because the particles flowed freely when tumbled and they did not retain air; bed collapse was virtually instantaneous. Lactose LP1, which was an A/B powder, gave lower σ_{ws} values than the free flowing B8; this behaviour was thought to be related to higher content of fine particles and wider size distribution in LP1, and different avalanching mechanisms, notwithstanding the fact that the powders themselves were very different.

Parameter σ_{ws} and Flow Index, Equation 6.1, were correlated with $1/d^*_{32}$; the observed general trend was that both σ_{ws} and Flow Index increased with increasing $1/d^*_{32}$. Increasing drum speed increased the scatter in the $[1/d^*_{32}]$:σ_{ws} plot. Scatter of a similar trend was also observed in the plot of Flow Index against $1/d^*_{32}$. When the plot of σ_{ws} at 5 RPM against $1/d^*_{32}$ was compared with the plot of Flow Index against $1/d^*_{32}$, the former showed a straightforward and neat relationship; measurement of σ_{ws} at 5 RPM and 50% fill level could be a better indicator in the context of rapid powder flowability measurement and characterization.

Chapter 7 – Summary

Powders are complex three-phase systems formed by solid particles that can come in different sizes and shapes with air in the interparticle voids, and moisture that can be in the air, in the particles, and attached to the surface of the particles. Information and knowledge of powder compressibility, fluidization, flowability, and also connections between them are important and helpful to the handling and processing of powders across many industries in operations such as mixing, milling, packaging, and storage. A multi characterization approach involving shear testing, powder tapping, fluidization and bed collapse, and powder tumbling was used to assess samples of milled and spray-dried lactose powders, sand, refractory dust, and glass beads; emphasis was given to lactose powders, an important commodity in the food and pharmaceutical industries.

7.1 Characterization

The powders were first characterized by shear testing following Jenike (1964) and Berry et al. (2014) in an annular shear cell. Preconsolidation stress, σ_{pre}, was set between 0.31 kPa and 4.85 kPa and yield locus, powder flow function, C, δ_e, Φ_w, ρ_B, and B were measured. Jenike's arbitrary powder flow divisions, namely *free flowing* ($\sigma_c/\sigma_D>10$), *easy flowing* ($4<\sigma_c/\sigma_D<10$), *cohesive* ($2<\sigma_c/\sigma_D<4$), and *very cohesive* ($\sigma_c/\sigma_D<2$) were referred to for flowability characterization. It was observed that at and below σ_{pre}=1.2 kPa, milled lactose powders were either *very cohesive*, *cohesive*, *easy flowing*, or *free flowing*, and the powders were mainly *easy* and *free flowing* beyond σ_{pre}=1.2 kPa; stress ratio σ_c/σ_y at σ_{pre}=1.2 kPa was therefore selected to assess the flowability of milled lactose powders following Jenike's flow divisions. The samples of spray-dried lactose powders, sand, and refractory dust were generally *easy* and *free flowing* regardless of σ_{pre}.

7.2 Cohesion

The powder yield loci were apparently linear and followed the Coulomb Yield Criterion, and powder cohesion, C, was obtained by linear extrapolation of the yield loci. For *very cohesive* and *cohesive* milled lactose powders, a new correlation that related C to particle surface area per unit volume, $\rho_B/(\rho_p d^*_{32})$, and σ_{pre}, was proposed; the correlation was valid for milled lactose of d^*_{32} in the range of ~29–58 μm, and the correlation error was about ±29%. For *easy flowing* and *free flowing* milled and spray-dried lactose powders, sand, and refractory dust, the C data were consistently below 0.2 kPa and scattered.

7.3 Bulk density

The bulk density, ρ_B, of powders preconsolidated at 0.31–4.85 kPa in the shear cell was modelled as a function of σ_{pre} with five correlations chosen from the literature; each correlation contained two fitting parameters, and all the correlations fitted the ρ_B data well. For milled lactose powders, a new correlation, which incorporated d^*_{32} and estimated ρ_B to within ±10% of the measured ρ_B when d^*_{32} was ~29–223 μm, was proposed; however the correlation was not applicable to unconsolidated powders. When this new correlation and the new correlation for C mentioned in Section 7.2 were simultaneously used for the estimation of C, estimates of C were within –30% and +24% of the measured values.

7.4 Flowability

The utility of hopper outlet diameter, B, which was previously not substantiated with experimental data as a measure of powder flowability according to Jenike's criteria, was evaluated with milled lactose powders. To facilitate the calculation of B, a new correlation that related ρ_B to σ_c and d^*_{32} was first derived; the equation estimated ρ_B to ±8% of the measured ρ_B and was used to estimate $\rho_{B,crit}$ at σ_{crit}. Subsequently, a straightforward connection between B and σ_c/σ_y at σ_{pre}=1.2 kPa, was demonstrated. The following are the tentative B values in mm and their corresponding Jenike's arbitrary flow divisions: *free flowing* (B<30), *easy flowing* (30<B<80), *cohesive* (80<B<190), and *very cohesive* (B>190); the B values were specific to milled lactose of d^*_{32} in the range of ~29–223 μm and stored in hoppers with smooth bottom surface made of 304 stainless steel with 2B finish, and θ_p from 12–25°.

7.5 Compressibility

Powder tapping for compressibility and flowability evaluation, which involved measurements of loose poured and tapped densities, was done following Niro (1978) and the European Pharmacopoeia (Schüssele & Bauer-Brandl, 2003). Tapped density, ρ_{tap}, was modelled with two correlations chosen from the literature; each of the correlation contained two fitting parameters. Both correlations fitted ρ_{tap} well and estimated loose poured bulk density, $\rho_{0,mNZS3111}$, to within ±3% of the measured values. It was also demonstrated that one of the correlations could be reduced to one fitting parameter, a_t, which was equivalent to $[1–(1/H_{R,1250})]$; $H_{R,1250}$ is Hausner ratio at 1,250 taps and a linear function of $1/d^*_{32}$ for milled and spray-dried lactose powders, sand, and refractory dust.

The relationships between C and σ_c/σ_y measured by shear testing and $H_{R,1250}$ by powder tapping were explored. The motivation was that when shear testing facilities were not accessible, $H_{R,1250}$ could provide quick assessments of powder flowability at σ_{pre} below 5 kPa; tapping devices are also cheaper than shear cells, and measurements of bulk densities are more straightforward. A correlation that related C to σ_{pre} and $H_{R,1250}$, and one that correlated σ_c/σ_y with

σ_{pre} and $H_{R,1250}$ were presented; however both correlations generally underestimated or overestimated C and σ_c/σ_y. The utility of $H_{R,1250}$ as a powder flowability index was therefore limited.

7.6 Fluidization

For fluidization and bed collapse experiments under ambient conditions, an in-house fluidized bed equipped with a pressure transducer for measurements of bed pressure drop and pressure fluctuations, a hot-wire anemometer for measurement of superficial gas velocity, and a double-drainage system for bed collapse experiments were specifically designed and built. The custom built hot-wire anemometer was highly sensitive to small changes in superficial gas velocity in both increasing and decreasing gas flow orders. Superficial velocities U_{mf}, $U_{mb,v}$, $U_{mb,\sigma}$, and U_{bv} were measured and the powders were classified into Groups A, A/B, and B according to Geldart Fluidization Diagram (Geldart, 1973) and based on $U_{mb,v}/U_{mf}$. Three internal states of powder beds were observed visually during fluidization; correlations between the internal states and the values of U_{mf}, $U_{mb,v}$, U_{bv}, and also pressure fluctuations data gave the following: packed bed state, $U<U_{mb,v}$, transitional state, $U_{mb,v}\leq U<U_{bv}$, and fully bubbling state, $U_{bv}\leq U$. When two statistical tools, namely standard deviation, σ, and the inverse of von Neumann ratio, T^{-1}, were applied in the manipulation of pressure fluctuations data, correlated with U_{mf}, $U_{mb,v}$, $U_{mb,\sigma}$, and U_{bv}, and subsequently compared, T^{-1} unequivocally peaked at or close to $U_{mb,v}$. It was demonstrated that T^{-1} was a useful indicator for identifying the onset of bubbling in fluidized beds.

Bed collapse was used as a method to assess the fluidization quality of powders from Geldart Groups A, A/B, and B. Standardized collapse time, t_c/H_{mf}, which gave a measure of a powder's ability to retain air, was determined and correlated with d^*_{32} and C_0, the cohesion at zero σ_{pre} obtained by shear testing. Parameter t_c/H_{mf} for milled lactose powders showed a trend different from those of spray-dried lactose powders, sand, and refractory dust; the exact reason for this observation was unknown but was attributed to the combined influence of particle size distribution, fines content, bed voidage, and particle density.

7.7 Tumbling

To assess the flowability of powders under controlled and unconfined conditions, powder tumbling in a novel Gravitational Displacement Rheometer, GDR, was carried out. Powder motion of Geldart Group C lactose, Group A sand, Group A refractory dust, Group A lactose, Group A/B lactose, and Group B glass beads was measured at drum speeds in the range 5 RPM to 30 RPM, and plots of standard deviation, σ_{ws}, of the GDR load cell signal against drum speed were used to represent powder avalanche activity. It was observed that σ_{ws} increased with increasing drum fill level, 20–50% on a volume basis, for Geldart Groups C and B powders, and the opposite trend occurred with Group A powders. Further observation of the σ_{ws} profile at 50%

fill level for each powder, which was different from the σ_{ws} data at other fill levels, revealed that σ_{ws} consistently showed changes between 10 RPM and 15 RPM.

In explaining and interpreting σ_{ws}, information on d^*_{32}, span of particle size distribution, C_0 measured by shear testing, t_c/H_{mf} measured by fluidization and bed collapse, and powder bed profiles during tumbling in the GDR were simultaneously taken into account and considered. In comparing the σ_{ws} profiles of sand and refractory dust, both Group A powders, which had similar d^*_{32} and span, the σ_{ws} for sand at 15–25 RPM was higher; this was attributed to lower C_0 and higher t_c/H_{mf} for sand. As for the Group A lactose, σ_{ws} was lower and relatively constant; observation of the bed profile during tumbling showed the absence of a horizontal bed surface, suggesting the lack of powder aeration. The Group A lactose also had a higher span and showed segregation when fluidized in the in-house fluidized bed. The σ_{ws} values for the most cohesive Group C lactose were highest; observation of the powder motion during tumbling showed that the powder moved as agglomerates. On the other hand, the σ_{ws} for the free flowing glass beads was lower; this material did not retain air and bed collapse was virtually instantaneous. The Geldart A/B lactose powder gave lower σ_{ws} values than the free flowing glass beads; this was thought to be influenced by higher level of fine particles and wider particle size distribution in the Group A/B lactose, and different avalanching mechanisms, as well as the fact that the two powders were very different.

Parameter σ_{ws} and Flow Index were correlated with $1/d^*_{32}$, a parameter that influenced powder cohesion, C, measured by shear testing, Hausner ratio at 1,250 taps, $H_{R,1250}$, and standardized bed collapse time, t_c/H_{mf}. Both σ_{ws} and Flow Index generally increased with increasing $1/d^*_{32}$, and the increase in drum speed increased the scatter in the $[1/d^*_{32}]$:σ_{ws} and $[1/d^*_{32}]$:[Flow Index] plots. It was further proposed that σ_{ws} at 5 RPM and 50% fill level could be a better indicator for rapid powder flowability measurement and characterization; this was because in comparing the $[1/d^*_{32}]$:[σ_{ws} at 5 RPM] and $[1/d^*_{32}]$:[Flow Index] plots, the $[1/d^*_{32}]$:[σ_{ws} at 5 RPM] plot showed a more straightforward and neat relationship.

References

Abdullah, E. C., & Geldart, D. (1999). The use of bulk density measurements as flowability indicators. *Powder Technology, 102*(2), 151-165.

Abrahamsen, A. R., & Geldart, D. (1980a). Behavior of gas-fluidized beds of fine powders part I. Homogeneous expansion. *Powder Technology, 26*(1), 35-46.

Abrahamsen, A. R., & Geldart, D. (1980b). Behavior of gas-fluidized beds of fine powders part II. Voidage of the dense phase in bubbling beds. *Powder Technology, 26*(1), 47-55.

Alexander, A. W., Chaudhuri, B., Faqih, A., Muzzio, F. J., Davies, C., & Tomassone, M. S. (2006). Avalanching flow of cohesive powders. *Powder Technology, 164*(1), 13-21.

Ashton, M. D., Cheng, D. C.-H., Farley, R., & Valentin, F. H. H. (1965). Some investigations into the strength and flow properties of powders. *Rheologica Acta, 4*(3), 206-218.

Baeyens, J., & Geldart, D. (1974). An investigation into slugging fluidized beds. *Chemical Engineering Science, 29*(1), 255-265.

Berry, R. J., & Bradley, M. S. A. (2007). Investigation of the effect of test procedure factors on the failure loci and derived failure functions obtained from annular shear cells. *Powder Technology, 174*, 60-63.

Berry, R. J., Bradley, M. S. A., & McGregor, R. G. (2014). Brookfield powder flow tester - Results of round robin tests with CRM-116 limestone powder. *Proceedings of the Institution of Mechanical Engineers, Part E: Journal of Process Mechanical Engineering, 0*(0), 1-16.

Billings, S. W., Bronlund, J. E., & Paterson, A. H. J. (2006). Effects of capillary condensation on the caking of bulk sucrose. *Journal of Food Engineering, 77*(4), 887-895.

Bronlund, J., & Paterson, T. (2004). Moisture sorption isotherms for crystalline, amorphous and predominantly crystalline lactose powders. *International Dairy Journal, 14*, 247-254.

Bruni, G., Lettieri, P., Newton, D., & Barletta, D. (2007). An investigation of the effect of the interparticle forces on the fluidization behaviour of fine powders linked with rheological studies. *Chemical Engineering Science, 62*, 387-396.

Carr, J. F., & Walker, D. M. (1968). An annular shear cell for granular materials. *Powder Technology, 1*(6), 369-373.

Carson, J. W., & Wilms, H. (2006). Development of an international standard for shear testing. *Powder Technology, 167*(1), 1-9.

Castellanos, A., Valverde, J. M., & Quintanilla, M. A. S. (2002). Fine cohesive powders in rotating drums: Transition from rigid plastic flow to gas-fluidized regime. *Physical Review E, 65*, 061301.

Chaouki, J., Chavarie, C., & Klvana, D. (1985). Effect of interparticle forces on the hydrodynamic behaviour of fluidized aerogels. *Powder Technology, 43*, 117-125.

Cherntongchai, P., & Brandani, S. (2005). A model for the interpretation of the bed collapse experiment. *Powder Technology, 151*(1-3), 37-43.

Choi, H., Lee, W., Kim, D.-U., Kumar, S., Ha, J., Kim, S., et al. (2009). A comparative study of particle size analysis in fine powder: the effect of a polycomponent particulate system. *Korean Journal of Chemical Engineering, 26*(1), 300-305.

Coulson, J. M., Richardson, J. F., Backhurst, J. R., & Harker, J. H. (2002). *Coulson and Richardson's Chemical Engineering Volume 2, Particle Technology and Seperation Processes* (5th ed.). Oxford: Butterworth Heinemann.

Davies, C. E., Carroll, A., & Flemmer, R. (2008). Particle size monitoring in a fluidized bed using pressure fluctuations. *Powder Technology, 180*(3), 307-311.

Davies, C. E., Jones, J. R., Hussein, K., Fievez, S., & Tallon, S. J. (2006). Flow mode characterization in a one metre diameter rotating drum. *Developments in Chemical Engineering and Mineral Processing, 14*(1/2), 135-141.

Davies, C. E., Krouse, D., & Carroll, A. (2007, 13-17 May). *Particle size estimation and monitoring in a bubbling fluidized bed using pressure fluctuation measurements.* Paper presented at the 12th International Conference on Fluidization - New Horizons in Fluidization Engineering, Vancouver, Canada.

Davies, C. E., Krouse, D., & Carroll, A. (2010). A new approach to the identification of transitions in fluidized beds. *Powder Technology, 199*(1), 107-110.

Davies, C. E., Tallon, S. J., Fenton, K., Brown, N., & Peterson, M. (2002, 21-25 July). *Direct sensing of the motion of solids in slowly rotating cylinders.* Paper presented at the World Congress on Particle Technology 4, Sydney, Australia.

Davies, C. E., Williams, A., Tallon, S. J., Fenton, K., & Brown, N. (2004). A new approach to monitoring the movement of particulate material in rotating drums. *Developments in Chemical Engineering and Mineral Processing, 12*(3-4), 263-275.

Dry, R. J., Judd, M. R., & Shingles, T. (1983). Two-phase theory and fine powders. *Powder Technology, 34*(2), 213-223.

Faqih, A. M., Chaudhuri, B., Alexander, A. W., Davies, C., Muzzio, F. J., & Tomassone, M. S. (2006). An experimental/computational approach for examining unconfined cohesive powder flow. *International Journal of Pharmaceutics, 324*(2), 116-127.

Faqih, A. M., Chaudhuri, B., Muzzio, F. J., Tomassone, M. S., Alexander, A., & Hammond, S. (2006). Flow-induced dilation of cohesive granular materials. *AIChE Journal, 52*(12), 4124-4132.

Faqih, A. N., Alexander, A. W., Muzzio, F. J., & Tomassone, M. S. (2007). A method for predicting hopper flow characteristics of pharmaceutical powders. *Chemical Engineering Science, 62*(5), 1536-1542.

Fitzpatrick, J. J., Barringer, S. A., & Iqbal, T. (2004). Flow property measurement of food powders and sensitivity of Jenike's hopper design methodology to the measured values. *Journal of Food Engineering, 61*, 399-405.

Fu, X., Huck, D., Makein, L., Armstrong, B., Willen, U., & Freeman, T. (2012). Effect of particle shape and size on flow properties of lactose powders. *Particuology, 10*(2), 203-208.

Geldart, D. (1972). Effect of particle size and size distribution on behavior of gas-fluidized beds. *Powder Technology, 6*(4), 201-215.

Geldart, D. (1973). Types of gas fluidization. *Powder Technology, 7*(5), 285-292.

Geldart, D. (1990). Estimation of basic particle properties for use in fluid particle process calculations. *Powder Technology, 60*(1), 1-13.

Geldart, D., Abdullah, E. C., Hassanpour, A., Nwoke, L. C., & Wouters, I. (2006). Characterization of powder flowability using measurement of angle of repose. *China Particuology, 4*(3-4), 104-107.

Geldart, D., Harnby, N., & Wong, A. C. (1984). Fluidization of cohesive powders. *Powder Technology, 37*, 25-37.

Geldart, D., & Wong, A. C. Y. (1984). Fluidization of powders showing degrees of cohesiveness–I. Bed expansion. *Chemical Engineering Science, 39*(10), 1481-1488.

Geldart, D., & Wong, A. C. Y. (1985). Fluidization of powders showing degrees of cohesiveness–II. Experiments on rates of de-aeration. *Chemical Engineering Science, 40*(4), 653-661.

Grace, J. R. (1992). Agricola aground: Characterization and interpretation of fluidization phenomena. *AIChE Symposium Series 289, 88*, 1-16.

Grey, R. O., & Beddow, J. K. (1969). On the Hausner ratio and its relationship to some properties of metal powders. *Powder Technology, 2*(6), 323-326.

Gu, Z. H., Arnold, P. C., & McLean, A. G. (1992). Consolidation-related bulk density and permeability models for bulk solids. *Powder Technology, 72*, 39-44.

Hausner, H. H. (1967). Friction conditions in a mass of metal powder. *International Journal of Powder Metallurgy, 3*, 3-17.

Hayes, G. D. (1987). *Food Engineering Data Handbook*. New York: John Wiley & Sons.

Henein, H., Brimacombe, J. K., & Watkinson, A. P. (1983). Experimental study of transverse bed motion in rotary kilns. *Metallurgical Transactions B, 14B*, 191-205.

Huang, Q., Zhang, H., & Zhu, J. (2009). Experimental study on fluidization of fine powders in rotating drums with various wall friction and baffled rotating drums. *Chemical Engineering Science, 64*(9), 2234-2244.

Huang, Q., Zhang, H., & Zhu, J. (2010). Onset of an innovative gasless fluidized bed - comparative study on the fluidization of fine powders in a rotating drum and a traditional fluidized bed. *Chemical Engineering Science, 65*, 1261-1273.

Ilić, I., Kása Jr., P., Dreu, R., Pintye-Hódi, K., & Srčič, S. (2009). The compressibility and compactibility of different types of lactose. *Drug Development and Industrial Pharmacy, 35*(10), 1271-1280.

Iyer, S. R., & Drzal, L. T. (1989). Behavior of cohesive powders in narrow-diameter fluidized beds. *Powder Technology, 57*, 127-133.

Jenike, A. W. (1964). Storage and flow of solids. *Bulletin No. 123 of the Utah Engineering Experimental Station, 53*(26).

Jenike, A. W. (1975). A measure of flowability for powders and other bulk solids. *Powder Technology, 11*(1), 89-90.

Kawakita, K., & Lüdde, K.-H. (1971). Some considerations on powder compression equations. *Powder Technology, 4*(2), 61-68.

Kaye, B. H. (1997). Characterizing the flowability of a powder using the concepts of fractal geometry and chaos theory. *Particle & Particle Systems Characterization, 14*(2), 53-66.

Kaye, B. H., Gratton-Liimatainen, J., & Faddis, N. (1995). Studying the avalanching behaviour of a powder in a rotating disc. *Particle & Particle Systems Characterization, 12*(5), 232-236.

Khoe, G. K., Ip, T. L., & Grace, J. R. (1991). Rheological and fluidization behavior of powders of different particle size distribution. *Powder Technology, 66*(2), 127-141.

Kunii, D., & Levenspiel, O. (1991). *Fluidization Engineering*. Stoneham: Butterworth-Heinemann.

Kurz, H. P., & Münz, G. (1975). The influence of particle size distribution on the flow properties of limestone powders. *Powder Technology, 11*(1), 37-40.

Lavoie, F., Cartilier, L., & Thibert, R. (2002). New methods characterizing avalanche behavior to determine powder flow. *Pharmaceutical Research, 19*(6), 887-893.

Lee, Y. S. L., Poynter, R., Pedczeck, F., & Newton, J. M. (2000). Development of a dual approach to assess powder flow from avalanching behavior. *AAPS PharmSciTech, 1*(3), Article 21.

Lindberg, N.-O., Pålsson, M., Pihl, A.-C., Freeman, R., Freeman, T., Zetzener, H., et al. (2004). Flowability measurements of pharmaceutical powder mixtures with poor flow using five different techniques. *Drug Development and Industrial Pharmacy, 30*(7), 785-791.

Lorences, M. J., Patience, G. S., Diez, F. V., & Coca, J. (2003). Fines effects on collapsing fluidized beds. *Powder Technology, 131*(2-3), 234-240.

Malave, J., Barbosa-Canovas, G. V., & Peleg, M. (1985). Comparison of the compaction characteristics of selected food powders by vibration, tapping and mechanical compression. *Journal of Food Science, 50*, 1473-1476.

McCabe, W. L., Smith, J. C., & Harriott, P. (2005). *Unit Operations of Chemical Engineering* (7th ed.). New York: McGraw-Hill.

McGlinchey, D. (2005). Bulk property characterization. In D. McGlinchey (Ed.), *Characterisation of Bulk Solids* (pp. 48-84). Oxford: Blackwell Publishing.

Mellmann, J. (2001). The transverse motion of solids in rotating cylinders - forms of motion and transition behavior. *Powder Technology, 118*(3), 251-270.

Molerus, O. (1975). Theory of yield of cohesive powders. *Powder Technology, 12*(3), 259-275.

Molerus, O. (1978). Effect of interparticle cohesive forces on the flow behaviour of powders. *Powder Technology, 20*(2), 161-175.

Molerus, O. (1993). *Principles of Flow in Disperse Systems*. London: Chapman and Hall.

Nedderman, R. M. (1992). *Statics and Kinematics of Granular Materials*. Cambridge: Cambridge University Press.

Niro (1978). Analytical methods for dry milk products, *Method No. A2a - Packed bulk density by the Niro method for milk powders and protein products* (pp. 2.3.1-2.3.4). Copenhagen, Denmark: A/S Niro Atomizer.

Niro, G. (2012). Particle density, occluded air and interstitial air by air pycnometer. Retrieved 3 October, 2012, from http://www.niro.com/niro/cmsdoc.nsf/WebDoc/webb7ceec8

Orband, J. L. R., & Geldart, D. (1997). Direct measurement of powder cohesion using a torsional device. *Powder Technology, 92*(1), 25-33.

Park, J. J., Park, J. H., Chang, I. S., Kim, S. D., & Choi, C. S. (1991). A new bed-collapsing technique for measuring the dense phase properties of gas-fluidized beds. *Powder Technology, 66*(3), 249-257.

Peleg, M. (1978). Flowability of food powders and methods for its evaluation - a review. *Journal of Food Process and Engineering, 1*, 303-328.

Peleg, M., & Mannheim, C. H. (1973). Effect of conditioners on the flow properties of powdered sucrose. *Powder Technology, 7*(1), 45-50.

Peleg, M., Mannheim, C. H., & Passy, N. (1973). Flow properties of some food powders. *Journal of Food Science, 38*(6), 959-964.

Pingali, K., & Kick, C. (2013). *Gravitational Displacement Rheometer: Operator's Guide*: Western Michigan University.

Punčochář, M., Drahoš, J., Čermák, J., & Selucký, K. (1985). Evaluation of minimum fluidizing velocity in gas fluidized bed from pressure fluctuations. *Chemical Engineering Communications, 35*(1), 81-87.

Rhodes, M. J. (1998). *Introduction to particle technology*. West Sussex: John Wiley & Sons Ltd.

Richardson, J. F. (1971). Incipient fluidization and particulate systems. In J. F. Davidson & D. Harrison (Eds.), *Fluidization* (pp. 26-64). London: Academic Press Inc.

Rietema, K. (1967). Application of mechanical stress theory to fluidization. In A. A. H. Drinkenberg (Ed.), *International Symposium on Fluidization* (pp. 154-175). Amsterdam, Netherlands: Netherlands University Press.

Rietema, K. (1984). Powders, what are they? *Powder Technology, 37*, 5-23.

Santomaso, A., Lazzaro, P., & Canu, P. (2003). Powder flowability and density ratios: the impact of granules packing. *Chemical Engineering Science, 58*(13), 2857-2874.

SANZ (1986). NZS 3111:1986 - Methods of test for water and aggregate for concrete, *Method for determining voids content, flow time and percentage oversize material in sand* (pp. 44-45). Wellington, New Zealand: Standards Association of New Zealand.

Schulze, D. (2008). *Powders and Bulk Solids: Behaviour, Characterization, Storage and Flow*. Berlin: Springer.

Schüssele, A., & Bauer-Brandl, A. (2003). Note on the measurement of flowability according to the European Pharmacopoeia. *International Journal of Pharmaceutics, 257*(1-2), 301-304.

Schwedes, J. (2003). Review on testers for measuring flow properties of bulk solids. *Granular Matter, 5*(1), 1-43.

Shaffer, K., Paterson, A. H. J., Davies, C. E., & Hebbink, G. (2011). Stokes shape factor for lactose crystals. *Advanced Powder Technology, 22*(4), 454-457.

Šmíd, J., Xuan, P. V., & Thýn, J. (1993). Effect of filling method on the packing distribution of a catalyst bed. *Chemical Engineering and Technology, 16*(2), 114-118.

Soh, J. L. P., Liew, C. V., & Heng, P. W. S. (2006). New indices to characterize powder flow bases on their avalanching behavior. *Pharmaceutical Development and Technology, 11*(1), 93-102.

Stanley-Wood, N., Sarrafi, M., Mavere, Z., & Schaefer, M. (1993). The relationships between powder flowability, particle re-arrangement, bulk density and Jenike failure function. *Advanced Powder Technology, 4*(1), 33-40.

Teunou, E., Fitzpatrick, J. J., & Synnott, E. C. (1999). Characterisation of food powder flowability. *Journal of Food Engineering, 39*(1), 31-37.

TSI (2005). *Model 3250 Aero-Flow Automated Powder Flowability Analyzer.* Retrieved 27 July, 2010, from www.kenelec.com.au/pdf/aeroflow.pdf

Tung, Y., & Kwauk, M. (1982). Dynamics of collapsing fluidized beds. In M. Kwauk & D. Kunii (Eds.), *Fluidization Science and Technology* (pp. 155-166). Beijing: Science Press.

USP-NF (2012). The United States Pharmacopeia and The National Formulary, *<616> Bulk and Tapped Density* (pp. 1-3). United States: The United States Pharmacopeial Convention.

Valverde, J. M., Ramos, A., Castellanos, A., & Watson, P. K. (1998). The tensile strength of cohesive powders and its relationship to consolidation, free volume and cohesivity. *Powder Technology, 97*(3), 237-245.

Vasilenko, A., Glasser, B. J., & Muzzio, F. J. (2011). Shear and flow behaviour of pharmaceutical blends - Method comparison study. *Powder Technology, 208*, 628-636.

Vasilenko, A., Koynov, S., Glasser, B. J., & Muzzio, F. J. (2013). Role of consolidation state in the measurement of bulk density and cohesion. *Powder Technology, 239*, 366-373.

Wang, Z., Kwauk, M., & Li, H. (1998). Fluidization of fine particles. *Chemical Engineering Science, 53*(3), 377-395.

Webster, E. S., & Davies, C. E. (2006, 17-20 September). *Behaviour of powders from different Geldart groups in a rotating drum.* Paper presented at the 34th Australasian Chemical Engineering Conference (Chemeca), Auckland, New Zealand.

Webster, E. S., & Davies, C. E. (2010, 16-21 May). *Geldart group indication from powder measurements with a rotating drum instrument.* Paper presented at the 13th International Conference on Fluidization - New Paradigm in Fluidization Engineering, Gyeong-ju, Korea.

Wilkinson, D. (1995). Determination of minimum fluidization velocity by pressure fluctuation measurement. *The Canadian Journal of Chemical Engineering, 73*(4), 562-565.

Xie, H. Y. (1997). Pressure probes in the measurement of collapse rate and dense-phase properties in the fluidization of fine particles. *Advanced Powder Technology, 8*(3), 237-250.

Yamashiro, M., Yuasa, Y., & Kawakita, K. (1983). An experimental study on the relationships between compressibility, fluidity and cohesion of powder solids at small tapping numbers. *Powder Technology, 34*(2), 225-231.

Yu, A. B., & Hall, J. S. (1994). Packing of fine powders subjected to tapping. *Powder Technology, 78*, 247-256.

Appendix 1.1

Refereed Journal Papers	2
Refereed Conference Papers	10
Non-refereed Abstracts	5
Invited Talk	1
Research and Scientific Talks	11

Last update: 22 February 2016

Refereed journal papers:

1) **Saw, H. Y.**, Davies, C. E., Jones, J. R., Brisson, G., & Paterson, A. H. J. (2013). Cohesion of lactose powders at low consolidation stresses. *Advanced Powder Technology, 24*(4), 796-800.
http://www.sciencedirect.com/science/article/pii/S0921883113001222

2) **Saw, H. Y.**, Davies, C. E., Jones, J. R., & Paterson, A. H. J. (2014). Shear testing of lactose powders: The influence of consolidation stress and particle size on bulk density and estimated cohesion. *Advanced Powder Technology, 25*(4), 1164-1170.
http://www.sciencedirect.com/science/article/pii/S0921883114001460

Refereed conference papers:

1) **Saw, H. Y.**, Davies, C. E., Paterson, A. H. J., & Brisson, G. (2011). Flow indices for fine food powders. *Papers of SCENZ-IChemE in New Zealand Annual Conference,* Hamilton, New Zealand.
http://www.icheme.org/communities/countries/new_zealand/events/2011/annual%20conference%20-%20dec%202011.aspx#.VL9sGRzbWP0

2) **Saw, H. Y.**, Davies, C. E., & Paterson, A. H. J. (2012). Tracking the transitions in gas-fluidized beds with measurements of pressure fluctuations. *Proceedings of 5th Asian Particle Technology Symposium,* Singapore.
http://rpsonline.com.sg/proceedings/9789810725181/html/281.xml

3) **Saw, H. Y.**, Davies, C. E., Brisson, G., Paterson, A. H. J., & Jones, J.R. (2012). Characterization of lactose powders at low consolidation stresses. *Proceedings of CHEMECA 2012 Conference,* Wellington, New Zealand.
http://search.informit.com.au/documentSummary;res=IELENG;dn=865528389653997

Appendix 1.1

4) **Saw, H. Y.**, Davies, C. E., Paterson, A. H. J., & Jones, J. R. (2013). Gas-fluidization and flow properties of fine lactose and mineral powders. *Proceedings of 14th International Conference on Fluidization – From Fundamentals to Products*, The Netherlands. http://dc.engconfintl.org/fluidization_xiv/40/

5) **Saw, H. Y.**, Davies, C. E., Brisson, G., Paterson, A. H. J., & Jones, J. R. (2013). Bulk density of lactose powders under low consolidation stresses. *Proceedings of CHEMECA 2013 Conference,* Brisbane, Australia. http://search.informit.com.au/documentSummary;dn=880913537723136;res=IELENG

6) **Saw, H. Y.**, Davies, C. E., Paterson, A. H. J., & Jones, J. R. (2013). The influence of particle size distribution and tapping on the bulk density of milled lactose powders. *Proceedings of CHEMECA 2013 Conference,* Brisbane, Australia. http://search.informit.com.au/documentSummary;res=IELENG;dn=881118500406976

7) **Saw, H. Y.**, Davies, C. E., Paterson, A. H. J., & Jones, J. R. (2014). Flowability of milled lactose powders. *Proceedings of CHEMECA 2014 Conference,* Perth, Western Australia. http://www.icheme.org/~/media/Documents/Conferences/CHEMECA/Chemeca%202014/full-papers/1349_Flowability%20of%20milled%20lactose%20powders-revised.pdf

8) **Saw, H. Y.**, Davies, C. E., Paterson, A. H. J., & Jones, J. R. (2015). Correlation between powder flow properties measured by shear testing and Hausner Ratio. *Procedia Engineering, 102*, 218-225 (*Proceedings of 7th World Congress on Particle Technology*, Beijing, China). http://www.sciencedirect.com/science/article/pii/S1877705815001332

9) **Saw, H. Y.**, Davies, C. E., & Paterson, A. H. J. (2015). Identification of bubbling onset using pressure fluctuations. *Procedia Engineering, 102*, 211-217 (*Proceedings of 7th World Congress on Particle Technology*, Beijing, China). http://www.sciencedirect.com/science/article/pii/S1877705815001319

10) **Saw, H. Y.**, & Davies, C. E. (2015). Characteristic behaviours and trends of powders from different Geldart Groups in a rotating drum. *Proceedings of Asia Pacific Confederation of Chemical Engineering Congress 2015: APCChE 2015, incorporating CHEMECA 2015,* Melbourne, Australia. http://search.informit.com.au/documentSummary;dn=731273719949387;res=IELENG

Appendix 1.1

Non-refereed abstracts

1) Davies, C. E., & **Saw H. Y.** (2012). Onset of bubbling in Geldart Group A powders. *Fundamentals of Fluidization III, Particle Technology Forum, AIChE 2012 Annual Meeting*, Pittsburgh, PA, USA.
http://www3.aiche.org/proceedings/Abstract.aspx?PaperID=283601

2) **Saw H. Y.**, Davies C. E., Brisson G., Paterson A. H. J., & Jones J. R. (2012). Relationships between particle properties of fine powders and flow properties under low compaction stresses. *Characterization and Measurement in Powder Processing, Particle Technology Forum, AIChE 2012 Annual Meeting*, Pittsburgh, PA, USA.
http://www3.aiche.org/proceedings/Abstract.aspx?PaperID=287835

3) Davies, C. E., **Saw H. Y.**, Jones, J. R., Brisson, G., & Paterson, A. H. J. (2013). Yield loci of lactose powders at low consolidation stresses: Measurement and modeling. *Characterization and Measurement in Powder Processing I, Particle Technology Forum, AIChE 2013 Annual Meeting*, San Francisco, CA, USA.
http://www3.aiche.org/proceedings/Abstract.aspx?ConfID=Annual-2013&GroupID=1779&SessionID=25189&PaperID=340638

4) **Saw, H. Y.**, & Davies, C. E. (2014). Avalanching, bed collapse and cohesion: Characteristic behavior of Geldart A, B and C Powders. *Fundamentals of Fluidization II, Particle Technology Forum, AIChE 2014 Annual Meeting*, Atlanta, GA, USA.
http://www3.aiche.org/proceedings/Abstract.aspx?ConfID=Annual-2014&GroupID=1884&SessionID=27170&PaperID=387785

5) Davies, C. E., & **Saw, H. Y.** (2015). Experimental measurement of minimum bubbling velocity. *Fundamentals of Fluidization III, Particle Technology Forum, AIChE 2015 Annual Meeting*, Salt Lake City, UT, USA.
http://www3.aiche.org/proceedings/Abstract.aspx?PaperID=433244

Invited Talk

1) **Saw, H. Y.** (2014). New solutions for processing food powders. *The Future of Food*, Student Showcase*, Grand Hall, Parliament House, Wellington, New Zealand, 19th February 2014.
**A public event hosted by Hon. Ian McKelvie, Member of Parliament of Rangitikei, in conjunction with Riddet Institute's 2014 Agri-Food Industry Summit*
http://webcast.massey.ac.nz/Mediasite/Play/d16e3d90af434cd6b5538661095b3f811d

Appendix 2.1

Table A2.1 BS 410 size apertures for the making of LP3 and LP2; 500 g of lactose monohydrate Pharmatose® 70M (LP1) were sieved at 20 W for 20 min (Procedure 1)

Powder code	LP3	LP2
Sieve apertures	−250 μm, +180 μm	−180 μm, +Pan

Table A2.2 BS 410 size apertures for the making of LM3 and LM8; 500 g of Hydrous Refined Lactose 100-mesh (LM1) were sieved at 20 W for 20 min (Procedure 1)

Powder code	LM3	LM8
Sieve apertures	−180 μm, +90 μm	−90 μm, +45 μm

Table A2.3 BS 410 size apertures for the making of LM6, LM2, and LM7; 500 g of Hydrous Refined Lactose 100-mesh (LM1) were sieved at 20 W for 20 min (Procedure 1)

Powder code	LM6	LM2	LM7
Sieve apertures	>150 μm	−150 μm, +75 μm	−75 μm, +Pan

Table A2.4 BS 410 size apertures for the making of LM5, LM4, and LM9; 50 g of Hydrous Refined Lactose 100-mesh (LM1) were sieved at 20 W for 5 min (Procedure 2)

Powder code	LM5	LM4	LM9
Sieve apertures	>180 μm	−180 μm, +125 μm	−106 μm, +Pan

Table A2.5 BS 410 size apertures for the making of LT1 and LT2; 500 g of spray-dried lactose SuperTab® were sieved at 20 W for 20 min (Procedure 1)

Powder code	LT2	LT1
Sieve apertures	−150 μm, +90 μm	−90 μm, +Pan

Table A2.6 BS 410 size apertures for the making of S2 and S3; 500 g of sand S1 were sieved at 20 W for 20 min (Procedure 1)

Powder code	S2	S3
Sieve apertures	−125 μm, +75 μm	−75 μm, +Pan

Table A2.7 BS 410 size apertures for the making of refractory dust RD1, RD2, and RD3; 500 g of refractory dust was sieved at 20 W for 20 min (Procedure 1)

Powder code	RD1	RD2	RD3
Sieve apertures	<150 μm	−150 μm, +53 μm	−53 μm, +Pan

Appendix 2.2

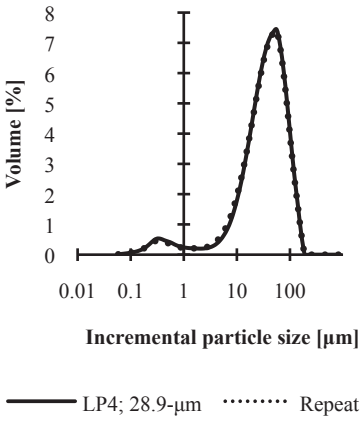

Figure A2.1 Plot of volume percentage versus incremental mean particle diameter for LP4

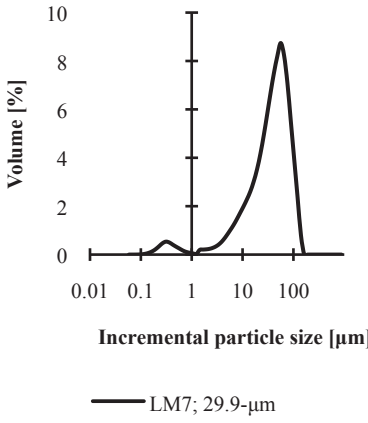

Figure A2.2 Plot of volume percentage versus incremental mean particle diameter for LM7

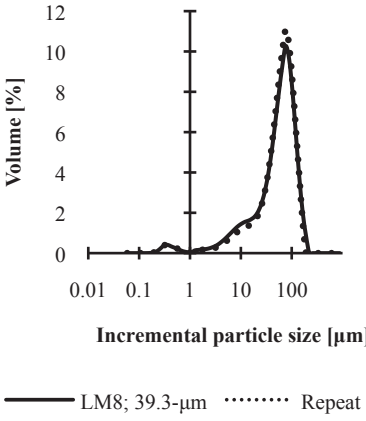

Figure A2.3 Plot of volume percentage versus incremental mean particle diameter for LM8

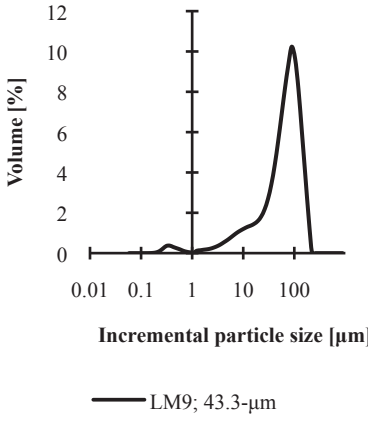

Figure A2.4 Plot of volume percentage versus incremental mean particle diameter for LM9

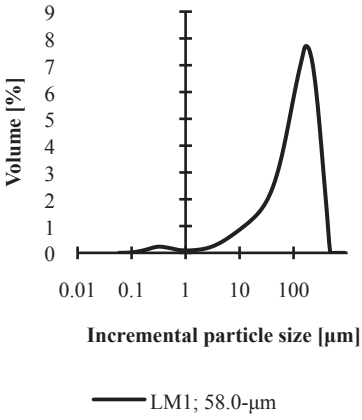

Figure A2.5 Plot of volume percentage versus incremental mean particle diameter for LM1

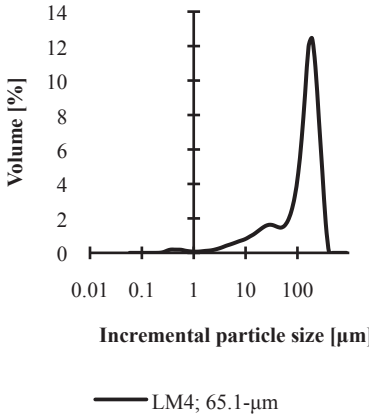

Figure A2.6 Plot of volume percentage versus incremental mean particle diameter for LM4

Appendix 2.2

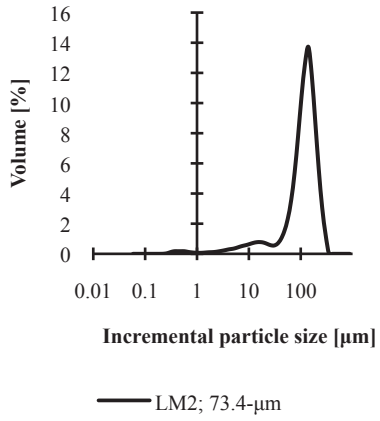

Figure A2.7 Plot of volume percentage versus incremental mean particle diameter for LM2

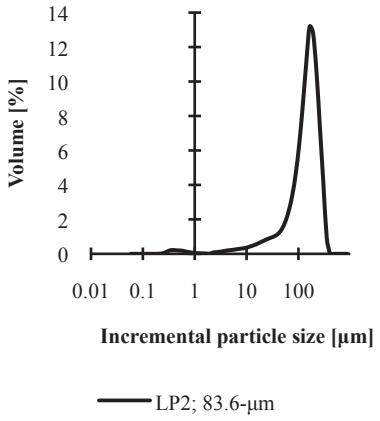

Figure A2.8 Plot of volume percentage versus incremental mean particle diameter for LP2

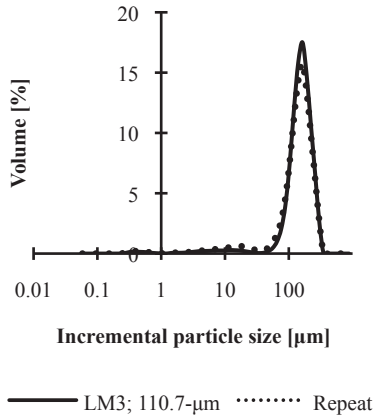

Figure A2.9 Plot of volume percentage versus incremental mean particle diameter for LM3

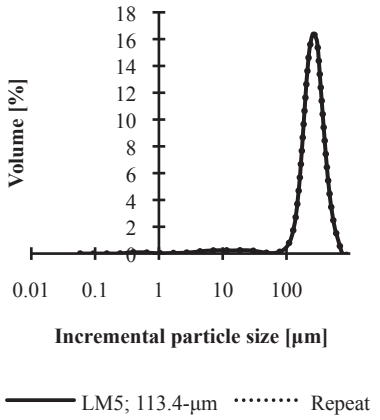

Figure A2.10 Plot of volume percentage versus incremental mean particle diameter for LM5

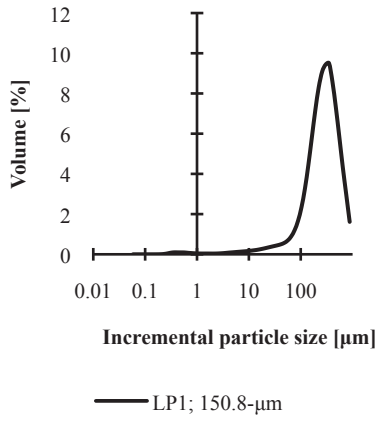

Figure A2.11 Plot of volume percentage versus incremental mean particle diameter for LP1

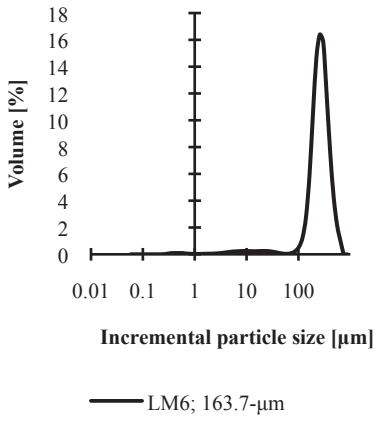

Figure A2.12 Plot of volume percentage versus incremental mean particle diameter for LM6

Appendix 2.2

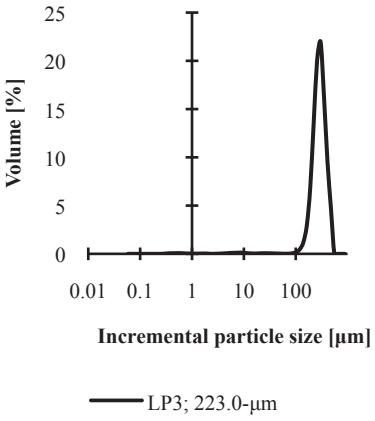

Figure A2.13 Plot of volume percentage versus incremental mean particle diameter for LP3

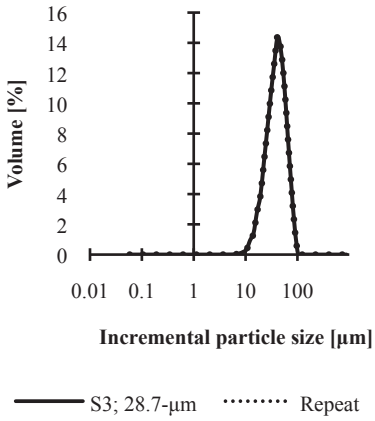

Figure A2.14 Plot of volume percentage versus incremental mean particle diameter for S3

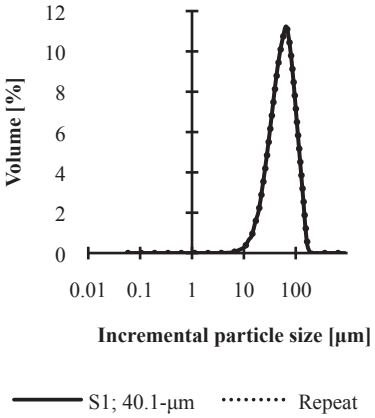

Figure A2.15 Plot of volume percentage versus incremental mean particle diameter for S1

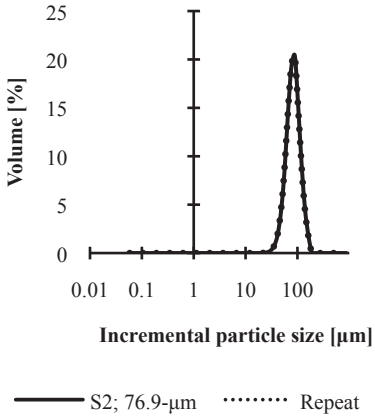

Figure A2.16 Plot of volume percentage versus incremental mean particle diameter for S2

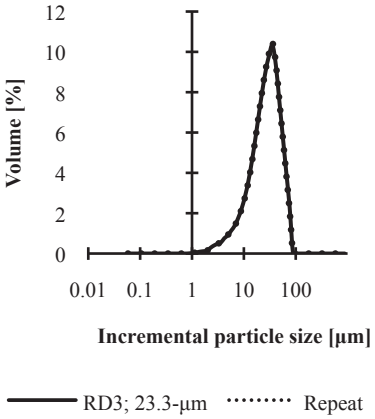

Figure A2.17 Plot of volume percentage versus incremental mean particle diameter for RD3

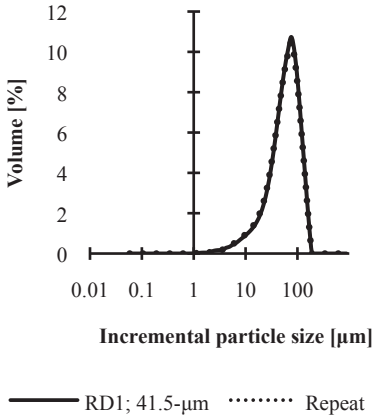

Figure A2.18 Plot of volume percentage versus incremental mean particle diameter for RD1

Appendix 2.2

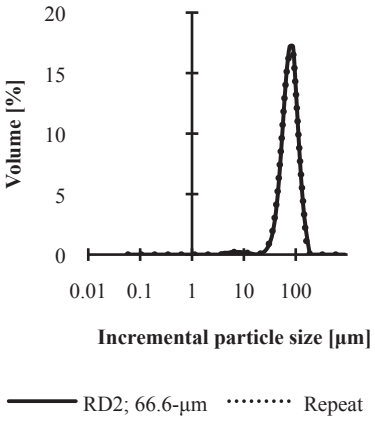

Figure A2.19 Plot of volume percentage versus incremental mean particle diameter for RD2

Appendix 3.1

Table A3.1 Yield data for milled lactose (LM) powders, spray-dried lactose (LT) powders, sand (S), and refractory dust (RD) measured at preconsolidation stresses of 0.31 kPa, 0.61 kPa, 1.20 kPa, 2.41 kPa, and 4.85 kPa with an annular shear cell

Powder	Preconsolidation stress, σ_{pre} [kPa]									
	0.31		0.61		1.20		2.41		4.85	
	Normal stress, σ [kPa]	Shear stress, τ [kPa]	Normal stress, σ [kPa]	Shear stress, τ [kPa]	Normal stress, σ [kPa]	Shear stress, τ [kPa]	Normal stress, σ [kPa]	Shear stress, τ [kPa]	Normal stress, σ [kPa]	Shear stress, τ [kPa]
LM1	0.309	0.264	0.604	0.48	1.202	0.935	2.406	1.858	4.843	3.674
	0.12	0.151	0.219	0.25	0.419	0.453	0.822	0.812	1.634	1.541
	0.215	0.208	0.413	0.373	0.811	0.693	1.615	1.333	3.239	2.591
	0.119	0.141	0.129	0.18	0.192	0.258	0.252	0.357	0.405	0.528
	0.311	0.253	0.607	0.476	1.204	0.929	2.41	1.829	4.846	3.652
LM1	0.308	0.263	0.606	0.482	1.203	0.916	2.407	1.855	4.844	3.699
(repeat)	0.12	0.154	0.219	0.259	0.419	0.438	0.822	0.797	1.634	1.498
	0.215	0.209	0.413	0.377	0.811	0.693	1.615	1.295	3.239	2.568
	0.119	0.152	0.141	0.195	0.186	0.253	0.226	0.309	0.332	0.441
	0.311	0.256	0.607	0.481	1.204	0.915	2.41	1.832	4.845	3.655
LM2	0.307	0.241	0.603	0.453	1.2	0.868	2.407	1.731	4.841	3.502
	0.119	0.128	0.218	0.215	0.417	0.389	0.82	0.715	1.631	1.284
	0.214	0.191	0.412	0.339	0.81	0.634	1.614	1.204	3.237	2.383
	0.118	0.125	0.12	0.147	0.141	0.168	0.18	0.225	0.153	0.196
	0.31	0.241	0.606	0.451	1.204	0.863	2.409	1.712	4.843	3.495
LM3	0.309	0.223	0.605	0.415	1.201	0.8	2.406	1.63	4.843	3.297
	0.119	0.104	0.217	0.184	0.417	0.323	0.818	0.605	1.631	1.173
	0.215	0.159	0.411	0.291	0.81	0.565	1.613	1.112	3.237	2.209
	0.119	0.107	0.119	0.123	0.121	0.122	0.121	0.114	0.121	0.112
	0.311	0.222	0.607	0.408	1.203	0.807	2.409	1.631	4.844	3.289
LM4	0.307	0.265	0.604	0.479	1.201	0.898	2.407	1.752	4.843	3.587
	0.121	0.156	0.219	0.241	0.419	0.429	0.822	0.761	1.633	1.355
	0.215	0.205	0.413	0.368	0.811	0.675	1.615	1.263	3.239	2.416
	0.12	0.153	0.122	0.167	0.182	0.239	0.239	0.306	0.194	0.254
	0.311	0.254	0.607	0.475	1.204	0.897	2.41	1.743	4.845	3.557
LM5	0.309	0.234	0.606	0.436	1.201	0.838	2.407	1.698	4.842	3.418
	0.122	0.12	0.22	0.191	0.419	0.342	0.821	0.628	1.632	1.189
	0.216	0.177	0.414	0.314	0.811	0.587	1.615	1.143	3.238	2.272
	0.121	0.114	0.123	0.125	0.124	0.124	0.126	0.137	0.127	0.144
	0.312	0.236	0.608	0.436	1.204	0.825	2.41	1.673	4.844	3.37
LM6	0.308	0.227	0.604	0.419	1.201	0.798	2.407	1.577	4.843	3.24
	0.12	0.112	0.219	0.183	0.417	0.31	0.82	0.599	1.631	1.088
	0.216	0.162	0.413	0.296	0.811	0.56	1.614	1.06	3.237	2.141
	0.12	0.108	0.121	0.115	0.123	0.126	0.123	0.12	0.123	0.119
	0.312	0.219	0.607	0.408	1.204	0.789	2.409	1.565	4.844	3.248
LM7	0.3	0.259	0.6	0.494	1.198	0.938	2.406	1.911	4.841	3.816
	0.114	0.173	0.213	0.289	0.414	0.51	0.817	0.857	1.63	1.7
	0.209	0.219	0.408	0.413	0.807	0.737	1.612	1.419	3.236	2.857
	0.127	0.162	0.181	0.256	0.273	0.4	0.295	0.487	0.574	0.752
	0.305	0.26	0.603	0.496	1.2	0.942	2.407	1.909	4.843	3.854
LM8	0.303	0.262	0.602	0.486	1.199	0.933	2.407	1.86	4.842	3.759
	0.115	0.164	0.215	0.27	0.415	0.488	0.819	0.843	1.631	1.555
	0.211	0.223	0.409	0.387	0.808	0.722	1.614	1.357	3.237	2.714
	0.115	0.157	0.155	0.217	0.245	0.348	0.294	0.442	0.401	0.559
	0.307	0.262	0.604	0.497	1.201	0.926	2.408	1.855	4.843	3.739
LM9	0.304	0.258	0.603	0.484	1.2	0.921	2.405	1.858	4.842	3.699
	0.116	0.167	0.215	0.262	0.416	0.485	0.819	0.828	1.631	1.589
	0.212	0.22	0.411	0.38	0.809	0.72	1.613	1.37	3.238	2.655
	0.121	0.155	0.144	0.207	0.25	0.351	0.28	0.415	0.461	0.604
	0.308	0.255	0.605	0.483	1.202	0.935	2.408	1.836	4.844	3.697
LM9	0.304	0.276	0.602	0.493	1.2	0.94	2.405	1.878	4.841	3.765
(repeat)	0.116	0.168	0.216	0.281	0.416	0.48	0.819	0.855	1.631	1.586
	0.212	0.231	0.41	0.405	0.809	0.724	1.613	1.38	3.237	2.721
	0.116	0.155	0.168	0.24	0.23	0.31	0.303	0.421	0.435	0.583
	0.307	0.266	0.604	0.492	1.202	0.944	2.408	1.87	4.843	3.764

LP1	0.311	0.223	0.608	0.42	1.204	0.813	2.41	1.584	4.845	3.354
	0.123	0.111	0.222	0.189	0.42	0.33	0.823	0.649	1.634	1.17
	0.218	0.162	0.415	0.296	0.813	0.586	1.618	1.117	3.241	2.187
	0.122	0.104	0.125	0.117	0.127	0.134	0.174	0.182	0.128	0.14
	0.314	0.218	0.61	0.422	1.207	0.818	2.412	1.589	4.847	3.315
LP1	0.31	0.226	0.607	0.429	1.204	0.82	2.408	1.631	4.844	3.344
(repeat)	0.123	0.117	0.221	0.198	0.421	0.348	0.822	0.655	1.634	1.208
	0.217	0.174	0.415	0.305	0.813	0.599	1.616	1.12	3.24	2.199
	0.122	0.114	0.124	0.13	0.127	0.137	0.151	0.163	0.129	0.145
	0.313	0.23	0.609	0.427	1.207	0.822	2.412	1.625	4.846	3.325
LP2	0.308	0.243	0.605	0.439	1.203	0.81	2.408	1.65	4.845	3.31
	0.121	0.133	0.22	0.209	0.419	0.366	0.822	0.662	1.633	1.223
	0.216	0.182	0.414	0.32	0.812	0.602	1.616	1.136	3.239	2.254
	0.12	0.121	0.122	0.139	0.143	0.158	0.15	0.185	0.161	0.179
	0.312	0.235	0.608	0.431	1.205	0.823	2.411	1.644	4.846	3.307
LP3	0.311	0.202	0.607	0.38	1.204	0.756	2.409	1.5	4.844	3.116
	0.121	0.083	0.219	0.15	0.418	0.271	0.82	0.538	1.632	1.055
	0.217	0.142	0.413	0.261	0.812	0.52	1.615	1.011	3.239	2.082
	0.121	0.086	0.121	0.088	0.122	0.092	0.122	0.088	0.122	0.09
	0.313	0.201	0.608	0.38	1.205	0.761	2.41	1.501	4.845	3.055
LP4	0.301	0.27	0.6	0.506	1.198	0.95	2.405	1.927	4.841	3.877
	0.114	0.186	0.213	0.318	0.414	0.58	0.818	0.986	1.63	1.749
	0.21	0.237	0.408	0.434	0.807	0.779	1.612	1.457	3.237	2.932
	0.143	0.198	0.218	0.325	0.372	0.55	0.454	0.718	0.615	0.915
	0.305	0.269	0.602	0.51	1.199	0.949	2.407	1.897	4.843	3.894
LP4	0.299	0.268	0.599	0.507	1.197	0.946	2.405	1.976	4.841	3.954
(repeat)	0.113	0.186	0.214	0.304	0.413	0.565	0.817	0.919	1.63	1.848
	0.209	0.232	0.408	0.404	0.807	0.784	1.611	1.457	3.236	2.988
	0.142	0.203	0.188	0.284	0.357	0.531	0.338	0.56	0.699	0.916
	0.303	0.264	0.602	0.497	1.2	0.954	2.407	1.951	4.842	3.915
LT1	0.307	0.214	0.603	0.404	1.2	0.781	2.405	1.564	4.84	3.165
	0.117	0.111	0.215	0.188	0.415	0.327	0.818	0.633	1.629	1.129
	0.213	0.156	0.41	0.295	0.808	0.57	1.612	1.1	3.235	2.104
	0.117	0.112	0.117	0.126	0.118	0.132	0.155	0.164	0.119	0.128
	0.309	0.208	0.604	0.399	1.201	0.785	2.407	1.577	4.842	3.18
LT2	0.305	0.194	0.603	0.362	1.199	0.703	2.405	1.416	4.839	2.909
	0.117	0.088	0.215	0.147	0.413	0.262	0.866	0.5	1.628	0.963
	0.213	0.135	0.409	0.259	0.807	0.498	1.611	0.952	3.234	1.946
	0.117	0.085	0.117	0.091	0.116	0.099	0.118	0.093	0.118	0.088
	0.309	0.174	0.604	0.362	1.2	0.703	2.406	1.421	4.84	2.912
S1	0.313	0.187	0.61	0.35	1.207	0.686	2.412	1.363	4.848	2.709
	0.123	0.105	0.222	0.17	0.421	0.286	0.823	0.516	1.636	0.986
	0.219	0.15	0.416	0.258	0.815	0.488	1.619	0.953	3.242	1.872
	0.123	0.102	0.124	0.107	0.125	0.126	0.126	0.118	0.132	0.105
	0.316	0.192	0.611	0.356	1.208	0.695	2.414	1.369	4.848	2.724
S2	0.313	0.179	0.61	0.33	1.205	0.646	2.411	1.268	4.846	2.519
	0.123	0.08	0.22	0.136	0.42	0.239	0.822	0.445	1.633	0.874
	0.218	0.132	0.415	0.238	0.813	0.439	1.617	0.867	3.239	1.709
	0.123	0.081	0.122	0.083	0.123	0.084	0.123	0.087	0.123	0.085
	0.314	0.185	0.61	0.332	1.206	0.65	2.411	1.269	4.846	2.526
S3	0.312	0.194	0.61	0.354	1.206	0.686	2.412	1.374	4.847	2.755
	0.122	0.11	0.222	0.17	0.42	0.291	0.823	0.529	1.636	0.972
	0.219	0.152	0.416	0.267	0.813	0.496	1.618	0.947	3.242	1.893
	0.122	0.109	0.123	0.126	0.124	0.136	0.124	0.112	0.126	0.102
	0.314	0.192	0.611	0.362	1.208	0.69	2.413	1.373	4.848	2.761
RD1	0.318	0.22	0.616	0.405	1.213	0.808	2.419	1.614	4.854	3.222
	0.129	0.131	0.228	0.2	0.428	0.344	0.831	0.657	1.642	1.199
	0.225	0.173	0.422	0.312	0.821	0.58	1.625	1.137	3.249	2.203
	0.129	0.128	0.13	0.146	0.131	0.161	0.171	0.203	0.173	0.201
	0.321	0.221	0.616	0.408	1.215	0.812	2.42	1.617	4.856	3.225
RD2	0.318	0.217	0.615	0.392	1.211	0.759	2.416	1.507	4.851	3.029
	0.127	0.102	0.226	0.168	0.424	0.295	0.827	0.551	1.639	1.04
	0.223	0.163	0.421	0.283	0.818	0.527	1.622	1.032	3.245	2.002
	0.127	0.102	0.128	0.125	0.128	0.113	0.129	0.113	0.129	0.115
	0.319	0.214	0.615	0.388	1.211	0.754	2.416	1.499	4.851	2.996
RD3	0.316	0.237	0.615	0.446	1.212	0.858	2.419	1.714	4.855	3.354
	0.127	0.143	0.227	0.231	0.427	0.422	0.83	0.752	1.643	1.322
	0.223	0.201	0.421	0.35	0.82	0.661	1.625	1.21	3.249	2.349
	0.126	0.147	0.129	0.177	0.201	0.255	0.242	0.31	0.278	0.345
	0.319	0.234	0.616	0.448	1.213	0.868	2.42	1.686	4.855	3.355

Appendix 3.2

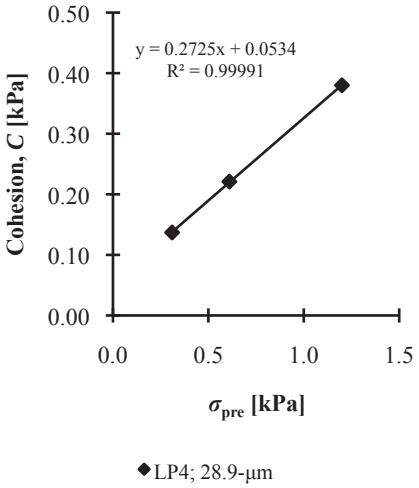

Figure A3.1 Plot of C versus σ_{pre} for LP4

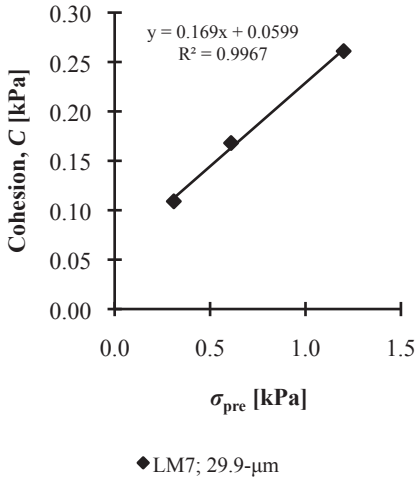

Figure A3.2 Plot of C versus σ_{pre} for LM7

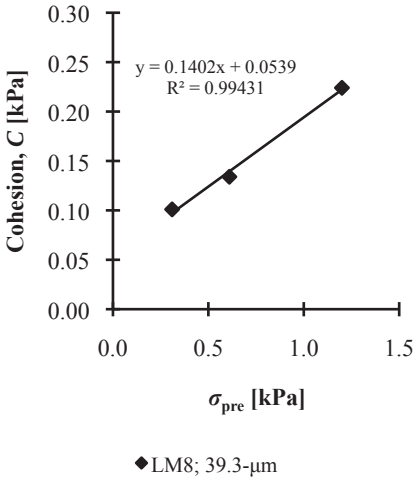

Figure A3.3 Plot of C versus σ_{pre} for LM8

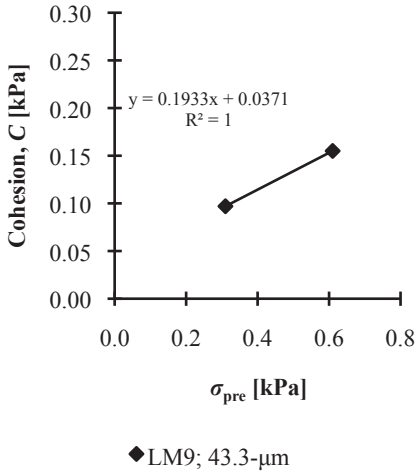

Figure A3.4 Plot of C versus σ_{pre} for LM9

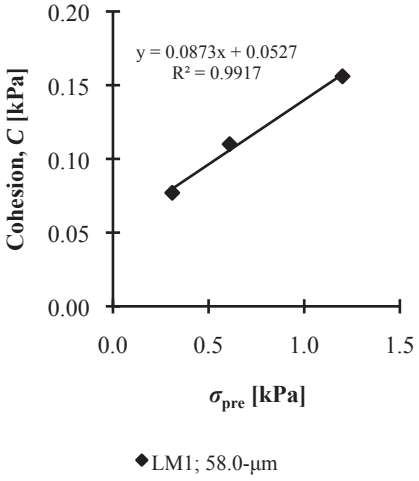

Figure A3.5 Plot of C versus σ_{pre} for LM1

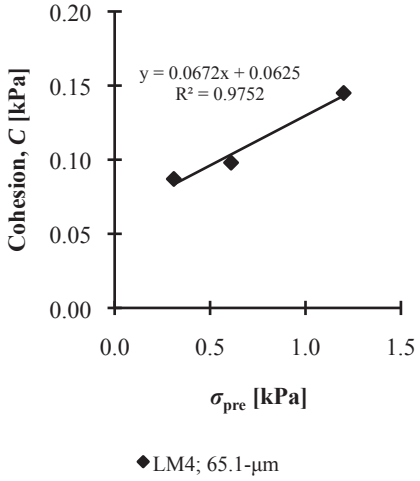

Figure A3.6 Plot of C versus σ_{pre} for LM4

Appendix 3.2

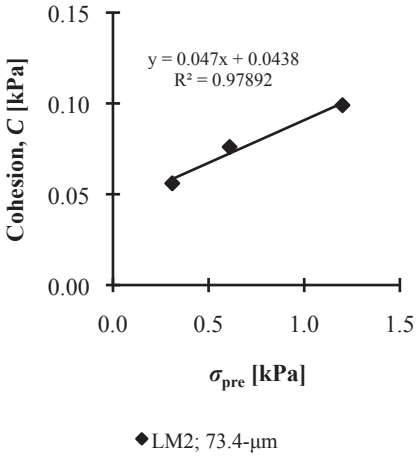

Figure A3.7 Plot of C versus σ_{pre} for LM2

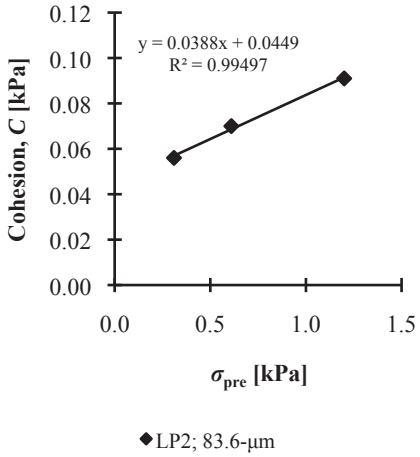

Figure A3.8 Plot of C versus σ_{pre} for LP2

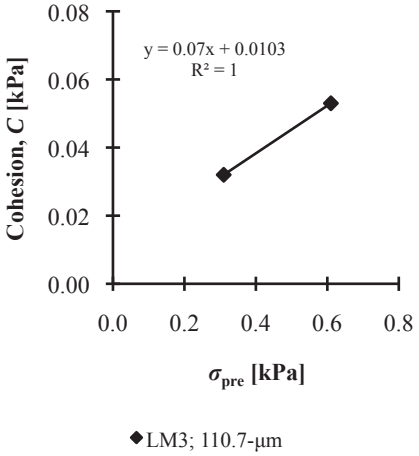

Figure A3.9 Plot of C versus σ_{pre} for LM3

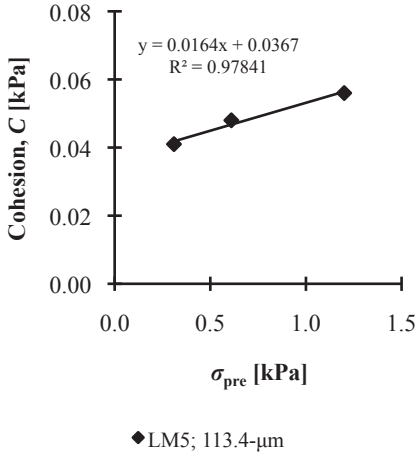

Figure A3.10 Plot of C versus σ_{pre} for LM5

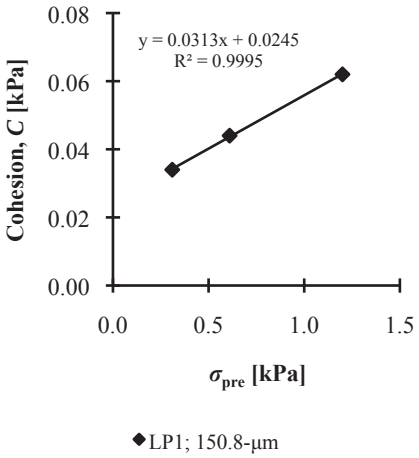

Figure A3.11 Plot of C versus σ_{pre} for LP1

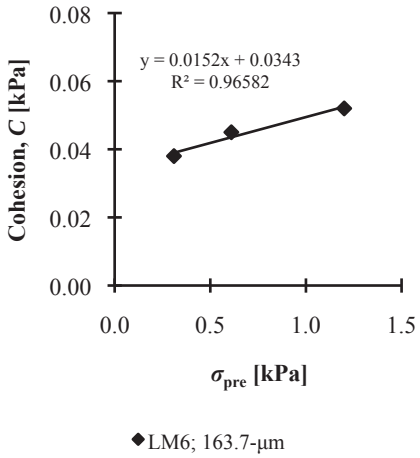

Figure A3.12 Plot of C versus σ_{pre} for LM6

Appendix 3.2

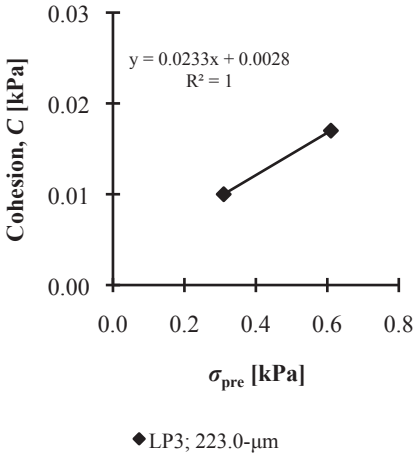

Figure A3.13 Plot of C versus σ_{pre} for LP3

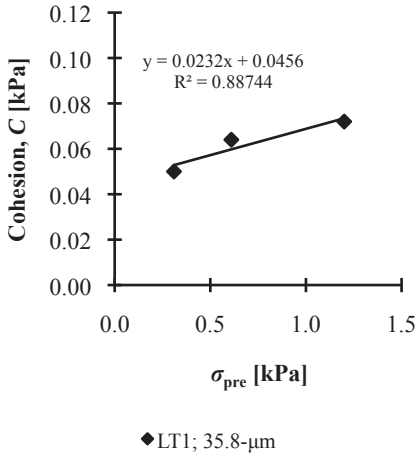

Figure A3.14 Plot of C versus σ_{pre} for LT1

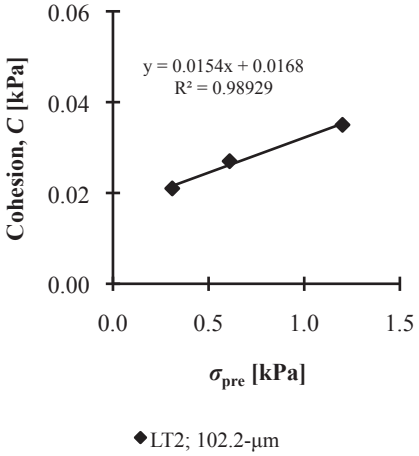

Figure A3.15 Plot of C versus σ_{pre} for LT2

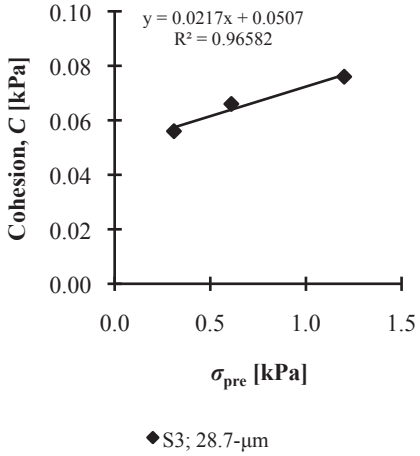

Figure A3.16 Plot of C versus σ_{pre} for S3

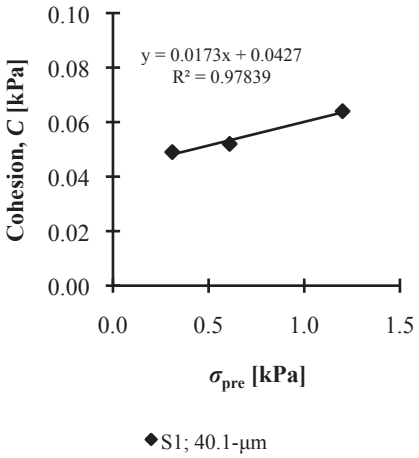

Figure A3.17 Plot of C versus σ_{pre} for S1

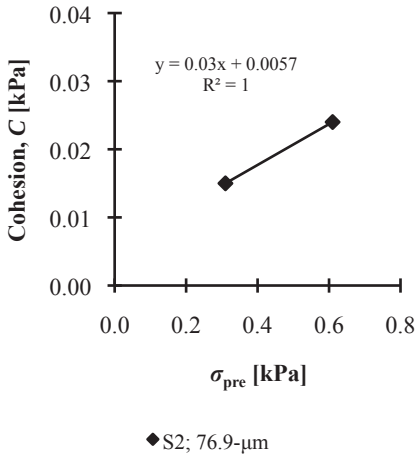

Figure A3.18 Plot of C versus σ_{pre} for S2

Appendix 3.2

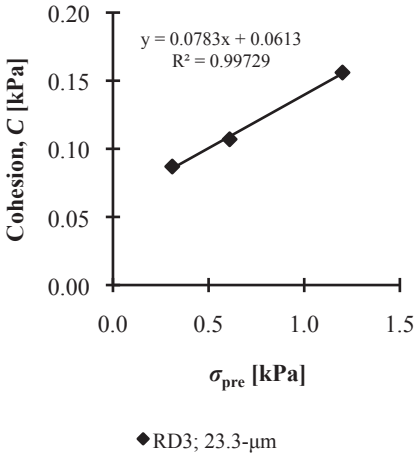

Figure A3.19 Plot of C versus σ_{pre} for RD3

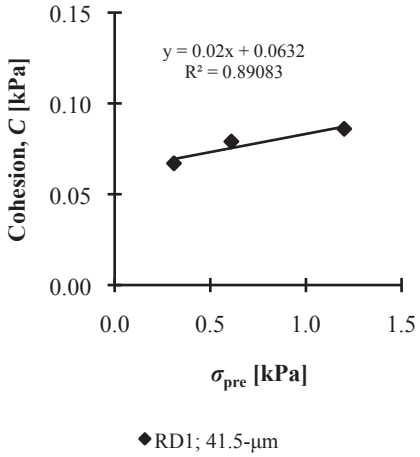

Figure A3.20 Plot of C versus σ_{pre} for RD1

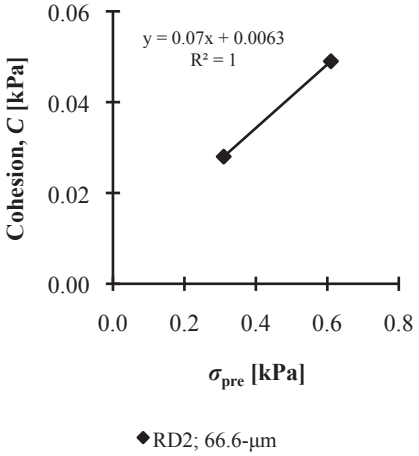

Figure A3.21 Plot of C versus σ_{pre} for RD2

Appendix 3.3

Table A3.2 Values of fitting parameters $k_{s,M1}$ and $k_{s,M2}$ of Equation 3.6

Powders	**Code**	$\boldsymbol{k_{s,M1}}$	$\boldsymbol{k_{s,M2}}$	$\boldsymbol{R^2}$
Unsieved milled lactose	LP4	0.5285	0.4750	0.998
	LM1	0.2314	0.2029	0.998
	LP1	0.1188	0.0939	0.999
Sieved milled lactose	LM7	0.4928	0.4239	0.999
	LM8	0.3678	0.3200	1.000
	LM9	0.3239	0.2691	0.999
	LM4	0.2007	0.1732	0.999
	LM2	0.1546	0.1369	0.998
	LP2	0.1652	0.1363	0.998
	LM3	0.1131	0.0847	0.999
	LM5	0.1022	0.0854	0.997
	LM6	0.1253	0.0840	0.999
	LP3	0.0765	0.0531	0.987
Spray-dried lactose	LT1	0.2082	0.1370	0.997
	LT2	0.0992	0.0589	0.999
Sand	S3	0.1509	0.0904	1.000
	S1	0.1242	0.0818	0.997
	S2	0.0636	0.0531	0.986
Refractory dust	RD3	0.2354	0.1865	0.998
	RD1	0.1359	0.1067	0.995
	RD2	0.0753	0.0563	0.996

Appendix 3.4

Table A3.3 Values of fitting parameters a_s and b_s of Equation 3.8

Powders	**Code**	a_s	b_s	R^2
Unsieved milled lactose	LP4	0.4988	2.349	0.999
	LM1	0.2985	1.788	0.999
	LP1	0.1706	1.771	0.999
Sieved milled lactose	LM7	0.4729	2.441	1.000
	LM8	0.4026	2.118	0.999
	LM9	0.3655	2.158	0.999
	LM4	0.2664	1.783	1.000
	LM2	0.2212	1.618	1.000
	LP2	0.2253	1.819	0.999
	LM3	0.1614	1.822	0.998
	LM5	0.1532	1.643	1.000
	LM6	0.1673	2.184	0.998
	LP3	0.1133	1.785	0.995
Spray-dried lactose	LT1	0.2461	2.619	0.999
	LT2	0.1304	2.527	0.999
Sand	S3	0.1879	2.556	0.998
	S1	0.1666	2.137	0.997
	S2	0.1058	1.336	0.991
Refractory dust	RD3	0.2885	2.104	0.999
	RD1	0.1898	1.837	0.999
	RD2	0.1138	1.711	0.997

Appendix 3.5

Table A3.4 Values of fitting parameters k_{N1} and k_{N2} of Equation 3.10

Powders	**Code**	k_{N1}	k_{N2}	R^2
Unsieved milled lactose	LP4	0.3970	0.3151	0.980
	LM1	0.1946	0.3430	0.975
	LP1	0.1062	0.3229	0.978
Sieved milled lactose	LM7	0.3764	0.3075	0.972
	LM8	0.2934	0.3245	0.972
	LM9	0.2643	0.3141	0.973
	LM4	0.1709	0.3457	0.964
	LM2	0.1339	0.3604	0.969
	LP2	0.1438	0.3330	0.970
	LM3	0.1022	0.3020	0.990
	LM5	0.0913	0.3472	0.969
	LM6	0.1136	0.2698	0.987
	LP3	0.0709	0.2783	0.997
Spray-dried lactose	LT1	0.1820	0.2593	0.972
	LT2	0.0916	0.2438	0.980
Sand	S3	0.1364	0.2375	0.991
	S1	0.1130	0.2623	0.995
	S2	0.0583	0.3367	0.999
Refractory dust	RD3	0.2000	0.3096	0.972
	RD1	0.1208	0.3158	0.981
	RD2	0.0693	0.3046	0.993

Appendix 3.6

Table A3.5 Values of fitting parameters k_{J1} and k_{J2} of Equation 3.12

Powders	**Code**	k_{J1}	k_{J2}	R^2
Unsieved milled lactose	LP4	23.34	0.1321	0.998
	LM1	18.38	0.0707	0.997
	LP1	21.81	0.0362	0.999
Sieved milled lactose	LM7	25.76	0.1212	0.997
	LM8	21.83	0.1001	0.998
	LM9	24.07	0.0871	0.997
	LM4	18.50	0.0621	0.997
	LM2	16.31	0.0511	0.997
	LP2	20.31	0.0504	0.997
	LM3	25.84	0.0328	0.999
	LM5	18.04	0.0335	0.997
	LM6	38.41	0.0322	0.999
	LP3	31.58	0.0213	0.988
Spray-dried lactose	LT1	46.73	0.0489	0.995
	LT2	58.22	0.0232	0.998
Sand	S3	62.24	0.0339	1.000
	S1	41.12	0.0314	0.998
	S2	17.38	0.0215	0.988
Refractory dust	RD3	25.21	0.0649	0.996
	RD1	22.87	0.0405	0.995
	RD2	24.58	0.0226	0.996

Appendix 3.7

Table A3.6 Values of fitting parameters k_{G1} and k_{G2} of Equation 3.14

Powders	**Code**	k_{G1}	k_{G2}	R^2
Unsieved milled lactose	LP4	224.2	0.3860	0.986
	LM1	150.1	0.3796	0.978
	LP1	94.6	0.3414	0.979
Sieved milled lactose	LM7	218.0	0.3723	0.979
	LM8	187.1	0.3772	0.978
	LM9	174.8	0.3598	0.978
	LM4	133.3	0.3777	0.969
	LM2	101.2	0.3866	0.972
	LP2	118.0	0.3589	0.973
	LM3	79.3	0.3187	0.991
	LM5	75.5	0.3642	0.971
	LM6	89.8	0.2863	0.988
	LP3	60.9	0.2891	0.997
Spray-dried lactose	LT1	123.5	0.2846	0.975
	LT2	63.1	0.2555	0.981
Sand	S3	125.5	0.2549	0.992
	S1	107.3	0.2784	0.996
	S2	54.0	0.3476	0.999
Refractory dust	RD3	214.4	0.3432	0.976
	RD1	138.1	0.3365	0.982
	RD2	75.3	0.3161	0.994

Appendix 3.8

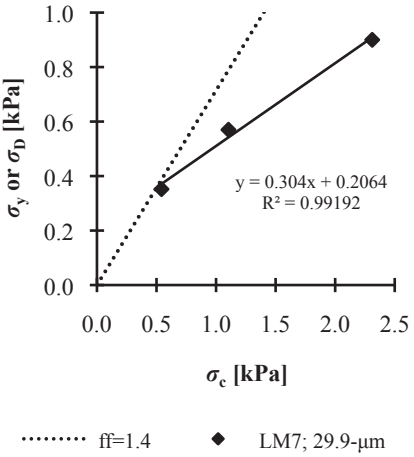

Figure A3.22 Plot of σ_y or σ_D versus σ_c for LM7

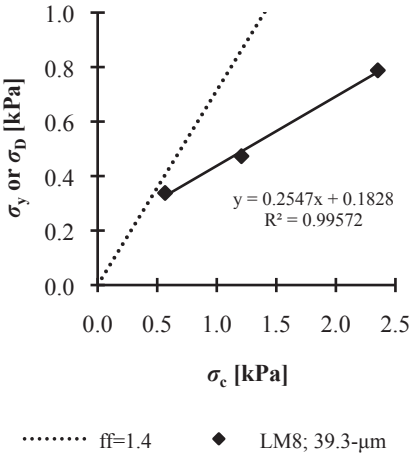

Figure A3.23 Plot of σ_y or σ_D versus σ_c for LM8

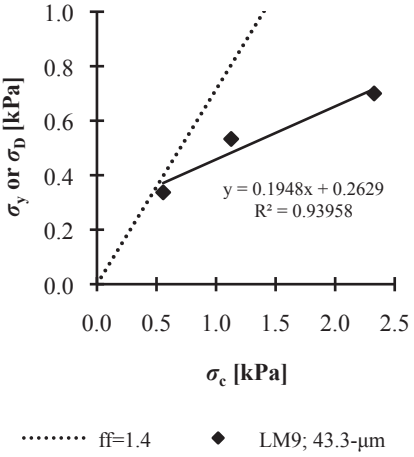

Figure A3.24 Plot of σ_y or σ_D versus σ_c for LM9

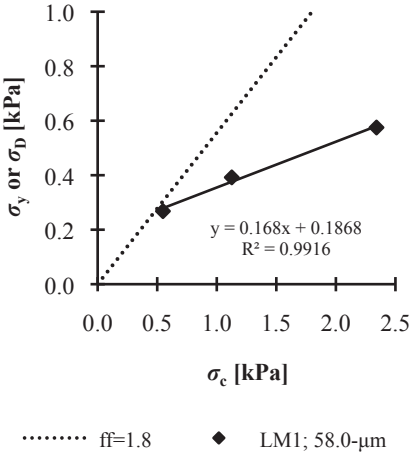

Figure A3.25 Plot of σ_y or σ_D versus σ_c for LM1

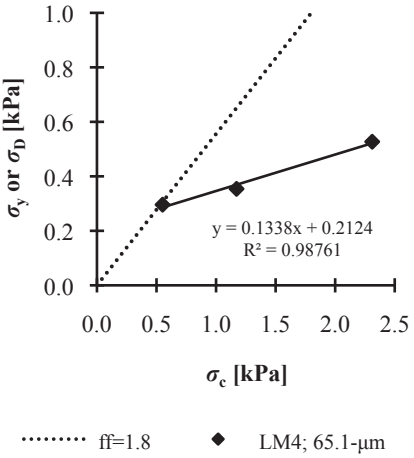

Figure A3.26 Plot of σ_y or σ_D versus σ_c for LM4

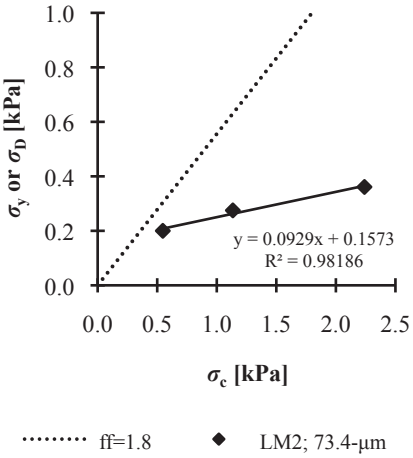

Figure A3.27 Plot of σ_y or σ_D versus σ_c for LM2

Appendix 3.8

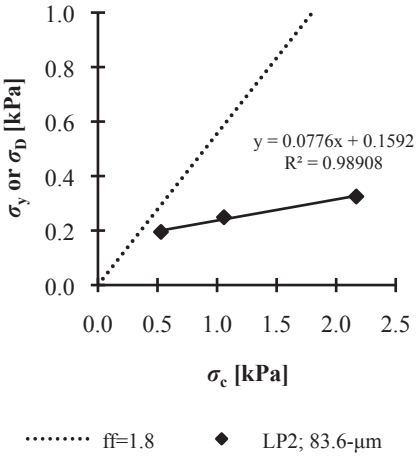

Figure A3.28 Plot of σ_y or σ_D versus σ_c for LP2

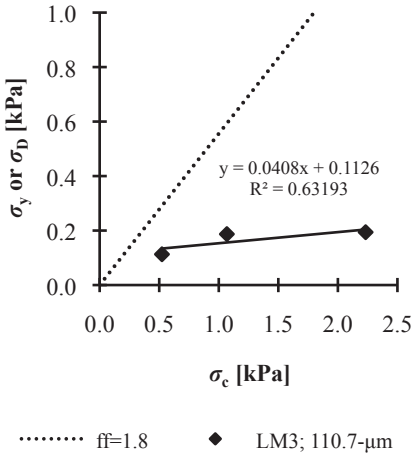

Figure A3.29 Plot of σ_y or σ_D versus σ_c for LM3

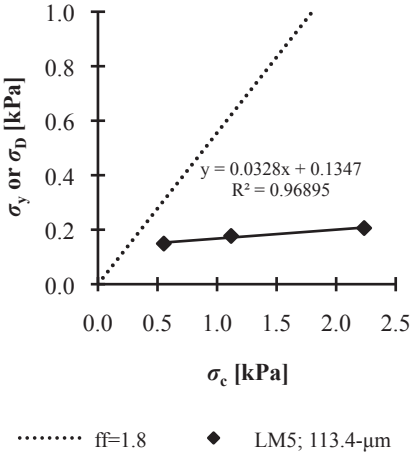

Figure A3.30 Plot of σ_y or σ_D versus σ_c for LM5

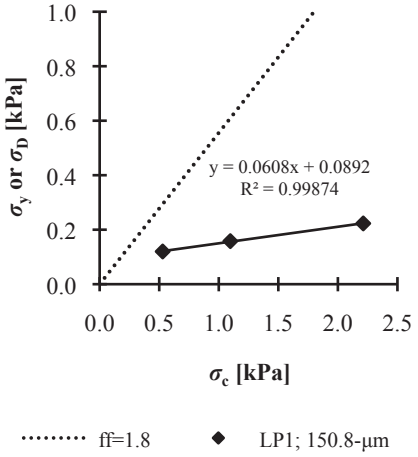

Figure A3.31 Plot of σ_y or σ_D versus σ_c for LP1

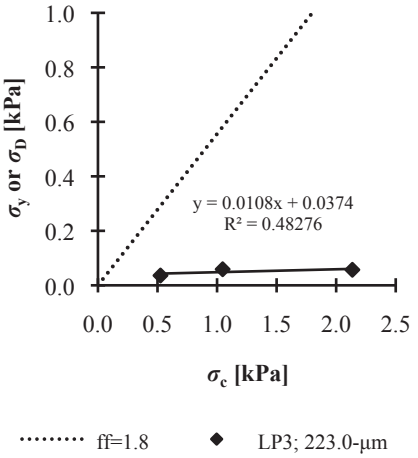

Figure A3.32 Plot of σ_y or σ_D versus σ_c for LP3

Appendix 3.9

To get Equation 3.29, Equation 3.6 is first rewritten as Equation A3.1; σ_c is the major consolidation stress and $k_{crit,1}$ and $k_{crit,2}$ are fitting parameters. Table A3.7 lists the $k_{crit,1}$ and $k_{crit,2}$ values determined by linear regression from plots of $[(\rho_B-\rho_0)/\rho_0]$ versus $\log(\sigma_c)$. With reference to Figures A3.33 and A3.34, Equations A3.2 and A3.3 are obtained by linear regression and forcing the fitting lines through the origin; R^2 is greater than 0.97. The substitution of Equations 3.27, A3.2, and A3.3 into Equation A3.1 gives Equation 3.29.

$$\frac{\rho_B-\rho_0}{\rho_0} = k_{s,M1} + k_{s,M2}\log\sigma_{pre} \tag{3.6}$$

$$\frac{\rho_B-\rho_0}{\rho_0} = k_{crit,1} + k_{crit,2}\log\sigma_c \tag{A3.1}$$

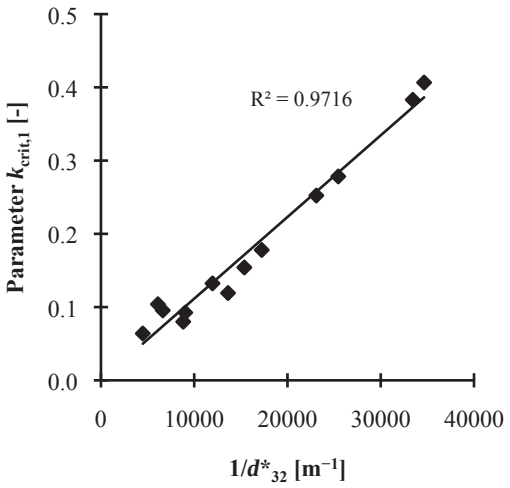

Figure A3.33 Plot of $k_{crit,1}$ versus $1/d^*_{32}$

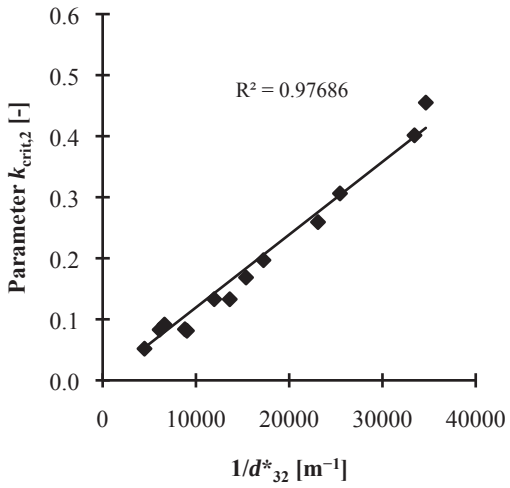

Figure A3.34 Plot of $k_{crit,2}$ versus $1/d^*_{32}$

$$k_{crit,1} = 1.115\times10^{-5}\frac{1}{d^*_{32}} \tag{A3.2}$$

$$k_{crit,2} = 1.193\times10^{-5}\frac{1}{d^*_{32}} \tag{A3.3}$$

$$\rho_0 = -0.0124\frac{1}{d^*_{32}} + 880.3 \tag{3.27}$$

Appendix 3.9

Table A3.7 Values of fitting parameters $k_{crit,1}$ and $k_{crit,2}$ of Equation A3.1

Powders	Code	d^*_{32} [µm]	$k_{crit,1}$	$k_{crit,2}$	R^2
Unsieved milled lactose	LP4	28.9	0.4065	0.4550	0.997
	LM1	58.0	0.1779	0.1969	0.998
	LP1	150.8	0.0955	0.0914	0.999
Sieved milled lactose	LM7	29.9	0.3830	0.4014	1.000
	LM8	39.3	0.2784	0.3062	0.999
	LM9	43.3	0.2523	0.2592	0.999
	LM4	65.1	0.1541	0.1685	0.999
	LM2	73.4	0.1192	0.1328	0.997
	LP2	83.6	0.1324	0.1330	0.998
	LM3	110.7	0.0925	0.0812	0.998
	LM5	113.4	0.0800	0.0837	0.998
	LM6	163.7	0.1039	0.0830	1.000
	LP3	223.0	0.0639	0.0519	0.985

Appendix 4.1

Table A4.1 The values of fitting parameters a_t, b_t, $k_{t,M1}$, $k_{t,M2}$ and coefficient of determination R^2 for milled lactose and spray-dried lactose powders, sand, and refractory dust

Powders	d^*_{32} **[µm]**	a_t	b_t	R^2	$k_{t,M1}$	$k_{t,M2}$	R^2
Unsieved milled lactose							
LP4	28.9	0.4447	0.0414	0.99	-0.0696	0.2867	0.96
LM1	58.0	0.2906	0.0483	0.99	0.0743	0.1112	0.93
LP1	150.8	0.1781	0.0292	0.99	0.0366	0.0564	0.99
Sieved milled lactose							
LM7	29.9	0.3903	0.0322	0.99	-0.1000	0.2428	0.96
LM8	39.3	0.3448	0.0669	0.99	0.0765	0.1546	0.87
LM9	43.3	0.3300	0.0449	0.99	0.0005	0.1651	0.94
LM4	65.1	0.2808	0.0597	0.99	0.0966	0.0980	0.96
LM2	73.4	0.2416	0.0585	0.99	0.1037	0.0710	0.96
LP2	83.6	0.2340	0.0414	0.99	0.0778	0.0728	0.99
LM3	110.7	0.1681	0.0493	0.99	0.0710	0.0424	0.98
LM5	113.4	0.2053	0.0550	0.99	0.0974	0.0521	0.99
LM6	163.7	0.1625	0.0322	0.99	0.0422	0.0480	0.99
LP3	223.0	0.0917	0.0218	0.99	0.0015	0.0314	0.99
Spray-dried lactose							
LT1	35.8	0.2143	0.0414	0.99	0.1130	0.0504	0.99
LT2	102.2	0.1238	0.0195	0.99	0.0147	0.0392	0.99
Sand							
S3	28.7	0.1908	0.0303	0.99	0.0095	0.0734	0.92
S1	40.0	0.1702	0.0441	0.99	0.0452	0.0527	0.97
S2	76.9	0.1182	0.0298	0.99	0.0375	0.0296	0.97
Refractory dust							
RD3	23.3	0.2980	0.0204	0.99	-0.0866	0.1617	0.97
RD1	41.5	0.2424	0.0718	0.99	0.0903	0.0781	0.92
RD2	66.6	0.1645	0.0587	0.99	0.0972	0.0317	0.99

Appendix 4.2

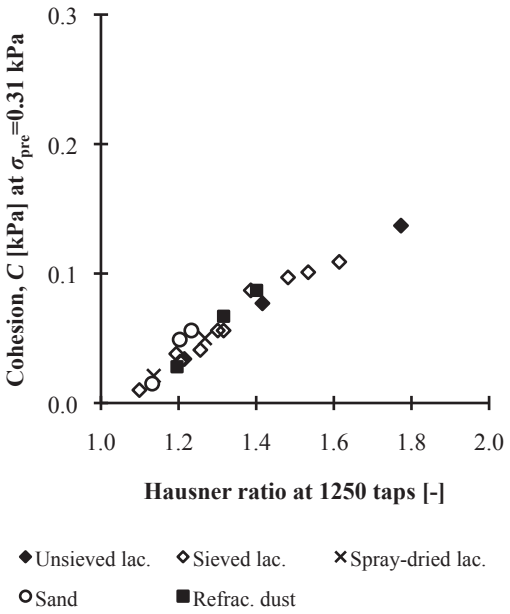

Figure A4.1 Plot of cohesion at σ_{pre}=0.31 kPa versus Hausner ratio at 1250 taps

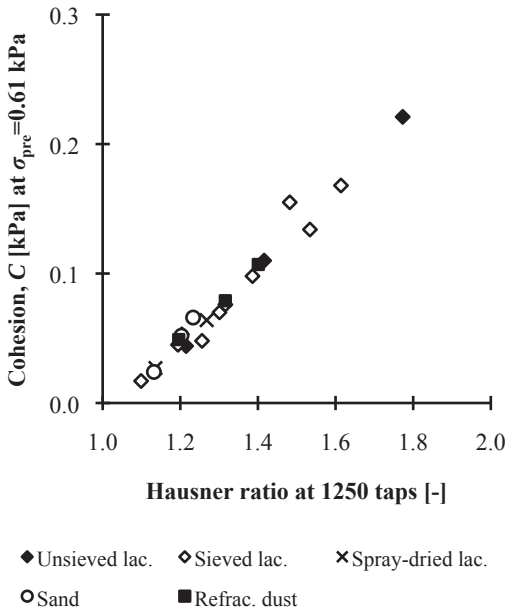

Figure A4.2 Plot of cohesion at σ_{pre}=0.61 kPa versus Hausner ratio at 1250 taps

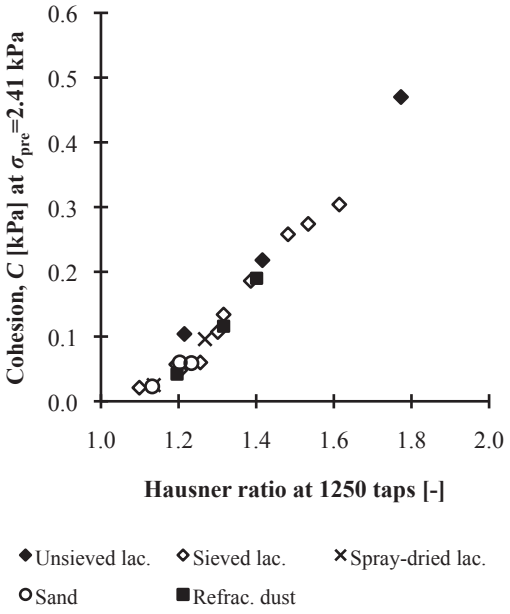

Figure A4.3 Plot of cohesion at σ_{pre}=2.41 kPa versus Hausner ratio at 1250 taps

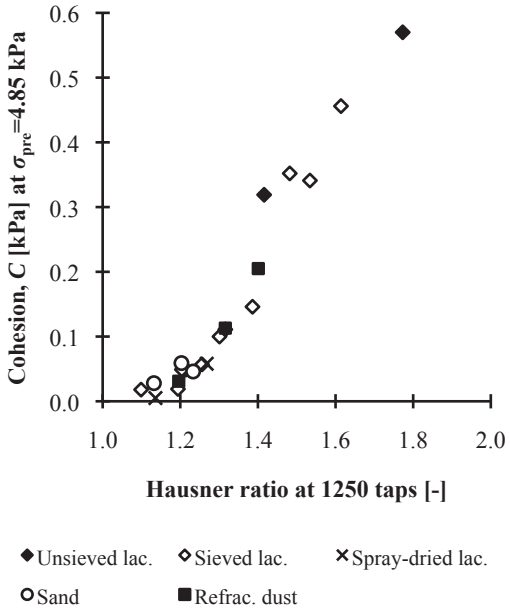

Figure A4.4 Plot of cohesion at σ_{pre}=4.85 kPa versus Hausner ratio at 1250 taps

Appendix 4.3

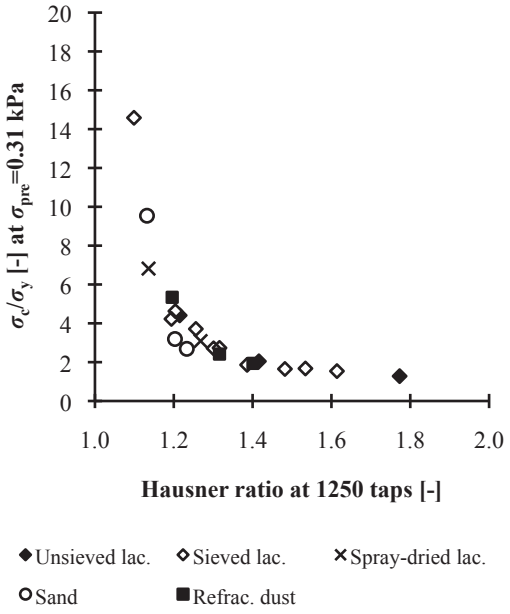

Figure A4.5 Ratio σ_c/σ_y at σ_{pre}=0.31 kPa versus Hausner ratio at 1250 taps

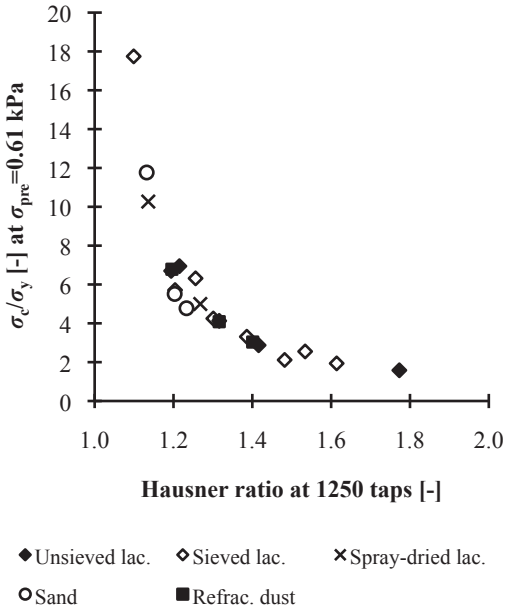

Figure A4.6 Ratio σ_c/σ_y at σ_{pre}=0.61 kPa versus Hausner ratio at 1250 taps

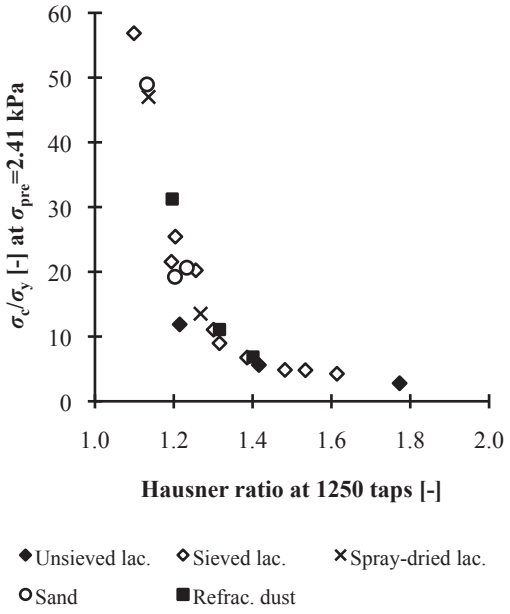

Figure A4.7 Ratio σ_c/σ_y at σ_{pre}=2.45 kPa versus Hausner ratio at 1250 taps

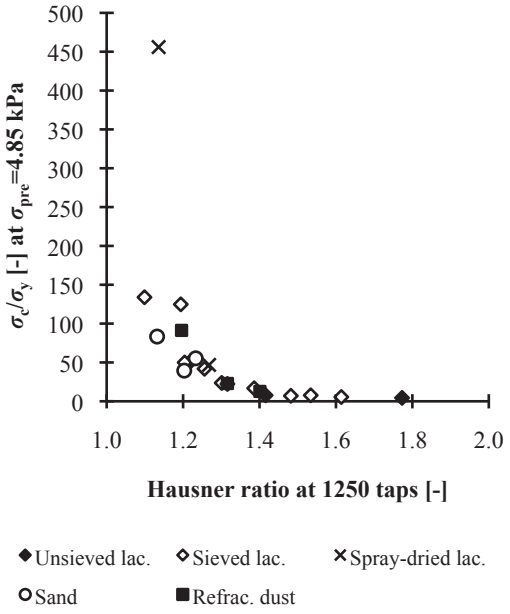

Figure A4.8 Ratio σ_c/σ_y at σ_{pre}=4.85 kPa versus Hausner ratio at 1250 taps

Appendix 4.4

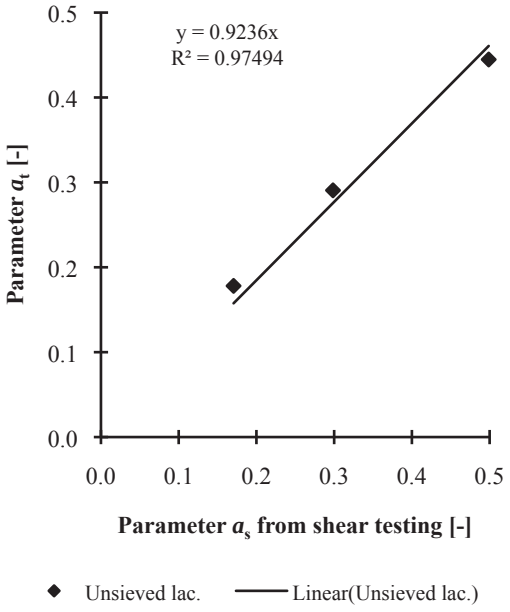

Figure A4.9 Plot of a_t against a_s for unsieved milled lactose powder

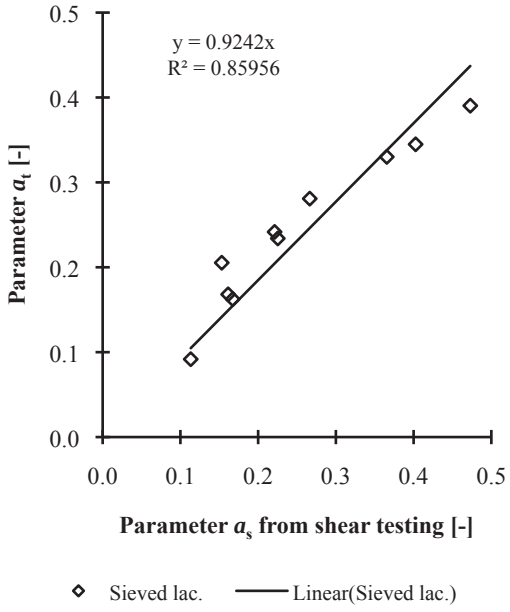

Figure A4.10 Plot of a_t against a_s for sieved milled lactose powder

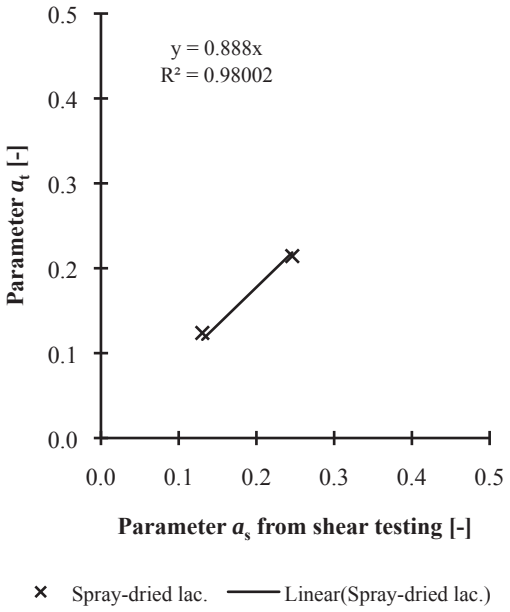

Figure A4.11 Plot of a_t against a_s for spray-dried lactose powder

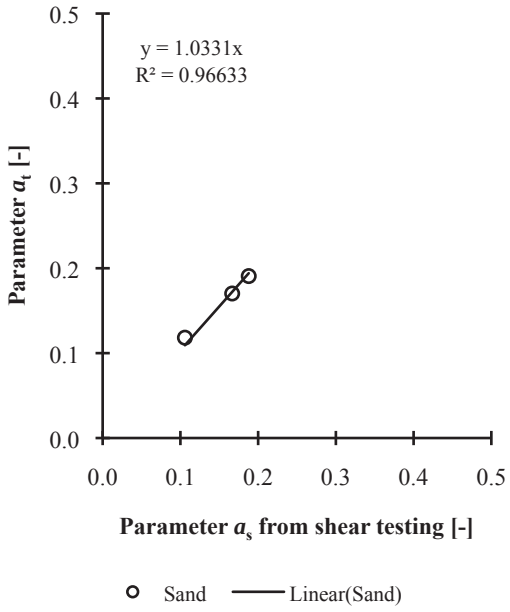

Figure A4.12 Plot of a_t against a_s for sand

Appendix 4.4

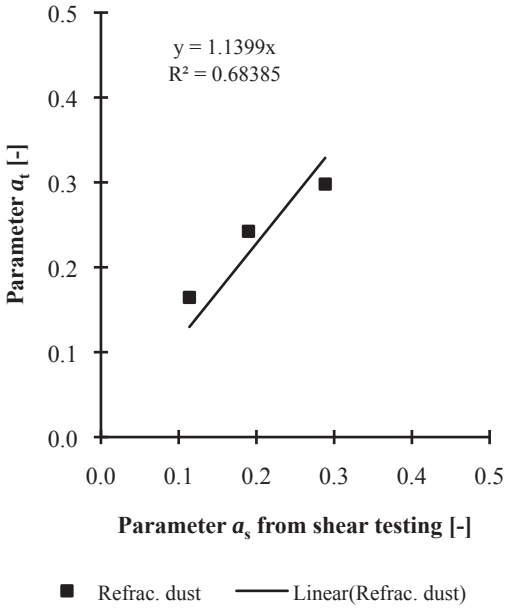

Figure A4.13 Plot of a_t against a_s for refractory dust

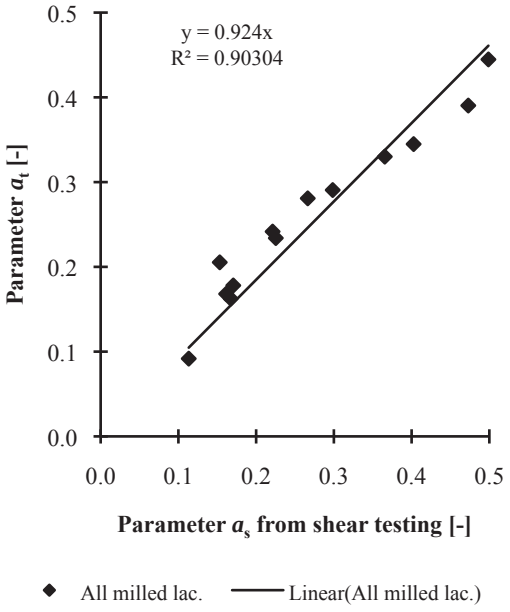

Figure A4.14 Plot of a_t against a_s for all milled lactose

Appendix 4.5

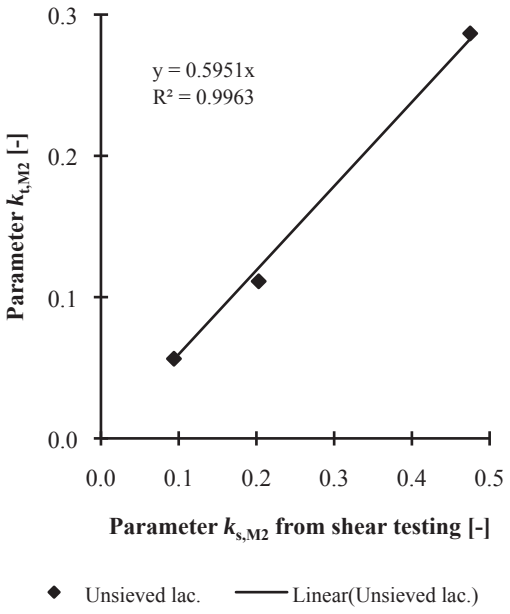

Figure A4.15 Plot of $k_{t,M2}$ against $k_{s,M2}$ for unsieved milled lactose

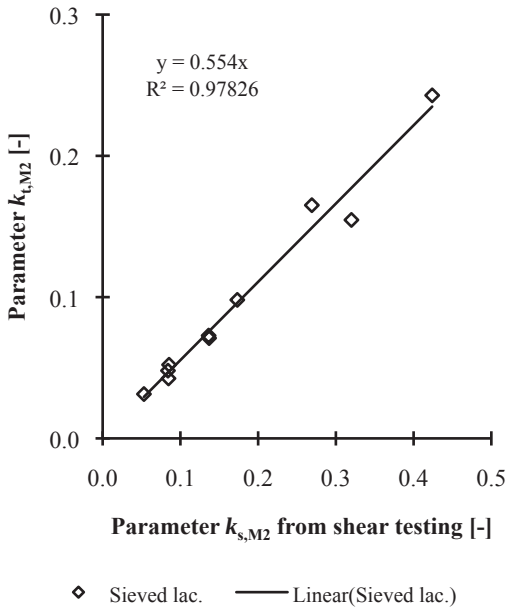

Figure A4.16 Plot of $k_{t,M2}$ against $k_{s,M2}$ for sieved milled lactose

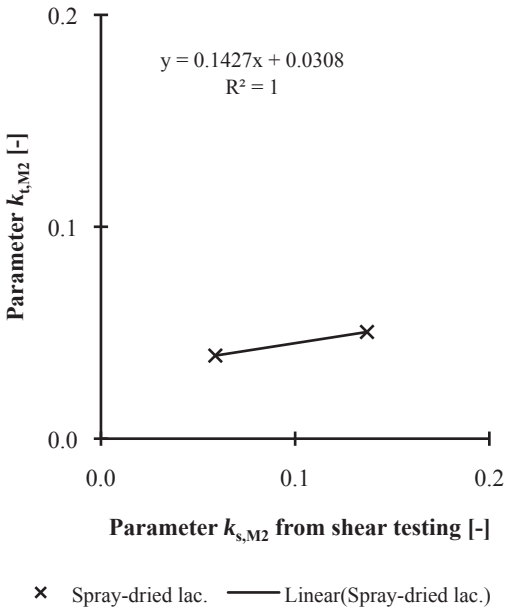

Figure A4.17 Plot of $k_{t,M2}$ against $k_{s,M2}$ for spray-dried lactose

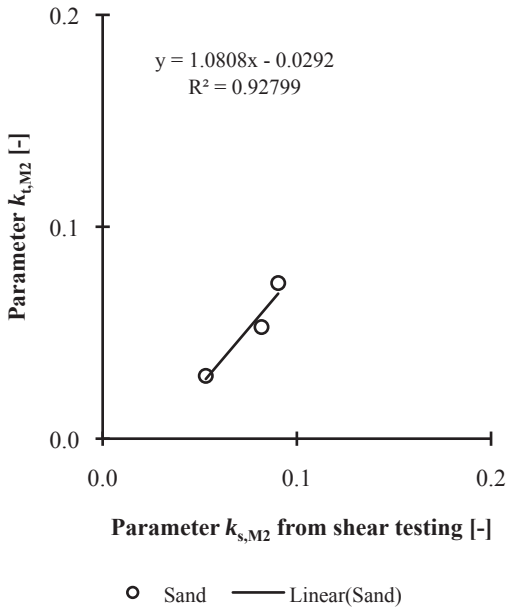

Figure A4.18 Plot of $k_{t,M2}$ against $k_{s,M2}$ for sand

Appendix 4.5

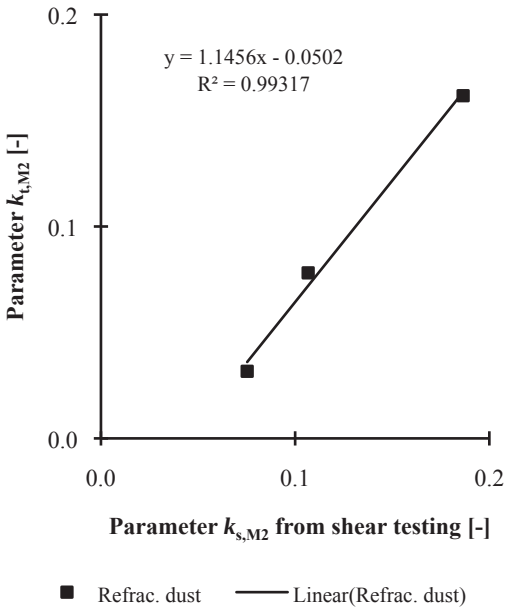

Figure A4.19 Plot of $k_{t,M2}$ against $k_{s,M2}$ for refractory dust

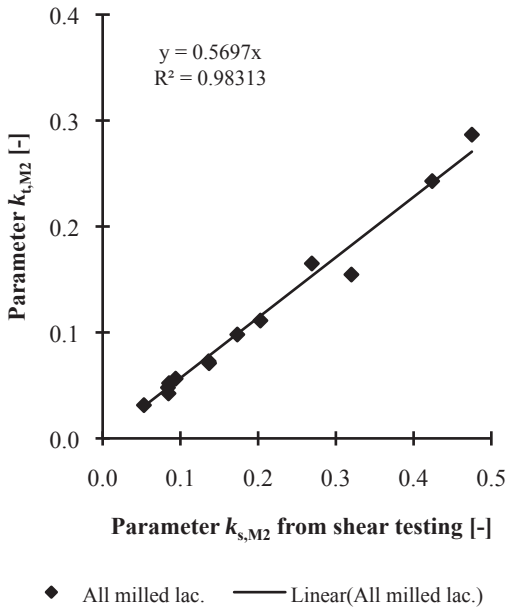

Figure A4.20 Plot of $k_{t,M2}$ against $k_{s,M2}$ for all milled lactose

Appendix 5.1

Figure A5.1 shows the calibration curve for Key Instruments (Ki) rotameter 0–5 L min^{-1} and Figure A5.2 shows the calibration curve for Ki rotameter 0–10 L min^{-1}; calibration was done with a soap film flowmeter (Model 311-1000, SKC, USA). The gas flow rates were accurate and consistent. No calibration was done with Ki rotameter 0–15 L min^{-1} because the maximum gas flow achieved with the soap film flowmeter was ~8 L min^{-1}; at higher flow rates soap films were unstable and broke.

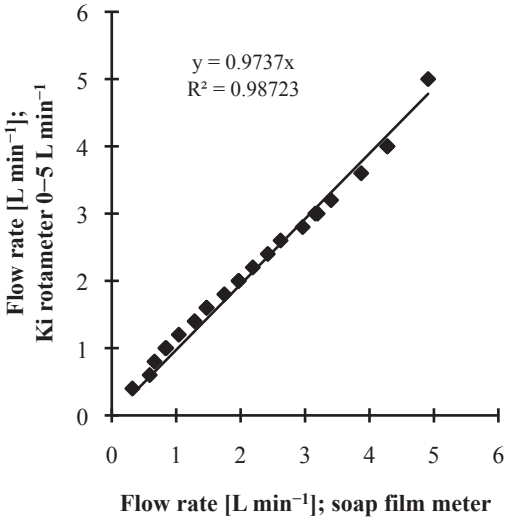

Figure A5.1 Calibration curve for Ki rotameter 0–5 L min^{-1}

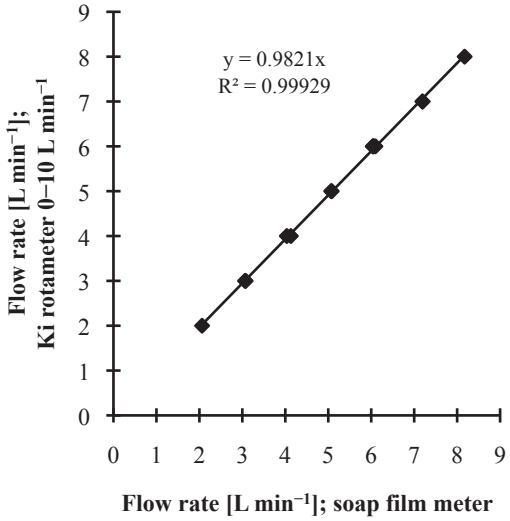

Figure A5.2 Calibration curve for Ki rotameter 0–10 L min^{-1}

Figures A5.3 (a) and (b) are two photographs of the hot-wire anemometer. A thermal mass flow sensor (Flow Sens FS1, IST Innovative Sensor Technology, Switzerland) was used; its technical data and recommendation on the construction of electronic circuit are available at http://www.farnell.com/datasheets/318594.pdf. The flow sensor was connected and sealed with glue to a gas tube of inner diameter of ~6 mm. The tube was straightened and supported by a wooden block; the tube length was ~350 mm.

Figure A5.4 shows the calibration curve for the hot-wire anemometer; the relationship between the anemometer signal, V, in volt and gas flow rate, Q, in L min^{-1} of the soap film meter is given by Equation A5.1, with R^2=0.997. To convert Q from L min^{-1} to m s^{-1}, Equation A5.2 was used; the measured inner diameter of the 80-mm cylindrical fluid bed was 0.080007 m, and the calculated cross-sectional area was 0.005027 m^2.

Appendix 5.1

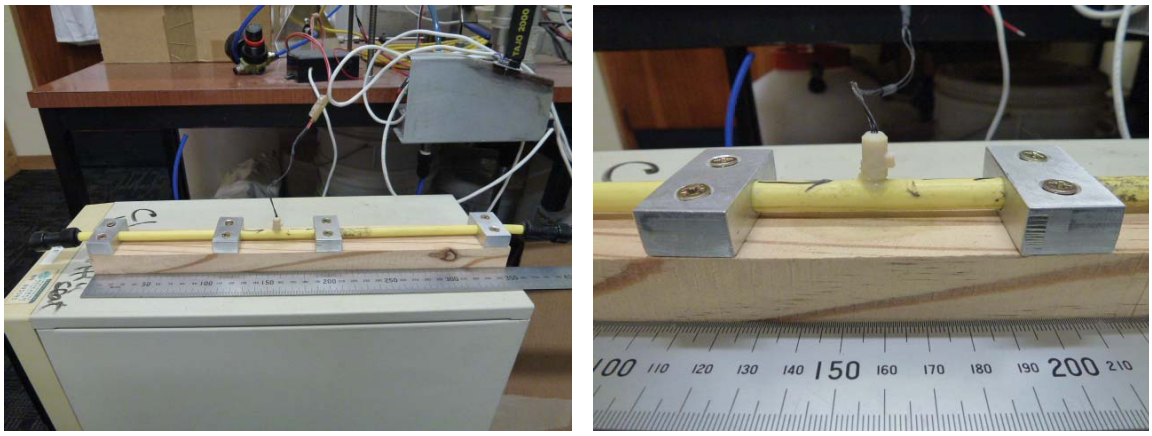

(a) (b)

Figure A5.3 Hot-wire anemometer developed in-house

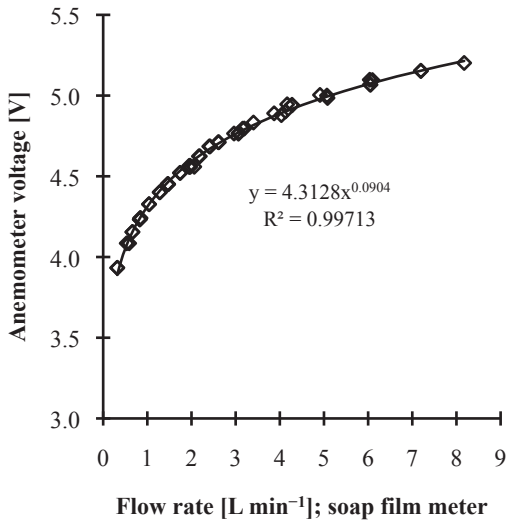

Figure A5.4 Calibration curve for in-house hot-wire anemometer

$$V = 4.3128Q^{0.0904} \tag{A5.1}$$

$$Q\left[\text{m s}^{-1}\right] = \frac{Q\left[\text{L min}^{-1}\right]}{60 \times 1{,}000 \times 0.005027} \tag{A5.2}$$

Appendix 5.2

Figure A5.5 shows the pressure offset, ($\Delta P_{b,f}$–ΔP_b), of the Motorola MPX10DP pressure transducer plotted against temperature increase, (T_f–T); T is initial temperature [^oC], ΔP_b is measured pressure drop [kPa] at T, T_f is final temperature [^oC], and $\Delta P_{b,f}$ is measured pressure drop [kPa] at T_f. Offset occurred because the transducer was not temperature-compensated. With ~55,000 data points, Equation A5.3 was obtained by linear regression, R^2=0.937. All ΔP_b values in Chapter 5 had been corrected with this equation to eliminate the effect of temperature.

$$\Delta P_{b,f} - \Delta P_b = 0.0189\left(T_f - T\right) \tag{A5.3}$$

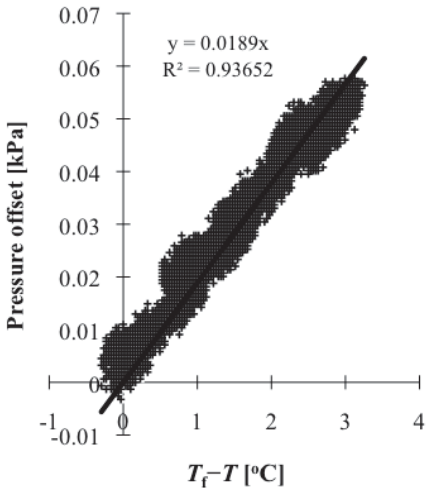

Figure A5.5 Plot of pressure offset, ($\Delta P_{b,f}$–ΔP_b), for Motorola MPX10DP pressure transducer versus temperature increase, (T_f–T)

The Motorola MPX10DP pressure transducer datasheet is available for download at http://www.alldatasheet.com/datasheet-pdf/pdf/5167/MOTOROLA/MPX10DP.html.

Appendix 5.3

Figure A5.6 shows the plot of gas distributor pressure drop, ΔP_d, against superficial velocity, U. The calibrated Motorola MPX10DP pressure transducer was used to measure ΔP_d. Equation A5.4 correlates ΔP_d with U; the relationship is linear with R^2=0.993.

$$\Delta P_d = 555132U \tag{A5.4}$$

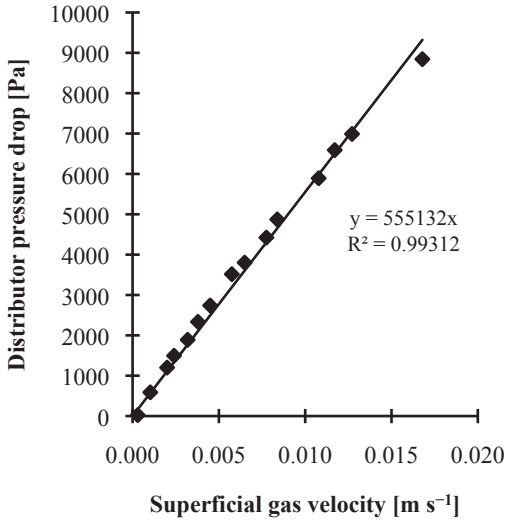

Figure A5.6 Plot of gas distributor pressure drop versus superficial velocity; the distributor was made of 16 layers of Whatman filter paper No. 3 stacked and held tightly around the edges by two cylindrical mild steel rings that were screwed together

Appendix 5.4

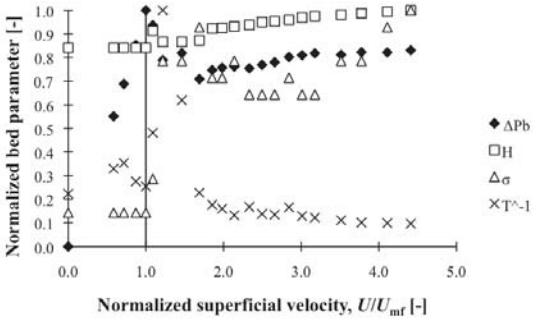

Figure A5.7 Plots of normalized bed parameters versus U/U_{mf} for lactose LP2 (repeat) and increasing U

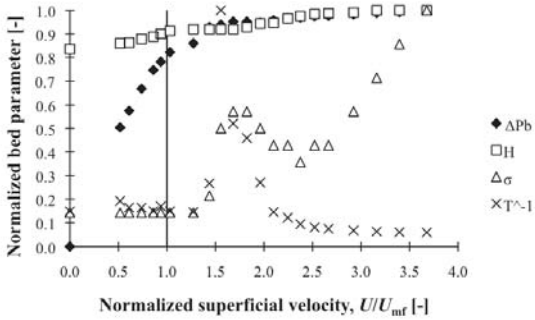

Figure A5.8 Plots of normalized bed parameters versus U/U_{mf} for lactose LP2 (repeat) and decreasing U

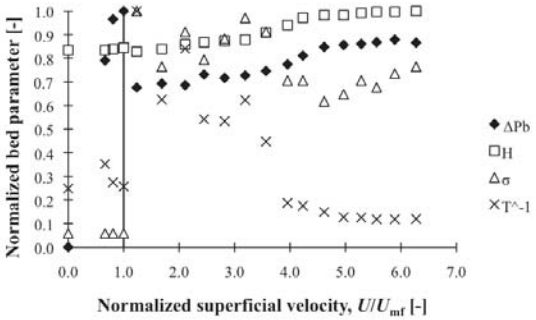

Figure A5.9 Plots of normalized bed parameters versus U/U_{mf} for lactose LM2 and increasing U

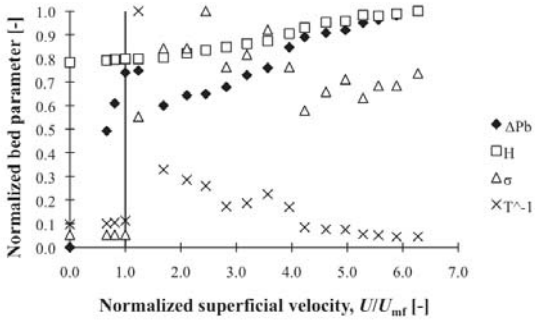

Figure A5.10 Plots of normalized bed parameters versus U/U_{mf} for lactose LM2 and decreasing U

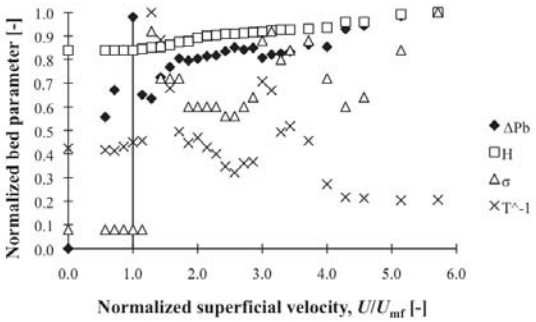

Figure A5.11 Plots of normalized bed parameters versus U/U_{mf} for lactose LM3 and increasing U

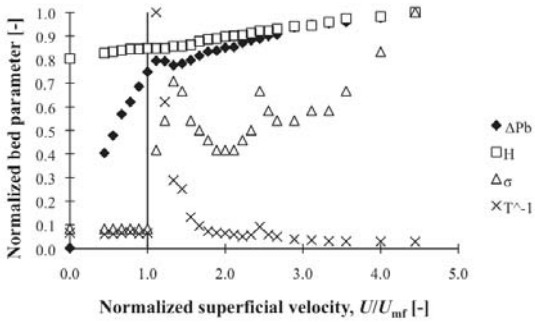

Figure A5.12 Plots of normalized bed parameters versus U/U_{mf} for lactose LM3 and decreasing U

Appendix 5.4

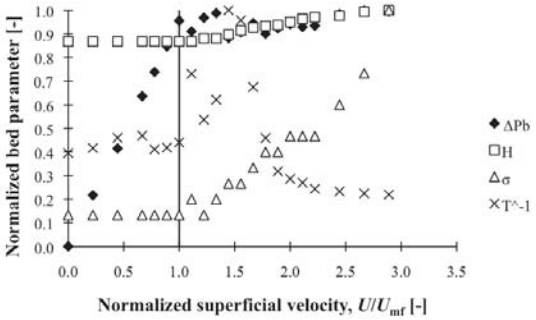

Figure A5.13 Plots of normalized bed parameters versus U/U_{mf} for lactose LM6 and increasing U

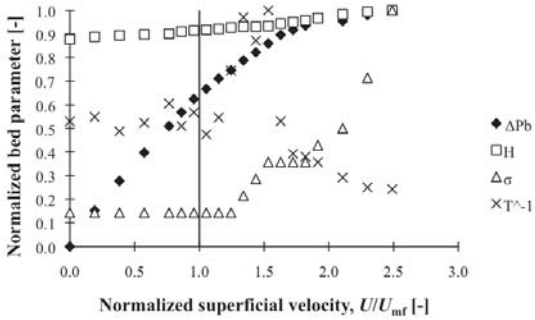

Figure A5.14 Plots of normalized bed parameters versus U/U_{mf} for lactose LM6 and decreasing U

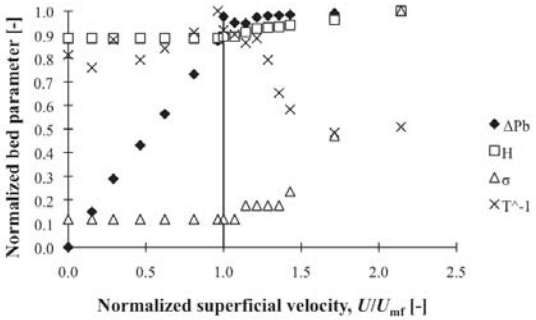

Figure A5.15 Plots of normalized bed parameters versus U/U_{mf} for lactose LP3 and increasing U

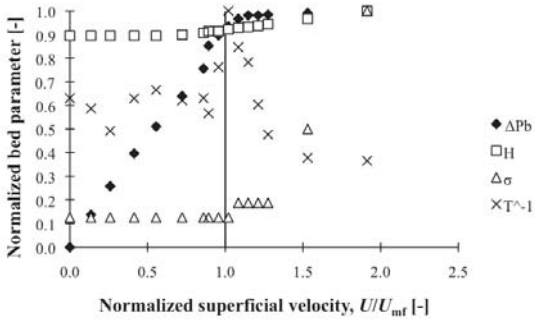

Figure A5.16 Plots of normalized bed parameters versus U/U_{mf} for lactose LP3 and decreasing U

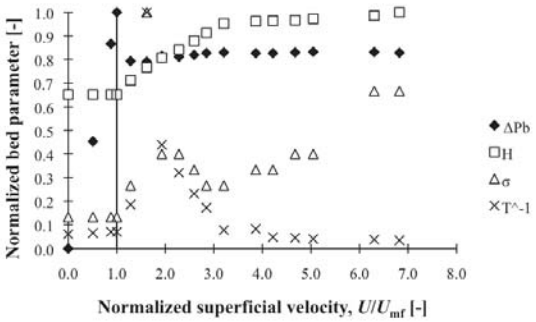

Figure A5.17 Plots of normalized bed parameters versus U/U_{mf} for lactose LT1 and increasing U

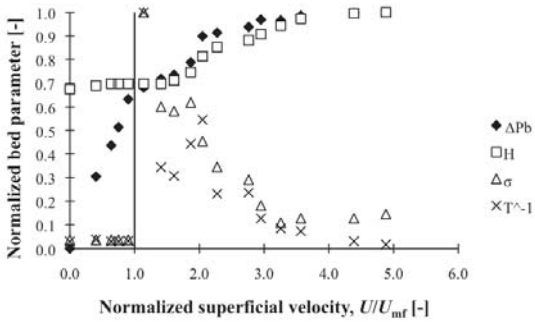

Figure A5.18 Plots of normalized bed parameters versus U/U_{mf} for lactose LT1 and decreasing U

Appendix 5.4

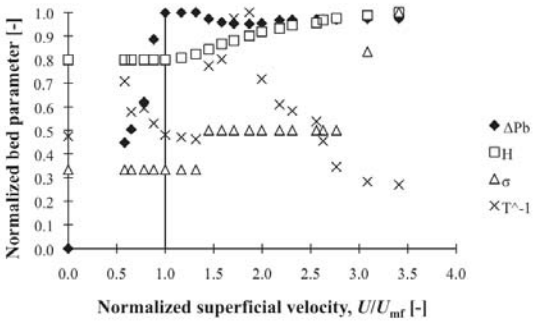

Figure A5.19 Plots of normalized bed parameters versus U/U_{mf} for lactose LT2 and increasing U

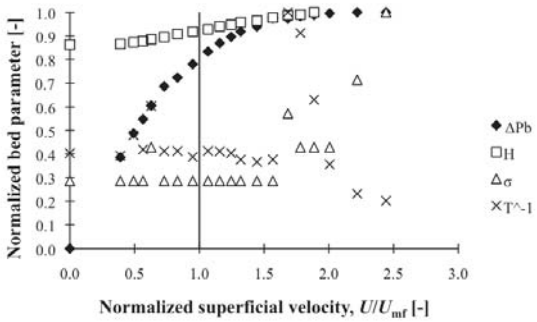

Figure A5.20 Plots of normalized bed parameters versus U/U_{mf} for lactose LT2 and decreasing U

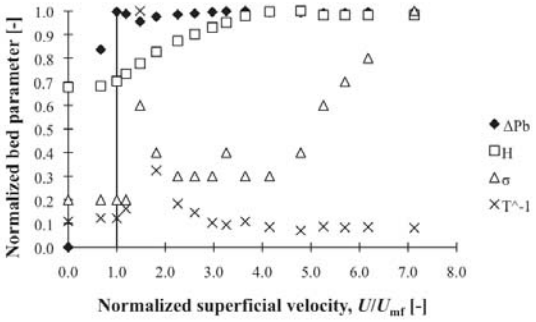

Figure A5.21 Plots of normalized bed parameters versus U/U_{mf} for sand S1 and increasing U

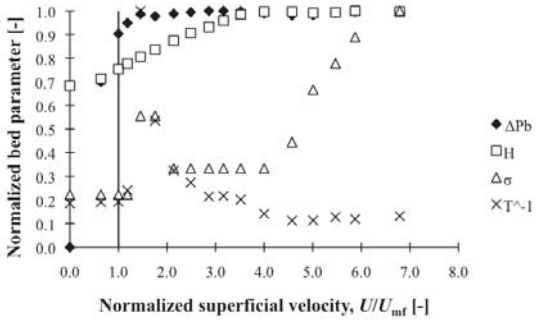

Figure A5.22 Plots of normalized bed parameters versus U/U_{mf} for sand S1 and decreasing U

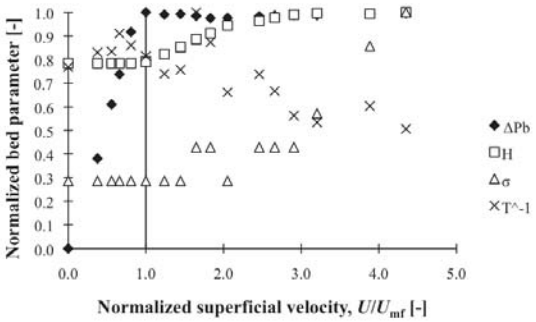

Figure A5.23 Plots of normalized bed parameters versus U/U_{mf} for sand S2 and increasing U

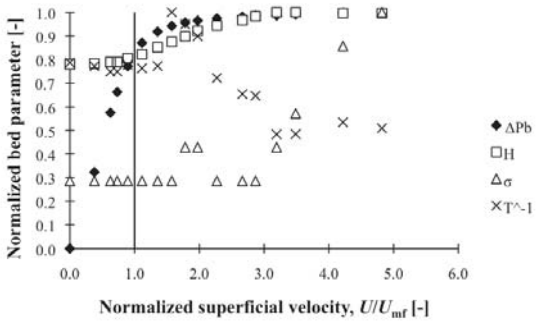

Figure A5.24 Plots of normalized bed parameters versus U/U_{mf} for sand S2 and decreasing U

Appendix 5.4

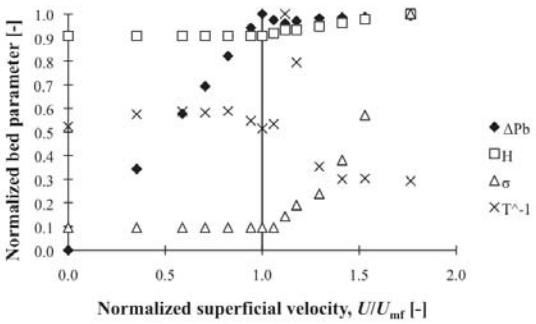

Figure A5.25 Plots of normalized bed parameters versus U/U_{mf} for sand SB and increasing U

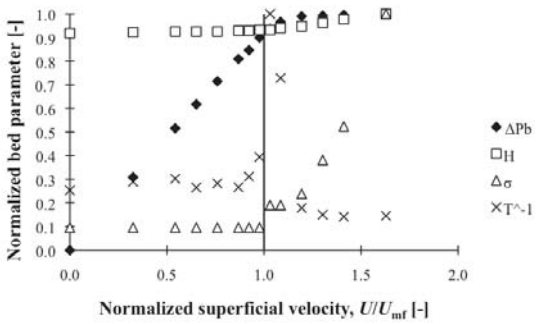

Figure A5.26 Plots of normalized bed parameters versus U/U_{mf} for sand SB and decreasing U

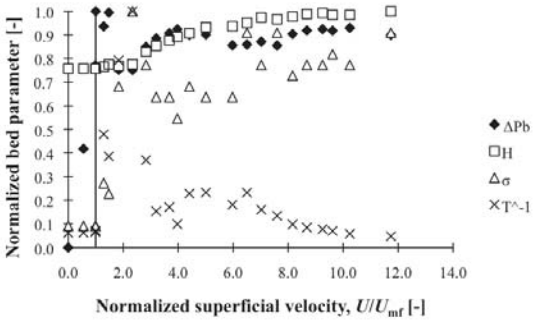

Figure A5.27 Plots of normalized bed parameters versus U/U_{mf} for refractory dust RD1 and increasing U

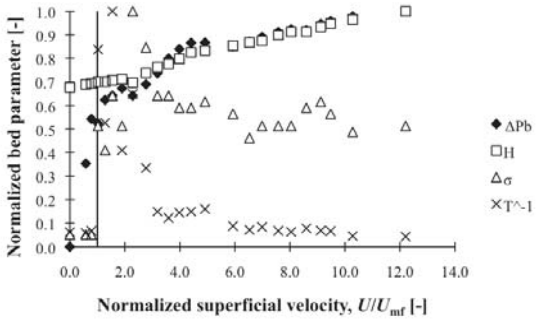

Figure A5.28 Plots of normalized bed parameters versus U/U_{mf} for refractory dust RD1 and decreasing U

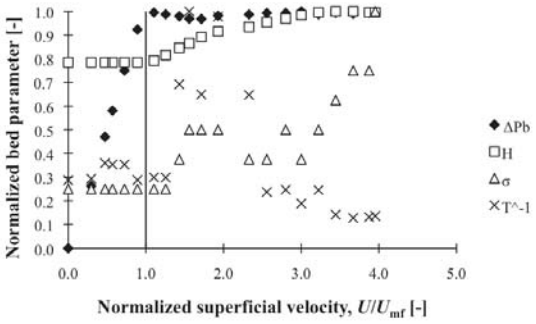

Figure A5.29 Plots of normalized bed parameters versus U/U_{mf} for refractory dust RD2 and increasing U

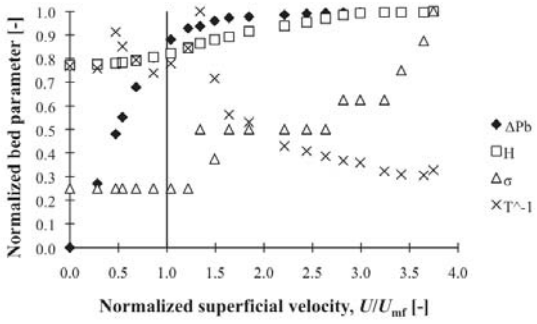

Figure A5.30 Plots of normalized bed parameters versus U/U_{mf} for refractory dust RD2 and decreasing U

Appendix 5.4

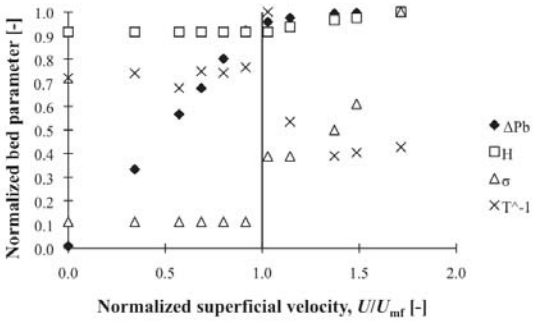

Figure A5.31 Plots of normalized bed parameters versus U/U_{mf} for glass beads B8 and increasing U

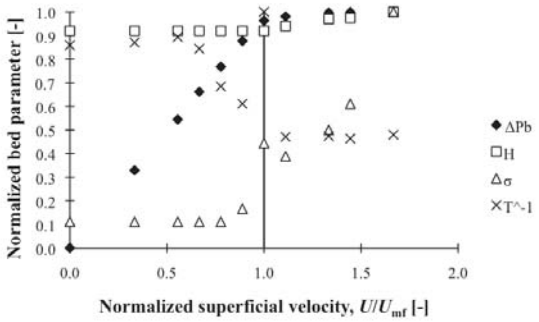

Figure A5.32 Plots of normalized bed parameters versus U/U_{mf} for glass beads B8 and decreasing U

Appendix 5.5

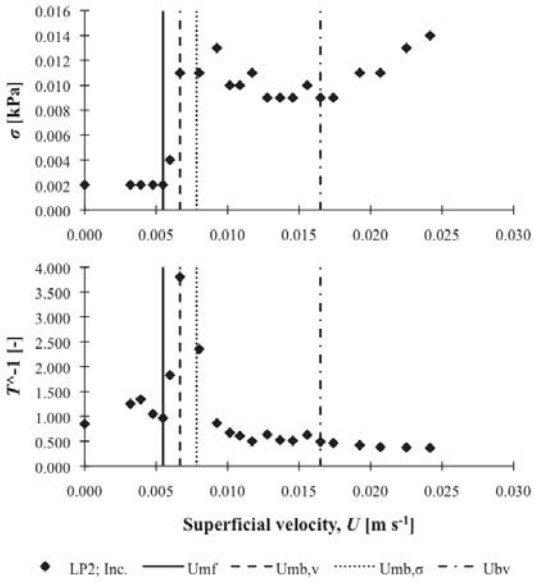

Figure A5.33 Plots of σ and T^{-1} versus U for lactose LP2 (repeat) and increasing U

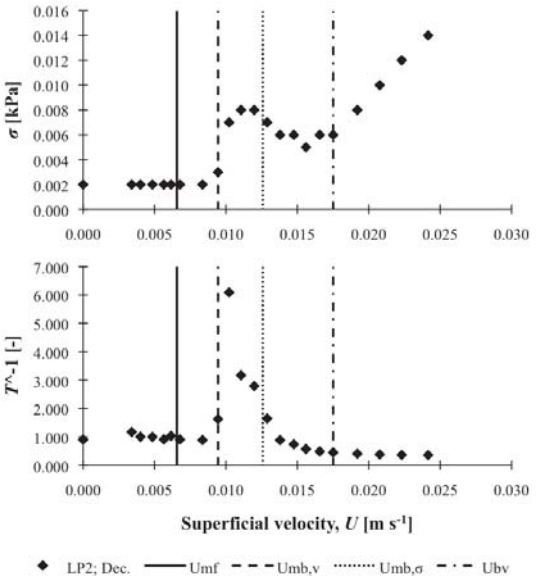

Figure A5.34 Plots of σ and T^{-1} versus U for lactose LP2 (repeat) and decreasing U

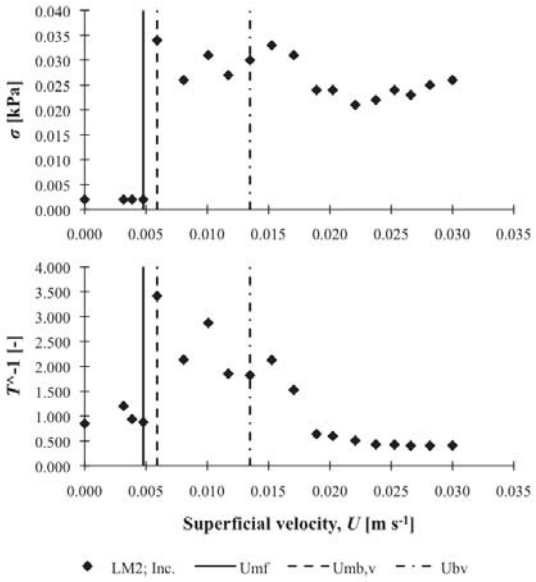

Figure A5.35 Plots of σ and T^{-1} versus U for lactose LM2 and increasing U

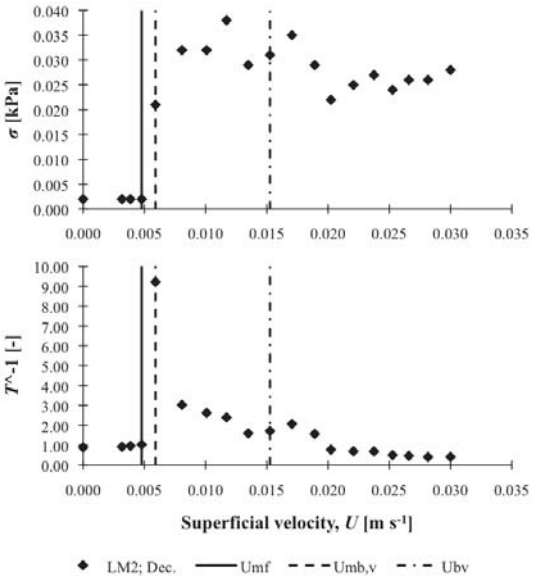

Figure A5.36 Plots of σ and T^{-1} versus U for lactose LM2 and decreasing U

Appendix 5.5

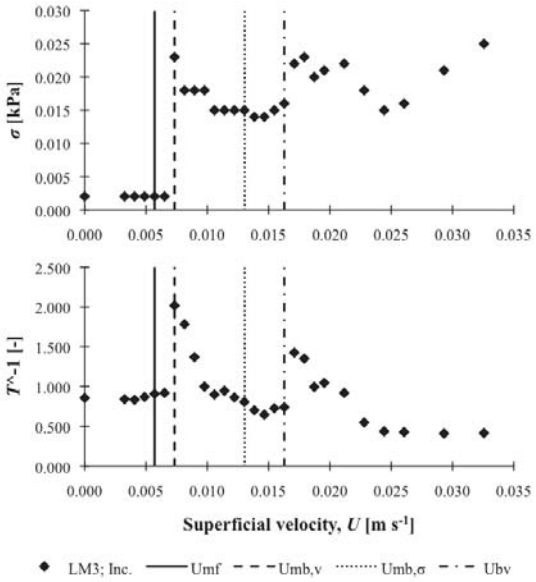

Figure A5.37 Plots of σ and T^{-1} versus U for lactose LM3 and increasing U

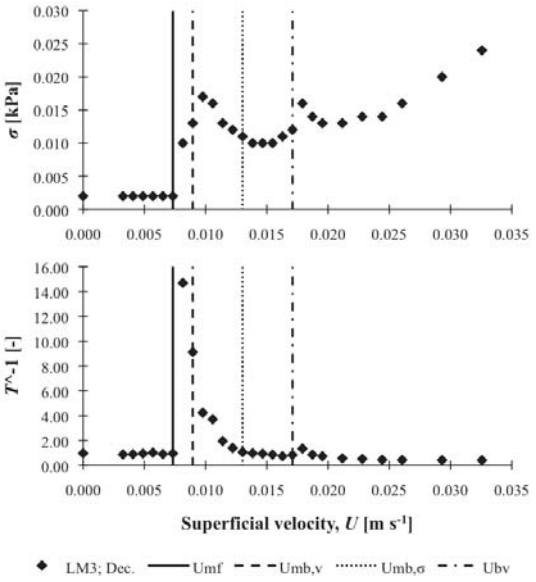

Figure A5.38 Plots of σ and T^{-1} versus U for lactose LM3 and decreasing U

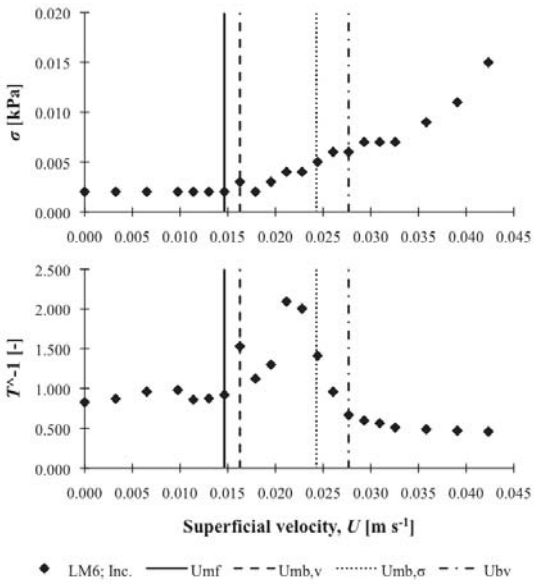

Figure A5.39 Plots of σ and T^{-1} versus U for lactose LM6 and increasing U

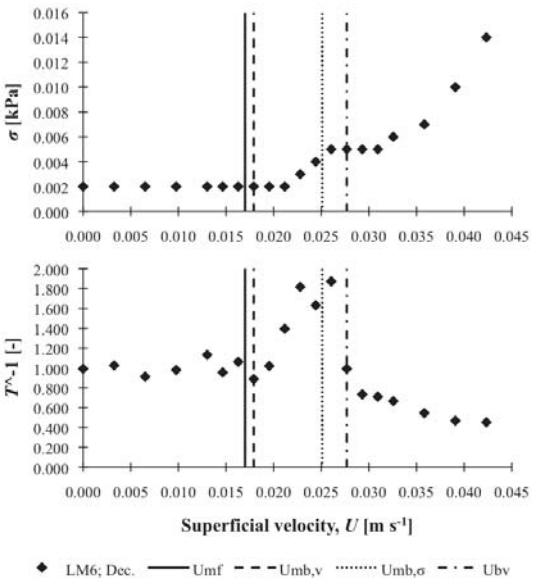

Figure A5.40 Plots of σ and T^{-1} versus U for lactose LM6 and decreasing U

Appendix 5.5

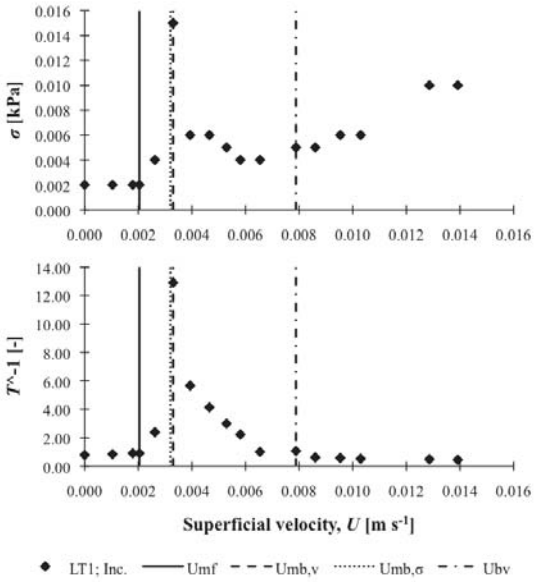

Figure A5.41 Plots of σ and T^{-1} versus U for lactose LT1 and increasing U

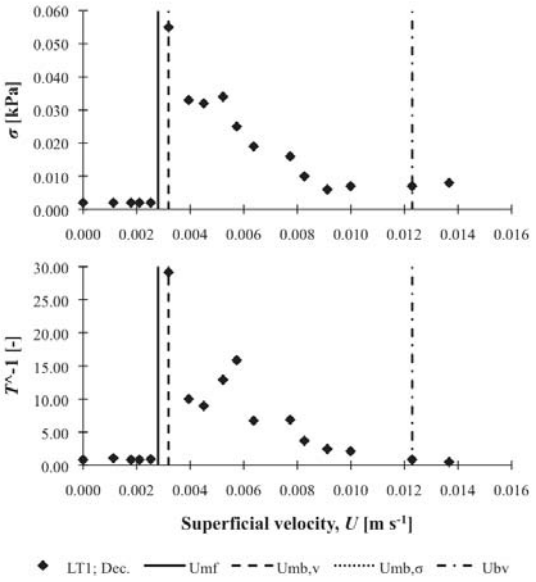

Figure A5.42 Plots of σ and T^{-1} versus U for lactose LT1 and decreasing U

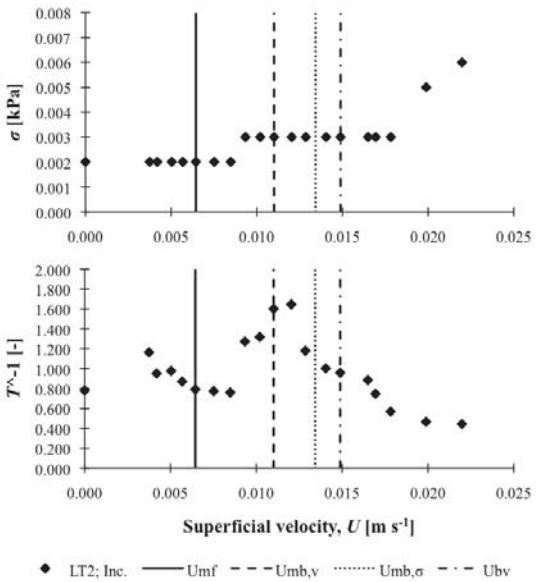

Figure A5.43 Plots of σ and T^{-1} versus U for lactose LT2 and increasing U

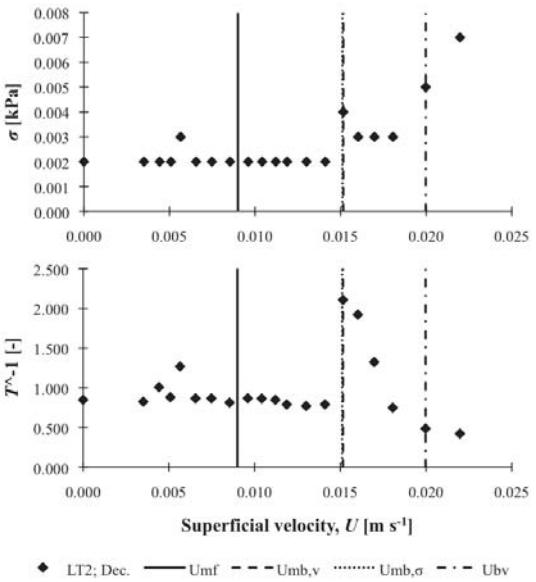

Figure A5.44 Plots of σ and T^{-1} versus U for lactose LT2 and decreasing U

Appendix 5.5

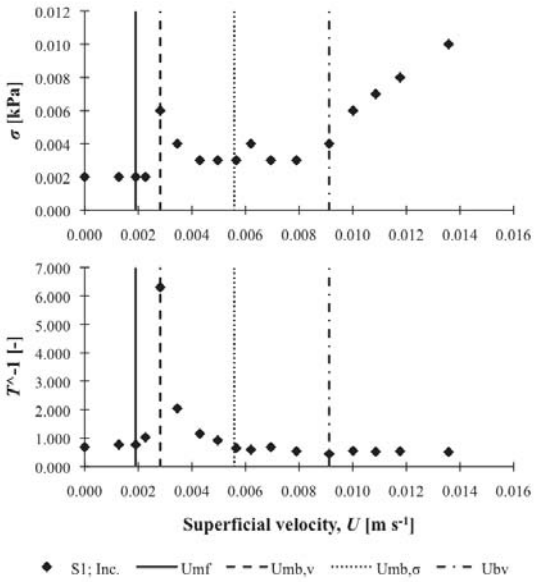

Figure A5.45 Plots of σ and T^{-1} versus U for sand S1 and increasing U

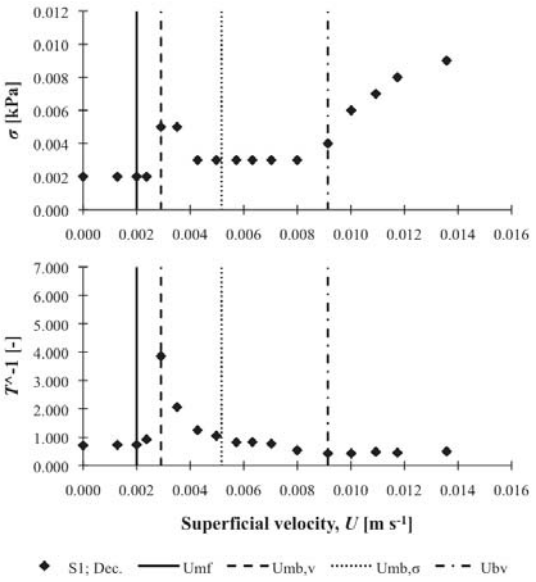

Figure A5.46 Plots of σ and T^{-1} versus U for sand S1 and decreasing U

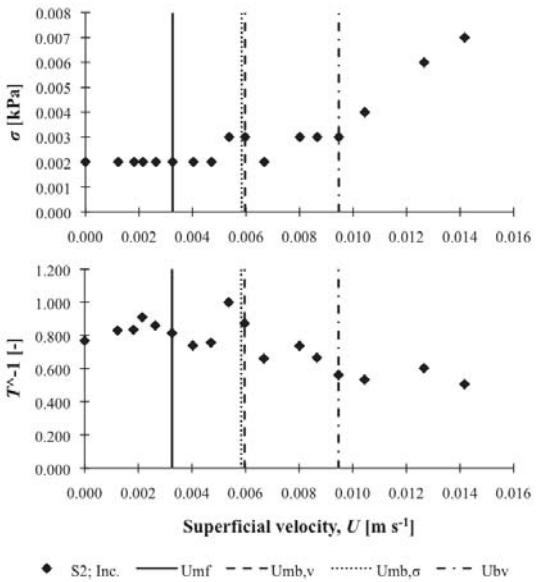

Figure A5.47 Plots of σ and T^{-1} versus U for sand S2 and increasing U

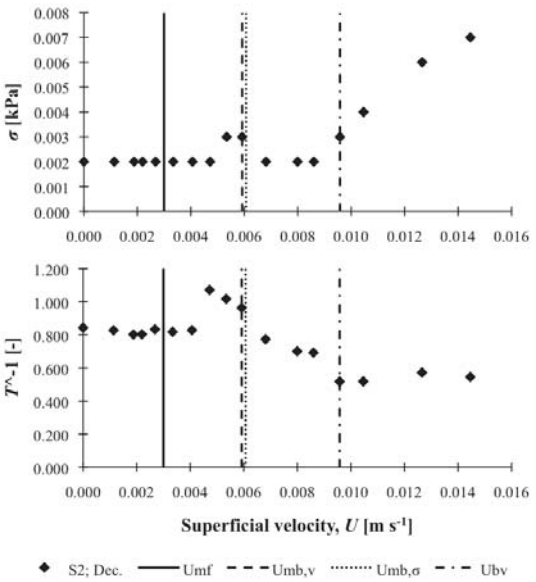

Figure A5.48 Plots of σ and T^{-1} versus U for sand S2 and decreasing U

Appendix 5.5

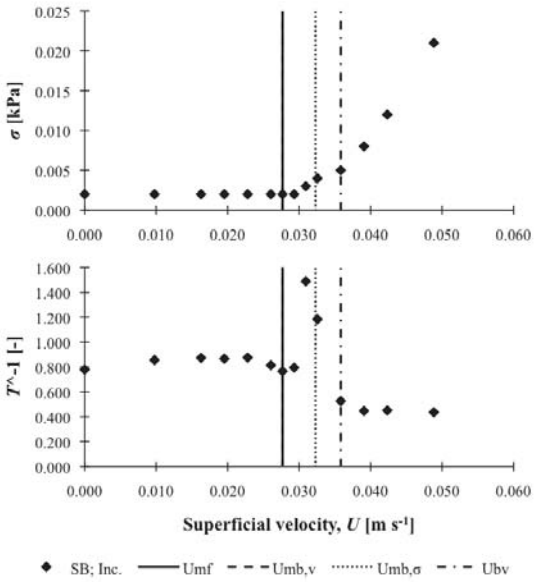

Figure A5.49 Plots of σ and T^{-1} versus U for sand SB and increasing U

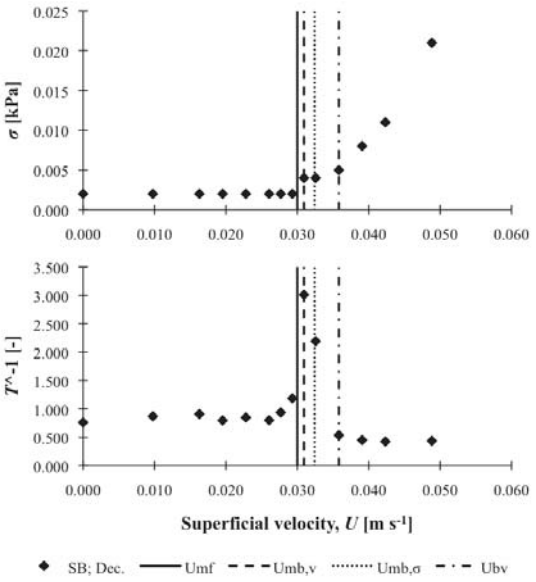

Figure A5.50 Plots of σ and T^{-1} versus U for sand SB and decreasing U

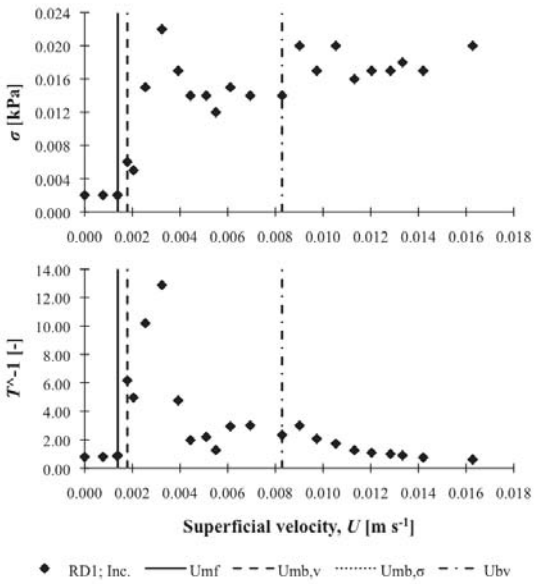

Figure A5.51 Plots of σ and T^{-1} versus U for refractory dust RD1 and increasing U

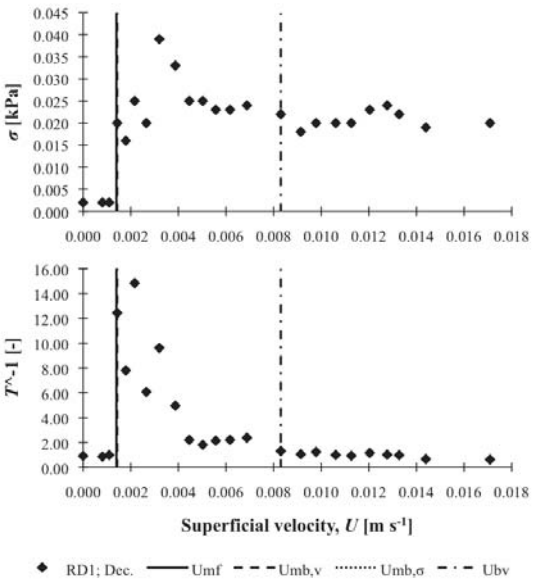

Figure A5.52 Plots of σ and T^{-1} versus U for refractory dust RD1 and decreasing U

Appendix 5.5

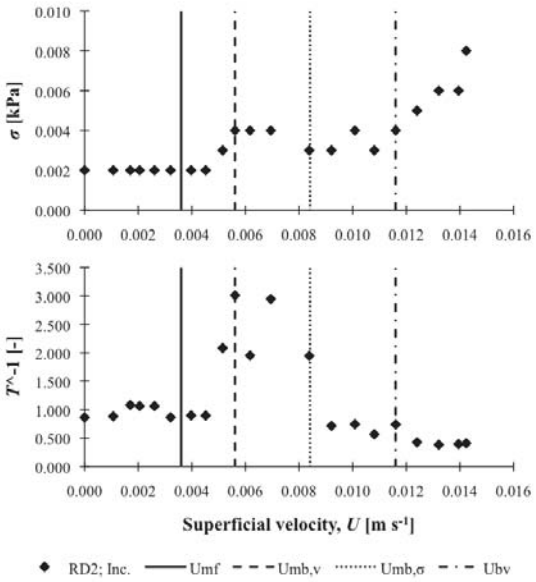

Figure A5.53 Plots of σ and T^{-1} versus U for refractory dust RD2 and increasing U

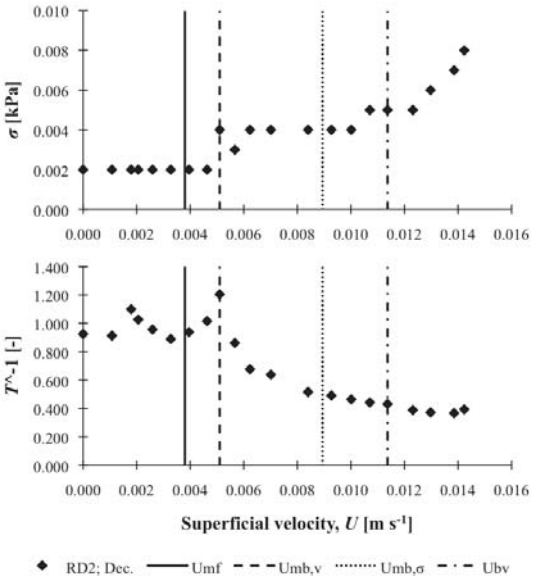

Figure A5.54 Plots of σ and T^{-1} versus U for refractory dust RD2 and decreasing U

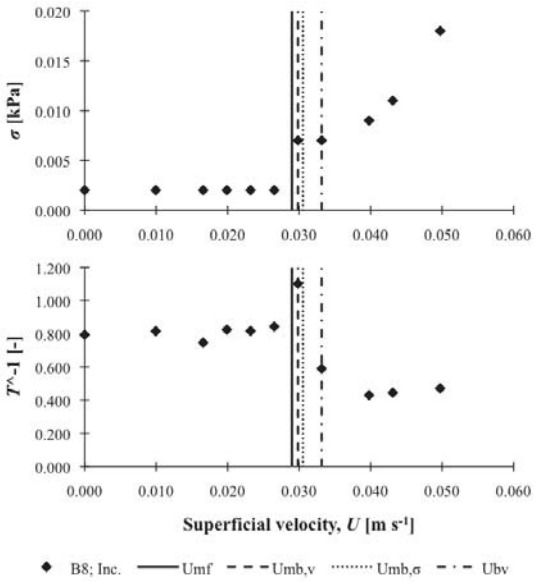

Figure A5.55 Plots of σ and T^{-1} versus U for glass beads B8 and increasing U

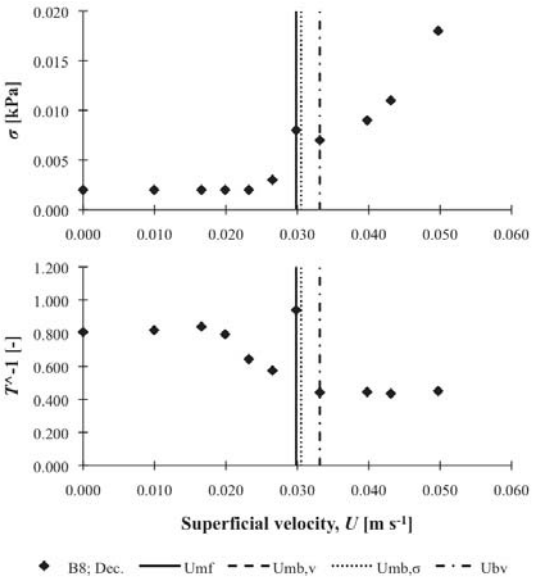

Figure A5.56 Plots of σ and T^{-1} versus U for glass beads B8 and decreasing U

Appendix 6.1

ELSEVIER LICENSE
TERMS AND CONDITIONS

Jan 09, 2015

This is a License Agreement between Horng Yuan Saw ("You") and Elsevier ("Elsevier") provided by Copyright Clearance Center ("CCC"). The license consists of your order details, the terms and conditions provided by Elsevier, and the payment terms and conditions.

All payments must be made in full to CCC. For payment instructions, please see information listed at the bottom of this form.

Supplier	Elsevier Limited The Boulevard,Langford Lane Kidlington,Oxford,OX5 1GB,UK
Registered Company Number	1982084
Customer name	Horng Yuan Saw
Customer address	Private Bag 11 222 Palmerston North, 4442
License number	3544690678976
License date	Jan 09, 2015
Licensed content publisher	Elsevier
Licensed content publication	Chemical Engineering Science
Licensed content title	Onset of an innovative gasless fluidized bed—comparative study on the fluidization of fine powders in a rotating drum and a traditional fluidized bed
Licensed content author	None
Licensed content date	1 February 2010
Licensed content volume number	65
Licensed content issue number	3
Number of pages	13
Start Page	1261
End Page	1273
Type of Use	reuse in a thesis/dissertation
Portion	figures/tables/illustrations
Number of figures/tables/illustrations	1
Format	both print and electronic
Are you the author of this Elsevier article?	No
Will you be translating?	No

Appendix 6.1

Will you be translating?	No
Original figure numbers	Fig. 1
Title of your thesis/dissertation	Characterization and Flow of Food Powders
Expected completion date	Nov 2015
Estimated size (number of pages)	300
Elsevier VAT number	GB 494 6272 12
Permissions price	0.00 USD
VAT/Local Sales Tax	0.00 USD / 0.00 GBP
Total	0.00 USD
Terms and Conditions	

INTRODUCTION

1. The publisher for this copyrighted material is Elsevier. By clicking "accept" in connection with completing this licensing transaction, you agree that the following terms and conditions apply to this transaction (along with the Billing and Payment terms and conditions established by Copyright Clearance Center, Inc. ("CCC"), at the time that you opened your Rightslink account and that are available at any time at http://myaccount.copyright.com).

GENERAL TERMS

2. Elsevier hereby grants you permission to reproduce the aforementioned material subject to the terms and conditions indicated.

3. Acknowledgement: If any part of the material to be used (for example, figures) has appeared in our publication with credit or acknowledgement to another source, permission must also be sought from that source. If such permission is not obtained then that material may not be included in your publication/copies. Suitable acknowledgement to the source must be made, either as a footnote or in a reference list at the end of your publication, as follows:

"Reprinted from Publication title, Vol /edition number, Author(s), Title of article / title of chapter, Pages No., Copyright (Year), with permission from Elsevier [OR APPLICABLE SOCIETY COPYRIGHT OWNER]." Also Lancet special credit - "Reprinted from The Lancet, Vol. number, Author(s), Title of article, Pages No., Copyright (Year), with permission from Elsevier."

4. Reproduction of this material is confined to the purpose and/or media for which permission is hereby given.

5. Altering/Modifying Material: Not Permitted. However figures and illustrations may be altered/adapted minimally to serve your work. Any other abbreviations, additions, deletions and/or any other alterations shall be made only with prior written authorization of Elsevier Ltd. (Please contact Elsevier at permissions@elsevier.com)

6. If the permission fee for the requested use of our material is waived in this instance, please be advised that your future requests for Elsevier materials may attract a fee.

Appendix 6.1

7. Reservation of Rights: Publisher reserves all rights not specifically granted in the combination of (i) the license details provided by you and accepted in the course of this licensing transaction, (ii) these terms and conditions and (iii) CCC's Billing and Payment terms and conditions.

8. License Contingent Upon Payment: While you may exercise the rights licensed immediately upon issuance of the license at the end of the licensing process for the transaction, provided that you have disclosed complete and accurate details of your proposed use, no license is finally effective unless and until full payment is received from you (either by publisher or by CCC) as provided in CCC's Billing and Payment terms and conditions. If full payment is not received on a timely basis, then any license preliminarily granted shall be deemed automatically revoked and shall be void as if never granted. Further, in the event that you breach any of these terms and conditions or any of CCC's Billing and Payment terms and conditions, the license is automatically revoked and shall be void as if never granted. Use of materials as described in a revoked license, as well as any use of the materials beyond the scope of an unrevoked license, may constitute copyright infringement and publisher reserves the right to take any and all action to protect its copyright in the materials.

9. Warranties: Publisher makes no representations or warranties with respect to the licensed material.

10. Indemnity: You hereby indemnify and agree to hold harmless publisher and CCC, and their respective officers, directors, employees and agents, from and against any and all claims arising out of your use of the licensed material other than as specifically authorized pursuant to this license.

11. No Transfer of License: This license is personal to you and may not be sublicensed, assigned, or transferred by you to any other person without publisher's written permission.

12. No Amendment Except in Writing: This license may not be amended except in a writing signed by both parties (or, in the case of publisher, by CCC on publisher's behalf).

13. Objection to Contrary Terms: Publisher hereby objects to any terms contained in any purchase order, acknowledgment, check endorsement or other writing prepared by you, which terms are inconsistent with these terms and conditions or CCC's Billing and Payment terms and conditions. These terms and conditions, together with CCC's Billing and Payment terms and conditions (which are incorporated herein), comprise the entire agreement between you and publisher (and CCC) concerning this licensing transaction. In the event of any conflict between your obligations established by these terms and conditions and those established by CCC's Billing and Payment terms and conditions, these terms and conditions shall control.

14. Revocation: Elsevier or Copyright Clearance Center may deny the permissions described in this License at their sole discretion, for any reason or no reason, with a full refund payable to you. Notice of such denial will be made using the contact information provided by you. Failure to receive such notice will not alter or invalidate the denial. In no event will Elsevier or Copyright Clearance Center be responsible or liable for any costs, expenses or damage incurred by you as a result of a denial of your permission request, other than a refund of the amount(s) paid by you to Elsevier and/or Copyright Clearance Center for denied permissions.

Appendix 6.1

LIMITED LICENSE

The following terms and conditions apply only to specific license types:

15. **Translation**: This permission is granted for non-exclusive world **English** rights only unless your license was granted for translation rights. If you licensed translation rights you may only translate this content into the languages you requested. A professional translator must perform all translations and reproduce the content word for word preserving the integrity of the article. If this license is to re-use 1 or 2 figures then permission is granted for non-exclusive world rights in all languages.

16. **Posting licensed content on any Website**: The following terms and conditions apply as follows: Licensing material from an Elsevier journal: All content posted to the web site must maintain the copyright information line on the bottom of each image; A hyper-text must be included to the Homepage of the journal from which you are licensing at http://www.sciencedirect.com/science/journal/xxxxx or the Elsevier homepage for books at http://www.elsevier.com; Central Storage: This license does not include permission for a scanned version of the material to be stored in a central repository such as that provided by Heron/XanEdu.

Licensing material from an Elsevier book: A hyper-text link must be included to the Elsevier homepage at http://www.elsevier.com . All content posted to the web site must maintain the copyright information line on the bottom of each image.

Posting licensed content on Electronic reserve: In addition to the above the following clauses are applicable: The web site must be password-protected and made available only to bona fide students registered on a relevant course. This permission is granted for 1 year only. You may obtain a new license for future website posting.

For journal authors: the following clauses are applicable in addition to the above: Permission granted is limited to the author accepted manuscript version* of your paper.

***Accepted Author Manuscript (AAM) Definition:** An accepted author manuscript (AAM) is the author's version of the manuscript of an article that has been accepted for publication and which may include any author-incorporated changes suggested through the processes of submission processing, peer review, and editor-author communications. AAMs do not include other publisher value-added contributions such as copy-editing, formatting, technical enhancements and (if relevant) pagination.

You are not allowed to download and post the published journal article (whether PDF or HTML, proof or final version), nor may you scan the printed edition to create an electronic version. A hyper-text must be included to the Homepage of the journal from which you are licensing at http://www.sciencedirect.com/science/journal/xxxxx. As part of our normal production process, you will receive an e-mail notice when your article appears on Elsevier's online service ScienceDirect (www.sciencedirect.com). That e-mail will include the article's Digital Object Identifier (DOI). This number provides the electronic link to the published article and should be included in the posting of your personal version. We ask that you wait until you receive this e-mail and have the DOI to do any posting.

Posting to a repository: Authors may post their AAM immediately to their employer's institutional repository for internal use only and may make their manuscript publically

Appendix 6.1

available after the journal-specific embargo period has ended.

Please also refer to Elsevier's Article Posting Policy for further information.

18. **For book authors** the following clauses are applicable in addition to the above: Authors are permitted to place a brief summary of their work online only.. You are not allowed to download and post the published electronic version of your chapter, nor may you scan the printed edition to create an electronic version. **Posting to a repository:** Authors are permitted to post a summary of their chapter only in their institution's repository.

20. **Thesis/Dissertation**: If your license is for use in a thesis/dissertation your thesis may be submitted to your institution in either print or electronic form. Should your thesis be published commercially, please reapply for permission. These requirements include permission for the Library and Archives of Canada to supply single copies, on demand, of the complete thesis and include permission for Proquest/UMI to supply single copies, on demand, of the complete thesis. Should your thesis be published commercially, please reapply for permission.

Elsevier Open Access Terms and Conditions

Elsevier publishes Open Access articles in both its Open Access journals and via its Open Access articles option in subscription journals.

Authors publishing in an Open Access journal or who choose to make their article Open Access in an Elsevier subscription journal select one of the following Creative Commons user licenses, which define how a reader may reuse their work: Creative Commons Attribution License (CC BY), Creative Commons Attribution – Non Commercial - ShareAlike (CC BY NC SA) and Creative Commons Attribution – Non Commercial – No Derivatives (CC BY NC ND)

Terms & Conditions applicable to all Elsevier Open Access articles:

Any reuse of the article must not represent the author as endorsing the adaptation of the article nor should the article be modified in such a way as to damage the author's honour or reputation.

The author(s) must be appropriately credited.

If any part of the material to be used (for example, figures) has appeared in our publication with credit or acknowledgement to another source it is the responsibility of the user to ensure their reuse complies with the terms and conditions determined by the rights holder.

Additional Terms & Conditions applicable to each Creative Commons user license:

CC BY: You may distribute and copy the article, create extracts, abstracts, and other revised versions, adaptations or derivative works of or from an article (such as a translation), to include in a collective work (such as an anthology), to text or data mine the article, including for commercial purposes without permission from Elsevier

CC BY NC SA: For non-commercial purposes you may distribute and copy the article,

Appendix 6.1

create extracts, abstracts and other revised versions, adaptations or derivative works of or from an article (such as a translation), to include in a collective work (such as an anthology), to text and data mine the article and license new adaptations or creations under identical terms without permission from Elsevier

CC BY NC ND: For non-commercial purposes you may distribute and copy the article and include it in a collective work (such as an anthology), provided you do not alter or modify the article, without permission from Elsevier

Any commercial reuse of Open Access articles published with a CC BY NC SA or CC BY NC ND license requires permission from Elsevier and will be subject to a fee.

Commercial reuse includes:

- Promotional purposes (advertising or marketing)
- Commercial exploitation (e.g. a product for sale or loan)
- Systematic distribution (for a fee or free of charge)

Please refer to Elsevier's Open Access Policy for further information.

21. **Other Conditions**:

v1.7

Questions? customercare@copyright.com or +1-855-239-3415 (toll free in the US) or +1-978-646-2777.

Gratis licenses (referencing $0 in the Total field) are free. Please retain this printable license for your reference. No payment is required.

Appendix 6.2

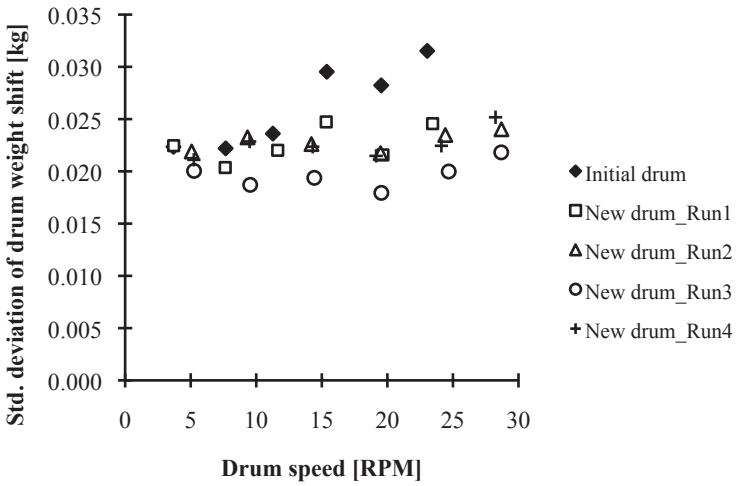

Figure A6.1 Plot of standard deviation of drum weight shift against drum speed for two empty cylindrical drums